
# CONTRIBUTIONS ON DC MICROGRID SUPERVISION AND CONTROL STRATEGIES FOR EFFICIENCY OPTIMIZATION THROUGH BATTERY MODELING, MANAGEMENT, AND BALANCING TECHNIQUES

**David García Elvira**

UNIVERSITAT ROVIRA I VIRGILI
CONTRIBUTIONS ON DC MICROGRID SUPERVISION AND CONTROL STRATEGIES FOR EFFICIENCY OPTIMIZATION THROUGH BATTERY MODELING, MANAGEMENT, AND BALANCING TECHNIQUES
David García Elvira

UNIVERSITAT ROVIRA i VIRGILI

# Contributions on DC microgrid Supervision and Control Strategies, for Efficiency Optimization through Battery Modeling, Management, and Balancing Techniques

---

DAVID GARCÍA ELVIRA

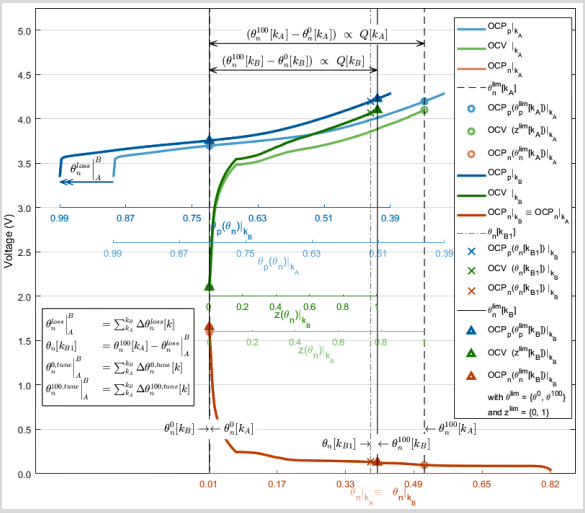


**DOCTORAL THESIS, May 2021**

UNIVERSITAT ROVIRA I VIRGILI
CONTRIBUTIONS ON DC MICROGRID SUPERVISION AND CONTROL STRATEGIES FOR EFFICIENCY OPTIMIZATION THROUGH BATTERY MODELING, MANAGEMENT, AND BALANCING TECHNIQUES
David García Elvira

UNIVERSITAT ROVIRA I VIRGILI
CONTRIBUTIONS ON DC MICROGRID SUPERVISION AND CONTROL STRATEGIES FOR EFFICIENCY OPTIMIZATION THROUGH BATTERY MODELING, MANAGEMENT, AND BALANCING TECHNIQUES
David García Elvira

UNIVERSITAT ROVIRA I VIRGILI
CONTRIBUTIONS ON DC MICROGRID SUPERVISION AND CONTROL STRATEGIES FOR EFFICIENCY OPTIMIZATION THROUGH BATTERY MODELING, MANAGEMENT, AND BALANCING TECHNIQUES
David García Elvira

UNIVERSITAT ROVIRA i VIRGILI

DAVID GARCÍA ELVIRA

# CONTRIBUTIONS ON DC MICROGRID SUPERVISION AND CONTROL STRATEGIES FOR EFFICIENCY OPTIMIZATION THROUGH BATTERY MODELING, MANAGEMENT, AND BALANCING TECHNIQUES

DOCTORAL THESIS

Thesis advisors:
Dr. Hugo Valderrama Blavi
Dr. Àngel Cid Pastor

Department of Electronic, Electric and Automatic Control Engineering
Automatic Control and Industrial Electronics Group
Tarragona, May 2021

UNIVERSITAT ROVIRA i VIRGILI

FAIG CONSTAR que aquest treball, titulat “Contributions on DC microgrid supervision and control strategies, for efficiency optimization through battery modeling, management, and balancing techniques”, que presenta David García Elvira per a l’obtenció del títol de Doctor, ha estat realitzat sota la meva Direcció al Departament d’Enginyeria Electrònica, Elèctrica i Automàtica d’aquesta universitat i acompleix els requisits per poder optar a la Menció Internacional.

HAGO CONSTAR que el presente trabajo, titulado “Contributions on DC microgrid supervision and control strategies, for efficiency optimization through battery modeling, management, and balancing techniques”, que presenta David García Elvira para la obtención del título de Doctor, ha sido realizado bajo mi dirección en el Departamento de Ingeniería Electrónica Eléctrica y Automática de esta universidad y cumple los requisitos para poder optar a la Mención Internacional.

I STATE that the present STUDY, entitled “Contributions on DC microgrid supervision and control strategies, for efficiency optimization through battery modeling, management, and balancing techniques”, presented by David García Elvira for the award of the degree of Doctor, has been carried out under my supervision at the Department of Electronic, Electrical and Automatic Control Engineering of this university and accomplishes all the requirements for being granted with the International Mention.

Tarragona, April 1, 2021
El/s director/s de la tesi doctoral
El/los director/es de la tesis doctoral
Doctoral Thesis Supervisor/s

Hugo Valderrama Blavi - DNI 39691310A (AUT)

Digitally signed by Hugo Valderrama Blavi - DNI 39691310A (AUT)
DN: c=ES, o=Universitat Rovira i Virgili, 2.5.4.97=VATES-Q9350003A, ou=Treballador públic de nivell alt d'autenticació, sn=Valderrama Blavi - DNI 39691310A, givenName=Hugo, serialNumber=IDCES-39691310A, cn=Hugo Valderrama Blavi - DNI 39691310A (AUT)
Date: 2021.03.30 16:20:28 +02'00'

Dr. Hugo Valderrama Blavi

Angel Cid Pastor - DNI 52605068C (AUT)

Firmado digitalmente por Angel Cid Pastor - DNI 52605068C (AUT)
Nombre de reconocimiento (DN): c=ES, o=Universitat Rovira i Virgili, 2.5.4.97=VATES-Q9350003A, ou=Treballador públic de nivell alt d'autenticació, sn=Cid Pastor - DNI 52605068C, givenName=Angel, serialNumber=IDCES-52605068C, cn=Angel Cid Pastor - DNI 52605068C (AUT)
Fecha: 2021.03.28 12:25:43 +02'00'

Dr. Àngel Cid Pastor

# ACKNOWLEDGEMENTS

Many colleagues have collaborated to make possible this dissertation. This section is dedicated to warmly acknowledging their works. Thanks to:

- Dr. Hugo Valderrama Blavi and Dr. Àngel Cid Pastor (PhD supervisors), for designing and building the GAEI's microgrid, for sharing their deep technical knowledge, and for being close colleagues.
- Dr. Josep Maria Bosque Moncusí (former GAEI laboratory manager), for building the GAEI's microgrid and the equalizer prototype studied here.
- Francisco Sevilla (URV student), for mounting the battery aging test platform.
- Maxime Buthiau (exchange student from Université de Bordeaux), for performing battery tests that would lead to characterize them.
- Remi Dubuc (exchange student from Université de Bordeaux), for starting to code the control scheme into the equalizer.
- Xavier Barthod (exchange student from Institut National des Sciences Appliquées de Toulouse), for completing and debugging the equalizer program, coding the battery model calculations into the algorithm, adding data logging and designing a current-sensor printed circuit board.
- Quentin Batac (exchange student from Université de Bordeaux), for identifying some problems in the current-sensor design and redesigning it.
- Xavi Genaro Muñoz (GAEI laboratory technician), for teaming himself with all the collaborators above and being an invaluable help in the process of enhancing, programming, and testing the equalizer prototype.
- Department of Electrical and Computer Engineering of the UCCS, for providing extensive information and support about battery modeling and for facilitating the test scripts used to characterize the batteries.
- Gemma Jenny (personal friend), for helping with the dissertation formatting.

I want to specially thank my mother and friends, for teaching me more than any book could, and for providing invaluable emotional support and care. All my love to them.

Thesis dissertation written by David García Elvira

Contributions on DC microgrid supervision and control strategies for efficiency optimization through battery modeling, management, and balancing techniques

Ph.D. in Technologies for Nanosystems, Bioengineering and Energy

The work presented in this PhD Thesis has been funded by the Spanish Ministry of Science, Innovation and Universities and the European Social Fund under grants BES-2016-077460, DPI2015-67292-R and DPI2017-84572-C2-1-R.

The research leading to the results presented here has been conducted at the Universitat Rovira I Virgili, Tarragona (Spain), under the supervision of Dr. Hugo Valderrama Blavi and Dr. Àngel Cid Pastor; and at the University of Colorado Colorado Springs, Colorado (USA), under the supervision of Dr. M. Scott Trimboli.

*Va por mis amigas, rebeldes, imperfectas,*
*lo que hay entre nosotras: afinidad y afecto.*
*Por mostrarme tantas veces que estamos juntas en esto,*
*seguir en el camino hacia adelante y todo recto.*
*Porque habláis con claridad en medio de tanto murmullo,*
*los años con vosotras se cumplen con orgullo.*
*Lo que compartimos para mí es oro en paño,*
*le estamos echando ganas y eso a veces hace daño...*
*Que si sangráis yo sangro, que si reís yo río,*
*que busco vuestro apoyo cuando me siento perdido,*
*que siempre me lo disteis a cambio de nada,*
*no hay calculadoras ni deudas apuntadas.*
*Las lágrimas me saltan por sentiros tan cercanas,*
*de madres diferentes la vida nos hizo hermanas.*
*Creedme cuando os diga que sois lo que más quiero,*
*y vuestro calor me abriga, aunque estemos bajo cero.*

*Pase lo que pase no bajéis los brazos,*
*por los puñetazos y por los abrazos.*

*FA3. XIII / XII*

# RESUM

Aquesta tesi presenta un conjunt d'equips, models i estratègies de control, que han estat desenvolupats amb l'objectiu final de millorar el funcionament d'una microxarxa de CC.

S'ha modelat i simulat una microxarxa de CC amb tensió de bus variable en Simulink, amb el propòsit d'avaluar estratègies d'optimització. La microxarxa es controla inicialment mitjançant Control d'Esdeveniments de Tensió (VEC, Voltage Event Control) complementat amb Control d'Esdeveniments d'Estat de Càrrega (SOCEC, State of Charge Event Control), que determina l'energia generada / consumida per cada unitat de la microxarxa segons els valors de la tensió del bus i l'estat de càrrega (SOC) de la bateria. Es proposen i avaluen dues estratègies complementàries per a millorar l'eficiència dels convertidors CC-CC que interconnecten les unitats de potència de la microxarxa amb el bus CC. La primera estratègia de control proposada és el Control Centralitzat d'Optimització de Tensió de Bus, que administra la potència del Sistema d'Emmagatzematge d'Energia en Bateries de la microxarxa per a fer que la tensió del bus segueixi la referència dinàmica de tensió òptima que minimitza les pèrdues dels convertidors. La segona estratègia de control és l'Optimització en Temps Real de la Freqüència de Commutació, que consisteix a operar localment cada convertidor a la seva freqüència de commutació òptima, de nou minimitzant les seves pèrdues de potència. Les dues estratègies d'optimització proposades s'han verificat en simulacions.

Addicionalment, s'ha proposat una nova topologia d'equilibrador actiu de bateries, amb un convertidor com a element central, i s'ha dissenyat la seva estratègia de control. Aquesta topologia d'equalitzador consta d'un únic convertidor CC-CC que realitza la transferència de càrrega cel·la a cel·la emprant encaminament de potència a través d'un sistema d'interruptors controlats, que funcionen com a multiplexors de potència. S'ha modelat i simulat un pack de bateries per a avaluar la seva tendència natural al desequilibri. L'estratègia de control de l'equalitzador s'ha dissenyat per a aconseguir un ràpid equilibratge del SOC alhora que s'evita la sobrecompensació del desequilibri. El seu funcionament ha estat validat en simulació. L'equalitzador demostra que és capaç d'equilibrar un pack de cinc bateries monobloc, compensant la discrepància de paràmetres i la desviació inicial del SOC. La influència de quatre paràmetres de bateria en la divergència del SOC ha estat analitzada.

Finalment, es proposa un model simple de degradació d'una cel·la d'ió-liti NMC amb elèctrode negatiu de grafit. El model combina la simplicitat d'un model de circuit equivalent, que explica la dinàmica ràpida de la cel·la, amb un model físic del procés de creixement de la capa d'Interfase Sòlid-Electròlit (SEI, Solid-Electrolyte Interphase), que prediu la pèrdua de capacitat i l'augment de la resistència interna en el llarg termini. La reacció SEI implica pèrdua

d'inventari de liti de l'elèctrode negatiu. Això produeix un desplaçament relatiu entre les finestres estequiomètriques dels elèctrodes negatiu i positiu que, al seu torn, modifica la corba de tensió de circuit obert (OCV, Open Circuit Voltage) vs. SOC de la cel·la. Atès que els límits de litiación dels elèctrodes es defineixen per a la cel·la modelada per valors extrems de OCV, la modificació de la corba de OCV vs. SOC provoca una recuperació secundària de capacitat. Després de la degradació, és necessari que una fracció de les reserves de liti prèviament no utilitzades de ambdós elèctrodes s'incorpori al rang de liti ciclable per a arribar als límits de tensió OCV. El model proposat quantifica aquest procés per a ajustar la predicció de pèrdua de capacitat. El model de degradació SEI es pot utilitzar per a realitzar un control predictiu de bateries orientat a estendre la seva vida útil.

Paraules clau: Microxarxa CC, Optimització del rendiment energètic, Sistema actiu d’equilibrat de bateries, Multiplexat de potencia cel·la a cel·la, Creixement de la capa Interfase-Sòlid-Electròlit, Model de degradació de bateries.

# RESUMEN

Esta tesis presenta un conjunto de equipos, modelos y estrategias de control, que han sido desarrollados con el objetivo final de mejorar el funcionamiento de una microrred de CC.

Se ha modelado y simulado una microrred de CC con tensión de bus variable en Simulink, con el propósito de evaluar estrategias de optimización. La microrred se controla inicialmente mediante Control de Eventos de Tensión (VEC, Voltage Event Control) complementado con Control de Eventos de Estado de Carga (SOCEC, State of Charge Event Control), que determina la energía generada / consumida por cada unidad de la microrred según los valores de la tensión del bus y el estado de carga (SOC) de la batería. Se proponen y evalúan dos estrategias complementarias para mejorar la eficiencia de los convertidores CC-CC que interconectan las unidades de potencia de la microrred con el bus CC. La primera estrategia de control propuesta es el Control Centralizado de Optimización de Tensión de Bus, que administra la potencia del Sistema de Almacenamiento de Energía en Baterías de la microrred para hacer que la tensión del bus siga la referencia dinámica de tensión óptima que minimiza las pérdidas de los convertidores. La segunda estrategia de control es la Optimización en Tiempo Real de la Frecuencia de Conmutación, que consiste en operar localmente cada convertidor a su frecuencia de conmutación óptima, de nuevo minimizando sus pérdidas de potencia. Las dos estrategias de optimización propuestas se han verificado en simulaciones.

Además, se ha propuesto una nueva topología de equilibrado activo de baterías, cuyo elemento central es un convertidor, y se ha diseñado su estrategia de control. Esta topología de ecualizador consta de un único convertidor CC-CC que realiza la transferencia de carga celda a celda empleando enrutamiento de potencia a través de un sistema de interruptores controlados, que funcionan como multiplexores de potencia. Se ha modelado y simulado un pack de baterías para evaluar su tendencia natural al desequilibrio. La estrategia de control del ecualizador ha sido diseñada para lograr un rápido equilibrado del SOC a la vez que se evita la sobrecompensación del desequilibrio. Su desempeño ha sido validado en simulación. El ecualizador demuestra que es capaz de equilibrar un pack de cinco baterías monobloc, compensando la discrepancia de parámetros y la desviación inicial del SOC. La influencia de cuatro parámetros de batería en la divergencia del SOC ha sido analizada.

Finalmente, se propone un modelo simple de degradación de una celda de ion-litio NMC con electrodo negativo de grafito. El modelo combina la simplicidad de un modelo de circuito equivalente, que explica la dinámica rápida de la celda, con un modelo físico del proceso de crecimiento de la capa de Interfase Sólido-Electrolito (SEI, Solid-Electrolyte Interphase), que predice la pérdida de capacidad y el aumento de la resistencia interna a largo plazo. La

reacción SEI implica pérdida de inventario de litio del electrodo negativo. Esto produce un desplazamiento relativo entre las ventanas estequiométricas de los electrodos negativo y positivo que, a su vez, modifica la curva de tensión de circuito abierto (OCV, Open Circuit Voltage) vs. SOC de la celda. Dado que los límites de litiación de los electrodos se definen para la celda modelada por valores extremos de OCV, la modificación de la curva de OCV vs. SOC provoca una recuperación secundaria de capacidad. Tras la degradación, es necesario que una fracción de las reservas de litio previamente no utilizadas de ambos electrodos se incorpore al rango de litio ciclable para alcanzar los límites de OCV. El modelo propuesto cuantifica este proceso para ajustar la predicción de pérdida de capacidad. El modelo de degradación SEI se puede utilizar para realizar un control predictivo de baterías orientado a extender su vida útil.

Palabras clave: Microrred CC, Optimización del rendimiento energético, Sistema activo de equilibrado de baterías, Multiplexado de potencia celda a celda, Crecimiento de la capa Interfase Sólido-Electrolito, Modelo de degradación de baterías

# ABSTRACT

This dissertation presents a set of equipment, models and control strategies, that have been developed with the final goal of improving the operation of a DC microgrid.

A variable bus voltage DC microgrid has been modeled and simulated in Simulink for optimization purposes. The microgrid is initially controlled with primary droop Voltage Event Control (VEC) supplemented with State of Charge Event Control (SOCEC), which determine the power generated/consumed by each unit of the microgrid based on bus voltage and battery State of Charge (SOC). Two supplementary strategies are proposed and evaluated to improve the efficiency of the DC-DC converters that interface the microgrid's power units with the DC bus. The first proposed control strategy is centralized Bus Voltage Optimization Control, which manages the power of the microgrid's Battery Energy Storage System to make the bus voltage follow the optimum-voltage dynamic reference that minimizes the converters' losses. The second control strategy is Online Optimization of Switching Frequency, which consists in locally operating each converter at its optimum switching frequency, again minimizing power losses. The two proposed optimization strategies have been verified in simulations.

Moreover, a new converter-based active balancing topology has been proposed and its control strategy has been designed. This equalizer topology consists of a single DC-DC converter that performs cell-to-cell charge transfer employing power routing via controlled switches, which are operated as power multiplexers. A battery pack has been modeled and simulated to assess its natural tendency towards imbalance. The control strategy of the equalizer has been designed to achieve rapid SOC balancing while avoiding imbalance overcompensation. Its performance has been validated in simulation. The equalizer balances a battery pack of five monobloc batteries, compensating parameter discrepancy and initial SOC deviations. The influence of four battery parameters in SOC divergence has been analyzed.

Finally, a simple degradation model of a lithium ion NMC battery cell with graphite negative electrode is proposed. The model combines the simplicity of an equivalent circuit model, which explains the fast dynamics of the cell, with a physics-based model of the Solid-Electrolyte Interphase (SEI) layer growth process, which predicts the capacity loss and the internal resistance rise in the long term. The SEI reaction involves loss of negative electrode's lithium inventory. This produces a relative displacement between the negative and the positive electrodes' stoichiometric windows which, in turn, modifies the cell's Open Circuit Voltage (OCV) vs. SOC curve. Since the electrodes' lithiation boundaries are defined for the modeled cell by extreme OCV values, modification of the OCV vs. SOC curve causes a secondary

capacity recovery. After degradation, a fraction of the previously unused lithium reserves of both electrodes needs to be incorporated into the cyclable lithium range to reach the OCV limits. The proposed model quantifies this process to fine-tune the capacity loss prediction. The SEI degradation model can be used to perform predictive control of batteries oriented toward extending their lifetime.

Keywords: DC microgrid, Energy efficiency optimization, Active battery balancing system, Cell-to-cell power multiplexing, Solid-Electrolyte Interphase growth, Degradation battery model.

# CONTENTS

# LIST OF FIGURES

# LIST OF TABLES

# LIST OF ACRONYMS

| Acronym | Meaning |
|---|---|
| AC | Alternating Current |
| B1, …, B5 | The five monobloc batteries that conform the battery pack conceived to validate the equalizer's performance in simulation |
| Batt1, …, Batt5 | The five monobloc batteries conforming the test battery pack conceived to experimentally validate the equalizer's performance |
| BESS | Battery Energy Storage System (microgrid) |
| BMS | Battery Management Systems |
| BOL | Beginning of Life |
| $B_{strong}$ | Strongest battery in a battery pack (battery balancing) |
| BVOC | Bus Voltage Optimization Control (optimization of the microgrid) |
| $B_{weak}$ | Weakest battery in a battery pack (battery balancing) |
| CC | Constant Current |
| CSLT | Capacity Single-Loop Test (SEI growth model) |
| CV | Constant Voltage |
| DC | Direct Current |
| DOD | Depth of Discharge |
| E-BCS | Events-Based Control System (base control layer of the microgrid) |
| EMS | Energy Management System |
| EOL | End of Life |
| ESC | Enhanced Self-Correcting (equivalent circuit model) |
| EV | Electric Vehicle |
| EZ | Electrolyzer (microgrid) |
| FC | Fuel Cell (microgrid) |
| FP07, …, FP15 | (Nine) Panasonic cells subjected to Self-Discharge Tests (SEI growth model) |
| GAEI | Grup d'Automàtica i Electrònica Industrial (Group of Automatic Control and Industrial Electronics) |
| HAWT | Horizontal Axis Wind Turbine |
| IGBT | Insulated-Gate Bipolar Transistor |
| INV | Bidirectional inverter (microgrid) |

| Acronym | Meaning |
|---|---|
| LCO | Li-Cobalt battery |
| LFP | Li-phosphate battery |
| LMO | Li-Manganese battery |
| LOAD | DC loads (microgrid) |
| LTO | LTO battery |
| MOSFET | Metal–Oxide–Semiconductor Field-Effect Transistor |
| MPP | Maximum Power Point |
| MPPT | Maximum Power Point Tracker |
| Na-S | Sodium–Sulfur battery |
| NCA | Nickel Cobalt Aluminum Oxide |
| NE | Negative electrode of the battery cell |
| Ni-CD | Nickel-cadmium battery |
| Ni-MH | Nickel Metal Hydride battery |
| NMC | Nickel Manganese Cobalt Oxide |
| OCP | Open Circuit Potential of the cell's electrode |
| OCV | Open Circuit Voltage of the battery cell |
| OCVT | Initial and final four-steps Open Circuit Voltage Test (SEI growth model) |
| OOSF | Online Optimization of Switching Frequency (optimization of the microgrid) |
| PE | Positive electrode of the battery cell |
| PEV | Plug-in Electric Vehicles |
| PT | Pulse Test (SEI growth model) |
| PV | Photovoltaic field (microgrid) |
| RES | Renewable Energy Sources |
| S0, S1 …, S9 | (Nine) simulation scenarios considered to validate BVOC and OOSF |
| SDT | Self-Discharge Test (SEI growth model) |
| SEI | Solid-Electrolyte Interphase |
| SOC | State of Charge |
| SOCEC | State of Charge Event Control (base control layer of the microgrid) |
| SOH | State of Health |
| UDDS | Urban Dynamometer Drive Schedule |

| Acronym | Meaning |
|---|---|
| V2G | Vehicle-to-Grid |
| VAWT | Vertical Axis Wind Turbine |
| VEC | Voltage Event Control (base control layer of the microgrid) |
| WT | Wind turbine (microgrid) |
| μG | Microgrid |
| $C$ | Capacitors used in microgrid's converters |
| $L$ | Inductors used in microgrid's converters |
| $S$ | Transistors used in microgrid's converters |
| $d$ | Diodes used in microgrid's converters |

# LIST OF PARAMETERS AND VARIABLES

| Symbol | Description | Is a variable | Units |
|---|---|---|---|
| $]f_{sw}[$ | Fixed switching frequency of a microgrid's converter when OOSF is not applied | | $Hz$ |
| $A$ | Battery-cell area | | $m^2$ |
| $A_C$ | Cross-sectional area of the inductor's core | | $m^2$ |
| $A_H$ | Hysteresis coefficient (ESC model) | ✓ | $-$ |
| $a$ | Specific interfacial surface area | | $1/m$ |
| $B$ | Discrete-time state-space state-transition matrix (used to parametrize the ESC model) | | $various$ |
| $BATTok$ | Logical variable indicating whether the microgrid's battery performs correctly (true) or presents some failure (false) | ✓ | $-$ |
| $BCPP$ | Balancing Charge Per Period | ✓ | $Ah$ |
| $C$ | Charge or discharge rate of a battery | | $A$ |
| $C_1, C_2$ | Diffusion capacitances (ESC model) | | $F$ |
| $C_p$ | Power coefficient of the wind turbine | | $-$ |
| $C_{pn}$ | Constant that links the stoichiometric windows of both electrodes | | $-$ |
| $c$ | Lithium concentration in the cell's phase | ✓ | $mol/m^3$ |
| $c_{e,0}$ | At-rest equilibrium concentration of lithium in the electrolyte | | $mol/m^3$ |
| $c^{max}$ | Maximum concentration of lithium in the material | | $mol/m^3$ |
| $D_{e,eff}$ | Effective diffusivity in the electrolyte | | $m^2/s$ |
| $D_s$ | Diffusivity of lithium in the solid | | $m^2/s$ |
| $D$ | Duty cycle of the microgrid's converter | ✓ | $-$ |
| $E$ | Energy | ✓ | $Wh$ |
| $EMSok$ | Logical variable indicating whether the microgrid's Energy Management System performs well (true) or fails (false) | ✓ | $-$ |
| $F$ | Faraday's constant | | $A\,s/mol$ |

| Symbol | Description | Is a variable | Units |
|---|---|---|---|
| $f_{\pm}$ | Mean molar activity coefficient | | $-$ |
| $f_{optim}$ | Optimum instantaneous switching frequency of the converter (OOSF) | ✓ | $Hz$ |
| $f_{sw}$ | Switching frequency of a microgrid's converter | ✓ (only in OOSF) | $Hz$ |
| $G$ | Irradiance | ✓ | $W/m^2$ |
| $I_{leak}$ | Sum of self-discharge current and current drained to feed external circuitry | | $A$ |
| $i_0$ | Exchange current density | ✓ | $A/mol$ |
| $i_{app}$ | Cell load current (discharge: $i_{app} > 0$) | ✓ | $A$ |
| $i_{lekage}$ | Current drawn from an individual cell in the battery pack to supply external circuitry | ✓ | $A$ |
| $i_{net}$ | Net cell current | ✓ | $A$ |
| $i_{self-discharge}$ | Self-discharge current | ✓ | $A$ |
| $J$ | Current density of the reaction | ✓ | $A/m^3$ |
| $j$ | Flux density (rate of lithium movement) of the reaction | ✓ | $mol/m^2 s$ |
| $K$ | Parameter of the inductor's magnetic core | | $-$ |
| $K_{demand}$ | Demand power gain, used in the microgrid model in Simulink | | $-$ |
| $K_{pv}$ | Photovoltaic power gain, used in the microgrid model in Simulink | | $-$ |
| $K_{wt}$ | Wind power gain, used in the microgrid model in Simulink | | $-$ |
| $k$ | Index of discrete time ($t = k\Delta t$) | | $-$ |
| $k_Q$ | Coefficient of capacity loss in the SEI reaction | | $m^3$ |
| $k_R$ | SEI resistance increase coefficient | | $\Omega\, m^3 \,/\, A\, s$ |
| $k_{SEI}$ | Lumped constant comprising $i_{0,side}$ and $U_{side}^{ref}$ | | $A/m^3$ |
| $k_{cv}$ | Coefficient that relates the span of measured stoichiometry values to the total range of stoichiometry values | | $-$ |

| Symbol | Description | Is a variable | Units |
|---|---|---|---|
| $k_f$ | Lumped rate constant in Dr. Safari's model of SEI growth | | $m/s$ |
| $k_n$ | Rate of electrochemical reaction | | $A\,m^{2.5} / mol^{1.5}$ |
| $k_{norm,0}$ | Normalized rate constant of the electrochemical reaction | | $mol/m^2\,s$ |
| $L$ | Inductor | | $H$ |
| $L_n$ | Thickness of the cell's negative electrode | | $m$ |
| $L_p$ | Thickness of the cell's positive electrode | | $m$ |
| $L_s$ | Thickness of the cell's separator | | $m$ |
| $L_{tot}$ | Total cell thickness | | $m$ |
| $M$ | SOC-dependent hysteresis coefficient (ESC model) | | $V$ |
| $M_0$ | Instantaneous hysteresis coefficient (ESC model) | | $V$ |
| $m_{SOCEC}$ | Power coefficient in SOC-Event Control | | $-$ |
| $m_{VEC}$ | Power coefficient in Voltage-Event Control | | $-$ |
| $m_p$ | Droop coefficient | | $V/W$ |
| $N$ | Number of turns of the inductor | | $-$ |
| $NCIR$ | Natural Charge Imbalance Rate | ✓ | $-$ |
| $n_{Li}^{cyclable}$ | Absolute number of cyclable lithium moles | ✓ | $mol$ |
| $OCP$ | Open Circuit Potential of the electrode vs $Li^+/Li$ | ✓ | $V$ |
| $OCV$ | Open Circuit Voltage | ✓ | $V$ |
| $P$ | Power | ✓ | $W$ |
| $P_{Bcontrol}$ | Power reference of the microgrid's Battery Energy Storage System ($P_{Bcontrol} \equiv P_{BESS}^{ref}$) | ✓ | $W$ |
| $P_C$ | Capacitor bank's power | ✓ | $W$ |
| $P_{Fe}$ | Core power losses | ✓ | $W$ |
| $P_{ctrl}$ | Power supply of the converter's driver | | $W$ |
| $P_{grid}$ | Power injected to the grid | ✓ | $W$ |

| Symbol | Description | Is a variable | Units |
|---|---|---|---|
| $Q$ | Battery capacity | ✓ | $Ah$ |
| $R$ | Resistance | | Ω |
| $R_0$ | Internal resistance of the fresh cell (ESC model) | | Ω |
| $R_1, R_2$ | Diffusion resistances (ESC model) | | Ω |
| $R_L$ | Parasitic series resistance of the inductor | | Ω |
| $R'_S$ | Parasitic series resistance of the transistor | | Ω |
| $R_{SEI}$ | Resistance of the SEI film | ✓ | Ω |
| $R_{WT}$ | Radius of the wind turbine | | $m$ |
| $R_d$ | Parasitic series resistance of the diode | | Ω |
| $R_g$ | Universal gas constant | | $J/mol\ K$ |
| $R_s$ | Average radius of the electrode particle | | $m$ |
| $R_z$ | SOC-dependent internal resistance (used only to calculate the $OCV$ vs. $SOC$ curve) | ✓ | Ω |
| $r$ | Pseudo-dimension of the reduced-order physics-based battery model | ✓ | $m$ |
| $r_{bal}$ | Rate of balancing | ✓ | $\%/h$ |
| $S$ | Logical variable indicating if the microgrid's bidirectional unit operates as a source (true) or as a sink (false) | ✓ | − |
| $SOC$ | State of Charge | ✓ | % |
| $SOCxBATTok$ | Logical fused variable equal to the product of $SOC$ by $BATTok$ | ✓ | % |
| $SOH$ | State of Health | ✓ | % |
| $s$ | Sign function with "memory" | ✓ | − |
| $T$ | Temperature | ✓ | $K$ |
| $T_{amb}$ | Ambient temperature in the photovoltaic field | ✓ | $K$ |
| $T_{bal}$ | Activation period in the balancing period | | $s$ |
| $T_{cycle}$ | Equalizer's balancing period | | $s$ |
| $T_{rest}$ | Rest period in the balancing period | | $s$ |

| Symbol | Description | Is a variable | Units |
|---|---|---|---|
| $t$ | Time | ✓ | $s$ |
| $t_+^0$ | Transference number of the cation with respect to the solvent | | $-$ |
| $t_{d(off)}$ | Turn-off delay of the transistor | | $s$ |
| $t_{d(on)}$ | Turn-on delay of the transistor | | $s$ |
| $t_f$ | Fall time of the transistor | | $s$ |
| $t_r$ | Rise time of the transistor | | $s$ |
| $t_{sw}$ | Total switching time of the transistor $(t_{sw} = t_{d(on)} + t_r + t_{d(off)} + t_f)$ | | $s$ |
| $U_{side}^{ref\,\Theta}$ | Fixed term in Dr. Fu's temperature-dependent model of equivalent reference potential of the SEI side reaction | | $V$ |
| $U_{side}^{ref}$ | Equivalent reference potential of the SEI side reaction | | $V$ |
| $V$ | Cut-off voltage | | $V$ |
| $Vol_C$ | Core's volume | | $m^3$ |
| $Vol$ | Volume | | $m^3$ |
| $V_f$ | Forward voltage of the inductor | | $V$ |
| $V_f'$ | Forward voltage of the transistor | | $V$ |
| $V_{min}'$ | Cut-off voltage of Lead Crystal batteries when discharging at $i_{app} \in [0.5C, 1C]$ | | $V$ |
| $v$ | Voltage | ✓ | $V$ |
| $v_{bus,0}$ | Voltage of the microgrid's DC bus at no load under droop control | | $V$ |
| $v_{optim}$ | Optimum instantaneous DC bus voltage (BVOC) | ✓ | $V$ |
| $v_{wind}$ | Wind speed | ✓ | $m/s$ |
| $X$ | Vector containing the voltage values not explained by OCV during the dynamic test (ESC model) | | $various$ |
| $x$ | Longitudinal coordinate across the cell | ✓ | $m$ |
| $Y$ | Vector containing the ESC model parameters to estimate | ✓ | $various$ |

| Symbol | Description | Is a variable | Units |
|---|---|---|---|
| $z$ | State of charge | ✓ | $p.u.$ |
| $\alpha$ | Parameter of the inductor's magnetic core | | $-$ |
| $\alpha_a, \alpha_c$ | Anodic and cathodic charge transfer coefficients | | $-$ |
| $\beta$ | Parameter of the inductor's magnetic core | | $-$ |
| $\gamma$ | Hysteresis time constant (ESC model) | | $-$ |
| $\Delta B$ | Flux density ripple in the inductor's magnetic core | ✓ | $T$ |
| $\Delta t$ | Time step used in the discretization | | $s$ |
| $\delta v_{bus,0}^{2ry}$ | Offset applied to $v_{bus,0}$ in all the microgrid's units in secondary droop control | ✓ | $V$ |
| $\delta v_{bus,0}^{2ry}$ | Offset applied to $v_{bus,0}$ in the microgrid's bidirectional inverter in tertiary droop control | ✓ | $V$ |
| $\delta_{SEI}$ | Thickness of the SEI film | ✓ | $m$ |
| $\varepsilon$ | Volume fraction of the cell's phase in an electrode | | $-$ |
| $\eta$ | Overpotential of the chemical reaction | ✓ | $V$ |
| $\eta_Q$ | Coulombic efficiency | | $p.u.$ |
| $\eta_{global}$ | Global efficiency of the microgrid system | ✓ | % |
| $\eta_{pc}$ | Efficiency of the equalizer's power converter | | % |
| $\theta$ | Electrode's stoichiometry (degree of lithiation of the electrodes) | ✓ | $-$ |
| $\theta^0$ | Degrees of lithiation of the electrode when the cell is at $z = 0$ (defined by $OCV = V_{min}$) | ✓ | $-$ |
| $\theta^{100}$ | Degrees of lithiation of the electrode when the cell is at $z = 100$ (defined by $OCV = V_{max}$) | ✓ | $-$ |
| $\kappa_{SEI}$ | Conductivity of the SEI layer | | $S/m$ |
| $\kappa_{eff}$ | Effective ionic conductivity in the electrolyte | | $S/m$ |
| $\lambda$ | Peukert constant | | $-$ |
| $\rho_{air}$ | Air density | | $kg/m^3$ |
| $\sigma_{eff}$ | Effective electronic conductivity of the solid material in the porous negative electrode | | $S/m$ |

| Symbol | Description | Is a variable | Units |
|---|---|---|---|
| $\phi$ | Electrostatic potential of the phase in the battery cell | ✓ | $V$ |

| Subscript or superscript | Description: Relative to … |
|---|---|
| $-$ | Measurements during discharge |
| ^ | Estimation |
| $+$ | Measurements during charge |
| $*$ | Negation of logical variable |
| $\cdot bus \cdot$ | DC-bus-side of the converter |
| $R_1, R_2$ | Diffusion resistances (ESC model) |
| $\theta_0$ | Associated to change in $\theta_0$ |
| $\theta_{100}$ | Associated to change in $\theta_{100}$ |
| $\boxed{\mu G}$ | Microgrid system |
| 0 | Corresponding to $SOC = 0\%$ |
| 100 | Corresponding to $SOC = 100\%$ |
| $A$ | Pre-degradation stage |
| $B$ | Post-degradation stage |
| $B1, \dots, B5$ | The five monobloc battery models conforming the battery pack conceived to validate the equalizer's performance in simulation |
| $BESS$ | Battery Energy Storage System (microgrid) |
| $BVOC$ | Bus Voltage Optimization Control |
| $Batt1, \dots, Batt5$ | The five monobloc batteries models conforming the test battery pack to experimentally validate the equalizer's performance |
| $bal$ | Contributing to cell balancing |
| $bus$ | Microgrid's DC bus |
| $ch$ | Charging Pulse Test (SEI growth model) |
| $csl$ | Capacity Single-Loop Test (SEI growth model) |
| $DYN$ | Dynamic test (ESC model) |

| Subscript or superscript | Description: Relative to … |
|---|---|
| $dch$ | Discharging Pulse Test (SEI growth model) |
| $demand$ | Demanded by DC loads |
| $E-BCS$ | Events-Based Control System |
| $EZ$ | Electrolyzer |
| $e$ | Electrolyte phase in the battery cell |
| $el$ | Either the positive or the negative electrode |
| $end$ | Final |
| $FC$ | Fuel Cell (microgrid) |
| $gain$ | Secondary recovery in the SEI growth process |
| $hyst$ | Hysteresis element (ESC model) |
| $i$ | Each of the elements in a list, for example $i = \{PV, WT, FC, LOAD, EZ, BESS, INV\}$ |
| $in$ | Input |
| $I$ | Intercalation reaction |
| $INV$ | Bidirectional inverter (microgrid) |
| $j$ | Each of the elements in a list, for example $j = \{PV, WT, FC, LOAD, EZ, INV\}$ |
| $L$ | Across the inductor |
| $LOAD$ | DC load (microgrid) |
| $loss$ | Loss |
| $MPP$ | Maximum Power Point |
| $m$ | Each of the microgrid's control strategies |
| $max$ | Maximum |
| $min$ | Minimum |
| $n$ | Negative electrode |
| $nom$ | Nominal |
| $OCV$ | OCV test (ESC model) |
| $OOSF$ | Online Optimization of Switching Frequency |
| $ocv$ | Initial and final four-steps Open Circuit Voltage Test (SEI growth model) |

| Subscript or superscript | Description: Relative to … |
|---|---|
| $off$ | During the ON time of the converter's duty cycle |
| $on$ | During the OFF time of the converter's duty cycle |
| $out$ | Output |
| $PV$ | Photovoltaic field (microgrid) |
| $p$ | Positive electrode |
| $real$ | Measured values |
| $ref$ | Reference |
| $rel$ | Relative |
| $SEI$ | Solid-Electrolyte Interphase |
| $s$ | Solid phase in the battery cell |
| $shift$ | Shift (offset) |
| $side$ | SEI side-reaction |
| $sim$ | Simulation result |
| $theor$ | According to theoretical model |
| $total$ | Total |
| $tune$ | Recalculation due to secondary capacity recovery |
| $UDDS$ | Urban Dynamometer Drive Schedule (dynamic test to parametrize the ESC model) |
| $WT$ | Wind Turbine (microgrid) |
| $\mu G$ | Microgrid |

| Accent | Description |
|---|---|
| ~ | Approximated function, reducing dependencies to one variable only ($v_{bus}$ in BVOC, Section 3.2.1, or $f_{sw}^{i}$ in OOSF, Section 3.2.2): for example, $\tilde{P}_{loss}^{PV}(v_{bus})\big\vert_{k} = \tilde{P}_{loss}^{PV}(v_{bus}, f_{sw}^{PV}[k], P^{PV}[k], v^{PV}[k])$, and $\tilde{P}_{loss}^{PV}(f_{sw}^{PV})\big\vert_{k} = \tilde{P}_{loss}^{PV}(v_{bus}[k], f_{sw}^{PV}, P^{PV}[k], v^{PV}[k])$ |
| ^ | Resulting from subtracting $OCV$ (ESC model parametrization, Section 4.2.2.4): $\hat{v}[k] = v[k] - OCV(z[k])$ |

# 1. General introduction

Planet Earth has finite energy resources, but humanity demands ever growing energy consumption (see Figure 1-1) [1, 2]. The utilization of non-renewable energy sources generates anthropogenic greenhouse gases emissions that instigate climate change.

Applying a sustainability perspective on power engineering can hopefully help mitigating the present and prospective problems caused by (excessive) industrial activity and transportation. Sustainability, according to [3], can be defined as:

- "Meeting the needs of the present without compromising the ability of future generations to meet their own needs." The Brundtland Report of 1987.
- "Sustainability is equity over time. As a value, it refers to giving equal weight in your decisions to the future as well as the present. You might think of it as extending the Golden Rule through time, so that you do unto future generations as you would have them do unto you." Robert Gilman, Director, Context Institute.
- "Leave the world better than you found it, take no more than you need, try not to harm life or the environment, make amends if you do." Paul Hawken, The Ecology of Commerce.

The main energy challenges faced today and possible solutions are reviewed next, following [4]. Sustainability applied into the electric-energy industry entails promoting "the

three Ds", namely, Decarbonization, Decentralization and Digitalization, by stimulating the deployment of distributed renewable energy sources (over fossil fuels) and maximizing efficiency of energy-consuming processes –if not completely moving towards an alternative conception of life in a de-growth society [5]. Nowadays, RES account for 20% of electricity generation which, in turn, only accounts for 20% of the total energy consumed. Figure 1-1 shows that most of the energy used has its origin in contaminant sources. Furthermore, around 55% of primary energy is lost in transformation to final energy or in end-use machines. Such inefficient processes are mainly found in the power and the transport sectors. Increasing **electrification** of both sectors can greatly help reducing contamination and power losses for two main reasons. Firstly, the electrical network can **integrate renewable energy generation**, mainly wind and photovoltaic (PV) energy, which neither exhaust limited energy resources nor do they emit greenhouse gas. Secondly, electrical machines typically operate at **efficiency** levels much higher than those that combustion processes can achieve. **Storage of electric energy in batteries** can drive a substantial change in the transport sector and facilitate integration of renewable energies to a great extent.

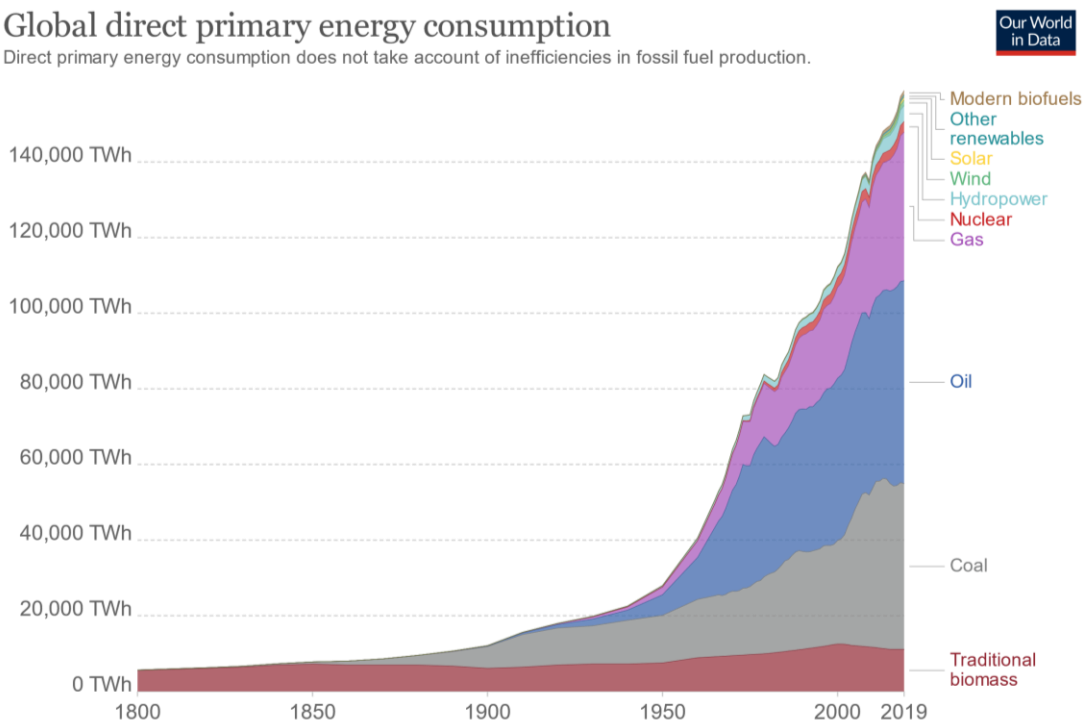


Figure 1-1. Global primary energy consumption, by energy source [1, 2].

Nowadays, wind and PV are already the cheapest new-build electricity option in most regions of the world. It is believed that the experience curves of these technologies will soon bring new-build wind or PV costs below the cost of running existing, commissioned coal and gas plants. A combination of cheap renewables, batteries, and other new sources of flexibility are expected to grow worldwide to reach 56% wind and PV in the electricity supply by 2050. But there is an obvious problem: wind and PV are not always available.

RES are envisioned to have a 69% penetration by 2050 worldwide (see Figure 1-2), and over 80% in some European countries. This future electrical network, producing most energy from variable non-controllable sources, will look very different to conventional power systems. Large coal or gas plants running 24 hours a day at high capacity factor will tend to disappear. Instead, cheap variable renewables will replace them, constituting the base generation, supported by batteries and conventional plants running at low capacity factors. This configuration will be characterized by high PV production during the day, complemented by wind in the evenings, and batteries that charge and discharge over short timeframes.

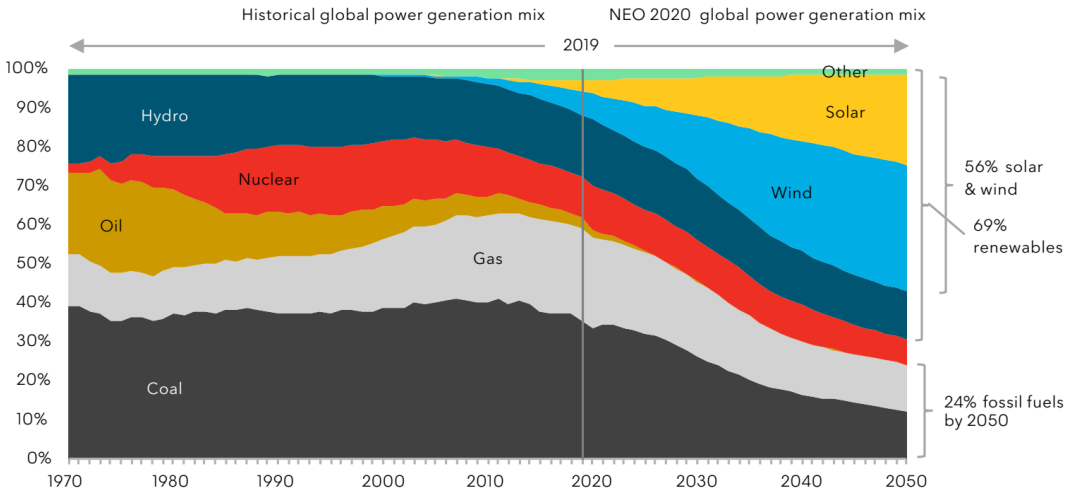


Figure 1-2. Global electricity generation mix. Reproduced from [4].

The integration of RES in the grid involves **challenges related to stability and reliability** caused by the unpredictable and variable nature of RES. Additional **flexibility, both on the supply and the demand side** will have increasing significance as it helps supporting variable renewables and ensuring security of supply. The most compelling technology to achieve the required flexibility is **lithium-ion batteries**. Batteries can contribute to load shifting, by charging when renewable are abundant and prices low, and to peak-shaving, by discharging

into the grid when the renewable resources (sun or wind) are not available and prices are high due to the activation of more expensive generators (gas turbines). Like in the case of wind and PV, the cost of lithium-ion batteries is rapidly decreasing thanks to the growing demand from the electric vehicles (EV) industry.

Large batteries used for grid energy storage and **Battery Energy Storage Systems (BESS) used in microgrids** (electrical infrastructures of relatively small power that reunite generation, consumption, and energy storage, all connected to the mains grid) will provide increasing flexibility and bidirectional interaction with the grid. Moreover, EVs' batteries will also start being widely used for grid-support by means of vehicle-to-grid and demand aggregators during the park time. If grid infrastructure is sufficiently developed to allow vehicles to be plugged-in during most of the time they are stationary (which is already most of the time), owners can benefit from charging at low prices at the same time that the grid benefits from greater demand-side flexibility.

Batteries are delicate and expensive elements that play a key role in the grid of the future. They suffer from both calendar and cycling aging, what compels to carefully study battery degradation to develop **management strategies** that guarantee that the revenues obtained from grid support services compensate battery amortization. Calendar aging is preeminently unavoidable (temperature is the only parameter that can be controlled to minimize degradation) but cycling aging can be reduced by operating the battery based on predictions of the capacity fade that different possible operation schemes would cause. **Modeling the main mechanisms implied in degradation** is, therefore, a key feature of battery management algorithms to **extend battery life**.

An additional source of accelerated battery aging is imbalance among the cells that comprise large battery packs. The cells in a battery pack are never exactly identical to each other due to manufacturing mismatch and to exacerbation of initial discrepancies with use. Consequently, Battery Management Systems (BMS) need to incorporate balancing strategies that **counter the degradation induced by imbalance** to extend battery life.

Summarizing, electrical networks are starting to experience a full renovation that will definitely change their conventional structure and operation scheme. This will facilitate to achieve sustainability goals such as electrification of consumptions, integration of RES, and increase of the efficiency of energy processes. However, there are many challenges that still need to be addressed to shift from a centralized unidirectional rigid power network to a decentralized bidirectional flexible model –evolved power networks will predictably include numerous interconnected microgrids. As power networks will grow in complexity, monitoring and automation will be essential to coordinately manage a high number of interconnected sub-systems (microgrids, electric vehicles, traditional consumers, generation

plants, transmission system, grid energy storage, etc.). This is what smart grids do: smart grids utilize increased capabilities of supervision and communication to coordinate multiple distributed generation and consumption units, making use of energy storage to diversify the traditional generator and consumer roles, with the final goal of providing increased flexibility and resilience.

**Microgrids and energy storage systems** are the two main topics studied in this PhD dissertation. The deployment of microgrids and battery energy storage systems can have a significant role in facilitating a shift towards sustainable renovated forms of energy production and consumption. In this framework, adequate control strategies need to be developed to effectively reach the sustainability goals while preserving the most sensitive elements –the batteries. This dissertation is dedicated to set the foundation for long-term economic optimization of a DC microgrid (μG), with a focus on preserving the μG's BESS. The microgrid placed in the laboratory of the Grup d'Automàtica i Electrònica Industrial (GAEI, Group of Automatic Control and Industrial Electronics), described in [6], has been taken as the case study.

The main objectives of this thesis are:

- To develop a model of the GAEI's microgrid that can be used to evaluate the performance of enhanced control schemes in simulation.
- To explore new control possibilities for the μG by introducing centralized control.
- To optimize the energy efficiency of the μG's converters.
- To study the effect that parameter dispersion has on battery-cell imbalance.
- To design and validate a control strategy for an active battery balancing system.
- To develop a battery model with capability of predicting both short-term battery response and long-term capacity fade for the purpose of BMS controls.

## 1.1. Structure of the dissertation

After the general introduction, Chapter 2 contains a review of the state of the art on the topics that are central to this dissertation, namely: battery types, battery modeling, battery balancing systems, smart grids and microgrids.

Afterwards, the three next chapters present the three main contributions of this dissertation. Figure 1-3 shows the structure of these chapters. The final objective of optimizing the operation of a DC microgrid is the common thread that connects the intermediate objectives, detailed below.

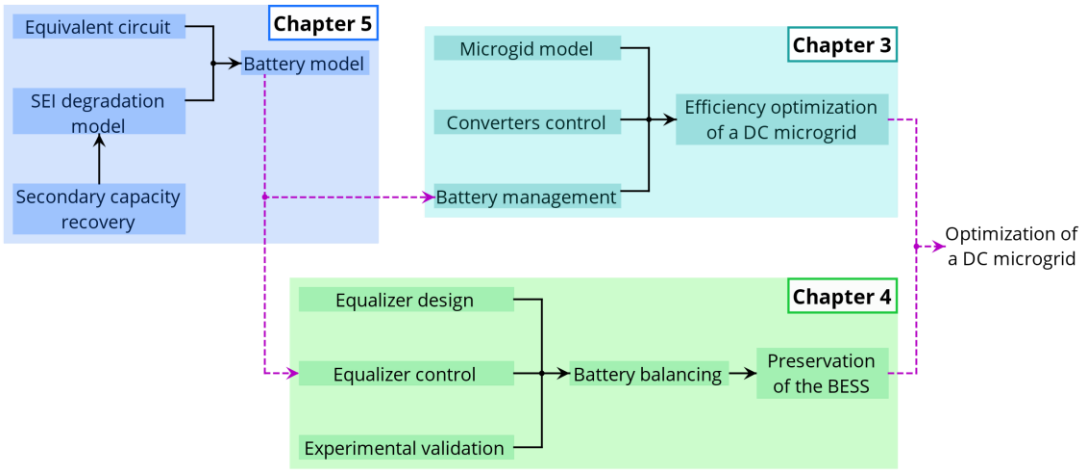


Figure 1-3. Structure of the research in this dissertation.

First, a model of the GAEI's microgrid is developed in Chapter 3 to evaluate the performance of new control schemes. Two control strategies oriented towards optimizing the μG's energy efficiency are proposed. On one hand, centralized control is implemented, with the BESS as the central element. The BESS' central controller supervises operation of all the μG's units and manages the power performed by the BESS to stably balance the existing input and output power flows to / from the DC bus, at the same time that it adaptively controls bus voltage to match the optimum voltage value –which minimizes power losses in the converters. On the other hand, a different, complementary approach to optimizing the converters' efficiency is applied individually to each converter: operating them at their instantaneous optimum switching frequencies –defined as value that minimizes the converter's losses given the converter's output power and its input and output voltages.

Second, active battery balancing is investigated in Chapter 4. An equalizer is studied, and a suitable control strategy is proposed. The battery pack to be balanced is modeled, tested, parametrized, and simulated. Simulation results of the battery pack operation with no external balancing are used to develop and parametrize a control strategy designed to overcome the battery pack's natural tendency towards imbalance while avoiding transferring excessive charge (ampere-hours), which could otherwise produce oscillatory behavior. The control strategy is then validated in simulation. Finally, works aimed at experimentally validating the equalizer's operation are described in this chapter too.

Third, a new battery model of lithium-ion batteries is proposed in Chapter 5. This model combines the simplicity of an equivalent circuit, which captures the dynamic short-term response, with the long-term prediction capability of a physics-based model of one of the most relevant causes of degradation, SEI growth. Both experimental testing and literature review are used to populate the model with adequate parameters. A study of the shift between the stoichiometric windows of the positive and the negative electrodes reveals a process that produces a small capacity recovery. This secondary process is also modeled to refine the capacity loss predicted by the SEI model.

The chapter order of the three main contributions corresponds to the chronological order in which the different topics were addressed, while Figure 1-3 represents the logical order, showing the interdependencies among the partial studies. Note that the comprehensive battery model (Chapter 5) was not available to be used in earlier investigations, namely, the efficiency optimization of the microgrid (Chapter 3) and the battery balancing system (Chapter 4). Nevertheless, it is planned to update the battery model for these investigations in the future – this is represented by the purple dashed arrows in the figure.

To finish, the conclusions of the research presented in this dissertation are summarized in Chapter 6, and Chapter 7 recapitulates the main contributions to the state of the art, presents possible future lines of research inspired by this dissertation, and lists the divulgation and teaching works performed by the author over the course of his PhD degree.

# 2. State of the art of battery and microgrid management

Literature on the principal topics addressed in this dissertation has been extensively reviewed. Firstly, an overview of smart grids and microgrids (μGs) is provided, together with the most common control strategies utilized in DC microgrids. Besides, the physical and the control layers of the DC microgrid of the GAEI's laboratory are described; this microgrid has been considered the case study in this dissertation. Afterwards, the most widespread battery types for energy storage systems are revised. Then, the most common equivalent-circuit and physics-based battery models are described, with special emphasis on methods for estimating State of Charge (SOC) and on modeling degradation caused by SEI layer growth. Finally, battery balancing topologies and control algorithms are reviewed. At the end of the chapter, some conclusions are extracted from the literature review, supporting the research objectives in this dissertation.

## 2.1. Smart grids and microgrids

Current electricity network was conceived more than 100 years ago, and it has been working largely based on the same principles since then. Conventional electricity networks were built to deliver power from a small number of huge generation plants (coal, gas, nuclear, hydro, and more recently, wind and solar), scattered in remote areas, to the end-users through complex transmission and distribution systems (the grid).

Nowadays, power electronics make feasible decentralized, flexible grid operation, with two-way information and power flows [7]. The topology of electric power transmission networks is currently being rethought and reformulated. Ecological, social, and economic perspectives recommend moving towards distributed generation. According to [8], distributed generation provides a range of benefits, including: generation, transmission, and distribution capacity investments deferral; ancillary services capability; environmental emissions benefits; system losses reduction; energy production savings; and reliability enhancement. The promising advantages of new electricity networks are being developed under the concepts of smart grids and microgrids, reviewed next.

### 2.1.1. Smart grids

According to [9], Smart grids are part of the modernization from the conventional electrical grid (where the power flow is unidirectional from the central generation plants to load locations) towards a grid where there are peer-to-peer consumer interactions and distributed generation, with bidirectional flow of energy and data. The smart grid is as an intelligent network that is automated and utilizes two-way communication and control capabilities that lead to a wide range of new functionalities and applications. The inclusion of energy storage (electrical or non-electrical) in smart grids provides further flexibility.

Smart grids offer a number of advantages with respect to the conventional grid. They make use of an numerous sensors to create a digitalized intercommunicated system that can respond fast to problems, minimizing the impact to consumers. Smart grids are driving a transition from radially-connected centralized power generation into dispersed distributed generation, where consumers can be informed and involved (“prosumers”) and can take an active role in providing demand response, extra generation capacity and ancillary services. Energy storage connected through power electronic converters can provide a series of benefits from the grid operation perspective, such as energy arbitrage, peak shaving, frequency regulation, spinning reserve, voltage support, black start capability, intermittency smoothing, congestion mitigation, load-following applications.

Smart meters generate updated accurate consumption data that, if processed wisely, can help managing consumption / generation profiles of all the elements in a smart grid. For example, the run schedule of smart appliances and devices can be arranged based on several models that anticipate the behavior of the consumers and the generators. Such models can forecast weather, consumption profiles, generation profiles, electricity pricing, etc. With this information, non-critical loads can be scheduled to support the overall operation of the mains grid. For example, peak shaving and valley filling are two strategies that flatten the aggregated consumption profile of an electricity network respectively by coordinately injecting power

into the grid and by reallocating loads. Peak shaving consists in supplying power from energy storage systems during the hours of highest electricity consumption; this contributes to lowering global generation costs as it reduces the activation of expensive peak (gas) power plants. Valley filling consists in deferring electricity usage away from peak hours and having appliances and devices run at times of low aggregated load in the system (demand shifting); this contributes to stability of the mains grid, simplifies the management of big power plants, and improves their energy efficiency.

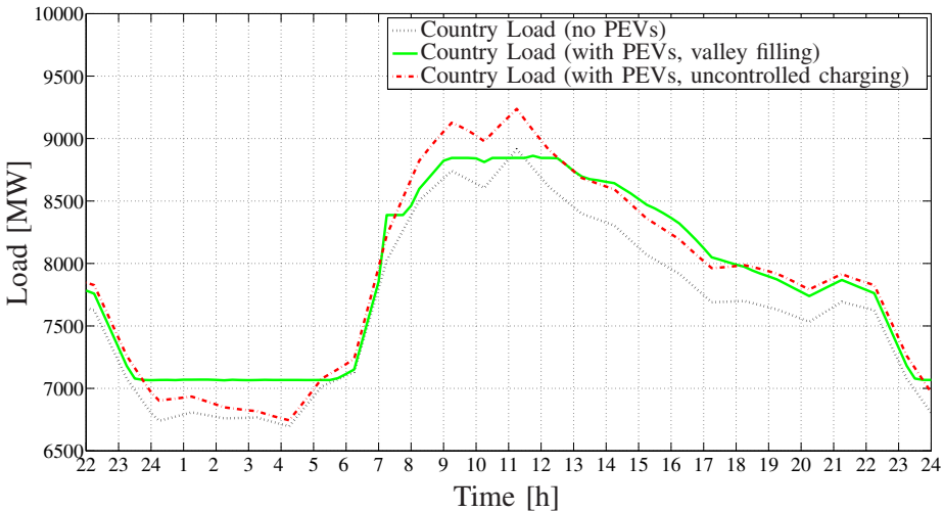


Figure 2-1. Swiss 24-hour aggregated consumption in three different scenarios of penetration of electric vehicles and charge scheduling strategies. Reproduced from [10].

One promising option to materialize smart grids policies consists in coordinately controlling the battery packs of a large fleet of electric vehicles (EV) as an energy storage reserve for the mains grid, enabling them to take active part in power network regulation through smart charging and discharging [11]. Power system operators may take advantage of high penetration of EVs to apply both peak shaving and valley filling through Vehicle-to-Grid (V2G) and demand aggregators, respectively [12], making use of the vehicles' batteries during parking time –which is most of the time. Figure 2-1 [10] shows these two strategies applied at country level (Switzerland), with coordinated charging of a large fleet of Plug-in Electric Vehicles (PEV). The base load profile is represented by the black dotted line (average consumption in a summer day with no PEVs), over which the power required to charge the PEVs is added: uncontrolled charging is represented by the red dashed line, while optimized aggregated management of the fleet is represented by the green solid line. The country's load

valley is filled during the night hours (23:30 to 6:15). Load peaks between 09:00 and 12:00 are reduced thanks to energy withdrawn from PEVs remaining capacity after arriving to their destinations. The energy discharged between 09:00 and 12:00 is reacquired later causing a small difference between the base load and the optimized load curves after 18:00 (note that vehicles often do not offer sufficient flexibility to postpone their charging until valley hours.)

### 2.1.2. Microgrids

Distributed generation promotes the development of a new grid paradigm, called microgrid [7]. "A microgrid is a group of interconnected loads and distributed energy resources within clearly defined electrical boundaries that acts as a single controllable entity with respect to the grid. A microgrid can connect and disconnect from the grid to enable it to operate in both grid-connected or island-mode", according to the definition by the US Department of Energy's Microgrid Exchange Group [13]. In other words, a microgrid is a small-scale electrical network (home, community, or larger level) that makes use of localized on-site energy production and consist of a number of interconnected and coordinated elements comprising generator(s), load(s), mains grid, and (generally) energy storage(s). One of the applications microgrids are best suited for is participation in smart grids. Microgrids equipped with real-time monitoring and communications allow for complex control strategies when coordinated with other microgrids and with the mains grid. All these interconnected elements constitute an automated and distributed advanced energy network, the smart grid [7].

There are two main types of microgrids, according to whether the point of common connection between the microgrid and the mains grid is an AC bus or a DC bus –hybrid topology, with both AC and DC buses, is also possible. Strong arguments indicate that implementing microgrids with a DC bus is simpler, more reliable, and more efficient than with an AC bus [14]:

- Most microgrid projects have been implemented as AC microgrids, where energy sources and loads are connected to an AC bus that matches the characteristics of the conventional AC grid through power converters. AC microgrids predominance is a logical outcome of the extensive experience with large AC grids, the wide availability of AC loads, and the maturity of the inverter industry. However, AC microgrids present some disadvantages compared to DC microgrids. They require frequency and phase regulation (which is more complex in small AC microgrids than in the large traditional AC grid) and reactive power-flow control. Furthermore, island detection can be more complex in AC microgrids.

- DC microgrids, in contrast, present some benefits but the technology is less mature and standardized. In fact, local distribution systems would greatly benefit from using DC rather than AC interconnection bus nowadays –contrarily to common practice. The most important reasons for DC distribution superiority are reviewed next. Firstly, most renewable sources produce DC power, and most modern loads are DC loads (although they are commercialized as AC loads, such as led lights, consumer electronics, and motor drives). These loads come with a front-end rectifier, while the load itself is served from an internal DC bus. These DC loads could be connected more efficiently to a DC bus because the losses produced in the rectification stage would be eliminated. With respect to generators, many rotating AC generators could operate more efficiently if they were connected through variable-frequency power converters instead of being forced to operate connected to a fixed-frequency AC bus. Regarding electric energy-storage devices, note that they are DC in nature and, in addition, electric vehicles (EV) are expected to proliferate over the next few years, which will bring high battery charging demand into the power distribution network. Fast battery chargers can be simplified and made more efficient if powered directly from a high-voltage DC bus. And with respect to power quality and stability, robust DC bus voltage control can easily manage power quality problems, such as sags, swells, imbalances, and flickering, among others, associated with the high penetration of renewable resources that present discontinuous power output, which are an important issue in AC microgrids. Advances in DC-DC converter technology have resulted in highly efficient and reliable converters providing the "DC transformer" effect that nowadays counterbalances the decisive factor that favored AC systems in the 1900s.

Microgrids contribute to "the three Ds", Decarbonization, Decentralization and Digitalization, which are said to be the main drivers against climate change in the electric energy field [15]. Microgrids have potential to stimulate self-sufficiency (because they enable to produce energy in the exact place where it is needed) [16], facilitate integration of renewable energy sources [17], provide resilience when the grid is lost thanks to energy storage [18], increase energy efficiency by reducing transmission losses [19], lower dependency on foreign energy sources [20], and reduce greenhouse gas emissions [21].

From the grid operation perspective, microgrids can insulate critical loads or even entire urban areas from potential power failures or blackouts, can provide auxiliary services (voltage, frequency, and power factor support) if controlled adequately, and can help providing service in areas where power lines are saturated or where there are no installed power lines at all, thus deferring or substituting investments in transmission and distribution capacity. From the customer point of view, it might be interesting to consider installing a

microgrid as an alternative to the grid (stand-alone applications). In general, the smaller the customer size, the larger the share of transmission and distribution costs in the electricity price, which is above 40% for households [22].

Microgrids are an essential part of the power networks of the future. For instance, it is expected that the US will see a central energy vs. distributed energy equilibrium start to form by 2035 at approximately 20% of the total electric energy supply being addressed by microgrids and distributed energy solutions. If transmission and distribution charges continue to escalate as observed over the last several years, then the equilibrium will settle at a higher distributed energy penetration (likely 30% of total electric energy supply) and a higher equilibrium energy cost in the 2050 timeframe [13].

#### 2.1.2.1. DC microgrid control strategies

Integration of microgrids into electricity grid requires managing power of the different elements of a microgrid to guarantee that the system operates always stably and that, whenever possible, Renewable Energy Sources (RES) operate at their Maximum Power Point (MPP) and critical loads are supplied. A review on the most common control algorithms, following [23] and [24], is provided next.

Local control algorithms for microgrids can be divided into three categories from the communication perspective, following [25]:

- Decentralized control: Digital communication links do not exist and power lines are used as the only channel of communication. It is invariably based on the interpretation of the voltage in the common DC bus.
- Centralized control: Data from distributed units are collected in a centralized aggregator, processed and feedback commands are sent back to them via digital communication links.
- Distributed control: Digital communication links are implemented between units and coordinated control strategies are processed locally.

The GAEI's microgrid is initially controlled with a decentralized scheme based on the DC bus voltage, complemented with distributed control based on the BESS' SOC. One of the proposed optimization strategies, bus voltage optimization, requires centralized control. Therefore, a combination of all three control categories is used in Chapter 3: Efficiency optimization of a DC microgrid.

- **Decentralized droop control**

Figure 2-2 and Figure 2-3 illustrate droop control, which is the basic diagram for decentralized control [24, 26]. In DC microgrids, primary droop control achieves power

sharing among the sources and bidirectional DC-DC converters connected in parallel to the DC bus. The control of each converter locally determines the power that it must provide / consume according to a linear control law solely based on bus voltage. Droop control modifies the power reference of the sources' converters as the bus voltage varies due to temporary power imbalance caused by variations in load or generation. For example, starting from a stable operation point, if load increases, bus voltage naturally tends to decrease. The decentralized control system reacts then by increasing the power supplied by each source according to their particular linear control law. Larger sources contribute with more power thanks to different droop coefficients for different units. Bus voltage can then be restored to its initial value implementing secondary and tertiary droop control.

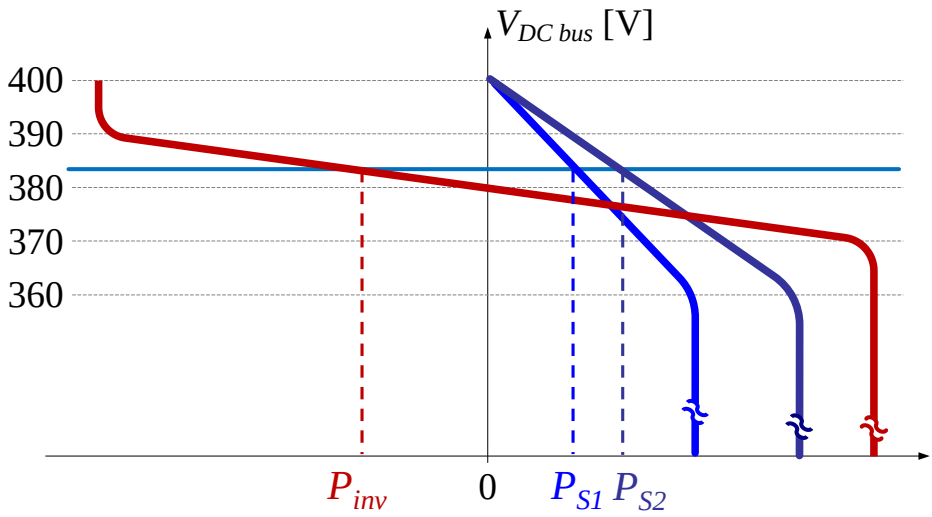


Figure 2-2. Primary droop control. Modified from Alexis Kwasinski's notes (University of Texas) based on [24].

A droop control loop governs power sharing among the parallel connected DC-DC converters of the microgrid's sources and bidirectional units. The control variable can be chosen to be either the converter's power, in microgrids with power-loads, or current, in microgrids with resistive loads. Figure 2-2 represents primary droop control laws of a bidirectional inverter (red curve) and two sources (S1 and S2, blue and purple curves), in a microgrid where power (in the x-axis) is the control variable. When current signal is used instead, droop coefficients can be regarded as virtual internal resistances. In that case, the implementation and design can be simplified to some extent as the control law is linear.

The primary droop control in the power-based case is as follows:

$$v_i^{ref} = v_{bus,0} - m_{p\,i} P_i^{\cdot bus\cdot} \tag{2.1}$$

$$\sum P_i^{\cdot bus\cdot} = P_{Load}^{\cdot bus\cdot} \Leftrightarrow v_1^{ref} = v_2^{ref} = \cdots = v_{bus}^{ref} \tag{2.2}$$

where $v_i^{ref}$ is the reference value of DC output voltage of the converter $i$, $v_{bus,0}$ is the output voltage reference at no load ($400\,V$ for sources, and $380\,V$ for the inverter in Figure 2-2), $m_{p\,i}$ is the droop coefficient of the converter $i$, $P_i^{\cdot bus\cdot}$ is the power of the converter $i$ at the DC-bus side (be it the input or the output), and $P_{Load}^{\cdot bus\cdot}$ is the input power of the converter interfacing consumed by the load. Droop control will lead the system to an operation point such that the sum of power injected by sources to the DC bus and power provided / absorbed by bidirectional units equals the total power consumed by the load, $P_{Load}^{\cdot bus\cdot}$. This point is characterized by the equilibrium voltage $v_{bus}^{ref}$ (2.2).

Secondary control can be implemented to keep bus voltage constant (see Figure 2-3). The voltage level in the microgrid, $v_{bus}$, is sensed and compared to the reference, $v_{bus}^{ref}$, to offset all the units $v_i$ vs. $P_i^{\cdot bus\cdot}$ droop curves by the error between the bus voltage and its desired (constant) value, $\delta v_{bus,0}^{2ry}$, in order to restore the output voltage ($\delta v_{bus,0}^{2ry}$ is the same for all the sources). This way, the reference voltage for droop calculations in (2.1) changes from $v_{bus,0}$ to $v_{bus,0} + \delta v_{bus,0}^{2ry}$ (2.3):

$$v_j^{ref} = \left(v_{bus,0} + \delta v_{bus,0}^{2ry}\right) - m_{p\,j} P_j^{\cdot bus\cdot} \tag{2.3}$$

When a DC microgrid with constant bus voltage operates in islanded mode, secondary control must regulate all the converters. But when in grid-connected operation mode, tertiary control can substitute secondary control in the converter that interfaces with the bidirectional inverter. Tertiary control introduces a voltage offset $\delta v_{bus,0}^{3ry}$ (in general, different to $\delta v_{bus,0}^{2ry}$) for this particular converter characteristic. Thus, its curve can be shifted up or down independently from the remaining sources' curves.

As a result of primary, secondary and tertiary droop controls combined, power sharing is achieved, bus voltage is stabilized, and the desired power profile can be injected / absorbed to/from the grid. Figure 2-3 shows control laws of a droop-controlled microgrid where all three control levels are implemented. Equations (2.3)–(2.5) show calculation of the voltage references in this case:

$$v_{inv}^{ref} = \left(v_{bus,0} + \delta v_{bus,0}^{3ry}\right) - m_{p\,inv} P_{inv}^{\cdot bus\cdot} \tag{2.4}$$

$$P_{inv}^{\cdot bus\cdot} + \sum P_j^{\cdot bus\cdot} = P_{Load}^{\cdot bus\cdot} \Leftrightarrow v_1^{ref} = v_2^{ref} = \cdots = v_{inv}^{ref} = v_{bus}^{ref} = cst \tag{2.5}$$

where $j$ represents each of the sources' converters (excluding the bidirectional inverter), subscript $inv$ refers to the converter connected to the bidirectional inverter, and $P_{grid} = \eta_{pc}^{inv} P_{inv}^{\cdot bus\cdot}$ is the power injected in the utility grid, with $\eta_{pc}^{inv}$ the efficiency of the inverter's converter. Note that in this case $v_{bus}^{ref}$ is constant.

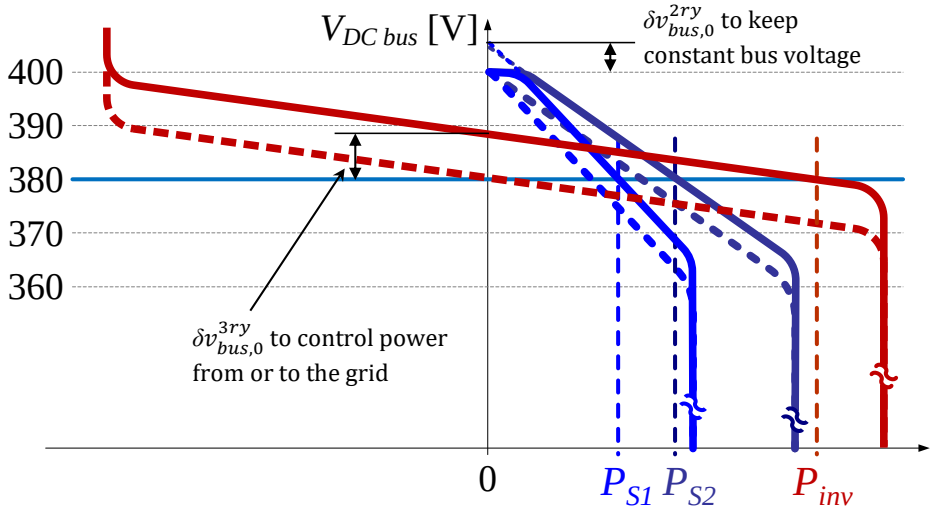


Figure 2-3 Secondary and tertiary droop controls (fixed bus voltage; bidirectional inverter controlled independently). Modified from Alexis Kwasinski's notes (University of Texas) based on [24].

The GAEI's microgrid presented in Section 2.1.3 fits in the power-based type. Only primary droop control has been implemented to explore the possibilities that varying bus voltage offers.

- **Centralized control**

Centralized control allows for more complex functions and is commonly employed for optimization purposes. A central controller and a digital communication network are required. Information from every DC-DC converter is received and processed in the central controller. In small-scale microgrids, the central controller can directly control every unit using a master-

slave configuration. For larger microgrids, hierarchical control is often preferred because it is more reliable, given that this way not all the control system falls on a single point.

- **Distributed control**

Distributed control requires no central controller, but digital communication links between local controllers are necessary. The main advantage of this approach is that the system can maintain full functionality even if some communication links fail, provided that the rest of the communication network remains connected. Optimization can be implemented using distributed control, but an intermediate step is needed: the information exchanged through communication links must be appropriately processed by means of a consensus algorithm to allow local controllers to have complete information about the other controllers' variables. Coordinated functions that can be achieved by this approach are similar to those of centralized control.

#### 2.1.2.1. Optimization of DC microgrids

Advanced control strategies enable to improve microgrid performance. Most microgrid management optimization studies focus on finding out the optimum economic dispatch. Some examples are summarized next. In [26], an optimization problem is formulated to achieve load sharing minimizing fuel and operation costs. In [27], a multi-objective optimization function is utilized to balance the tradeoff between maximizing the microgrid revenue and minimizing the microgrid operation cost, including penalties for bid deviation, renewable energy curtailment, and involuntary load shedding. In [28], a genetic algorithm is used to solve an optimization problem to minimize the instantaneous (no forecasting considered) microgrid total operation cost, taking into account real-time pricing of electricity from the utility grid. In [29], a genetic algorithm is implemented to minimize the daily net cost of the Battery Energy Storage System (BESS) scheduling. In [30]w, a genetic algorithm schedule is used to minimize economic operation cost, including demand response price policy in the model. In [31], a linear optimization problem is solved to determine the day ahead and intraday markets bids that maximize the overall profit for a photovoltaic plant with BESS, considering battery aging, forecast uncertainty and incomes due to provision of ancillary services and penalties due to deviation of the generation schedule.

The objective of the two optimization strategies presented in Chapter 3 is different. They are Bus Voltage Optimization Control (BVOC) and Online Optimization of Switching Frequency (OOSF). Their goal is not economic optimization but energy efficiency optimization, that is, minimizing the power losses of the microgrid's DC-DC converters. To the best of the author's knowledge, online bus voltage optimization of a DC microgrid has never been addressed before. The most similar study to BVOC optimization found is [32],

which determines optimum bus voltage for residential and commercial DC microgrids applications. In this case, though, constant optimum voltages were obtained, so it provides a design criterion rather than an online optimization algorithm. In [33, 34], bus voltage control is addressed with different approaches, namely, double loop PI control and droop coefficients optimization, but considering a fixed and predetermined bus voltage value in both cases. Switching frequency optimization of individual DC-DC converters has been previously modeled in [35–38] and implemented online in [39–41].

### 2.1.3. Description of the GAEI's microgrid

This section describes the most recent configuration of the microgrid present in the laboratory of the Grup d'Automàtica i Electrònica Industrial (GAEI, Group of Automatic Control and Industrial Electronics) [6]. This microgrid has inspired many research projects over the last years [42–50]. The research and development of this microgrid is still ongoing. Figure 2-4 to Figure 2-8 show the GAEI's microgrid in its current state.

#### 2.1.3.1. Architecture of the microgrid

The GAEI's microgrid is a low voltage DC system (Figure 2-8) of energy sources, energy storage and electrical loads, connected to the three-phase grid through an AC point of common coupling. A DC bus is the central element that interconnects all the components, namely:

- Four photovoltaic strings (Figure 2-4) independently connected to the DC bus and controlled by individual Maximum Power Point (MPPT) boost converters (Figure 2-5 and Figure 2-6). The open circuit voltage of the strings at $25\ °C$ is $176.8\ V$ and their total nominal power is $5.20\ kWp$.
- Two AC three-phase wind turbines with permanent magnet synchronous generators: a Vertical Axis Wind Turbine (VAWT), the Four Seasons Windpower Gyro, 1 k$W$ (Figure 2-4), and a Horizontal Axis Wind Turbine (HAWT), the Southwest Windpower Whisper 200, 1 $kW$ (Figure 2-7). The first one is connected to the DC bus through a step-up converter, and the latter one, through a Vienna rectifier controlled as a loss-free resistor for power factor correction [50].
- Fuel cell Ballard Nexa: $1.2\ kW$ nominal power, $24\ V$ nominal voltage. This unit works with hydrogen supplied from a non-refillable hydrogen tank. This unit is connected to the DC bus through a two-cascade boost converter.
- Battery Energy Storage System consisting of fifteen $12\ V$, $250\ Ah$ lead acid batteries, connected to the DC bus through a bidirectional converter.

- Three single-phase unidirectional Maximum Power Point Tracking (MPPT) solar inverters StecaGrid 2000+, controlled as AC regenerative loads thanks to the ingenious Smart Panel Devices described in [51].
- AC-loads can be connected directly to the grid (output of the solar inverters).
- DC-loads can be connected directly to the DC bus through several sockets. DC-loads are normally simulated by means of an electronic load.
- Three-phase Vienna rectifiers allow to consume AC power from the grid and inject it to the DC bus.
- Electrolytic capacitor bank, $144\ mF$, $400\ V$. It acts as a fast energy storage system with very low capacity, but high power. It also determines the dynamics of the DC bus voltage.
- Control drivers of the DC-DC converters get power supply from external devices.

Figure 2-4. Four Seasons Windpower Gyro wind turbine and PV field of the GAEI's microgrid.

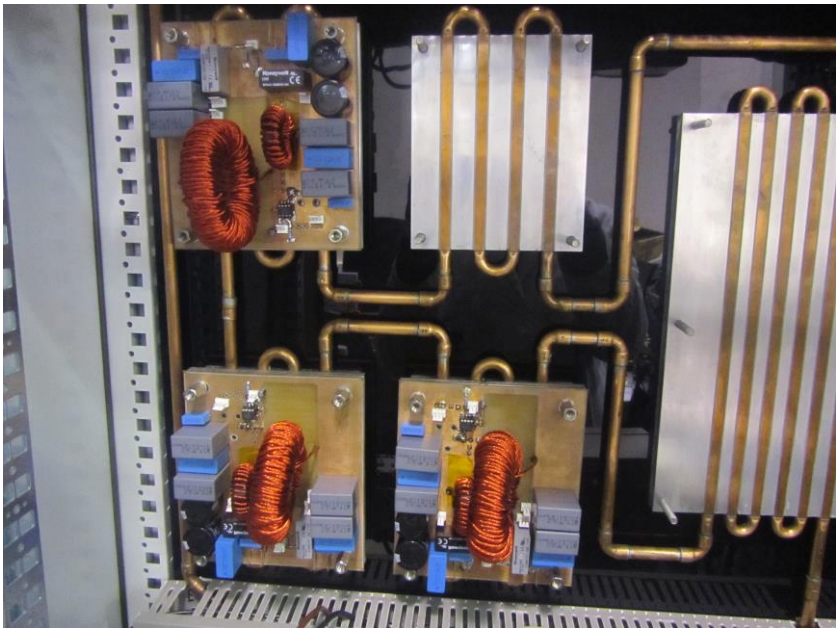

Figure 2-5. DC-DC converters interfacing the photovoltaic generator with the DC bus and refrigeration circuit.

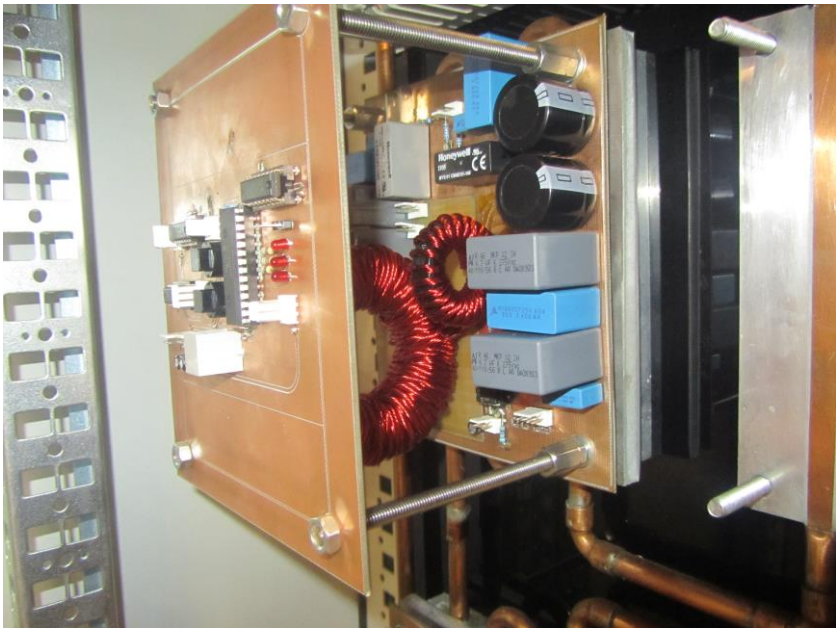

Figure 2-6. Control board of one of the DC-DC converters interfacing the photovoltaic field with the DC bus.

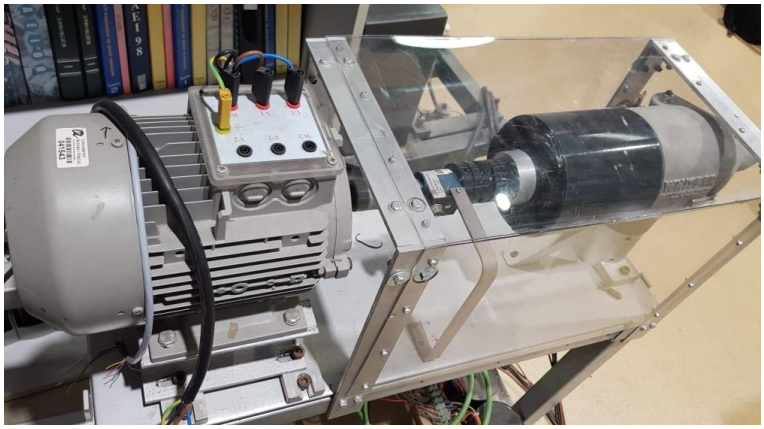

Figure 2-7. Southwest Windpower Whisper 200 wind turbine simulator of the GAEI's microgrid.

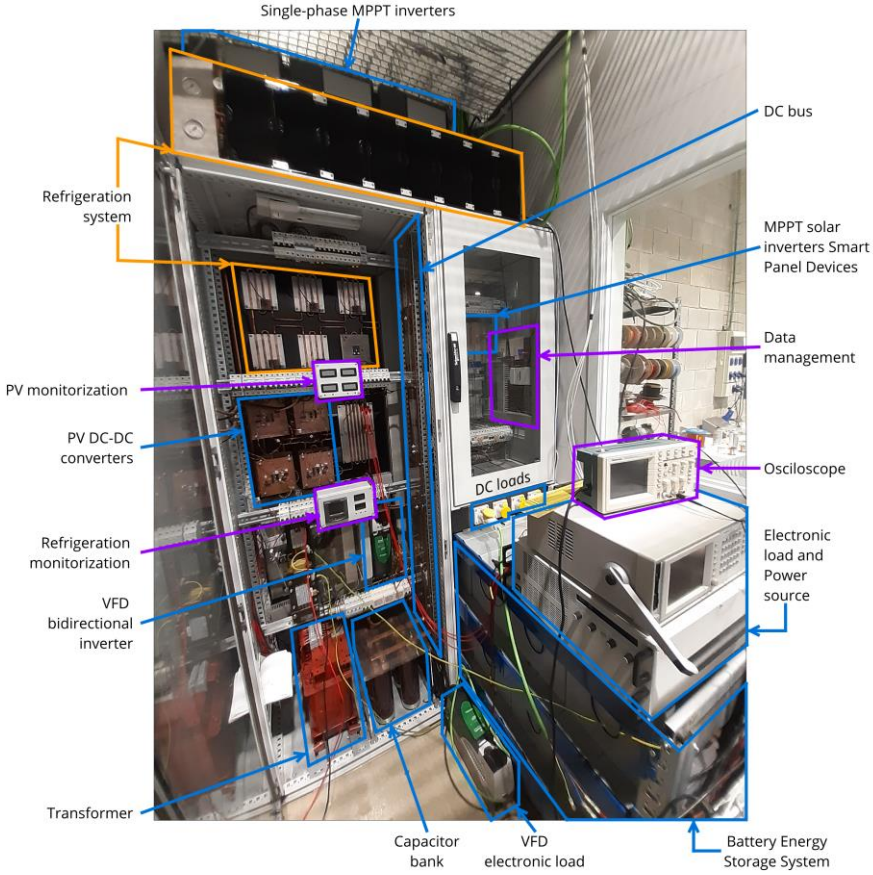


Figure 2-8. Actual configuration of the distribution and protection board of the GAEI's microgrid.

It is planned to expand the microgrid by introducing additional power elements, which are object of future research projects:

- An electrolyzer will make possible to store energy surplus in the form of chemical energy: the electrolyzer will produce hydrogen that will be stored in a refillable hydrogen tank (possibly in the form of metal hydrides), to supply the fuel cell with on-site produced hydrogen. The cycle efficiency of this form of energy storage is considerably lower than that of the battery.
- A variable frequency drive modified to work as a controllable three-phase bidirectional inverter will substitute the existing solar inverters and the Vienna rectifiers, in order to simplify the system. A transformer provides galvanic isolation.
- A variable frequency drive modified to allow inverse operation as a regenerative electronic load.

Apart from the listed power elements, the microgrid has a water refrigeration system that keeps DC-DC converters temperature within safe operation range. There is also a data-logging and monitorization system. The microgrid electronics consist of a set of self-produced DC-DC converters with advanced topologies and complex control strategies based on sliding mode control. All these elements are present in Figure 2-8.

#### 2.1.3.2. Autonomous droop control

The comprehensive microgrid (including the abovementioned enhancements) includes the following units: photovoltaic field (PV), wind turbine (WT), fuel cell (FC), DC loads (LOAD), electrolyzer (EZ), Battery Energy Storage System (BESS), three-phase bidirectional inverter (INV). It is controlled with a primary droop control, without secondary and tertiary control. Thus, stable operation is always achieved, while the DC bus voltage is not fixed but varying. This configuration has been selected to allow exploring the control possibilities that variable bus voltage enables.

The microgrid's control system consists of a decentralized Voltage Event Control (VEC) of every unit, supplemented with State of Charge Event Control (SOCEC) of the fuel cell, the electrolyzer and the bidirectional inverter. VEC is a primary droop control that intentionally uses no secondary or tertiary droop control to stabilize bus voltage. The comprehensive control system is denominated Events-Based Control System (E-BCS=VEC+SOCEC). Figure 2-9 illustrates VEC and SOCEC control laws. Each microgrid unit follows a linear control law based on bus voltage, $v_{bus}$ (VEC) and, additionally, the fuel cell, the electrolyzer and the bidirectional inverter also follow control laws based on battery State of Charge, $SOC$ (SOCEC). E-CBS determines the coefficient $m_i$ that multiplies the absolute value of the

nominal or maximum power of the source/load/bidirectional unit $i$, with $i = \{PV, WT, FC, LOAD, EZ, BESS, INV\}$. The coefficient $m_i[k]$ is the saturated sum of the VEC coefficient, $m^i_{VEC}[k]$, plus the SOCEC coefficient, $m^i_{SOCEC}[k]$, as shown in (2.6). The coefficients $m^i_{VEC}$ and $m^i_{SOCEC}$ are defined in Figure 2-9.

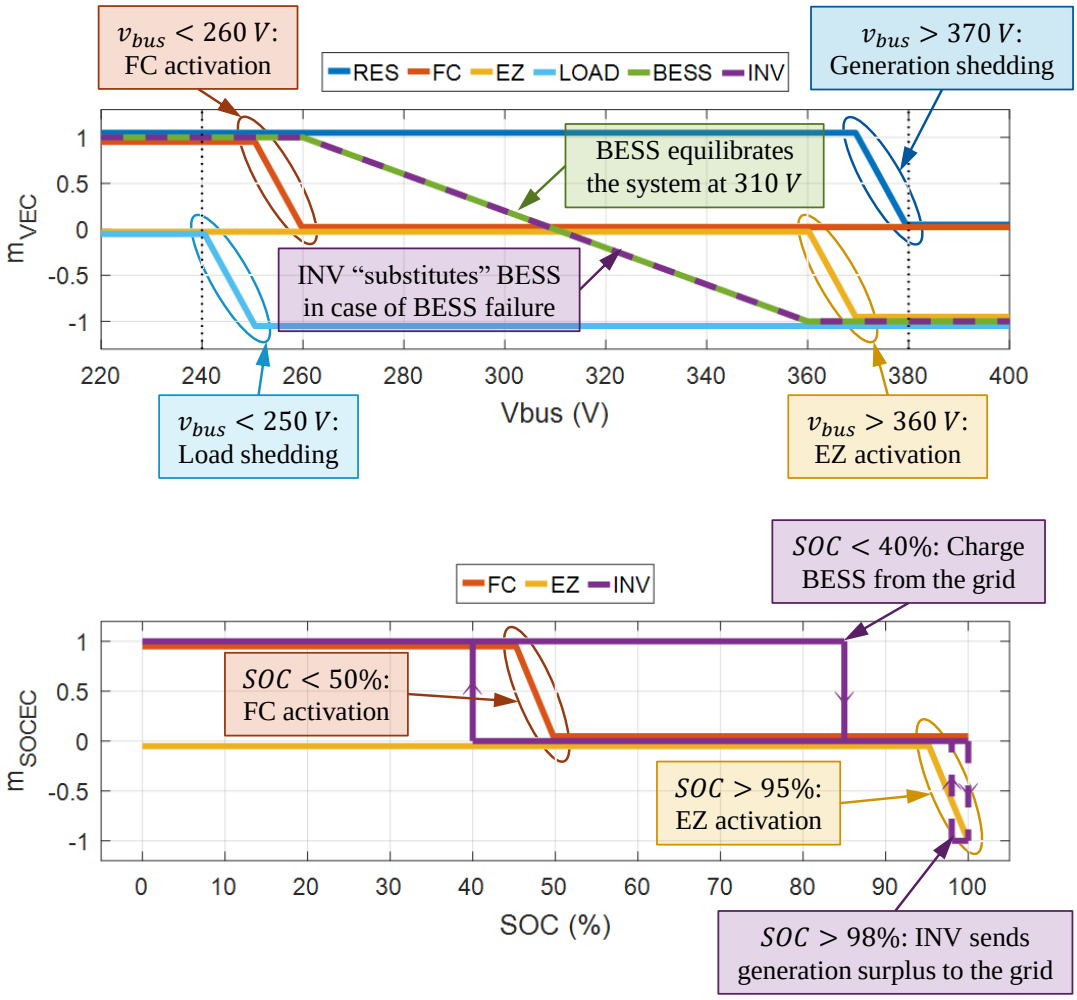


Figure 2-9. E-BCS control laws: VEC in the graph above and SOCEC in the graph below. Explanation boxes have been superposed for clarity.

The power reference $P_i[k]$ imposed to the converter $i$ in the time step $k$ is calculated as in (2.7). The sign convention is: $P_i$ is positive when power is injected into the DC bus and negative when power is withdrawn from the DC bus.

$$m_i[k] = \begin{cases} min\left(1, m_{VEC}^{i}(v_{bus}[k])\right), & i = PV, WT \\ min\left(1, m_{VEC}^{FC}(v_{bus}[k]) + m_{SOCEC}^{FC}(SOC[k])\right), & i = \quad FC \\ max\left(-1, m_{VEC}^{LOAD}(v_{bus}[k])\right), & i = LOAD \\ max\left(-1, m_{VEC}^{EZ}(v_{bus}[k]) + m_{SOCEC}^{EZ}(SOC[k])\right), & i = \quad EZ \\ min\left(1, max\left(-1, m_{VEC}^{BESS}(v_{bus}[k])\right)\right), & i = BESS \\ min\left(1, max\left(-1, m_{VEC}^{INV}(v_{bus}[k]) + m_{SOCEC}^{INV}(SOC[k])\right)\right), & i = \quad INV \end{cases} \tag{2.6}$$

$$P_i[k+1] = \begin{cases} P_{PV}[k+1] & = min(P_{PV\ MPP}, m_{PV}[k]P_{nom\ PV}) \\ P_{WT}[k+1] & = min(P_{WT\ MPP,} m_{WT}[k]P_{nom\ WT}) \\ P_{FC}[k+1] & = m_{FC}[k]P_{nom\ FC} \\ P_{LOAD}[k+1] & = max(P_{demand}[k], m_{LOAD}[k]P_{max\ demand}[k]) \\ P_{EZ}[k+1] & = m_{EZ}[k]P_{nom\ EZ} \\ P_{BESS}[k+1] & = m_{BESS}[k]P_{nom\ BESS} \\ P_{INV}[k+1] & = \begin{cases} m_{INV}[k]P_{nom\ INV}, & with\ SOC < 98\%\ and\ BESS\ ok \\ m_{BESS}[k]P_{nom\ INV}, & with\ SOC > 98\%\ or\ BESS\ fail \end{cases} \end{cases} \tag{2.7}$$

where $P_{nom\ i}$ is the nominal power (absolute value) of the source/load/bidirectional unit $i$, $P_{PV\ MPP}$ and $P_{WT\ MPP}$ are the instantaneous Maximum Power Point (MPP) that PV and WT, the Renewable Energy Sources (RES), can generate from the available solar and wind resources, and $P_{max\ demand} = 6\ kW$ is the maximum power demand that can be connected to the microgrid.

This control scheme achieves the following goals:

- Prioritizing cycling BEES over consuming/injecting power from/to the AC grid. INV is only used in case of BESS failure or with battery either fully charged or at $SOC_{min}$.
- Limiting maximum Depth of Discharge (DOD) of BESS to 60%. Self-regulation already starts providing extra power to the DC bus (to charge the battery if possible) with $DOD \geq 50\%$. If despite that, discharge continues, bulk charge from the grid (through INV) starts when $DOD$ exceeds 60%. In islanded mode, BESS is disconnected when $DOD$ reaches 60%.
- Utilizing MPP generation from RES in grid connected mode. RES generation is only limited in islanded mode with fully charged battery.

- Always supplying the demanded power to LOAD in grid connected mode. (LOAD represents the essential loads of the system.) The microgrid will only fail to supply power to LOAD in islanded mode and battery below $SOC_{min}$.
- Using FC and EZ as emergency support source/load. (EZ represents an adaptable, opportunistic load, that is only activated when there is energy surplus in the system.)

The top graph in Figure 2-9 shows the control laws of Voltage Event Control (VEC), which manages power balance in order to keep the system stable. On one hand, power from renewable energy sources (PV and WT, dark-blue curve) is limited when $v_{bus}$ is too high (over $370\ V$), which only can happen if the microgrid operates in islanded mode, with excess renewable generation and with nearly fully charged battery. On the other hand, LOAD power (light blue curve) is limited when $v_{bus}$ is too low (under $250\ V$), which can only happen in islanded mode with battery $SOC$ near $SOC_{min} = 40\%$. BESS power (green curve) tends to equilibrate the system at the middle voltage ($310\ V$). FC and EZ (brown and yellow curves) are utilized as emergency support source/load when $v_{bus}$ approaches the lower/higher voltage limit (under $260\ V$ / over $360\ V$).

The top graph in Figure 2-9 shows the control laws of State of Charge Event Control (SOCEC), which are applied in addition to VEC laws. The fuel cell, the electrolyzer and the bidirectional inverter are the only units that incorporate SOCEC, on one hand to avoid deep discharge of the BESS and, on the other hand, to avoid missing renewable-energy generation when $SOC$ is near $100\%$. Hydrogen production/consumption is activated when $SOC$ reaches high ($95\%$) / low ($50\%$) values.

INV (purple curves) follows the VEC control law of the BESS (dashed purple curves) in case of BESS failure or when SOC exceeds 98%, and will deliver full power to the DC bus when $SOC$ drops down to 40% until $SOC = 85\%$ is reached. Apart from SOCEC laws, if SOC gets too low ($SOC < 40\%$), further discharging the battery is prevented to protect the battery and will not discharge again until $SOC$ surpasses $50\%$.

All control laws apply simultaneously, except the VEC control law of the INV (dashed line in Figure 2-9), which only applies in case of BESS failure. The control scheme described above is effective and robust, yet simple as it requires very limited communications among the microgrid converters –$v_{bus}$ and $SOC$ values are the only data that the converters require to generate their power references. It is, therefore, a decentralized control in which each DC-DC converter is autonomous or self-managed based on $v_{bus}$, complemented with distributed control based on the BESS' $SOC$ in three of the microgrid's units (FC, EZ and INV).

The control system avoids cycling the battery with high Depth of Discharge (DOD) because it causes fast degradation in lead-acid batteries. Maximum DOD has been set in 60% as a trade-off between effective utilization of the battery's capacity and its lifetime. A very oversized battery pack would suffer minor degradation, but the pack's available capacity would be largely unused. High initial cost makes this option unfeasible. On the opposite extreme, a non-oversized battery pack (with capacity just enough to perform cycles of $DOD = 100\%$) would age extremely fast. Battery manufacturers usually facilitate graphs that relate DOD with battery life, such as Figure 2-10, that reveal rapid capacity decay with high DOD.

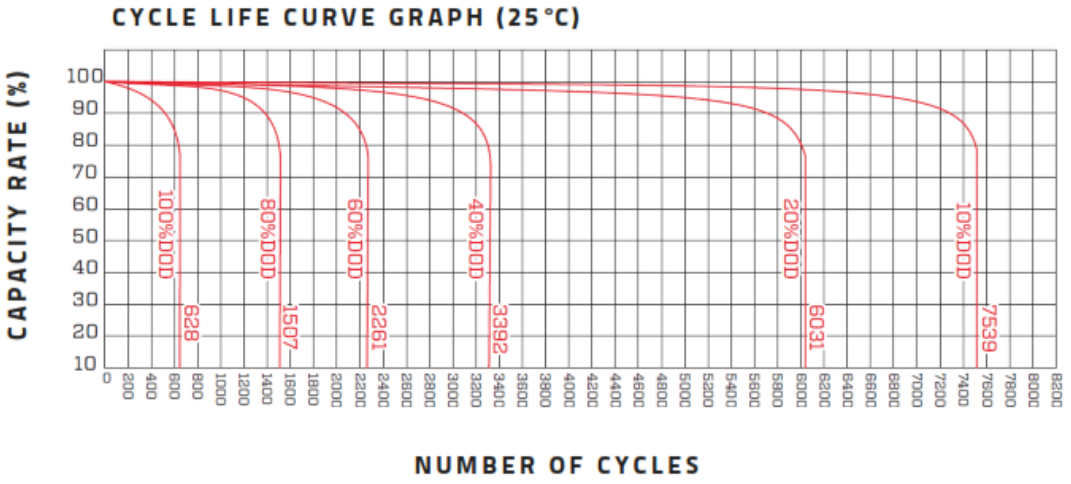


Figure 2-10. Capacity fade vs. DOD graph of Lead Crystal batteries. Reproduced from the datasheet from the manufacturer, Betta Batteries.

## 2.2. Battery types

Nowadays, batteries are attracting great interest, especially battery packs for electric vehicles and Battery Energy Storage Systems (BESS) for grid support –the main applications for medium and large-scale batteries. These two thriving applications (together with consumer electronics) have driven a transformation of the battery market from one dominated by traditional lead-acid batteries towards one dominated by lithium-ion.

The automotive industry is progressively introducing electric models, in an exhibition of commitment to greener transportation, powered by electric motors. The first generation of pure electric vehicles (EVs) began in 2010, with a 150 km range or below: Nissan Leaf and Ford Focus had ranges of about 100 km. Nowadays, EVs reach high ranges greater. For

instance, Tesla Model S, launched in 2012, has a range greater than 300 km; and Chevrolet Bolt, launched in January 2017, has a range of 380 km [52]. Up to date, Tesla Model S Long Range Plus, launched in 2020, has the highest range of all EVs, with 647 km.

Regarding the possibilities that EVs' batteries offer for grid-support applications, Vehicle to Grid (V2G) is expected to allow EV owners to benefit from cooperating with smart grids (see Section 2.1.1) in the near future. Grid operator(s) will be able to demand specific generation profiles from a great number of parked vehicles in coordinated operation. The owners will get some revenue in exchange for the energy or the auxiliary services provided. This possibility, though, entails extra cycling the batteries and, thus, extra degradation. Accurate online degradation models should be employed to determine whether it is worth to participate in V2G markets or not [53].

Apart from the EV industry, BESS are used in stationary electrical systems to support the operation of the mains grid. BESS can provide many valuable services to the grid [54], including energy reserve and power support, with nearly instantaneous response times [55]. Compared to conventional generators, battery storage can ramp much more rapidly, providing faster response to automatic generation control commands, with better performance. Currently, providing regulation is one of the most profitable applications for battery storage [56], although it is necessary to model battery degradation to anticipate whether sacrificing battery life for regulation revenues results economically advantageous [57]. BESS can also help to integrate renewable energy sources: the impact of generation variability can be significantly reduced by utilizing energy storage in conjunction with photovoltaic and wind power generation. Moreover, BESS can be used as uninterruptible power supply systems in critical applications –battery energy backup in data centers, life support systems, etc. Finally, BESS can contribute to make a grid stable in case of electricity distribution being interrupted or degraded by natural events, and in remote areas where the grid is weak due to lengthy power lines between the conventional generating plant and the consumers.

In all cases, the strategic use of storage systems can be a major component of a stable and comprehensive grid solution. It offers an extra layer of flexibility that can help to stabilize the grid and offer better energy management support during periods of normal and peak demand. To date, various battery technologies have been developed to comply with the increasing interest in grid-level energy storage, such as lead-acid batteries, Nickel-cadmium (Ni–Cd) batteries, Nickel Metal Hydride (Ni–MH) batteries, Sodium–Sulfur (Na–S) batteries, lithium-ion batteries, and flow batteries [58].

Lead-acid and lithium-ion are the historical and current standard battery technologies, respectively. Lead-acid has been displaced by lithium-ion because the latter outscores the former (and all other commercially available technologies) in terms of energy density,

efficiency, and power density, yet with a moderate price –see Figure 2-11. Economies of scale are pushing the cost of lithium-ion batteries down (Figure 2-12), which, together with their outstanding characteristics, explains the domination it has gained in the battery market [59].

Lead-acid and lithium-ion batteries have been employed at different points of the research works in this doctoral dissertation. They are examined next in consideration of their relevance. Afterwards, battery modeling, battery management systems, and battery balancing are reviewed as well, focusing on lithium-ion.

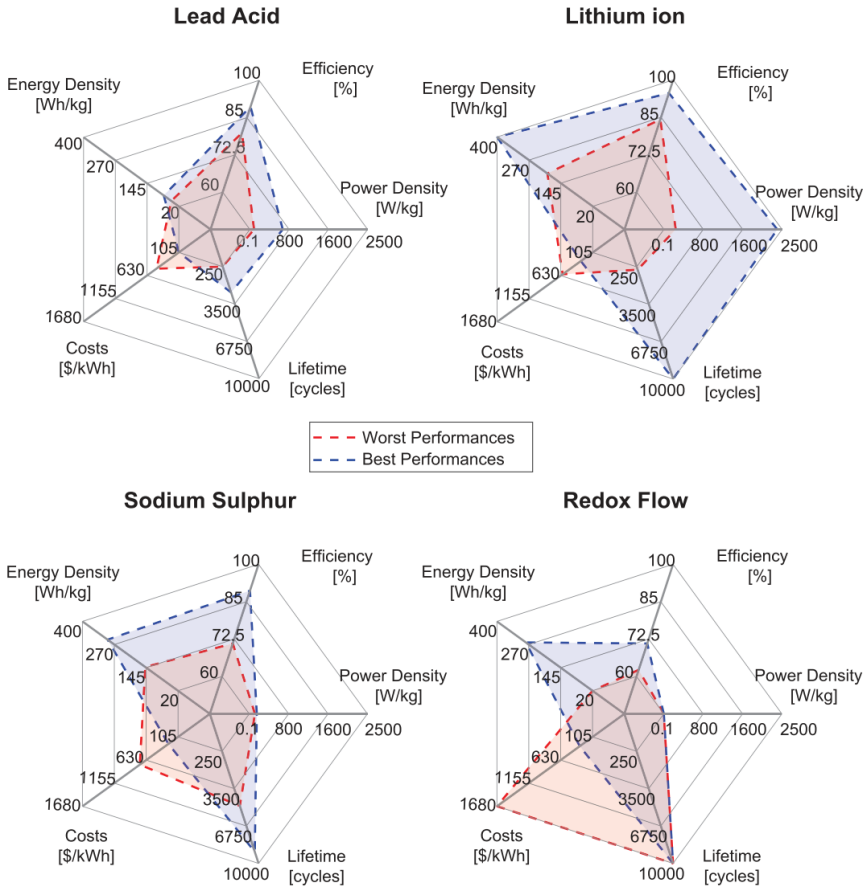


Figure 2-11. Characteristics of lead-acid and lithium-ion batteries. Reproduced from [59].

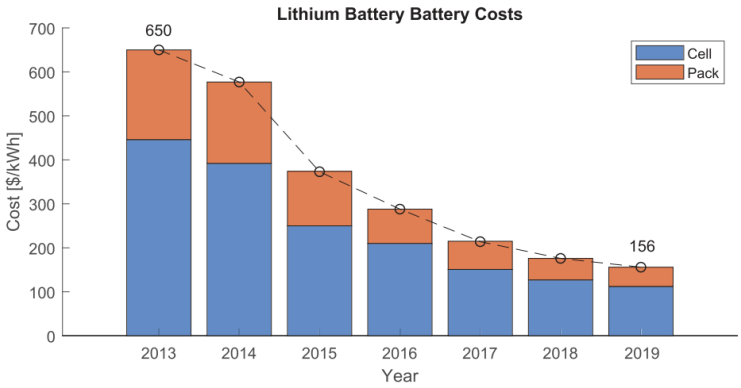


Figure 2-12. Evolution of the price of lithium-ion batteries. Reproduced from [59].

### 2.2.1. Lead-acid battery

Lead-acid is the most mature and less expensive battery technology. In contrast, its energy and power densities are low, its cycle life is relatively short, its low-temperature performance is poor, its charging process is slow, its capacity significantly decreases with deep and/or rapid discharge, and (some variants) require maintenance and emit hazardous gases [60–63].

Typically, lead-acid batteries have a lead peroxide (PbO2) positive cathode and a lead (Pb) negative terminal. Electrolyte is a sulfuric corrosive arrangement with particular specific gravity in the range $[1.12, 1.30]$ (28% to 39% in weight) [63]. The operation of lead-acid secondary battery is based on:

$$\mathrm{Pb} + \mathrm{PbO_2} + 2\mathrm{H_2SO_4} \Leftrightarrow 2\mathrm{PbSO_4} + 2\mathrm{H_2O}$$

Several types of lead-acid batteries exist in the market, such as the flooded battery and the sealed maintenance-free battery, which includes Valve-Regulated Lead-Acid, gel, and Absorbent Glass Mat lead-acid batteries. The Valve-Regulated Lead-Acid stationary battery utilizes the recombination of oxygen and hydrogen released on the positive and negative plates, respectively, to generate water, thereby eliminating the need of water replenishment required by conventional lead-acid batteries [64]. Lead-acid battery has an round-trip efficiency of $75-80\%$ with an energy density of $30-50$ Wh/kg. The nominal voltage of the lead-acid battery is approximately 2 V. It is easy to manufacture and allows easy recycling of the battery components ($> 97\%$ of all battery lead can be recycled) [58].

Nowadays, lead-acid batteries are mainly used for starting internal-combustion vehicles (typically, $12\,V$, $40\,Ah$ batteries) and for backup power supplies (Uninterrupted Power Supply, station batteries) [61].

### 2.2.2. Lithium-ion battery

Since the first commercial Li-ion batteries were produced in 1991 by Sony, lithium-ion batteries have become one of the most important battery technologies, leading the market in the field of energy storage [58]. They offer relatively high energy density (240 Wh/kg), no need for maintenance, broad operation temperature range, rather long cycle life, long shelf life, high efficiency, low self-discharge and rapid-charge capability. Their disadvantages include poor high-temperature performance, requirement of protective circuitry, and potential risk of explosion due to overcharging or over-heating (because internal pressure due to electrolyte decomposition forms gases that can cause swelling and even thermal runaway) [58, 60, 63, 65]. A large number of vendors produce the technology: Bosch, Panasonic, Johnson Controls, LG Chem, NEC, Samsung, Saft, BYD, Hitachi, and GS Yuasa (Mitsubishi) [55].

Lithium-ion batteries comprise positive and negative electrodes and $Li^+$-conducting electrolyte. The most extensively used negative electrode (NE) material is graphite carbon on a copper current collector. Graphite electrodes have sufficient specific capacity (up to 372 mAh/g, theoretically) and high voltage with respect to the lithium deposition potential (which is good prevent lithium plating). However, dendrite crystal-induced short circuit can develop during rapid charging, which introduces significant potential risks. At present, efforts are made to develop graphite substitutes with higher specific capacities (over 600 mAh/g), including the use of silicon, metallic tin and their oxides [66]. Typically, positive electrode (PE) materials are metal oxides with layered or tunneled structures on an aluminum current collector. Li-ion batteries have different categories based on PE materials: Li-Cobalt (LCO), Li-Manganese (LMO), Li-Phosphate (LFP), Lithium Nickel Manganese Cobalt Oxide (NMC), Lithium Nickel Cobalt Aluminum Oxide (NCA), and Li-Titanate (LTO). Electrolytes for Li-ion batteries can be divided into two categories, namely, liquid and semisolid/solid-state electrolytes. Liquid electrolytes are usually composed of lithium salts (e.g., $LiPF_6$, $LiBF_4$, $LiN[CF_3SO_2]_2$ and lithium bis-oxalato borate [LiBOB]) dissolved in organic carbonates (e.g., propylene carbonate, ethylene carbonate, dimethyl carbonate, ethyl methyl carbonate, and diethyl carbonate and their mixtures). The semisolid electrolyte is typically a polymer electrolyte, which is an ion-conducting material composed of lithium salts and high-molecular-weight polymer matrices (e.g., poly(ethylene oxide), polyvinylidene fluoride, polyvinylidene fluoride-hexafluoropropylene) with or without solvents [55, 58, 61].

Lithium ions move between the two electrodes by intercalating or de-intercalating from the interstitial space between atomic layers of electrode materials during discharge–charge processes. The overall chemical reaction that takes place in the cell is:

$$Li_xC + Li_{1-x}MO_2 \Leftrightarrow LiMO_2 + C$$

Lithium-ion batteries are typically characterized by their PE material. The NMC battery is the most used type in EVs due to its higher energy and power densities. In contrast to the NMC battery, the LFP technology is a lower-cost battery, with low energy density, intermediate power density, that presents constant discharge voltage over most of the SOC range, and is highly safer compared to other Li-ion chemistries. LTO has fast charging characteristic and is considered a stable Li-ion chemistry with higher than average cycle lifetime and a high power density. Unlike NMC and LFP, the LTO technology has a lower energy density with a higher cost compared to the others [55].

Given that lithium-ion batteries nowadays account for the majority of EV battery packs and BESS, the next section is centered in this technology.

## 2.3. Battery modeling

Battery models are used for simulating and anticipating battery response during operation. The most commonly used battery models are equivalent circuit models, which can predict cell dynamic response in the short-term –i.e., disregarding degradation. Electrical models are considered intuitive and useful for most applications as they make a compromise between accuracy and computation time. Alternatively, physics-based models, although far more complex, use a system of partial differential equations to describe physical characteristics and processes of the battery, which can mean a great advantage to produce more accurate results and to model long-term operation, including the effects of degradation [61].

A battery is a non-linear system which internal states (such as the State of Charge) cannot be obtained by direct measurement. Different approaches to SOC estimation and some of the most relevant comprehensive battery models are reviewed next, following [67].

### 2.3.1. State of Charge estimation techniques

The State of Charge (SOC) is a measurement of the capacity stored in a battery cell. It is defined as the quotient between the stored ampere-hours (Ah) and the cell's remaining capacity –i.e., they maximum capacity the battery can still hold at that time (also in Ah). SOC limits (100% and 0% SOC) are generally defined by the cut-off voltage limits ($V_{max}$ and $V_{min}$) provided by the manufacturer [68]. SOC, is usually calculated in terms of cell parameters and cell current:

$$z[k] = z[0] - \frac{\Delta t}{Q[k]} \sum_{0}^{k} \eta_Q[k] i_{net}[k] \tag{2.8}$$

where $z$ represents the cell's SOC, $k$ is the index of discrete time, $\Delta t$ is the time step used in the discretization ($t = k\Delta t$), $Q$ is the cell's capacity (note that $Q$ is variable in general, to account for the effects of degradation), $i_{net}$ is the net cell current (discharge current is positive), and $\eta_Q$ is the coulombic efficiency, which is modeled to have effect during the charge process only ($\eta_Q[k] = 1$ when $i_{net} \geq 0$ and $\eta_Q[k] = \eta_Q < 1$ when $i_{net} < 0$). Note that net cell current, $i_{net}$, is constituted by three contributions:

$$i_{net}[k] = i_{app}[k] + i_{self-discharge}[k] \; + \; i_{leakage}[k] \tag{2.9}$$

where $i_{app}$ is the battery-pack load current, $i_{self-discharge}$ is the rate of self-discharge of the cell, and $i_{leakage}$ is the current drawn from the cell to power external circuitry. Since it is not always feasible to measure $i_{net}$, it is often approximated by $i_{app}$, the applied current.

Alternatively, SOC can also be defined electrochemically, in terms of the cell electrodes' stoichiometry [69] (2.10):

$$z[k] = \frac{\theta_n[k] - \theta_n^0[k]}{\theta_n^{100}[k] - \theta_n^0[k]} = \frac{\theta_p^0[k] - \theta_p[k]}{\theta_p^0[k] - \theta_p^{100}[k]} \tag{2.10}$$

where $\theta_p$ and $\theta_n$ are the positive and the negative electrode's stoichiometries (that is, the degree of lithiation of the electrodes), $\theta_p^0$ and $\theta_n^0$ are the degrees of lithiation of the positive electrode (PE) and the negative electrode (NE) when the cell is at $z = 0$ (defined by $OCV = V_{min}$), and $\theta_p^{100}$ and $\theta_n^{100}$ are the degrees of lithiation of the PE and the NE when the cell is at $z = 1$ (defined by $OCV = V_{max}$).

SOC estimation is a fundamental component in a Battery Management Systems (BMS) because SOC is an input variable for other calculations such as remaining stored energy, available power, and cells' imbalance. The benefits of a BMS with precise SOC estimations include [70]:

- Prevention of damage by avoiding abusive conditions for the battery. This can potentially extend battery life.
- Increase of the battery pack's performance thanks to battery balancing and optimization of battery operation.
- Increase of the reliability of battery-operated devices.

- Improvement of the battery power density in battery packs.

SOC is therefore a key variable for BMS but, unfortunately, it cannot be directly measured –SOC can only be estimated. Many different approaches to estimate the SOC of a battery cell have been proposed in the literature, but they all relay on a limited number of variables that can be measured. These are namely the current, the terminal voltage, the operation time, and the cell temperature [71]. Some of the standard estimation approaches are overviewed next, following [63].

The coulomb counting method, the Open Circuit Voltage (OCV) method, and the impedance estimation method require simple calculations so they are, consequently, easy to implement in basic BMS microcontrollers. Nevertheless, the accuracy of these techniques is limited by the precision of the current and voltage sensors employed. There are other estimation methods that tolerate a certain level of measurement imprecision, relaying on complex mathematical calculations to estimate SOC, such as machine learning and Extended Kalman Filter. Techniques that utilize machine-learning-based estimation (for example, artificial neural network and fuzzy logic) require a high computational effort because they require building and utilizing extensive datasets to model the nonlinear behavior of a battery. State-space-based estimation strategies (for example, Extended Kalman Filter) are being considered for online SOC estimation as they reduce the computational time, increase the accuracy, and are self-correcting [63].

#### 2.3.1.1. Coulomb Counting

Coulomb counting, also known as ampere-hour counting, results from integrating the battery current [72], which is directly derived from the SOC definition (2.8). Coulomb counting is an easy to implement technique that provides reasonable estimations of battery SOC with low computational complexity [69]. The downside of this technique is that it is heavily dependent on the initial SOC estimation and on the precision of the current sensor [73], as shown in Figure 2-13. Incorrect initial SOC estimation causes estimation offset (upper red estimation line in Figure 2-13) and current sensor presenting bias error causes the estimated SOC to diverge from the actual SOC with time (two lower red estimation lines in Figure 2-13), since coulomb counting is an open-loop method.

Self-discharge current, which is not measured by the current sensor, is an additional factor affecting the coulomb-counting method accuracy. The initial SOC value of the battery, the battery capacity, and the current sensor drift should be corrected and adjusted regularly for improved accuracy [69]. Otherwise, the estimation error will increase indefinitely [74]. Coulomb counting is usually combined with model-based or data-driven SOC estimators for improved performance [73].

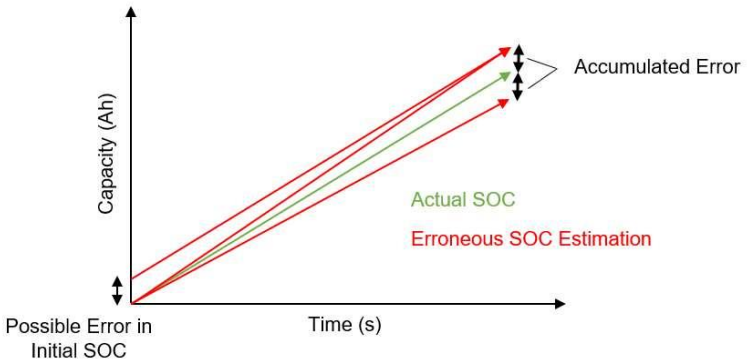


Figure 2-13. Capacity estimation errors in coulombic counting. Reproduced from [75].

#### 2.3.1.2. Open Circuit Voltage look-up table

Open Circuit Voltage (OCV) method consists in identifying the relation OCV vs. SOC and using it inversely to obtain SOC based on the stabilized terminal voltage of the cell. Two conditions are required: 1) this relation has to be known and monotonous, and 2) it has to remain unchanged during the battery lifetime, or changes have to be tracked otherwise. This method is accurate when a good battery model (including the hysteresis effect [76]) is used to estimate $OCV$ online, together with detailed $OCV$ vs. $SOC$ look-up tables at various temperatures, $T$.

SOC estimation from OCV requires, first, to estimate the cell's OCV online (given that most applications do not allow to have the cell unloaded until cell OCV is stabilized, which can take more than two hours [77]). OCV is estimated from the cell's terminal voltage and the applied current, by means of a battery model. Once the (estimated) OCV is known, the SOC can be easily computed from the look-up table $OCV(z,T)$ [78].

The use of the OCV vs. SOC relation is not feasible for LFP cells. In fact, the flatness of the OCV curve and its remarkable hysteresis behavior make the diagnostic of this cell particularly difficult. In addition, aging impacts LFP's OCV curve significantly [20].

#### 2.3.1.3. Impedance estimation

Impedance estimation strategy consists in injecting small-amplitude current in a certain range of frequencies (typically in the range $[10^{-5}, 10^{5}]$ $kHz$ [79]) to find the cell's impedance by analyzing the cell's response. Impedance phase and magnitude are related to SOC, with higher impedance variation at low SOCs. However, online application of electrical impedance spectroscopy has some drawbacks: a sinusoidal AC signal generator for various frequencies

is required, the SOC-impedance relationship is not as stable as the $OCV$ vs. $SOC$ one, the relationship could be non-monotonic, impedance is more affected by temperature and SOH than by SOC and this is difficult to compensate, and the cost of the required equipment is rather high [77, 80].

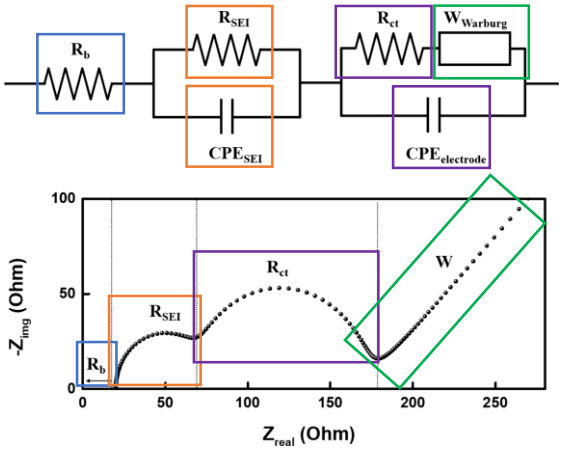


Figure 2-14. Impedance-based model of a lithium ion half-cell system. Reproduced from [81]

Equivalent circuit models of the cell can be created from the Nyquist plot (imaginary vs real impedance), by identifying the underlying physical processes causing of some characteristic regions of the curve (see Figure 2-14). Impedance-based models can identify series resistance, Solid-Electrolyte Interphase RC pair, and elements representing intercalation charge-transfer (RC pair), and low-frequency diffusion (Warburg element) effects [81–85].

#### 2.3.1.4. Kalman Filters

Kalman Filter is an adaptive, self-correcting algorithm that can be used to minimize measurement noise and to estimate a system state that cannot be directly measured, such as SOC. This algorithm uses a linearized model of the battery cell to calculate the value of the (measurable) cell terminal voltage, given certain inputs (current, temperature, time). The system model relates the input and output variables through system state (SOC, and maybe other variables, such as capacity and SOH). The estimation is then compared to the real measured value (cell voltage), and the Kalman Filter corrects the state estimation (see Figure 2-15).

Kalman Filter is defined by a state space model of two discrete-time functions: a process equation and a measurement equation. The process equation is a linear function that uses the previous values of voltage and SOC to estimate the present value of voltage. The measurement equation corrects the estimated SOC to make the predicted voltage value converge to the real value.

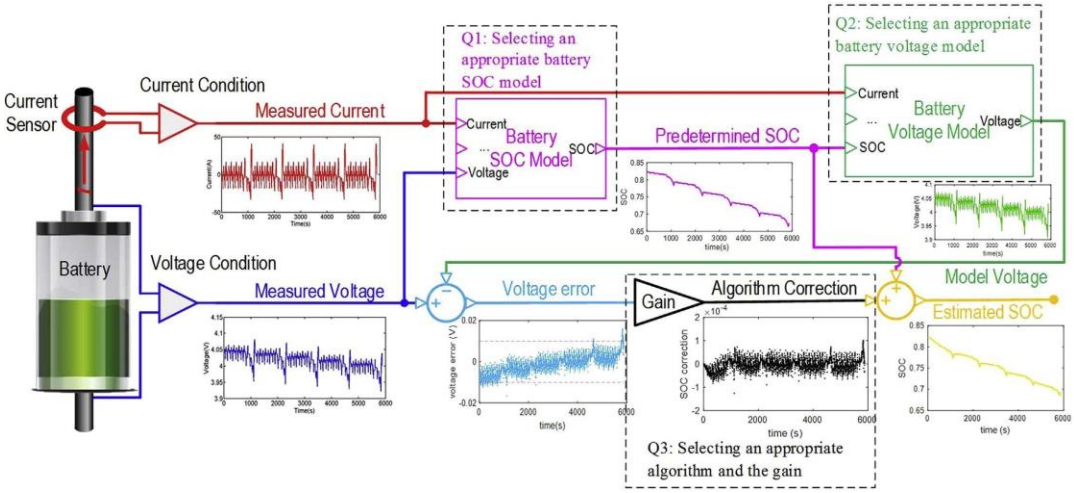


Figure 2-15. Flow chart of adaptive filter algorithms for SOC estimation. Reproduced from [77].

Some variants of the algorithm, such as Extended Kalman Filter [86–88] or Sigma-Point Kalman Filter [89], are more suitable for battery modeling, because they admit non-linear state function and measurement equations (respectively allowing for analytic partial derivatives and for numeric approximations). This technique is very computationally intensive since it continually evaluates the model equations recursively, performs comparisons to previous and current values of the output variable, and corrects the state estimation.

Kalman-Filter-based SOC estimators can work well with a simple battery model and are highly accurate under all operation conditions. The main drawback for Kalman-Filter-based SOC estimators is that the recursive processing of the Kalman algorithms requires elevated computational power.

#### 2.3.1.1. Artificial Neural Networks

An artificial neural network is a data-based estimation approach employed to generate models of complex non-linear processes (such as battery operation) to produce certain outputs

(such as SOC estimation). Artificial neural network receives battery variables as the input nodes, assigns them different weight coefficients and maps them to the hidden nodes, which then combine to produce one or various outputs, applying activation function(s). The artificial neural network technique is computationally intensive and requires to store large amounts of data [69] but, in exchange, it can be very accurate and adaptive to SOH changes, especially in the non-linear regions of the $OCV$ vs. $SOC$ curve.

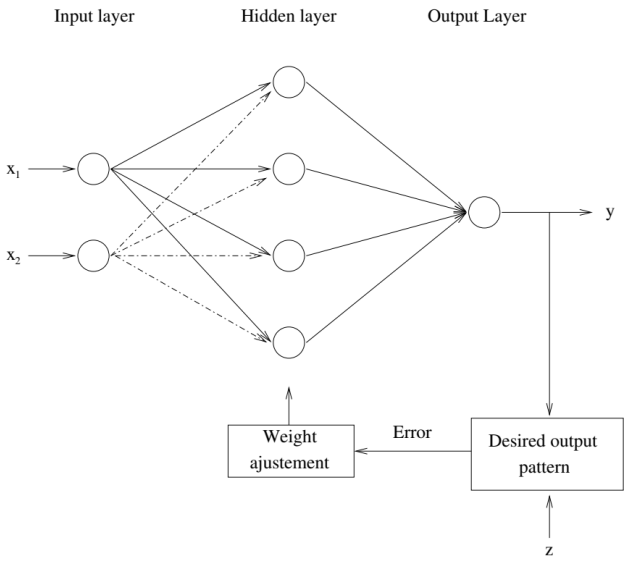


Figure 2-16. Adaptive artificial neural network with three layers. Reproduced from [89].

Artificial neural networks need a “learning” stage during which the neural network is fed with a large set of training data, consisting of measured input and the correspondent outputs they produce (SOC). The measured inputs are: current profile, terminal voltage, and temperature, and other variables that result from combining the previous three among them and with time (discharged ampere hours, time-average voltage, twice time-averaged voltage, time-derivative of voltage, second time-derivative of voltage) [90]. SOC can only be accurately measured under lab conditions, using highly accurate sensors in a controlled environment. The estimated model heavily depends on the training dataset. Thus, in order to obtain a generic model reliable under any operation conditions, extensive training is required to include many possible situations [79, 89]. The artificial neural network is initialized with all node weights set to zero and characteristic weightings which recreate battery operation are

developed as the neural networks is trained, thus producing a battery model. This model can be then used recurrently to produce an output –in this case, the cell's SOC.

#### 2.3.1.2. Fuzzy Logic

Fuzzy Logic computation works in a somewhat similar manner to human thinking, it typically involves different clusters of data and has input variables that have a certain degree of membership to each cluster (partial truth, instead of binary truth, is employed), for example, {extreme low, very low, low, average, high average, high, very high} [91]. A linguistic set of rules based on the formula "if → then" is then built, instead of mathematical equations, analogously to the human decision making process [71].

The flow chart of an estimation method based on fuzzy logic is reviewed next following [92]. The process starts with fuzzification, that is, transforming the input set of numerical variables into a set of linguistic variables: the degree of membership to predefined clusters is determined based on the numerical value of the input variables. Different membership functions can be used: triangular, trapezoidal, Gaussian, piecewise linear, singleton, etc. The "if → then" rule set is created based on human expert knowledge and trials. The rule set has two outcomes: establishing input-output relationships and generating parameters for the fuzzy inference engine. The inference engine processes the mapping from a given input to an output utilizing the rules, providing a basis from which decisions can be made. Finally, the fuzzy output set is de-fuzzificated, which transforms it into numerical outputs –SOC, in this case.

Estimation methods based on fuzzy logic are suitable to model non-linear systems, such as batteries. They have excellent adaptation to different loading scenarios and to battery aging [69]. Disadvantages of fuzzy logic estimators are that they require large computational capability, they require extensive data to train the model (as in the case of artificial neural network) and they are susceptible to inaccuracies from external factors that vary from the training model [93].

### 2.3.2. Equivalent Circuit Models

Equivalent circuit models are robust and easy to use in real-time applications; thus they are widely implemented. Equivalent circuit models are empirical and utilize common electrical circuit components to emulate the external behavior of a cell. Therefore, circuit analysis can relate terminal voltage to applied current [94]. They cannot describe the electrochemical and physical characteristics of battery cells, but they work as analogy models, where each circuit element produces a response similar to the response caused by a given physical process in the cell. System-identification techniques are used to estimate equivalent-circuit component values by using input-output measurements from cells.

A number of different equivalent circuit model topologies are used for battery modeling in [95, 96]. In [96], a comprehensive systematic study was carried out to compare twelve equivalent circuit models. They were evaluated based on their practicality, complexity, generalizability for multiple cells, and accuracy under both training and validation data. Two types of lithium-ion batteries were considered, Li-NMC and Li-$FePO_4$. This study found that first-order RC models, such as the Thevenin model (Figure 2-17.a), are better at representing Li-NMC chemistries. Similarly, a first-order RC model with one-state hysteresis, the Enhanced Self-Correcting model (ESC) [97] (Figure 2-17.b) was found to represent LiFePO4 chemistries better than other equivalent circuit models.

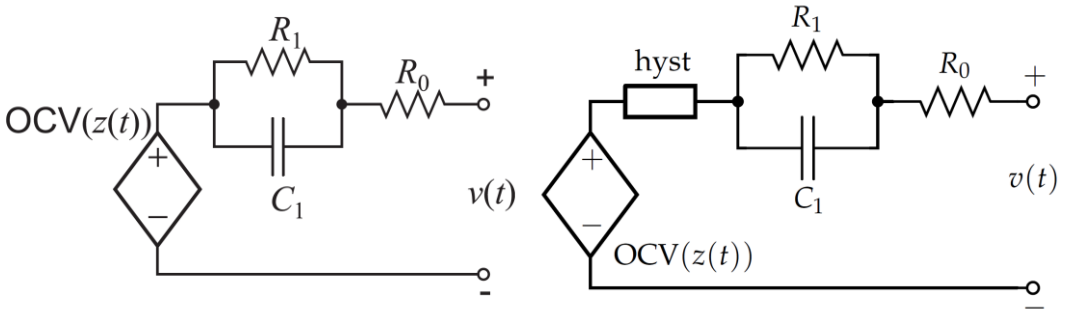


Figure 2-17. Thevenin equivalent circuit model (left) and Enhanced Self-Correcting Model (right). Reproduced from [67].

The Thevenin model, as seen in Figure 2-17 (left), comprises a single resistor and an RC pair; $R_0$ represents the internal resistance that causes instantaneous voltage drop when a current is applied, $R_1$ is the diffusion resistance, and $C_1$ is the diffusion capacitance. The RC pair represents the transient portion of the response during charge and discharge. The ESC model contains the same components as the Thevenin model but with the addition of a hysteresis element. Hysteresis is a phenomenon that causes a nonlinear relationship between SOC and terminal voltage, and is dependent on the charge/discharge history of the cell [98].

Although equivalent circuit models are convenient and have fast computational speed, they are limited to predicting only terminal voltage and SOC. They do not provide insight into the internal electrochemical reactions taking place within the cell. For this purpose, physics-based models are needed.

### 2.3.3. Physics-Based Models

Physics-Based Models utilize a set of coupled partial-differential equations and one algebraic closure term to describe the internal behavior of a lithium-ion cell. Such models can potentially enable the implementation of advanced control strategies to mitigate the effects of degradation.

Full-order models encompasses all cell electrochemical behavior utilizing four coupled partial-differential equations and one algebraic equation. These are known as the first-principles governing equations of a physics-based model:

1) Potential in the solid phase
2) Potential in the electrolyte phase
3) Concentration of lithium in the solid phase
4) Concentration of lithium in the electrolyte phase
5) Lithium flux

The charge balance equations are described in terms of potentials, and the mass balance equations in terms of concentrations. Additionally, the Butler-Volmer equation describes lithium movement between different phases.

Full-order models are too complex for the purpose of real-time battery management. The battery is an infinite-dimensional system with a transcendental transfer function. Realization algorithms can transform the full-order model's continuous-time transfer functions into discrete-time state-space models. That is, reduced-order models are produced retaining, as much as possible, the fidelity of the continuum-scale system of partial differential equations but simplify the calculations to a great extent. The derivation of reduced-order models is based on linearizing the physics-based model's partial differential equations. From them, discrete-time realization algorithms can be accomplished by creating transfer functions based on the locally linear model. The discrete-time realization algorithm produces a state-space reduced-order models that faithfully matches the behavior of the battery. Different approaches to derive discrete-time realization algorithms have been proposed [99–103].

Lithium ion batteries electrodes are porous, which increases the interfacial area between the solid and the electrolyte solution, thus diminishing the negative effects of the slow electrochemical reactions. Due to the complex geometry of the porous media, simplifications must be made to model the intercalation process, which takes place through the surface of the electrodes. Doyle et al. [104] introduced a pseudo-two-dimensional (see Figure 2-18 [105]) reduced-order model that accounts for the first-principles. This is considered one of the most detailed and accurate electrochemical models. The key assumption is that the chemical reaction dynamics do not show significant variations over the $y$ and $z$ coordinates, and thus

the process can be reduced to a one dimensional ($x$ coordinate) problem. In addition, to account for the intercalation / de-intercalation of lithium in the electrode's solid matrix and the diffusion on electrolyte over a single dimension, small spherical solid particles are conceptually superimposed with the electrolyte. These particles are considered to exist at every position inside the electrode, and lithium is stored inside them. The diffusion of lithium inside these particles is calculated over the pseudo-dimension $r$, the radius of the particles [106]. The pseudo-two-dimensional is described next.

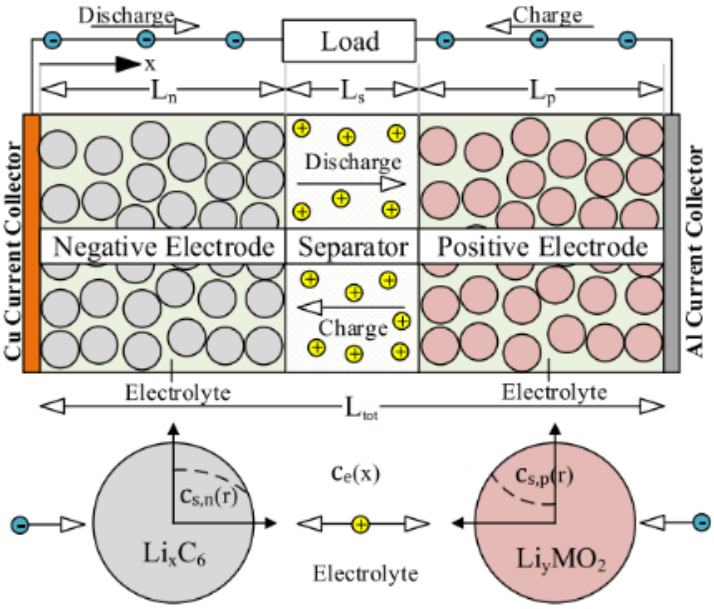


Figure 2-18. Pseudo-two-dimensional model of the lithium ion cell. Reproduced from [105].

1) Potential in the solid phase

The potential in the solid phase equation models the movement of electrons within the solid material of an electrode:

$$\frac{\partial}{\partial x}\sigma_{eff}\frac{\partial}{\partial x}\phi_s = a_s F j_I \tag{2.11}$$

where $x$ is the longitudinal coordinate of the cell measured from the interface between the NE's current collector and the NE, $\sigma_{eff}$ is the effective electronic conductivity of the solid material in the porous electrode, $\phi_s$ is the potential of the solid, $a_s$ is the specific interfacial

surface area, $F$ is the Faraday's constant, and $j_I$ is the rate of intercalation in $mol/m^2s$. The corresponding boundary conditions are:

$$\sigma_{eff}\frac{\partial}{\partial x}\phi_s\Big|_{x=0} = \sigma_{eff}\frac{\partial}{\partial x}\phi_s\Big|_{x=L_{tot}} = -\frac{i_{app}}{A} \tag{2.12}$$

$$\frac{\partial}{\partial x}\phi_s\Big|_{x=L_n} = \frac{\partial}{\partial x}\phi_s\Big|_{x=L_n+L_s} = 0 \tag{2.13}$$

where $i_{app}$ is the current applied to the cell, $A$ is the current-collector plate area, $L_n$ is the thickness of the NE, $L_s$ is the thickness of the separator, and $L_{tot} = L_n + L_s + L_p$ is the total cell thickness, with $L_p$ being the thickness of the PE.

2) Potential in the electrolyte phase

The potential in the electrolyte phase equation models the movement of ions within the electrolyte:

$$\frac{\partial}{\partial x}\kappa_{eff}\left(\frac{\partial}{\partial x}\phi_e + \frac{2R_gT(t_+^0-1)}{F}\left(1+\frac{\partial\, ln\, f_{\pm}}{\partial\, ln\, c_e}\right)\frac{\partial\, ln\, c_e}{\partial x}\right) + a_sFj_I = 0 \tag{2.14}$$

where $\kappa_{eff}$ is the effective conductivity of the ions in the electrolyte, $\phi_e$ is the potential of the electrolyte, $R_g$ is the universal gas constant, $T$ is the temperature, $t_+^0$ is the charge transference number of the lithium ion with respect to the solvent, $f_{\pm}$ is the mean molar activity coefficient, and $c_e$ is the lithium concentration in the electrolyte. The potential in the electrolyte phase has the following boundary conditions:

$$-\kappa_{eff}\left(\frac{\partial}{\partial x}\phi_e + \frac{2R_gT(t_+^0-1)}{F}\left(1+\frac{\partial\, ln\, f_{\pm}}{\partial\, ln\, c_e}\right)\frac{\partial\, ln\, c_e}{\partial x}\right)\Bigg|_{x=0} = 0 \tag{2.15}$$

$$-\kappa_{eff}\left(\frac{\partial}{\partial x}\phi_e + \frac{2R_gT(t_+^0-1)}{F}\left(1+\frac{\partial\, ln\, f_{\pm}}{\partial\, ln\, c_e}\right)\frac{\partial\, ln\, c_e}{\partial x}\right)\Bigg|_{x=L_{tot}} = 0 \tag{2.16}$$

$$-\kappa_{eff}\left(\frac{\partial}{\partial x}\phi_e + \frac{2R_gT(t_+^0-1)}{F}\left(1+\frac{\partial\, ln\, f_{\pm}}{\partial\, ln\, c_e}\right)\frac{\partial\, ln\, c_e}{\partial x}\right)\Bigg|_{x=L_n} = \frac{i_{app}}{A} \tag{2.17}$$

$$-\kappa_{eff}\left(\frac{\partial}{\partial x}\phi_e + \frac{2R_gT(t_+^0-1)}{F}\left(1+\frac{\partial\, ln\, f_{\pm}}{\partial\, ln\, c_e}\right)\frac{\partial\, ln\, c_e}{\partial x}\right)\Bigg|_{x=L_n+L_s} = \frac{i_{app}}{A} \tag{2.18}$$

3) Concentration of lithium in the solid phase

The concentration in the solid phase equation describes the concentration of ions within the solid:

$$\frac{\partial c_s}{\partial t} = \frac{1}{r^2}\frac{\partial}{\partial r}\left(D_s r^2 \frac{\partial c_s}{\partial r}\right) \tag{2.19}$$

where $c_s$ is the concentration of lithium in the solid, $t$ is time, $r$ is the radial coordinate of the solid particle ($r$ is the pseudo-dimension of the model), and $D_s$ is the diffusivity of lithium in the solid. The concentration of lithium in the solid phase equation has the following boundary conditions:

$$D_s \frac{\partial c_s}{\partial r}\bigg|_{r=0} = 0 \tag{2.20}$$

$$D_s \frac{\partial c_s}{\partial r}\bigg|_{r=R_s} = -j_I \tag{2.21}$$

where $R_s$ is the radius of the solid particle.

4) Concentration of lithium in the electrolyte phase

The concentration of lithium in the electrolyte phase models the concentration of ions within the electrolyte:

$$\frac{\partial(\varepsilon_e c_e)}{\partial t} = \frac{\partial}{\partial x} D_{e,eff} \frac{\partial}{\partial x} c_e + a_s(1 - t_+^0) j_I \tag{2.22}$$

where $\varepsilon_e$ is the volume fraction of the electrolyte, and $D_{e,eff}$ is the effective diffusivity –often assumed to be $D_{e,eff} = D_e \varepsilon_e^{brug}$, with $brug \simeq 1.5$ [94]. The concentration of lithium in the electrolyte phase equation has the following boundary conditions:

$$\frac{\partial c_e}{\partial x}\bigg|_{x=0} = \frac{\partial c_e}{\partial x}\bigg|_{x=L_{tot}} = 0 \tag{2.23}$$

$$D_{e,eff}^n \frac{\partial c_e}{\partial x}\bigg|_{x=(L_n)^-} = D_{e,eff}^s \frac{\partial c_e}{\partial x}\bigg|_{x=(L_n)^+} \tag{2.24}$$

$$D_{e,eff}^s \frac{\partial c_e}{\partial x}\bigg|_{x=(L_n+L_s)^-} = D_{e,eff}^p \frac{\partial c_e}{\partial x}\bigg|_{x=(L_n+L_s)^+} \tag{2.25}$$

$$c_e|_{x=(L_n)^-} = c_e|_{x=(L_n)^+} \tag{2.26}$$

$$c_e|_{x=(L_n+L_s)^-} = c_e|_{x=(L_n+L_s)^+} \tag{2.27}$$

5) Lithium flux

The Butler-Volmer equation models the rate of intercalation or de-intercalation of lithium ions occurring at the surface of the solid-mass and the electrolyte:

$$j_I = \frac{i_0}{F}\left[exp\left(\frac{\alpha_a F}{R_g T}\eta_I\right) - exp\left(\frac{-\alpha_c F}{R_g T}\eta_I\right)\right] \tag{2.28}$$

$$i_0 = k_{norm,0}\left(1 - \frac{c_{s,e}}{c_s^{max}}\right)^{\alpha_a}\left(\frac{c_{s,e}}{c_s^{max}}\right)^{\alpha_c}\left(\frac{c_e}{c_{e,0}}\right)^{\alpha_a} \tag{2.29}$$

Where $i_0$ is the exchange current density, $k_{norm,0}$ is the normalized rate constant for the electrochemical reaction, $\alpha_a$ and $\alpha_c$ are the anodic and cathodic charge transfer coefficients, $c_e$ is the concentration of lithium in the electrolyte phase, $c_{e,0}$ is the at-rest equilibrium concentration of lithium in the electrolyte, $c_s^{max}$ is the maximum concentration of lithium in the solid phase, $c_{s,e}$ is the concentration in the solid at the solid/electrolyte boundary, and $\eta_I$ is the overpotential of the intercalation reaction. The overpotential is expressed by:

$$\eta_I = \phi_s - \phi_e - OCP_n - \frac{\delta_{SEI}}{\kappa_{SEI}} F j_I \tag{2.30}$$

where $OCP_n$ is the open-circuit potential (which is a function of $c_{s,e}$), $\kappa_{SEI}$ is the conductivity of the SEI layer formed, and $\delta_{SEI}$ is the SEI film thickness. Typically, the last term of equation (2.30) is assumed to be negligible; however, it becomes important in the presence of degradation.

### 2.3.4. Degradation mechanisms

In the pursuit of safer and more durable batteries, degradation mechanisms must be mitigated. Models of the most important degradation mechanisms make possible to apply preventive control, selecting appropriate loading profiles to avoid rapid aging. Figure 2-19 represents the physical impact of a comprehensive catalog of degradation mechanisms, and Figure 2-20 shows their causes and their effects [107].

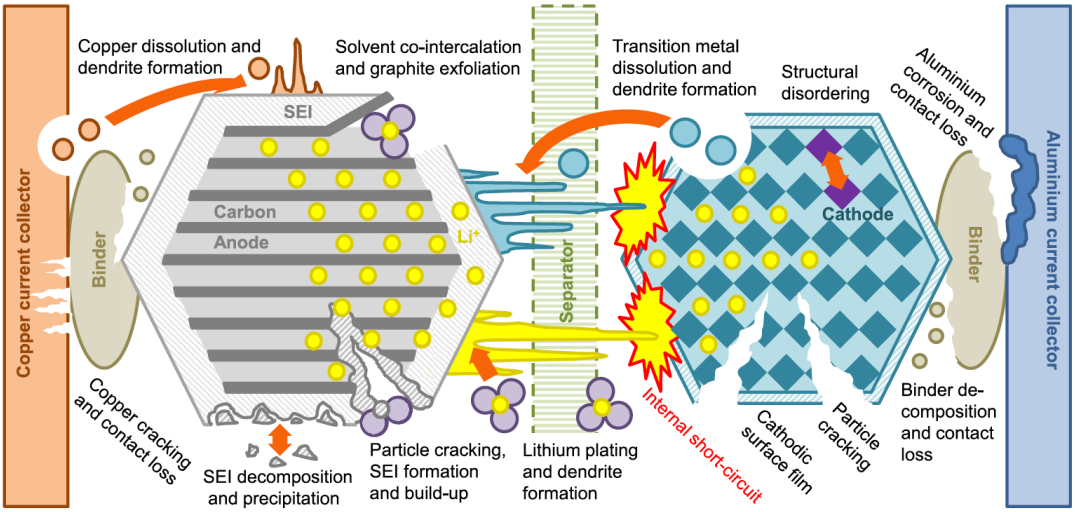


Figure 2-19. Degradation mechanisms in lithium-ion cells. Reproduced from [107].

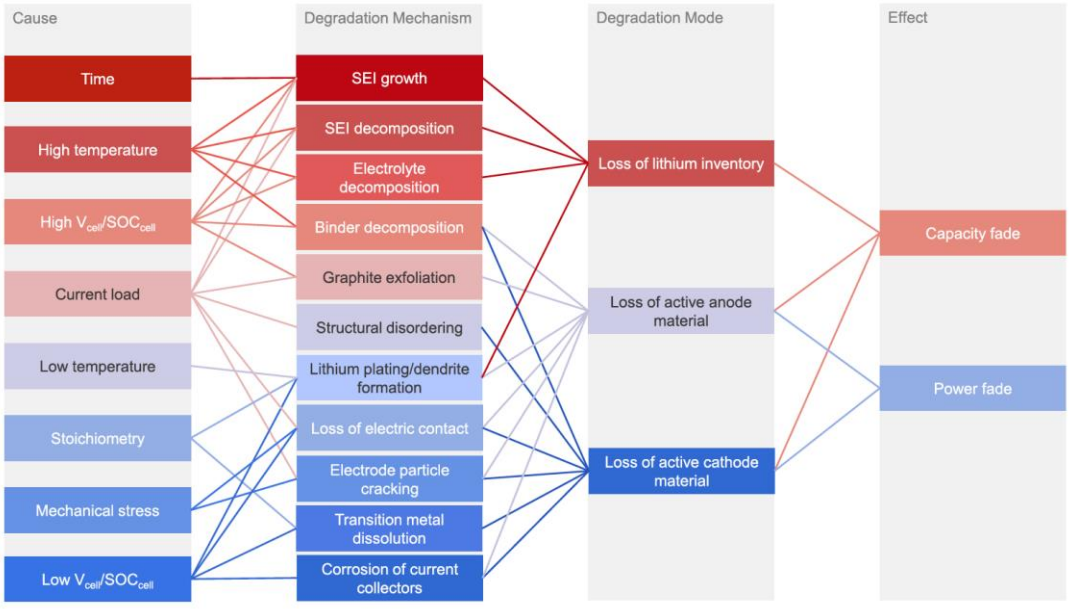


Figure 2-20. Degradation mechanisms and associated degradation modes. Reproduced from [107].

Degradation has a reflection on two measurable variables: cell capacity (which determines the storable energy) and internal resistance (which determines the maximum power). State of Health (SOH) is a measurement of the "age" of a battery. It is defined as the quotient between the battery's remaining capacity and its nominal capacity when new (both in Ah). An $SOH = 80\%$ is commonly regarded as the End of Life (EOL) criterion for a battery.

The remaining capacity of a cell can be measured by fully discharging it while measuring the discharge current. The integral of the current over the discharge time is the remaining capacity the cell can still retain. Occasional precise capacity calibrations help Battery Management Systems (BMSs) to adjust the parameters of the battery model but, in most applications, it is unfeasible to perform full discharges at any arbitrary moment since it induces cell degradation (because prevailing degradation mechanisms occur near the SOC boundaries) [61], and, above all, it is not possible to dispense with energy storage for the time of the discharge test.

The aging process is multifactorial and is influenced by the conditions of operation of the battery [108]. Given that energy storage systems are expensive, it is interesting to model battery degradation to be able to anticipate how different operation conditions would affect the battery and, thus, to extend battery life through appropriate management. Some of the most important mechanical processes and internal chemical side-reactions that cause degradation [52, 109] are:

- Growth of Solid-Electrolyte Interphase (SEI) layer on the carbon active particles of the graphite negative electrode (NE) is one of the major reasons behind the loss of cyclable lithium ions. The SEI side-reaction is promoted at high SOC, high charge current, and high temperature. SEI growth causes capacity loss and contributes to the internal resistance of the battery [108].
- Lithium plating (dendrite formation) occurs when the battery's charge rate is higher than the insertion rate (the diffusion of Li+ into the graphite's layered structure), causing Li+ to pile up at the graphite surface. Therefore, lithium plating takes place with high charging current rates, high SOC (restricted diffusion within graphite due to already inserted lithium) and low temperatures (slow diffusion within graphite), and results in loss of lithium and subsequent capacity fade.
- Delamination of the current collector from the electrode due to electrolyte gassing can significantly increase the cell's internal resistance.
- Crack propagation, rupture, and isolation of portions of active particles of the electrodes due to mechanical stress can also cause loss of active sites where lithium atoms can intercalate, resulting in effective capacity fade.

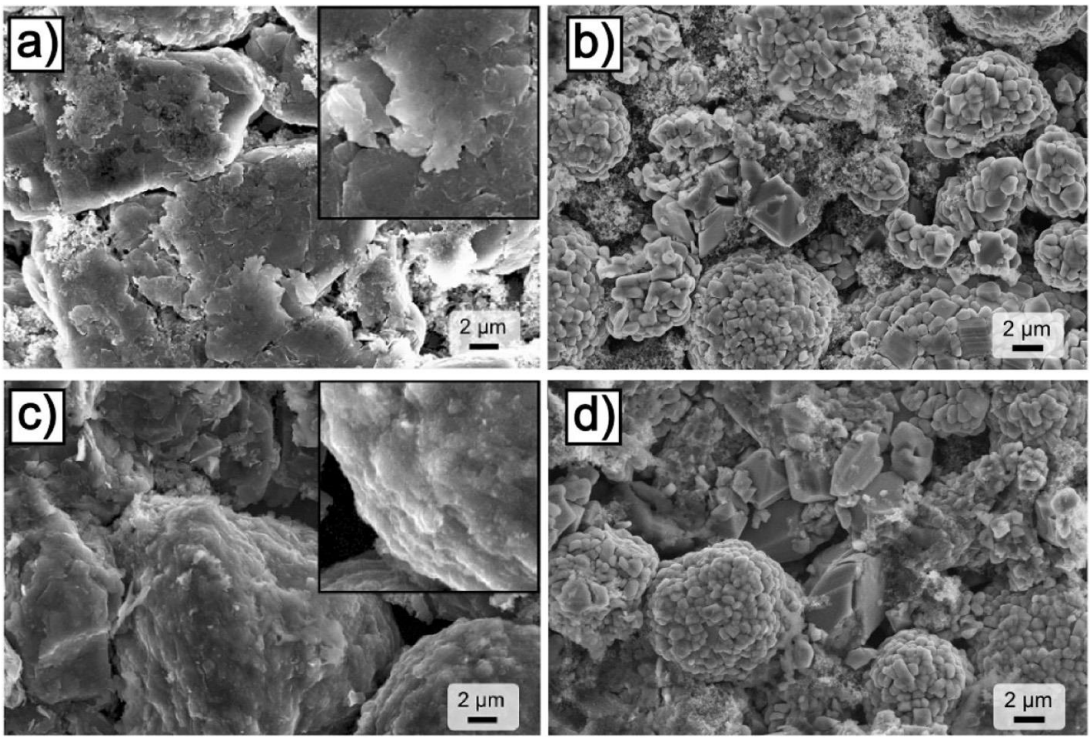


Figure 2-21. Scanning electron microscope images of an un-aged ($SOH = 100\%$) a) NE and b) blend PE; and an aged ($SOH = 80\%$, cycled at $T = 70\ °C$) c) NE and d) blend PE. Insets in a) and c) show magnifications of graphite particles. Reproduced from [108].

There are many other degradation mechanisms that take place concurrently also leading to capacity fade and power loss: SEI decomposition, electrolyte decomposition, binder decomposition, graphite exfoliation, structural disordering, transition metal dissolution, and corrosion of current collectors [107]. They are not presently well understood so, at this point, it is uncertain whether all mechanisms can be modeled or not. However, it is not necessary to perfectly model all mechanisms to achieve a useful result. Modeling the most severe degradation mechanisms reasonably well, can help designing controls that make a difference [97]. Due to the complexity of degradation modeling, this dissertation focuses (see Chapter 5) on one of the main mechanisms only: SEI layer growth in graphite NEs, which is considered a dominant degradation mechanism [107, 110–114]. Three models of SEI layer growth (developed by Ramadass, Safari and Fu) are reviewed next.

Figure 2-21 and Figure 2-22 illustrate that degradation principally affects the NE. Increased SEI thickness is observable in Figure 2-21.c (aged NE) with respect to Figure 2-21.a

(fresh NE), while the aged PE looks similar to its un-aged situation –compare Figure 2-21.b (fresh PE) and Figure 2-21.d (aged PE) [108]. Figure 2-22 shows cross-section images of a fresh and a degraded negative electrode, where a thick deposit layer has been developed as a consequence of aging.

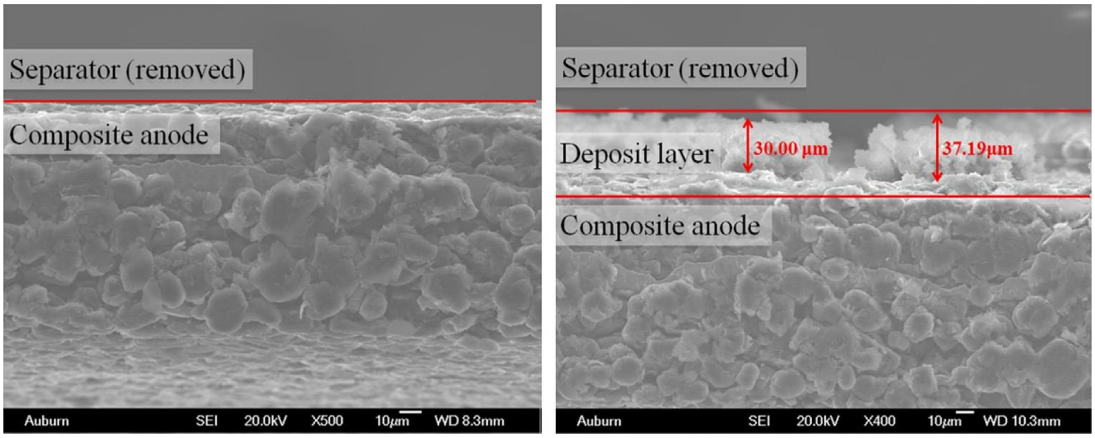


Figure 2-22. Scanning electron microscope of cross-sections of a fresh carbon anode (left) and a degraded carbon anode (right) after 600 cycles under $15\% - 80\%$ SOC using $4C$ charge rate. Reproduced from [115].

Chapter 5 of this dissertation is devoted to combine an equivalent circuit model with a reduced-order physics-based model of SEI layer growth, the dominant degradation mechanism over most of the battery life. This model can help optimizing battery operation to extend its life.

#### 2.3.4.1. Solid-Electrolyte Interphase (SEI) growth

In lithium-ion batteries, the electrodes operate at potentials outside of the thermodynamic stability limits of the electrolyte to maximize energy storage [116]. This causes a Solid-Electrolyte Interphase (SEI) layer to form at the interface between the electrode and the electrolyte, decomposing the latter. The SEI layer initially passivates the negative electrode surface, which prevents parasitic reactions and kinetically stabilizes the system [117]. During the initial cycles, 10% of the original capacity is generally consumed in irreversible SEI formation (irreversible capacity loss) in the anode [118], while the cathode experiences apparent capacity loss due to kinetic limitations –most of which is recoverable by applying a constant potential step during first cycle discharge [119]. Lithium ion cells are generally assembled with fully lithiated positive electrode and fully de-lithiated negative electrode; thus lithium consumed in the formation process comes from the positive electrode. Pre-lithiation

of the positive or the negative electrode, electrode coatings, and electrolyte additives can help forming an optimized SEI layer on the initial cycling [120–122]. An optimized SEI layer is expected to have negligible electronic conductivity and high electrolyte diffusion resistance while having high lithium ion selectivity and permeability [118].

Right after the formation cycle the usable capacity of both electrodes is balanced [123]. Afterwards, the negative electrode generally limits the cell capacity (due SEI growth, lithium plating, and other mechanisms). Graphite is currently the most common active anode material in lithium-ion batteries. Loss of active lithium (also called lithium inventory loss) occurs on the graphite surface due to irreversible plating and due to the formation of a solid-electrolyte interphase. While plating can be restrained to some extent by applying an optimized charge process, SEI formation on the graphite particle surface is inevitable. Liquid electrolytes for lithium-ion batteries are not stable below a potential of 1.5 $V$ vs. $Li/Li^+$. They decompose at the graphite surface in a lithium-consuming reaction [124].

SEI layer growth in graphite negative electrodes is generally regarded as a dominant degradation mechanism [107, 110–114]. Indeed, after the initial passivation of the negative electrode, the electrolyte still diffuses through the SEI layer and keeps reacting at the electrode's surface, consuming cyclable lithium in the reduction reaction, especially with low negative electrode's potential –high SOC. This happens at an ever-slowing rate as the thickness of the SEI layer increases. The SEI reaction is thus self-limiting [111], but the reaction never fully stops due to the porous nature of the SEI layer [125]. The gradual growth of the SEI layer consumes $Li^+$ ions, solvent and electrolyte salts. This growth increases the cell's internal resistance and reduces its capacity and coulombic efficiency [118].

The reduced-order physics-based models of SEI growth presented in [115, 126, 127] are examined next. These three models derive an intrinsic equation of the current density of the SEI side-reaction, $J_{side}$, that can be used to estimate the capacity loss. Current densities ($J$) are expressed in $A/m^3$ while flux densities ($j$) are expressed in $mol/m^2 s$. The relationship between them is $J = Fa_n j$.

- **Ramadass SEI Model**

Ramadass et al. [126] developed a first-principles model of the capacity fade caused by the negative electrode current density that can be described as follows:

$$J_{total}(x,t) = J_I(x,t) + J_{side}(x,t) \tag{2.31}$$

where $J_{total}$ is the total current density, $J_I$ is the intercalation current density, and $J_{side}$ is the SEI side-reaction lithium-flux density. The side-reaction current density can be modeled with the Tafel equation:

$$J_{side}(x,t) = -i_{0,side} a_n \, exp\left(\frac{\alpha_{a,side} F}{R_g T} \eta_{side}(x,t)\right) \tag{2.32}$$

where $i_{0,side}$ is the exchange current density for the side-reaction. The side-reaction overpotential, $\eta_{side}$, is expressed by:

$$\eta_{side}(x,t) = \phi_s(x,t) - \phi_e(x,t) - U_{side}^{ref} - \frac{J_{total}(x,t)}{a_n} R_{SEI}(t) A_n \tag{2.33}$$

where $U_{side}^{ref}$ is the equivalent reference potential of the SEI side reaction (assumed as $0.4\ V$ vs. Li/Li$^+$) and $R_{SEI}$ is the SEI film resistance: $R_{SEI}(t) = \delta_{SEI}(t)/\kappa_{SEI} A_n$, where the SEI film thickness, $\delta_{SEI}$, grows at a rate proportional to $J_{side}$.

In addition, [126] presents an open-loop method to calculate the capacity loss by integrating the lithium loss with respect to time:

$$\frac{\partial Q_{side}^{loss}}{\partial t} = -A_n \int_0^{L^n} J_{side}(x,t)\, dx \tag{2.34}$$

This capacity loss, $Q_{side}^{loss}$, corresponds to the amount of lithium inventory loss.

- **Safari kinetic and diffusion SEI model**

Safari et al. [127] developed a single-particle SEI model that considers a kinetic-limited mode and a diffusion-limited mode. This model assumes that the SEI layer that forms around a particle has uniform thickness. For this reason, this model is only accurate for low current rates. The film layer thickness follows a parabolic growth law. The diffusion model is better suited to capture the behavior of a cell during cell storage.

In [127], the development of the SEI degradation model begins with the flux equation of the intercalation reaction (2.28), the overpotential of the intercalation reaction (2.30), and the NE flux density (2.31). The model uses a lumped parameter $k_{f,side}$ to account for both the exchange current density, $i_{0,side}$, and the equilibrium potential, $U_{side}^{ref}$, of the SEI side reaction. The potentials are referred to the potential of the electrolyte phase (instead of to the metal Li/Li$^+$ reference electrode), thus $\phi_e = 0\ V$ . The expressions for $J_{side}$ and $\eta_{side}$ result:

$$J_{side} = -a_n F k_{f,side} c_e \, exp\left(\frac{\alpha_{a,side} F}{R_g T} \eta_{side}\right) \tag{2.35}$$

$$\eta_{side} = \phi_s - \frac{J_{total}}{a_n} R_{SEI} A_n \tag{2.36}$$

- **Fu SEI self-discharge tests**

Fu et al. [115] proposed a SEI model and validated the integrated model with experimental data obtained under cycling with different aging environments. The model equations are identical to the Tafel side-reaction current density (2.32) and the overpotential of the intercalation reaction (2.33), but incorporates temperature-dependence to $U_{side}^{ref}$:

$$U_{side}^{ref} = U_{side}^{ref\ \Theta} + \frac{R_g T}{2F} ln\left(\frac{c_e}{c_{e,0}}\right) \tag{2.37}$$

where $U_{side}^{ref\ \Theta}$ is assumed to be $0.4\ V$.

## 2.4. Battery balancing systems

Most energy storage applications (microgrids, electric vehicles, etc.) require a number of battery cells to be connected in series to form a battery pack with appropriate capacity and voltage. It is of uttermost importance that cells of a battery pack have the same characteristics to prevent early degradation [60]. But, even when they are all the same model from the same manufacturer and even from the same batch of production, imbalance among them always exists [128, 129].

There are internal and external sources of imbalance that affect the electric parameters of individual cells [130, 131]. Internal sources of imbalance result from a diversity of factors, such as the manufacturing techniques, coatings, ingredients, and unevenness of the impure contents of the battery. Non-homogeneous materials and manufacturing processes cause differences in the battery initial performance (initial capacity, internal DC resistance, coulombic efficiency, self-discharge rate, etc.) [132, 133]. Manufacturing mismatch in capacities, for instance, can be in the range of 1% or 2% at beginning of life [68], but even with this tight level of initial matching, cell imbalance will grow throughout the whole life of the battery [134]. External sources of imbalance include uneven temperature distribution and different power consumption from external circuitry connected to each cell [135]

Cell imbalance causes performance issues that tend to self-amplify if not faced. Battery balancing compensates the effects of cell mismatch, providing a series of benefits: safety strengthening, battery life extension, and complete use of the pack's capacity [136, 137]:

- Safety. When a lithium-ion cell voltage exceeds 4.2V by a few hundred millivolts, it can undergo thermal runaway (highly exothermic breakdown).

  Figure 2-23 illustrates temperature distribution during externally induced explosion (or violent venting) in a Li-NMC cell. The cell was kept at $4.2\ V, > 250$ ℃ for this test [138].

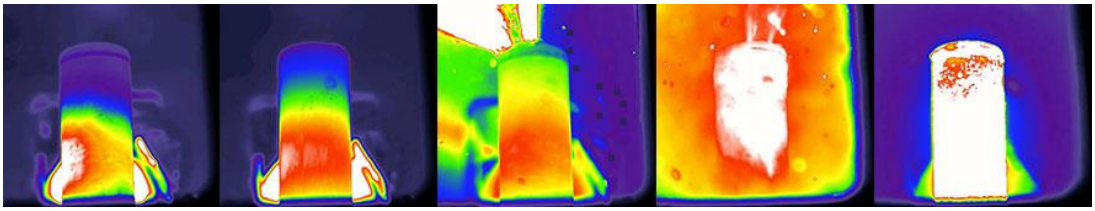

Figure 2-23. Thermal images of thermal runaway of a cylindrical Li-NMC battery, caused by external thermal abuse. Reproduced from [138].

- Longevity. Exceeding the maximum recommended charging voltage causes very accelerated degradation in Li-ion cells. As for lead-acid batteries, over-voltage leads to corrosion on the positive electrode grid, gassing and water-loss [139], while deep discharge causes irreversible damages, originating sulfation and loss of capacity [140]. If voltage protection applies at pack level, a misbehaving cell will almost certainly get overcharged and/or overdischarged and will thus degrade faster. Furthermore, the EOL is typically determined by the worst cell in a series-connected pack, so cell mismatch produces a significant reduction in the lifetime of a battery pack.

  Figure 2-24 exemplifies the effect that deficient balancing management has on the State Of Health (SOH) of the NMC 30 $kWh$ battery packs of Nissan Leaf hybrid vehicles manufactured between 2011 and 2017, versus better management accomplished in the LMO 24 $kWh$ battery packs of the same model [141]. Plausible causes of disparity in SOH decline rates include different chemistry of the positive electrodes, potentially higher temperature experienced by the 30 $kWh$ model (due to higher energy density and volumetric density, combined with higher charging currents), and higher maximum SOC reached in the charging process in the 30 $kWh$ model.

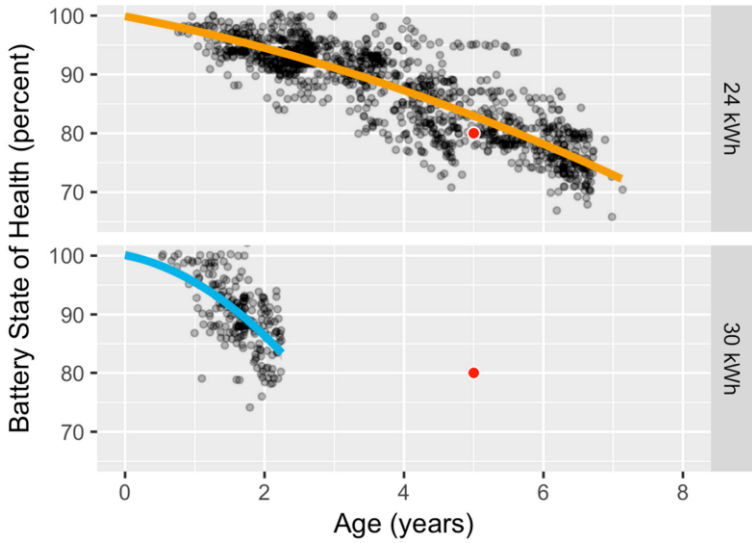


Figure 2-24. SOH evolution of hybrid electric vehicles Nissan Leaf. Reproduced from [141].

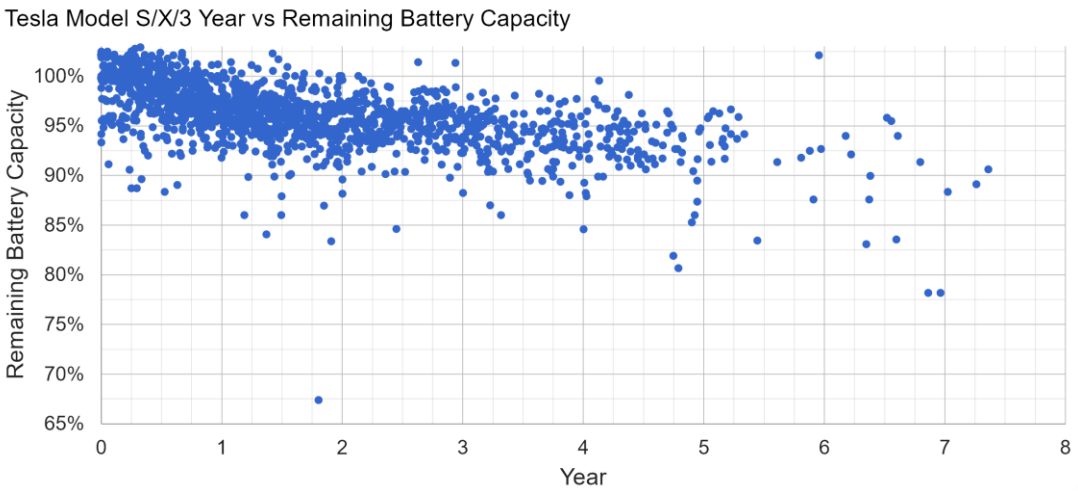


Figure 2-25. Public survey of SOH evolution of Tesla electric vehicles. Modified from [142].

Figure 2-25 (adapted from [142]) has been included to contrast lifespan of Nissan Leaf's battery packs with lifespan of Tesla's battery packs, renowned for its batteries' outstanding service life. Unlike the abovementioned Nissan Leaf's battery packs, Tesla electric vehicles' batteries are equipped with active thermal management systems that cool the pack and counter uneven temperature distribution within the battery pack.

- Incomplete use of pack energy. Cell mismatch makes them drift to different SOCs. Weaker cells (those that limit the performance of the battery-pack, for example due to lower capacity) reach charge and discharge voltage limits sooner than the stronger ones. Therefore, if voltage protection applies at cell level, the usable capacity of a battery pack will be limited by its weakest cell.

  Figure 2-26 represents a paradigmatic (extreme) case of incomplete use of the stored capacity. The battery pack is composed of only two series-connected cells which are extremely imbalanced: the strongest cell ($B_{strong}$) is fully charged, while the weakest ($B_{weak}$) cell is almost discharged. On one hand, discharging the pack is not possible because $B_{weak}$ soon reaches the minimum SOC. On the other hand, charging is not possible either because $B_{strong}$ immediately reaches the maximum SOC.

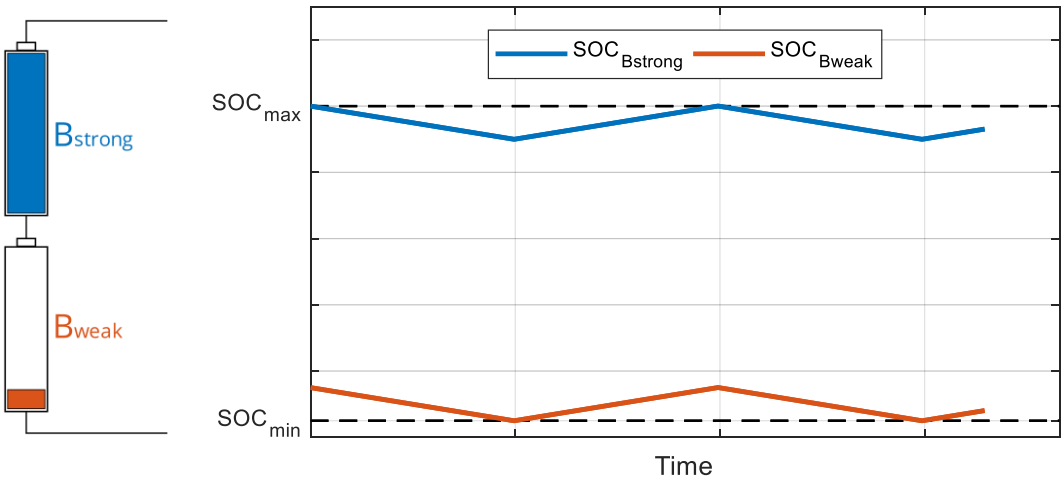


Figure 2-26. Battery pack composed of two extremely imbalanced cells and graph representing their SOC evolution: the pack can only be shallowly cycled.

A balanced battery pack is defined as one in which, at some point in its cycle, all the cells are at exactly the same SOC [143]. Therefore, a cause of imbalance is anything that can make one cell's SOC diverge from another's. Causes of imbalance are analyzed next following [97] based on the discrete-time SOC relationship expressed in (2.8), reproduced here for convenience:

$$z[k] = z[0] - \frac{\Delta t}{Q[k]} \sum_{0}^{k} \eta_Q[k] i_{net}[k]$$

In view of the equation, the effect of imbalance in each parameter is analyzed independently. The following terminology is used in the analysis: a "weak" cell is a cell that limits battery-pack performance, while a "strong" cell is a cell that is impeded to deliver its charge (to accept more charge) to avoid overdischarging (overcharging) a weak cell [97]. Differences in coulombic efficiency, self-discharge current, leakage current, and temperature, are causes of imbalance:

- Cells with different coulombic efficiencies get charged up to different SOC levels with an equal charge current. In a cell with high coulombic efficiency (strong cell), the majority of the charge current ($i_{app} < 0$) is converted to a change in the cell's SOC. In a cell with low coulombic efficiency (weak cell), on the contrary, a smaller fraction of the charge current converts to a change in the cell's SOC. During discharge, coulombic efficiency is assumed to be perfect for all cells, thus the divergence caused during charging will not be neutralized. Imbalance will tend to grow indefinitely as the battery pack is subjected to more cycling.

- The SOCs of cells experiencing different net current tend to diverge. Recall that the relationship stated in (2.9):

  $$i_{net}[k] = i_{app}[k] + i_{self-discharge}[k] \; + \; i_{leakage}[k]$$

  While $i_{app}$ is the same for all cells, the self-discharge and leakage currents of individual cells can be different, leading to different net currents. Considering a cell with low self-discharge and low leakage current (strong cell), and a cell with higher self-discharge and/or leakage current (weak cell), the higher net discharge current experienced by the weak cell causes its SOC to decrease more rapidly than that of the strong cell under all operation scenarios. When the pack is subsequently charged the strong cell will charge more quickly than the weak cell because its net current is not drawn down as much by self-discharge and leakage, thus the imbalance will continue to grow.

- Temperature is not a direct cause of imbalance but a gradient of temperature across a battery pack can be a contributing factor to imbalance. Cell-parameter values are temperature-dependent, so self-discharge rates, electronics' performance, and coulombic efficiency will be different for cells that experience different internal temperatures. This will cause imbalance. Also, high temperatures tend to accelerate degradation, therefore, a persistent temperature gradient will lead different rates of degradation in different cells in the battery pack, which will lead to accelerated

imbalance because of the resulting different self-discharge rates and coulombic efficiencies among the cells. Maintaining uniform temperatures across the battery pack (i.e., thermal management) helps to prolong the battery-pack life but, in general, balancing will still be needed.

In contrast, different internal resistance is not a direct cause of imbalance:

- Examination of (2.8) reveals that resistance is not a factor in the SOC equation. However, different cell resistances cause cell terminal voltages to be different when subjected to an applied current, but not their SOCs. Therefore, a cell with high resistance does tend to reach an upper or lower design voltage limit before other cells in the battery pack. While this does not cause imbalance, it does limit the available battery-pack power and the available energy.

Different capacities, while not a direct cause of imbalance, do cause imbalance indirectly:

- Different cell total capacities theoretically cause a temporary imbalance that is corrected automatically when the charge-discharge cycle is completed. According to the definition of causes of imbalance provided above, capacity inconsistency is not considered a cause of imbalance. However, a cell with diminished capacity (weak cell) limits the battery pack's performance and experiences extreme SOC more often than one with preserved capacity (strong cell), which results in faster aging [144].

  A battery balancing system can transfer charge continuously from the strong cell into the weak cell while discharging (and vice versa while charging) to keep both cells' SOCs equal at all points in time.

Cells degrade unevenly throughout life due to growth of the initial mismatch, temperature differences, and other physical asymmetries across the battery pack. A cell with small capacity, large internal resistance and high self-discharge rate is more likely to become overcharged, overdischarged, and to over-heat in the process of charging and discharging. This accelerates the decline in cell performance, demonstrating "positive feedback", which rapidly amplifies the battery consistency problem. As a result, parameter mismatch can exceed 10% at End of Life (EOL) [145].

Cell voltage inconsistency is the most direct manifestation of imbalance. Voltage inconsistency reflects discrepancy of other parameters, such as internal resistance, SOC, and capacity, to a certain extent. Figure 2-27 shows the terminal voltage of couples of battery cells that differ in one parameter only, assuming they have identical $OCV$ vs. $SOC$ curves [132]. In Figure 2-27.a), the internal resistance of Battery 1 is higher than that of Battery 2, so the terminal voltage of the first is higher than that of the latter during the charging process (and

lower during discharging, which is not represented in the figure). In Figure 2-27.b), Battery 1 and Battery 2 have different polarization voltages, so their terminal voltages diverge when they are subjected to the same current. In Figure 2-27.c), the SOC of Battery 1 is higher than that of Battery 2, so the terminal voltage of the first is always higher than that of the latter. Note that while SOC imbalance remains constant during the represented charge process, voltage differences between the cells vary with state of charge because $dV/dSOC$ varies with $SOC$ [146]. Finally, in Figure 2-27.d), Battery 1 has smaller capacity than Battery 2, so the terminal voltage of the latter varies more slowly than that of the first. In actual use, battery terminal voltage differences may result from many simultaneous causes, which makes the battery consistency analysis more difficult.

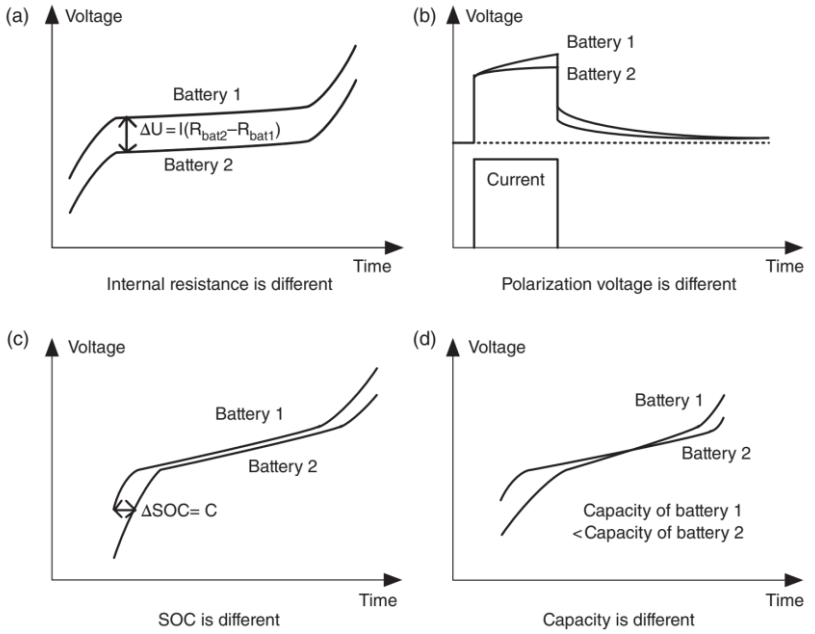


Figure 2-27. Effect of battery parameters inconsistency on external voltage: a) internal resistance, b) polarization voltage, c) SOC, d) capacity. Reproduced from [132].

SOC difference among cells is the most critical outcome of cell imbalance for the battery pack in terms of usable energy. Since the whole pack should be cut off from charging / discharging as soon as one cell reaches the upper / lower voltage values indicated by the manufacturer to avoid danger, the cell with the lowest SOC restricts the usable capacity, and the one with the highest SOC limits the rechargeable capacity of the entire pack. This forces to use the battery cells under conservative premises [147]. By using a battery balancing

system, the battery cells can be balanced which improves cell consistency, increases battery-pack capacity and prolongs battery-pack life [137].

Battery balancing topologies and strategies are reviewed next. Chapter 4 proposes a novel active balancing topology, with a suited control strategy, and validates its performance.

### 2.4.1. Battery balancing topologies

Battery balancing topologies are normally divided into passive and active. Passive balancing methods remove the excess charge from the stronger cells through resistors when they are fully charged, until their SOCs match the pack's average SOC. Active cell balancing methods take charge from stronger cells and deliver it to weaker cells [148–150]. Passive balancing is reliable and easy to implement but is slow and wastes energy. In turn, active balancing is faster and presents high energy efficiency, but is more expensive, more complex, and less reliable [63]. Some of the most common balancing topologies are reviewed next, following [151]. The diagram in Figure 2-28 [152] classifies different topologies based on whether they perform passive or active balancing and, within those fitting in the active balancing category, based on the element chosen to transfer charge (capacitor, inductor or converter). The list of topologies is not exhaustive, other variants can be found in different review articles, such as [153–155].

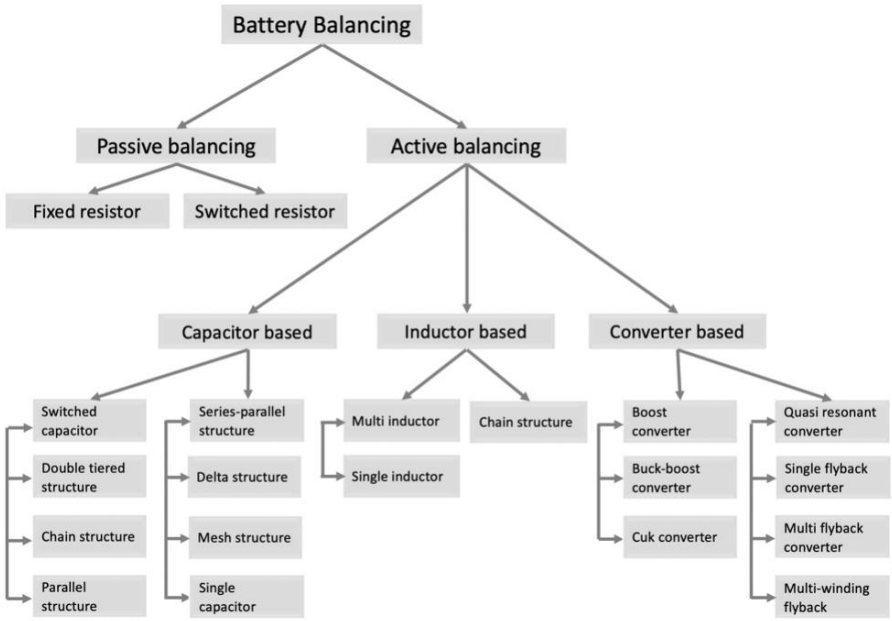


Figure 2-28. Battery balancing topologies. Reproduced from [152]

Passive and active balancing were experimentally compared in [156] by cycling two identical battery packs with the same current profile, while balancing each with one strategy. The battery packs were subjected to 2600 cycles with $0.75C$ current, at ambient temperature of $20\ °C$. Final results suggest that active balancing reduces aging (in terms of capacity loss) of the whole pack more than passive balancing. The increase of internal resistance of both tested batteries was mainly identical.

#### 2.4.1.1. Passive balancing topologies

Passive balancing topologies dissipate the excess energy from the strongest cells by paralleling them to shunt resistors. There are two basic passive balancing topologies: fixed resistor balancing and switched resistor balancing.

- Fixed resistor balancing (Figure 2-29) consists in permanently connecting each cell to a parallel shunt resistor. This method balances cell voltages with no control system because the bypass currents are proportional to cell terminal voltages. Advantages of this method: simplicity, no control system, robustness, and low cost. Disadvantages: continuous energy waste (bypass currents always exist), slow balancing speed, and overcharging and overdischarging not impeded (which is not acceptable in lithium-ion batteries). Only lead-acid batteries and nickel-based batteries still use this method nowadays [148].

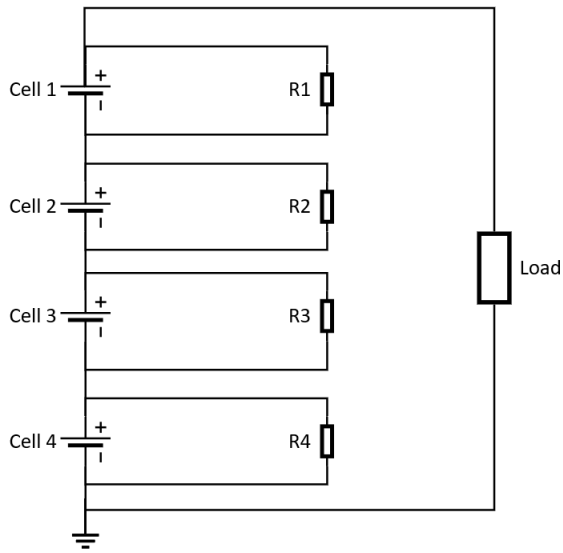


Figure 2-29. Fixed resistor balancing. Reproduced from [151].

- Switched resistor balancing (Figure 2-30) introduces an additional switch connected to each shunt resistor. This provides some control capability. The cells in the battery pack can be balanced at any moment (charging, discharging, and idling) by dissipating excess energy from the strongest cells, based on cell voltage. Advantages of this method: simplicity, basic control system, robustness, low cost, overcharge and overdischarge protection is possible. Disadvantages: energy waste and slow balancing speed [157, 158].

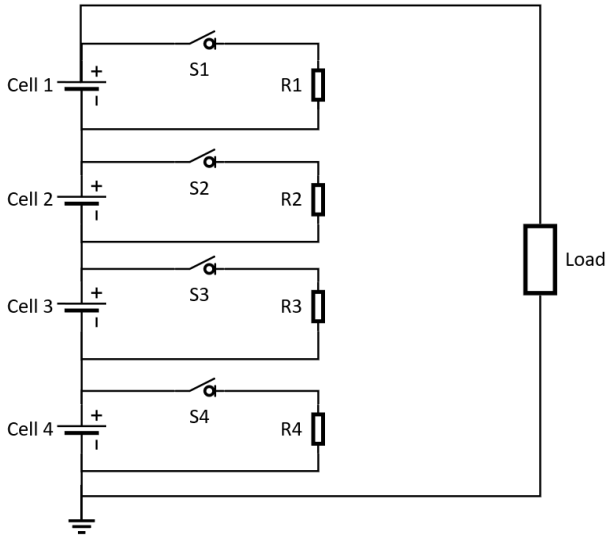


Figure 2-30. Switched resistor balancing. Reproduced from [151].

#### 2.4.1.2. Active balancing topologies

In active balancing, the excess charge (ampere-hours) from the strongest cell(s) is transferred to weaker cell(s) through energy-storage components (capacitors, inductors) or converters, which can be controlled either analogically or digitally [159]. Active balancing topologies require more complex configurations and control schemes but, in exchange, allow for better use of the energy stored in the battery. Active topologies are characterized by the element responsible of charge transfer and by its interconnection with the battery cells.

- **Capacitor-based topologies**
  - Switched-capacitor balancing (Figure 2-31) alternately connects one capacitor to two adjacent cells, which produces energy transfer from the higher voltage cell to the lower voltage cell. All the Single Pole Double Throw (SPDT) switches interfacing between the cells and the capacitors are operated with the same frequency.

    The balancing time is quite long, mainly for two reasons. First, when the balancing process among two adjacent cells is almost finished, the voltage difference between them is very small. This small voltage difference charges the capacitor very slowly. And second, within one balancing cycle, energy can only be transferred between two adjacent cells. If energy needs to be transferred between two distant cells, many balancing cycles will be needed [160].

    In order to improve balancing speed, some structures can be added to the switched-capacitor balancing, providing more paths to transfer energy between not-adjacent cells and to introduce modularization. Improved switched-capacitor topologies are: double-tiered structure, chain structure, parallel structure, delta structure, mesh structure, single-capacitor structure, modularized switched-capacitor structure, and modularized double-tiered switched-capacitor structure. The latter is reviewed next, as it unites some of the characteristics of the other topologies.

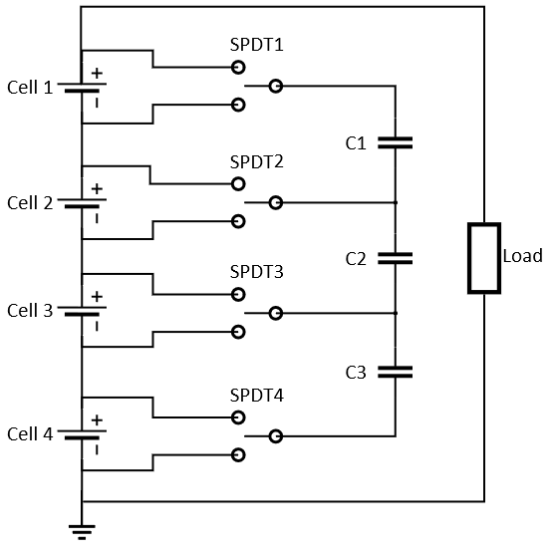


Figure 2-31. Switched-capacitor balancing. Reproduced from [151].

- Modularized double-tiered switched-capacitor balancing (Figure 2-32) has been selected (among the mentioned improvements to the basic switched-capacitor topology) to exemplify both additional energy-transfer paths and modularization. As shown in Figure 2-32, *C1*, *C2*, *C3* form the first layer of capacitors, and $C4, C5$ form the second layer of capacitors. All the Single Pole Double Throw (SPDT) switches are operated at the same frequency. This topology provides extra paths that accelerate energy transfer between distant cells. For instance, if there is an SOC difference between Cell 1 and Cell 3, energy can be transferred directly via *C4*, thus saving one step with respect to the basic switched-capacitor topology. Additionally, modularization allows to transfer energy among groups of cells: the capacitor *C0* is used to balance cell-group 1 (Cell 1 and Cell 2) and cell-group 2 (Cell 3 and Cell 4). The switches are controlled such that, when SPDT1 to 4 are in the upper position, *Sa1* and *Sa2* are off, and *Sb1* and *Sb2* on, and vice versa.

  Advantages of this method: improved balancing speed and efficiency thanks to the extra capacitors and extra balancing paths, modularization in batteries with a large number of series-connected cells [161, 162]. Disadvantages: larger number of elements and increased complexity.

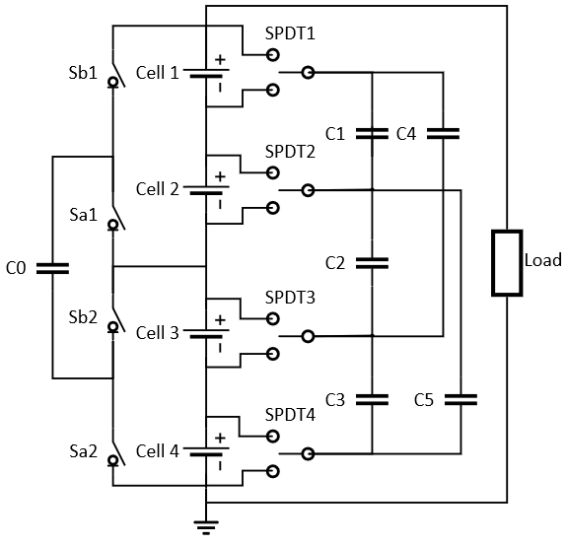


Figure 2-32. Modularized double-tiered switched-capacitor balancing. Reproduced from [151].

- **Inductor-based topologies**
  - Multi-inductor balancing (Figure 2-33) can balance various couples of cells synchronously. When balancing is required between Cell 1 and Cell 2, with Cell 1 having higher SOC, *M1* is first turned on while *M2* is turned off, so Cell 1 starts to charge the inductor *L1*. After the current of *L1* reaches the upper boundary, *M1* is turned off while *M2* is turned on, so *L1* works as an energy source to charge Cell 2. Similarly, the *L2* and *L3* are used to balance Cell 2 with Cell 3, and Cell 3 with Cell 4, respectively. Balancing is slow with this topology because only adjacent cells can be balanced directly [163].

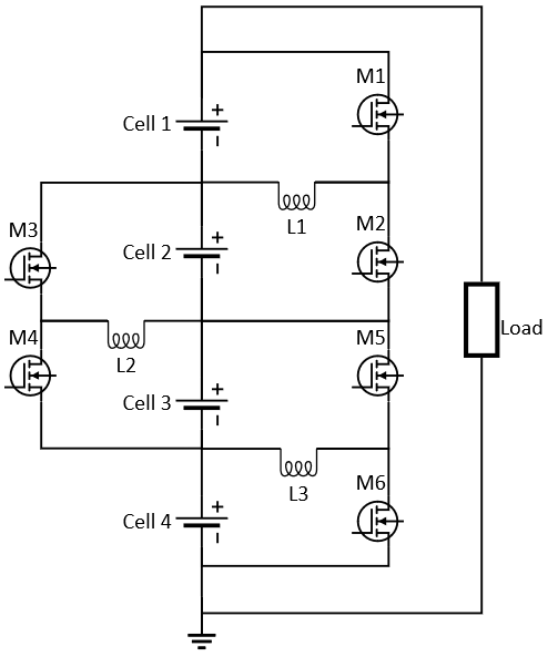


Figure 2-33. Multi-inductor balancing. Reproduced from [151].

Analogously to the capacitor-based topologies, there exist improved versions of this topology that include extra inductors and switches to accelerate balancing. Such improved topologies are: chain structure multi-inductor balancing, multi-tiered inductor balancing, and single-inductor balancing. The first one is described to exemplify the advantages that more complex topologies can bring.

- Chain structure multi-inductor balancing (Figure 2-34) has been selected to illustrate the mentioned improved inductor-based topologies. An additional capacitor, *C0*, is used to improve the balancing speed. It connects the cells in the first and last positions. During the balancing process, the MOSFETs are controlled as in the previous case to transfer energy between adjacent cells via inductors. At the same time, *SC1*, *SC2* are first turned on, while *SC3*, *SC4* are turned off. *C0* is therefore charged by Cell 4. Second, *SC1*, *SC2* are turned off, while *SC3*, *SC4* are turned on, which transfers energy stored in *C0* to Cell 1 (if voltage of Cell 1 is lower than that of Cell 4). Advantage of this method: the maximum number of steps required to transfer energy between any two cells is reduced to half compared to the multi-inductor balancing. Disadvantage: increased balancing circuit size and cost [164].

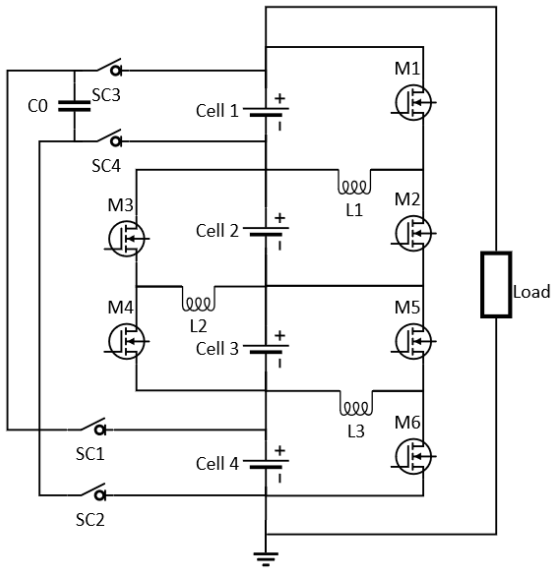


Figure 2-34. Chain structure multi-inductor balancing. Reproduced from [151].

- **Converter-based topologies**

Control of the balancing current(s) is possible with these topologies.

- In boost converter balancing (Figure 2-35), each cell is connected to a boost converter (dashed box). The combination of a battery cell and its boost converter works as an individual cell equalization unit. All equalization units are connected in series, what causes all converters to have the same output current. The output

voltages of the converters are controlled by the duty cycles employed to achieve power sharing according to the cells' SOC. By controlling the voltage conversion ratios of different converters, the SOCs of the cells can be balanced [165].

The duty cycle of each converter is determined based on the SOC of the corresponding cell. Control signals are used to switch the MOSFETs of the boost converters. If the maximum SOC difference of all cells is smaller than a threshold value (no balancing is needed), all MOSFETs are set to off status. Otherwise, balancing is activated. MOSFETs connected to the strongest cells (those with higher SOC) are controlled to perform higher duty cycles, so these cells provide more power during the discharging process. In contrast, cells will lower SOC have smaller duty cycles and, consequently, smaller power output.

Additional switches (*S1-S4*) are present in every boost converter to bypass fault cells. Permanently opening *Si* and closing *Mi* (with *i* being the fault-cell number) isolates the fault Cell *i*, so it does not get charged or discharged any further. The other converters can be adjusted to perform higher duty cycles to meet the full battery voltage required at the output. Bypassing fault cells allows to defer battery pack replacement when only one or few cells are damaged, thus increasing the pack's life [165].

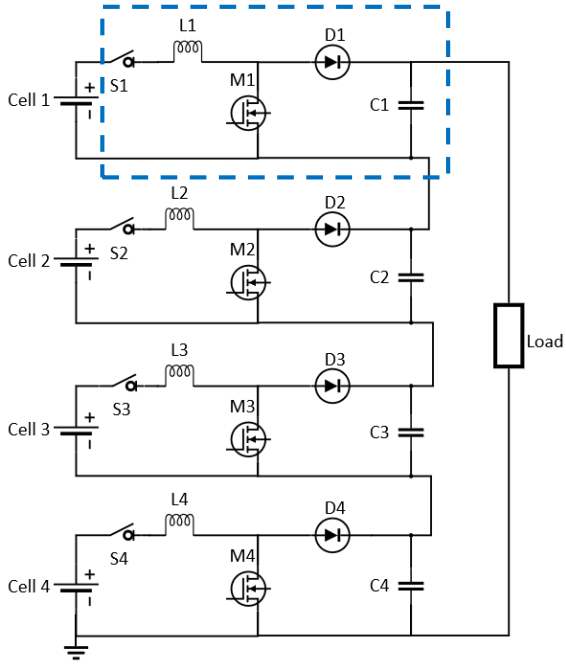


Figure 2-35. Boost converter balancing. Reproduced from [151].

In this topology, the cells are not connected in series, and the diodes impede inverse current. Thus, balancing is restricted to the discharge process only, while charging requires a different configuration. Two options are possible: 1) temporarily opening all the switches *S1* to *S4*, and connecting the cells in series (through SPDT switches), or 2) substituting the diodes with MOSFETs to allow for bidirectional power flow. The second option permits balancing at any moment (i.e., while charging and while discharging the battery pack).

- Buck-boost converter balancing (Figure 2-36) has a similar structure to the boost converter balancing. One buck-boost converter (dashed box) is connected to each cell in this case, allowing for voltage conversion ratios both higher and lower than one, making control algorithms more flexible [166, 167].

  In this case, charging the battery requires the same considerations as in the boost converter balancing topology.

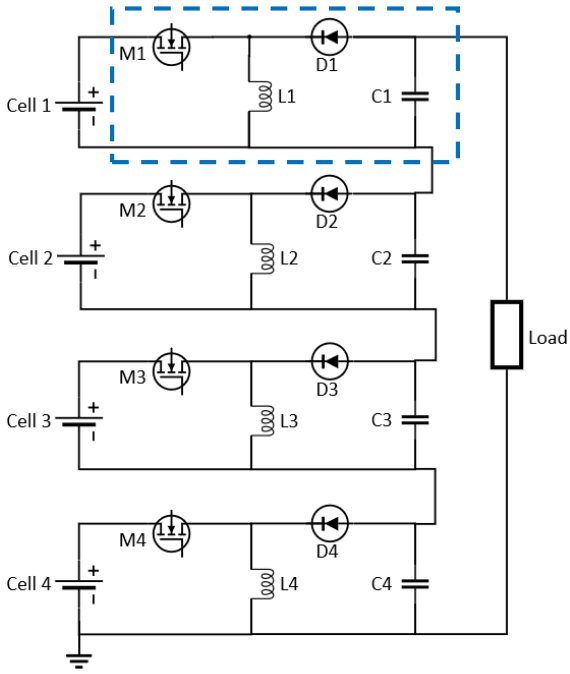


Figure 2-36. Buck-boost converter balancing. Reproduced from [151].

- Ćuk converter balancing (Figure 2-37) shares some similarities with multi-inductor balancing but capacitors are added as an extra energy storage element. One Ćuk converter (dashed line in Figure 2-37 left) is connected between every two adjacent cells to perform bidirectional charge transfer. The MOSFETs are operated alternately, in synchronous patterns with 50% duty cycle. Balancing between non-adjacent cells is slow because several steps of energy conversion are needed. The number of required MOSFETS is equal to the number of cells in the battery pack [168, 169].

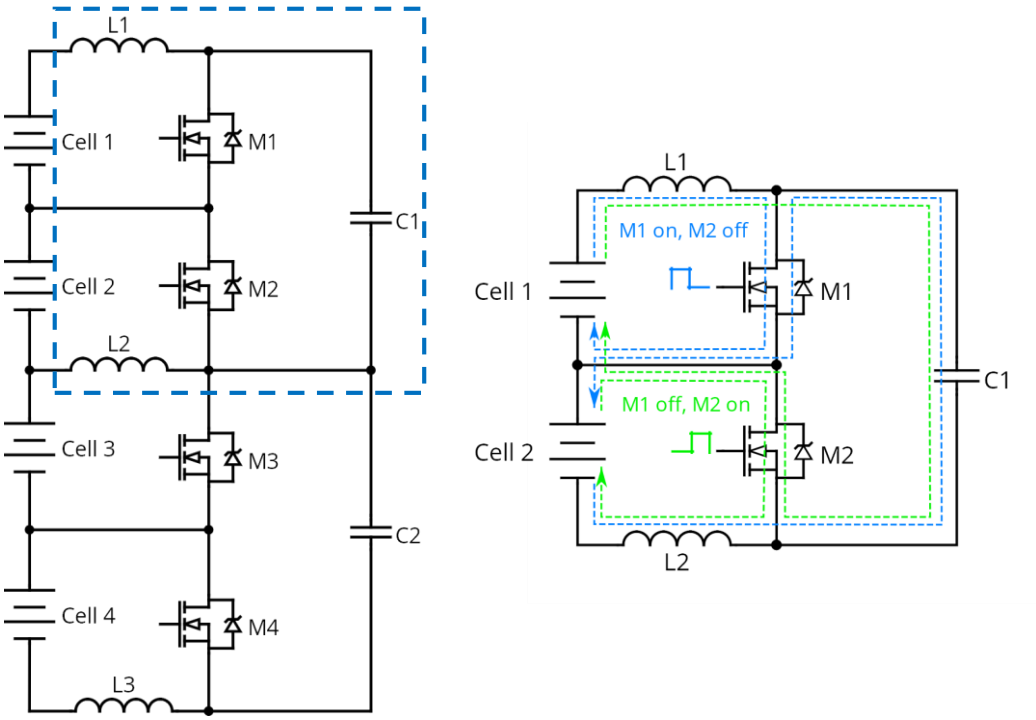


Figure 2-37. Ćuk converter balancing topology and operation of one Ćuk converter equalization cell. Adapted from [169].

- Quasi-resonant converter balancing (Figure 2-38) has a quasi-resonant converter (dashed box) connected between every two adjacent cells. During the balancing process, MOSFETs are controlled to transfer energy between adjacent cells. In every quasi-resonant converter *i*, *Lqi* and *Cqi* work as a resonant tank that make possible that the switching current of the MOSFET becomes zero –quasi-resonant converters cut turn-on losses at the power switch. Switching losses and electromagnetic interference emissions are thus significantly reduced, and balancing efficiency is improved. However, energy transfer between non-adjacent cells is slow and less efficient [170, 171].

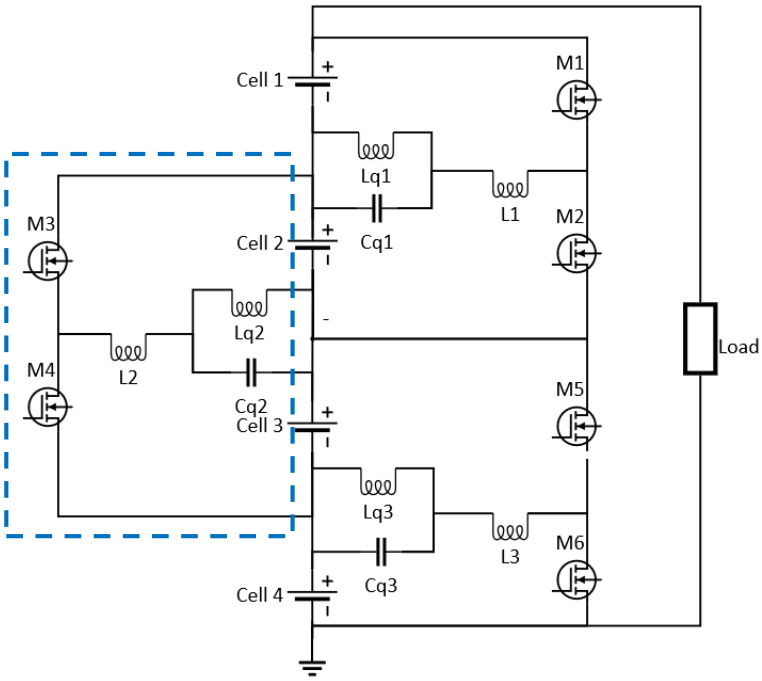


Figure 2-38. Quasi-resonant converter balancing .Reproduced from [151].

- Single flyback converter balancing (Figure 2-39) uses a switched transformer to balance cells. The cell with the highest SOC is identified and connected to the transformer input to transfer part of its charge to the complete battery pack via the transformer –which actually behaves as a coupled inductor. For example, if Cell 1 has more energy than the other cells, Pulse width modulation (PWM) signals will be given to *S1P* and *S1N*. First, *S1P* and *S1N* are turned on and the current in the transformer increases till its upper limit, storing energy in the form of magnetic flux. At this moment, there is no flyback current because the diode *D1* blocks current flow in the secondary winding of the transformer. Second, *S1N* and *S1P* are turned off, and the energy stored in the transformer flybacks through *D1* to charge the complete battery pack. Thus, SOC of all the cells are modified towards balance. The other diodes are used to protect cells from any possible short-circuits through the anti-parallel diodes of the MOSFETs. Only one flyback converter is used in the balancing circuit, so the costs are relatively low. Balancing is realized from one cell to the complete battery pack, achieving higher balancing speed than the adjacent-cell balancing methods described before. Constant-duty control with fixed frequency scheme is widely used due to its simplicity although more complex control strategies can be used to accelerate the balancing process [172]. The isolation provided by the transformer is essential in this topology to separate the system-ground from the (in general) floating-ground of the primary terminal.

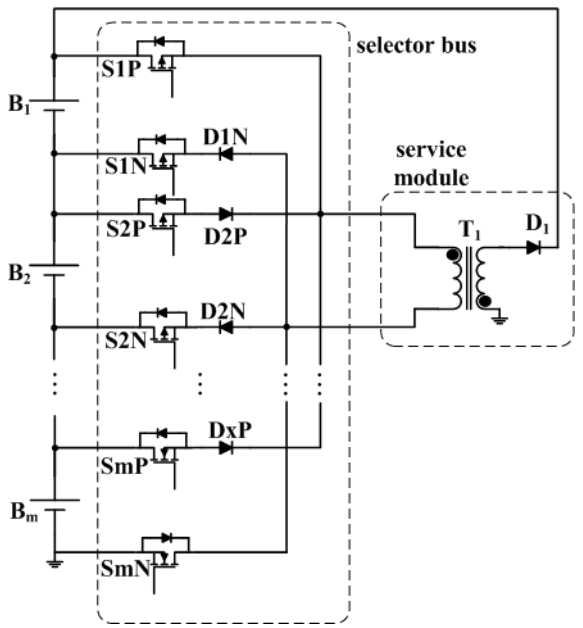


Figure 2-39. Flyback converter balancing. Reproduced from [172].

- Multi-flyback converter balancing (Figure 2-40) has one flyback converter connected to each cell (dashed box). The output sides of the flyback converters are connected to the cells, while the input sides are coupled together and connected across the complete battery pack. If Cell 1 has the lowest SOC, operation is as follows. First, *S0* and *S1* are turned on, while *S2*, *S3*, *S4* remain off. The complete battery pack starts to charge the magnetizing inductor of the transformer (coupled inductor, actually) until its primary side winding current reaches the maximum value. There is no current in the secondary winding side because of the diode *D1*. Second, *S0* is turned off, *S1* can be kept on, and *S2*, *S3*, *S4* are all kept off. The energy stored in the transformer then flybacks to Cell 1. By this way, balancing occurs between the complete battery pack and the cell with the lowest SOC. The balancing performance of this method is similar to the single flyback converter balancing. The multi-flyback converter balancing topology has more electrical components and higher costs, but its design is simpler for modular balancing [173].

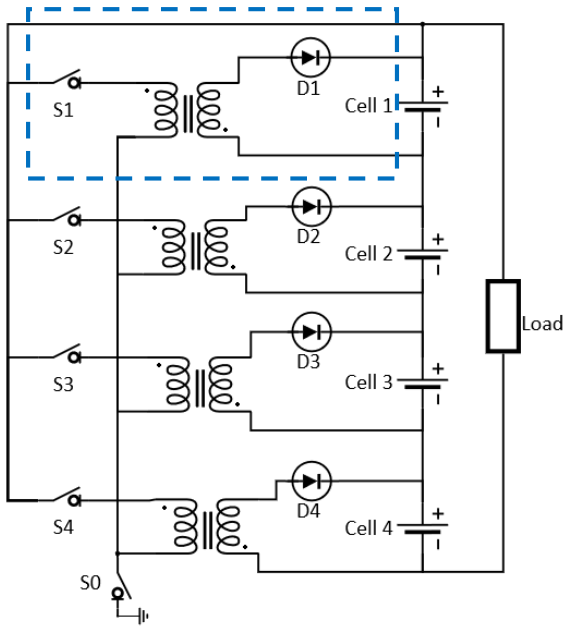


Figure 2-40. Multi-flyback converter balancing. Reproduced from [151].

Two configurations of multi-winding flyback converter balancing (Figure 2-41 and Figure 2-42) are found in the literature. In both configurations, the primary winding is connected to the complete battery pack, while each cell is connected to one secondary winding. For both configurations, physical implementation is difficult because it is hard to have many secondary windings coupled with a common core, and a large magnetic device has higher leakage inductance and energy losses.

- The first configuration (Figure 2-41) can perform two balancing modes, depending on the control applied. In the first balancing mode, the complete battery pack first charges the magnetizing inductor of the transformer, to then deliver the energy stored to the cell with the lowest SOC. In the second balancing mode, on the contrary, the cell with the highest SOC first charges the transformer, and then the energy stored in the transformer flybacks to the complete battery pack [174].

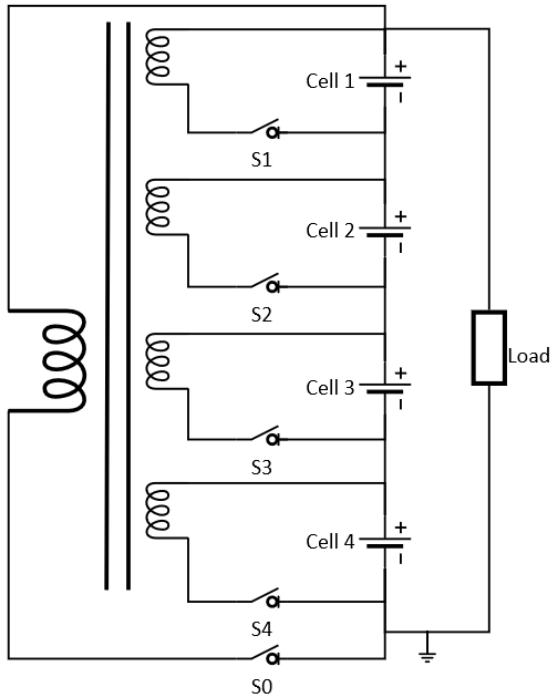


Figure 2-41. Multi-winding flyback converter balancing (type 1). Reproduced from [151].

- The second configuration (Figure 2-42) has a much easier control algorithm. By turning on *S0*, the complete battery pack first charges the magnetizing inductor of the transformer until the current in the primary winding reaches its upper boundary. Then *S0* is turned off, and energy stored in the transformer is transferred to all cells from their respective secondary windings. Since all secondary windings have the same number of turns, cells with lower voltage will experience higher charging current than cells with high voltage. All cells are balanced by these different currents. However, balancing performance is limited by the different leakage inductance of secondary windings [175].

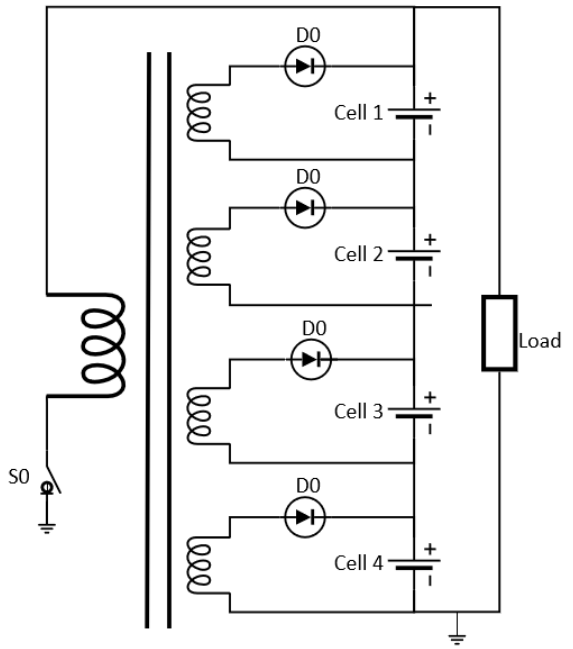


Figure 2-42. Multi-winding flyback converter balancing (type 2). Reproduced from [151].

## 2.4.2. Battery balancing control

Cell inconsistency is modeled by different values of the cells' parameters, such as internal resistance, coulombic efficiency, self-discharge, maximum available capacity, etc. Moreover, it affects some cell variables such as the cells' SOC and terminal voltage. Parameter discrepancy cannot be directly neutralized by equalizing the battery pack –although balancing does hinder divergence of cell parameters in the long term. Indeed, only a small variety of

actions can be taken to improve cell imbalance, namely, adequate design of the battery pack, which can minimize initial cell mismatch and reduce temperature gradients, and battery balancing, which has a direct effect only over the cell variables (voltage or SOC), but not over the cells' parameters [146]. Control actions are therefore aimed at either balancing voltage (in simple, cheap equalizers) or SOC (in high-end equalizers) because they are the only two variables over which balancing can act. However, cell voltage does not represent the cell state as well as SOC estimations. For this reason, the ultimate goal is usually SOC balancing (even when the chosen control variable is voltage). Under the precondition that all batteries will not be overcharged or discharged, the maximization of the battery capacity and energy utilization can be achieved [132].

Control strategies for battery balancing can be categorized in three different ways, according to different aspects of the balancing process:

- By the destination of the excess charge [176]. Passive or active balancing, as explained in Section 2.4.1. This categorization depends on the equalizer topology, so it is generally determined by design. Figure 2-43 schematize the different options to allocate the excess charge.
    - Passive balancing: controlled or uncontrolled shunt resistors remove excess energy from strong cells ("cell-to-null").
    - Active balancing. Charge transfer can be performed from one cell to the complete battery pack ("cell-to-stack"), from one cell to another cell ("cell-to-cell") or from one cell to the whole battery pack ("stack-to-cell").
- By the controlled variable. As mentioned above, either cell terminal voltage or SOC are the two variables that can be controlled.
    - Voltage-based balancing is simple but does not effectively counter SOC imbalance because cell voltage is not a good indicator of cell SOC. However, this is actually the most common control approach due to its simplicity and low cost [130].
    - SOC-based balancing, in contrast, is a better strategy for SOC balancing because it deals directly with SOC estimations, which already represent the cells' states. SOC estimation methods need to be precise to avoid transferring charge among the wrong cells.
- By the control objective. SOC balancing is the most frequent objective found in the literature, but other, more complex, predictive control strategies have been studied, such as optimizing the battery pack's power performance, energy performance (considering SOC and SOH), or lifetime [145, 177].

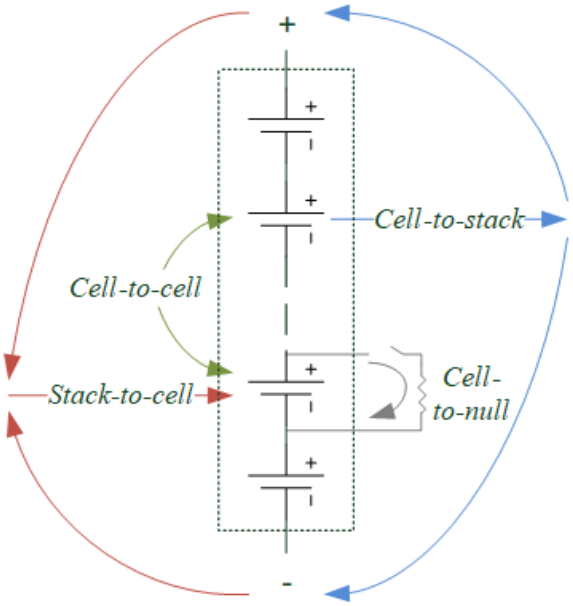


Figure 2-43. Classification of battery balancing by the destination of the excess charge. Reproduced from [176].

#### 2.4.2.1. When to balance?

There are two basic options for scheduling battery balancing during the battery usage cycle. They are detailed next following [97]:

- If the battery pack is ever plugged to the mains grid, the first option is to balance only when the battery pack is being charged. This approach can be used for EVs, for example. Since balancing is performed only when the battery pack is connected to an external power source, any energy dissipated by the balancing circuitry can be recharged immediately from the external source, maximizing the level of usable charge in the pack. This maximizes the energy stored by the battery pack that will be available for use when the pack is disconnected from the charger –this is of special interest for automotive applications, where limited range is one of the main concerns.
- The second option is continuous balance. That is, at every point in time that the battery pack is being used, cells in need of balancing are identified and the appropriate balancing circuits are activated or deactivated. This balancing schedule is necessary for applications such as hybrid-electric vehicles and stand-alone applications, in which the battery pack operates with no plug-in charging.

#### 2.4.2.2. Balancing speed

The rate at which charge must be transferred to effectively overcome the battery pack's natural tendency towards imbalance can be assessed by means of simulations. Specifically, the rate of charge transfer (balancing speed) must be higher than the rate at which SOC imbalance rises.

Simulation analysis is described in [97, 178]. Both references simulate hundreds of virtual battery packs, each with a certain combination of parameters, where parameter discrepancy results from certain pre-assumed statistical distributions. Cell discrepancy should be representative of the types and magnitudes of variation expected in real cells. The battery packs are simulated without balancing, applying a current profile typical of the application for which the battery pack is intended. The resulting SOC imbalance is assessed over each simulation and correlated to the specific parameter set of that simulation. The output of this process permits to identify which cell and battery-pack characteristics are the greatest contributors to imbalance.

Afterwards, the virtual battery packs are simulated with the balancing strategy on. For fixed set point balancing (that is, countering average SOC imbalance over a period of one charge-discharge cycle), the balancing rate must be higher than the one-cycle-average rate at which imbalance grows, to have a stable steady-state solution. For dynamic set point balancing (that is, countering SOC imbalance at every moment), charge transfer must be faster than the instantaneous rate at which imbalance grows to overcome imbalance as soon as it starts to have a noticeable effect. Co-simulating the imbalancing and the balancing processes ensures that the balancing methods studied can keep up.

## 2.5. Conclusions

The conclusions of the analysis of the state of the art are focused on summarizing topics that had not been previously covered in the literature. Some of that topics have been addressed in the three main approaches studied, in chapters 3, 4 and 5 of this dissertation, to contribute to scientific knowledge and promote the development of DC microgrids, with an emphasis on optimizing efficiency and prolonging battery lifetime.

Most common control strategies of DC microgrids (Section 2.1) utilize decentralized rules to keep bus voltage constant and/or to manage battery power to achieve more elaborated goals –such as the provision of ancillary services or optimum scheduling of loads and power injection into the grid. In Chapter 3, new control strategies have been proposed to minimize power losses in the DC-DC converters of the GAEI's DC microgrid. Departing from the

decentralized and distributed control strategy described in Section 2.1.3.2, two approaches have been modeled and evaluated: real-time optimization of the bus voltage (centralized control of the microgrid's battery) and real-time optimization of the switching frequencies at which the converters are operated (decentralized control of each converter based on local measurements). The first strategy has never been studied before in the literature, to the best of the author's knowledge, while the latter has been proposed for individual converters, although its relevance in the context of a DC microgrid has never been evaluated before.

Two battery types have been studied in this dissertation, lead-acid and lithium-ion (reviewed in Section 2.2), in consideration of their leading relevance. They have been described, highlighting their characteristics and typical usages. The study of batteries must account for their non-linear nature, utilizing battery models (Section 2.3) that faithfully represent both short-term and long-term battery response, producing accurate estimations of SOC and SOH, which are of the uttermost importance for battery management applications. Even adhering to these requirements of versatility and accuracy, the models must still be simple enough to facilitate their integration into Battery Management Systems (BMSs).

Equivalent circuits models are simple to parametrize and use, but they do neither reflect the physical processes inside the cell nor produce SOH estimations. Full-order physics-based models, on the contrary, do reflect the physical mechanisms that make the cell work and have the capability to produce SOH estimations, but they are too complex for programming them in BMS microcontrollers. Reduced-order electrochemical models (ROMs) simplify the full-order models maintaining much of their precision and insight on the internal processes taking place in the cell. Reduced-order models result sufficiently simple for most BMS applications, but they still involve intricate mathematical calculations that make them unsuitable for bigger long-term optimization problems of highly complex systems. With the objective of paving the way for real-time economic optimization of microgrid operation, a new model has been proposed in Chapter 5, consisting of an equivalent circuit battery model that has some of its parameters updated from the results of a reduced-order physics-based degradation model running in parallel.

Regarding battery balancing systems (Section 2.4), many different passive and active topologies have been reviewed. A gap is detected in the field of converter-based topologies: to the best of the author's knowledge, there is no record of any converter-based topology analogous to the switched-capacitor or switched-inductor topologies presented in this state-of-the-art review. Indeed, converter-based topologies tend to use many DC-DC converters to allow for fast charge transfer among the battery cells. Nevertheless, a high number of converters rises the prize of the equalizer and complicates its control strategy. A novel converter-based topology has been proposed in Chapter 4 inspired in switched-capacitor or

switched-inductor topologies but substituting the passive charge-storage element by an active, controllable, element. The main advantage is that it reduces the number of converters to just one, thanks to the power-multiplexing technique. The equalizer control strategy has been carefully designed to guarantee that charge is transferred sufficiently rapid to counteract the natural imbalance caused by parameter discrepancy among the battery pack's cells. Battery balancing can achieve battery life extension, which redounds to indirectly optimizing the operation of the system of which the battery is part –in this dissertation, a DC microgrid.

# 3. Efficiency optimization of a DC microgrid

Adequate management of power of the microgrid's units is a key element to accomplish stable operation, improve energy efficiency, extend battery lifetime and achieve maximum economic yield. Microgrid stable operation require to coordinately control all the microgrid's elements. In the GAEI's microgrid (μG) this is achieved by E-BCS, the base control layer, described in Section 2.1.3.

This chapter presents two control strategies that complement E-BCS to achieve efficiency optimization (rather than economic optimization, which has been more frequently addressed in the literature). The objective of both strategies is to minimize the μG DC-DC converters' losses. The two proposed strategies, which can be applied independently or simultaneously, are:

- Bus Voltage Optimization Control (BVOC).
- Online Optimization of Switching Frequency (OOSF).

BVOC consists in adaptively operating the DC microgrid at its instantaneous optimum bus voltage, defined as the voltage value that produces minimum power losses in the set of DC-DC converters, given the specific power sharing scheme among the μG's units at every moment. OOSF consists in adaptively operating every DC-DC converter at its instantaneous optimum switching frequency. Both strategies can be applied independently or simultaneously to increase the DC-μG efficiency to a small extent.

First, a simplified simulation model of the GAEI's μG is developed, including models of the power losses of the DC-DC converters. Then, the optimization problem is stated for both control algorithms. Afterwards, the μG is simulated with basic and optimized control to analyze the efficiency improvement achieved. Finally, the optimization parameters are examined to evaluate if different sets of parameters could further improve the μG's efficiency.

## 3.1. Microgrid model

A simplified model of the GAEI's microgrid has been developed for the optimization study. Since the GAEI's microgrid (described in Section 2.1.3) is extraordinarily complex, studying optimization strategies for this μG would be too specific and the results, would be of limited interest. For this reason, a simplified version of the GAEI's μG has been modeled in order to produce more universal results. Specifically, more basic topologies have been considered for the DC-DC converters while energy sources/loads/storage elements have been fairly realistically modeled (although minor modifications and simplifications have been considered too). The purpose is to broaden the scope of the efficiency optimization research presented here, so the results are representative of a greater number of DC-μGs or, at least, they can be easily adapted to most common μG architectures and basic control schemes. The simplified μG architecture and control is described and modeled next.

### 3.1.1. Simplified model of the microgrid

The microgrid (μG) studied is modeled in Simulink and is used to validate the proposed optimization control strategies in simulations. The μG model comprises the same units as the GAE's microgrid, modeled considering some simplifications:

- The photovoltaic field is modeled as a five-strings array, being all the strings identical. A single MPPT boost converter connects the array to the DC bus, instead of one converter per each one of the five independent strings that the real μG has.
- Only one DC wind turbine is considered, with a nominal power of 1.5 $kW$. The model of the wind turbine is inspired on the Bornay 1500, 120 $V$. This wind turbine is connected to the DC bus through an MPPT boost converter. The output characteristic is modeled as a constant 120 $V$ DC voltage to simplify the model, although the output voltages of the two microgrid's wind turbines are actually AC and vary with rotational speed (since permanent-magnets induction generators are employed). The 120 $V$ DC constant voltage is consistent with the output characteristic of the Bornay 1500, 120 $V$ wind turbine, which has an factory-installed front-end rectifier.

- DC loads are connected through a quadratic buck converter that keeps voltage constant at $48\ V$, although the GAEI's μG can also feed loads directly from the DC bus.
- The electrolyzer voltage has also been modeled as constant ($24\ V$) to simplify the model, although its characteristic actually depends on current, due to activation, ohmic and concentration polarization losses. The fuel cell output voltage, in contrast, is modeled by a realistic look-up table that relates voltage and current.
- The Battery Energy Storage System has been modeled as a battery pack of batteries 15 Lead Crystal 6-CNFJ-200, $200\ Ah, 12\ V$ (from the manufacturer Betta Batteries).
- One three-phase bidirectional inverter $\pm 5\ kW$ has been considered instead of three single-phase unidirectional MPPT inverters.
- The DC bus voltage boundaries have been widened a little (from $[270, 370]\ V$ to $[240, 380]\ V$) so voltage optimization (described below) has higher margin of energy efficiency improvement.

From now on, "the μG" refers to this microgrid model. Figure 3-1 shows the μG's units, which are interconnected to a variable voltage DC bus through DC-DC converters. The topology of each converter is specified in the figure. It is convenient to differentiate between power provided/consumed by each unit $i = \{PV, WT, FC, LOAD, EZ, BESS, INV\}$ at the unit side and at the DC bus side. For this reason, power at the DC bus side has been denoted $P_i^{bus\cdot}$ while power at the unit side is simply $P_i$.

Bus voltage, $v_{bus}$, is constrained by the boundaries $240\ V \leq v_{bus} \leq 380\ V$. The lower limit has been chosen such that $v_{bus}$ always remains over the maximum PV voltage ($190\ V$ approximately, considering open circuit voltage at the historic lowest temperature in Tarragona) and the maximum BESS voltage ($220.5\ V$, considering that the maximum BESS voltage corresponds to absorption charge of each of the 15 monobloc batteries at $14.7\ V$). With the selected low voltage boundary, it is avoided to use buck-boost (for PV) and bidirectional buck-boost (for BESS) converters in favor of more efficient solutions. The higher voltage boundary results from applying a safety margin of $20\ V$ with respect to the maximum voltage of the capacitor bank ($400\ V$). This safety margin is proven sufficient thanks to the robustness of the autonomous control E-BCS maintaining voltage peaks within the boundaries.

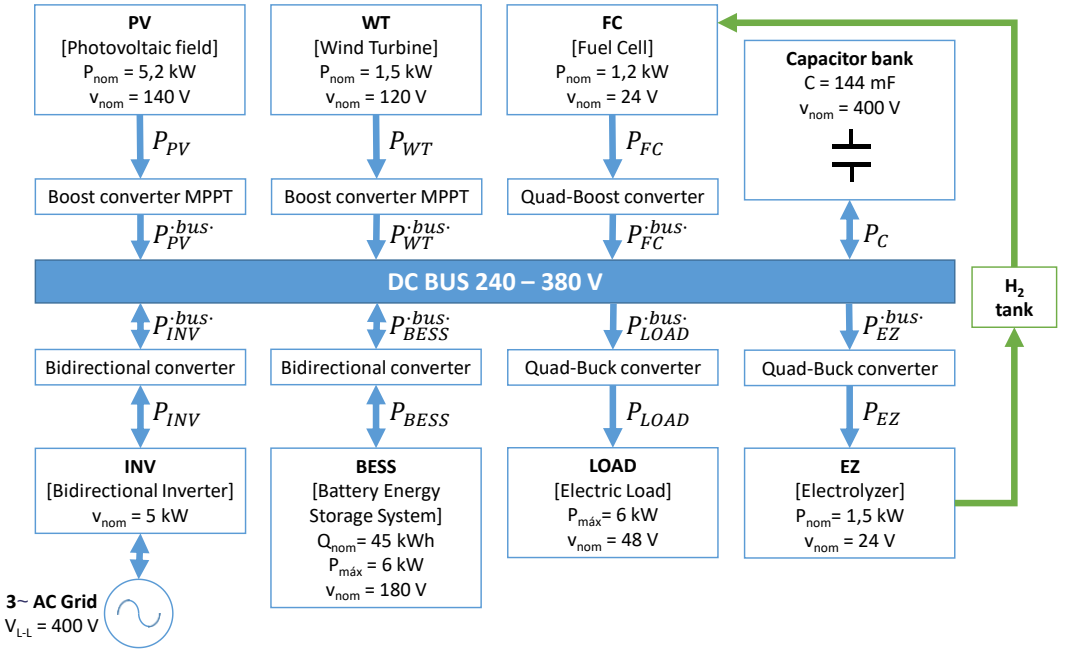


Figure 3-1. Microgrid architecture. The µG is composed of a DC bus that interconnects the following elements: two renewable energy sources (PV and WT), a controllable source (FC), a capacitor bank, a bidirectional grid-inverter (INV), a battery system (BESS), critical loads (LOAD), and a controllable load (EZ).

### 3.1.2. Models of the DC-DC converters

Modeling the efficiency of the converters is necessary to evaluate their power losses under different operation conditions and to study how they may change when modifying certain parameters. Averaged models of the converters' losses based on small-signal analysis are utilized for this purpose.

All the µG's converters are controlled as power sources. Converters with nominal power over 3 kW utilize IGBTs (the converters of PV, LOAD, BESS and INV) while those with lower nominal power utilize MOSFETs (the converters of WT, FC and EZ). The ranges of possible switching frequencies, $f_{sw}$, are $3\ \text{kHz} \leq f_{sw} \leq 10\ \text{kHz}$ for IGBTs and $20\ \text{kHz} \leq f_{sw} \leq 100\ \text{kHz}$ for MOSFETs. Inductor current ripple lower than 20% is imposed by design in the worst-case scenario, that is, nominal power and minimum switching frequency ($3\ kHz$ for IGBT converters and $20\ kHz$ for MOSFET converters). Average current values are used since low current ripple ensures small error. Transistors operate hard switching in continuous conduction mode. Core losses and conduction and switching losses have been modeled, following [179–181].

Table 3-1. Parameters of the converters' component.

| Element | Parameter | PV | WT | FC | LOAD | EZ | BESS | INV |
|---|---|---|---|---|---|---|---|---|
| Inductors | $L_1\ (mH)$ | 1.124 | 1.368 | 0.189 | 0.985 | 2.000 | 1.246 | 0.457 |
| | $R_{L1}\ (m\Omega)$ | 120 | 140 | 25 | 110 | 230 | 130 | 110 |
| | $N_1$ | 183 | 245 | 72 | 166 | 210 | 189 | 222 |
| | $A_{C1}\ (cm^2)$ | 9.87 | 9.87 | 6.78 | 9.87 | 6.78 | 9.87 | 1.76 |
| | $Vol_{C1}\ (cm^3)$ | 407 | 407 | 220 | 407 | 220 | 407 | 34.5 |
| | $L_2\ (mH)$ | - | - | 2.477 | 0.150 | 0.152 | - | - |
| | $R_{L2}\ (m\Omega)$ | | | 300 | 25 | 2 | | |
| | $N_2$ | | | 219 | 65 | 59 | | |
| | $A_{C2}\ (cm^2)$ | | | 6.78 | 9.87 | 6.78 | | |
| | $Vol_{C2}\ (cm^3)$ | | | 220 | 407 | 220 | | |
| Diodes | $R_{d1}\ (m\Omega)$ | 23.2 | 11.3 | 2.2 | 11.2 | 39 | 39 | 23.2 |
| | $V_{f1}\ (V)$ | 1.7 | 1.8 | 0.83 | 1.5 | 1.3 | 1.3 | 1.7 |
| | $R_{d2}\ (m\Omega)$ | - | - | 11.3 | 11.2 | 11.2 | 39 | 23.2 |
| | $V_{f2}\ (V)$ | | | 1.5 | 1.5 | 1.5 | 1.3 | 1.7 |
| | $R_{d3}\ (m\Omega)$ | - | - | 150 | 1.6 | 3 | - | - |
| | $V_{f3}\ (V)$ | | | 1.4 | 0.89 | 0.74 | | |
| Transistors | $R'_{S1}\ (m\Omega)$ | 80 | 7.9 | 63 | 9.8 | 22 | 15 | 3.3 |
| | $V'_{f1}\ (V)$ | 1.75 | - | - | 2.0 | - | 2.5 | 1.55 |
| | $t_{sw1}\ (ns)$ | 135 | 78 | 106 | 287 | 174 | 131 | 197 |
| | $]f_{sw1}[\ (kHz)$ | 4 | 50 | 50 | 4 | 50 | 4 | 4 |
| | $R'_{S2}\ (m\Omega)$ | - | - | - | - | - | 15 | 3.3 |
| | $V'_{f2}\ (V)$ | | | | | | 2.5 | 1.55 |
| | $t_{sw2}\ (ns)$ | | | | | | 131 | 197 |
| | $]f_{sw2}[\ (kHz)$ | | | | | | 4 | 4 |
| Driver's power supply | $P_{ctrl}\ (W)$ | 10 | 5 | 5 | 10 | 5 | 10 | 10 |

The elements that compose the converters are inductors, $L$; Schottky diodes, $d$; capacitors, $C$; and transistors, $S$ (either MOSFETs or IGBTs). Parasite elements associated to inductors (series resistance), diodes (direct polarization series resistance and forward voltage) and transistors (anti-parallel diode, series resistance and forward voltage) have been modeled to

estimate the power losses that they cause using piecewise-linear analysis. The parameters that characterize the seven converters of the μG are provided in Table 3-1, (3.1) and (3.2).

The nomenclature used in Table 3-1 is as follows: $R_L$ is the parasitic series resistance of the inductor, $N$ is the number of turns of the inductor, $A_C$ is the cross-sectional area of the inductor's core, $Vol_C$ is the core's volume, $R_d$ is the parasitic series resistance of the diode, $V_f$ is the forward voltage of the diode, $R'_S$ is the on-resistance of the IGBTs and MOSFETs, $V'_f$ is the forward voltage drop of the IGBTs, $t_{sw}$ is the total switching time that results from adding up $t_{d(on)} + t_r + t_{d(off)} + t_f$ (turn-on delay + rise time + turn-off delay time + fall time), $]f_{sw}[$ is the fixed switching frequency of the transistor when OOSF is not in action, and $P_{ctrl}$ is the power supply of the converter's driver.

Core losses are modeled by the Steinmetz equation $P_{Fe} = Vol_c K(\Delta B/2)^{\beta} f_{sw}^{\alpha}$ [179], where $\Delta B$ is the flux density ripple calculated by using the Faraday's Law (3.6) [179] and $f_{sw}$ is the instantaneous switching frequency. The characteristic parameters of the inductor's magnetic core, $\beta, K, \alpha$, are dependent on switching frequency. Core parameters have been taken from Magnetics® Inductor Design tool [182]:

$$\beta = 1.774$$

$$K = \begin{cases} 170.17, & with\ f_{sw} \le 5\ kHz \\ 170.17 - 124.69 \cdot \dfrac{f_{sw}(kHz) - 5}{10}, & with\ 5\ kHz \le f_{sw} \le 10\ kHz \\ 45.48, & with\ f_{sw} > 15\ kHz \end{cases} \quad (3.1)$$

$$\alpha = \begin{cases} 1.03, & with\ f_{sw} \le 5\ kHz \\ 1.03 + 0.43 \cdot \dfrac{f_{sw}(kHz) - 5}{10}, & with\ 5\ kHz \le f_{sw} \le 10\ kHz \\ 1.46, & with\ f_{sw} > 15\ kHz \end{cases} \quad (3.2)$$

#### 3.1.2.1. Topologies

Four different DC-DC converter topologies are present in the microgrid (μG) (see Figure 3-1): boost, quadratic-boost, quadratic-buck and bidirectional. The following notation is used: $v_{in}$, $i_{in}$, $v_{out}$ and $i_{out}$ are the measured input and output voltages and currents (note that either $v_{in}$ or $v_{out}$ is $v_{bus}$ in all cases). The control system of each converter $i$ imposes the unit's power, $P_i$, while power in the μG's DC bus side, $P_i^{bus}$, remains unrestricted –it only depends on $P_i$ and on the converter's efficiency.

Circuit diagrams of the four topologies are provided next. Parasite elements have been represented in pale blue.

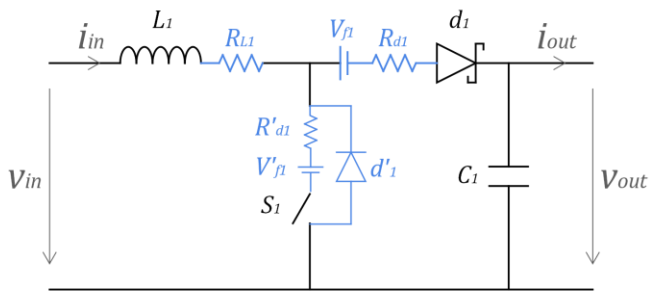


Figure 3-2. Topology of boost converter (used in PV and WT).

- Figure 3-2 shows the circuit diagram of the boost converter, where $v_{out} = v_{bus}$. PV and WT use this type of DC-DC converter. Note that when the transistor is a MOSFET (that is, in the WT converter), the forward voltage drop $V'_{f1}$ is nil. In both cases (PV and WT), the controlled variables are the converters' input powers, $P_{PV}$ and $P_{WT}$, performing MPPT to maximize renewable energy generation whenever possible.

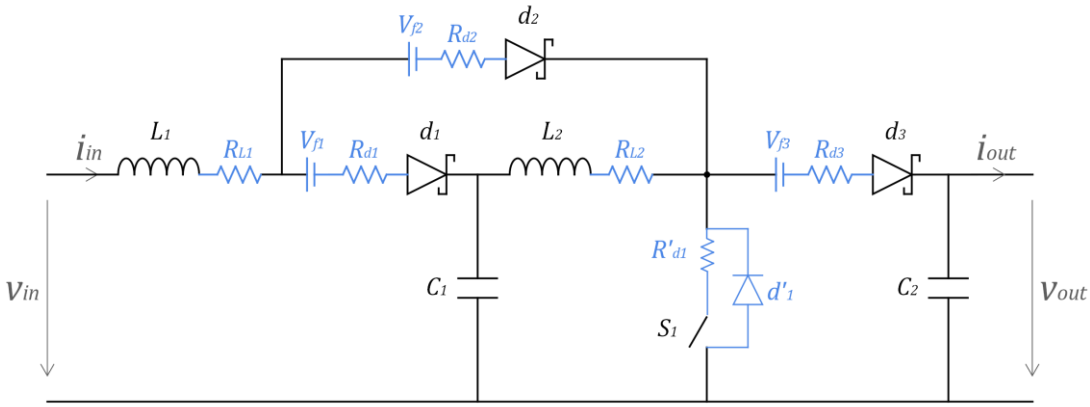


Figure 3-3. Topology of single-transistor quadratic-boost converter (used in FC).

- Figure 3-3 shows the circuit diagram of the single-switch quadratic-boost converter, where $v_{out} = v_{bus}$. FC uses this type of DC-DC converter. This topology has been selected over the two-cascaded boost topology because it uses one transistor less. The controlled variable is the converter's input power, $P_{FC}$.

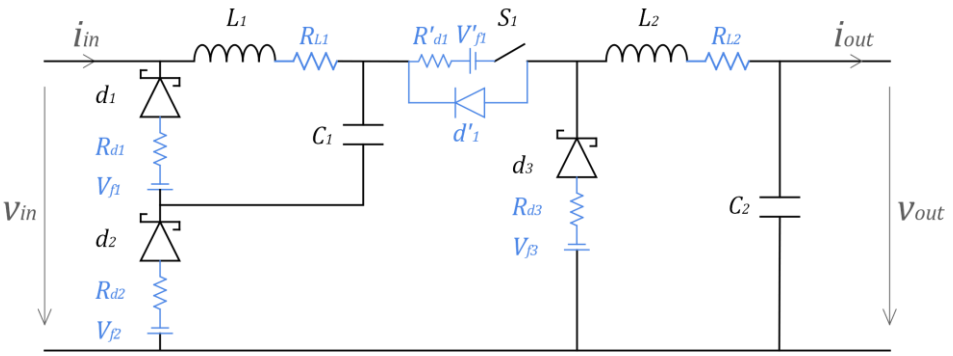


Figure 3-4. Topology of quadratic-buck converter (used in EZ and LOAD).

- Figure 3-4 shows the circuit diagram of the quadratic-buck converter, where $v_{in} = v_{bus}$. EZ and LOAD use this type of DC-DC converter. Note that when the transistor is a MOSFET (that is, in the EZ converter), the forward voltage drop $V'_{f1}$ is nil. In both cases (EZ and LOAD), the controlled variables are the converters' output powers, $P_{EZ}$ and $P_{LOAD}$, to use surplus generation and to meet the demanded power, $P_{demand}$, respectively, whenever possible.

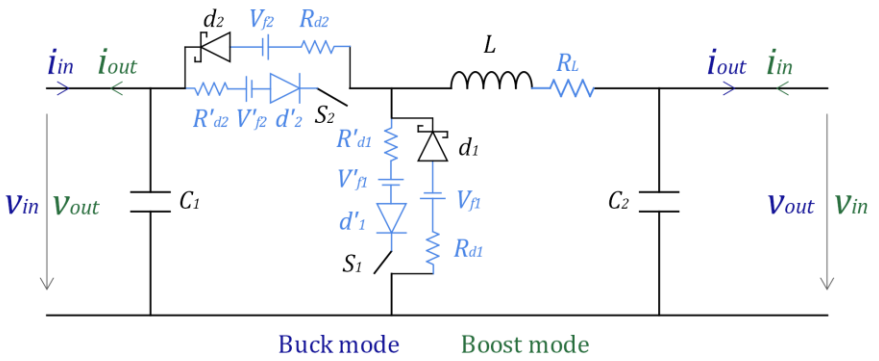


Figure 3-5. Topology of bidirectional converter (used in BESS and INV).

- Figure 3-5 shows the circuit diagram of the bidirectional converter. BESS and INV use this type of DC-DC converter. In the case of BESS, $v_{in} = v_{bus}$ in buck mode and $v_{out} = v_{bus}$ in boost mode because BESS' voltage, $v_{BESS}$, is always lower than that of the DC-bus ($v_{BESS} < v_{bus}$); in the case of the INV's converter, $v_{in} = v_{bus}$ in boost mode and $v_{out} = v_{bus}$ in buck mode because the DC voltage input

to the inverter, $v_{INV(DC)}$, is always higher than that of the DC-bus $(v_{INV(DC)} > v_{bus})$. The logical variables $S_{BESS}$ and $S_{INV}$ are defined to track when the bidirectional units operate as power sources or sinks $S_{BESS}[k] := P_{BESS}[k] > 0$ (BESS operates as a power source) an $S_{INV}[k] := P_{INV}[k] > 0$ (INV operates as a power source). The controlled variables are:

- In boost mode ($S_{BESS} = 1$), BESS converter's input power, $P_{BESS}$.
- In buck mode ($S_{BESS} = 0$), BESS converter's output power, again $P_{BESS}$.
- In boost mode ($S_{INV} = 0$), INV converter's output power, $P_{INV}$.
- In buck mode ($S_{INV} = 1$), INV converter's input power, again $P_{INV}$.

$P_{BESS}^{\cdot bus\cdot}$ and $P_{INV}^{\cdot bus\cdot}$, in turn, remain unregulated.

Note that in unidirectional converters, the current never passes through the anti-parallel diode ($d_1'$ in Figure 3-2, Figure 3-3 and Figure 3-4). Thus, representing them as ideal diodes does not introduce imprecision into the model, as they do not cause power loss. In the bidirectional converters, on the contrary, current does pass through the anti-parallel Schottky diodes ($d_1$ and $d_2$ in Figure 3-5).

#### 3.1.2.2. Equations of the converters' models

Equations (3.1)–(3.6) apply to all the DC-DC converters of the μG:

$$v_{out} i_{out} = v_{in} i_{in} \eta_{pc} \tag{3.3}$$

$$i_{out} = i_{in} f(D) \tag{3.4}$$

$$v_{out} = \frac{\eta_{pc} v_{in}}{f(D)} \tag{3.5}$$

$$\Delta B = \left| \frac{v_L^{on} D}{N A_C f_{sw}} \right| = \left| \frac{v_L^{off} (1 - D)}{N A_C f_{sw}} \right|, \tag{3.6}$$

where $\eta_{pc}$ is the efficiency of the power converter, $D$ is the transistor's duty cycle, $f(D) = i_{out}/i_{in} = v_{in}\eta_{pc}/v_{out}$ is the $D$-dependent relationship between the output and the input current, $\Delta B$ is the flux density ripple calculated with the Faraday's Law [179], $v_L^{on}$ is the voltage across the inductor during the ON time of the duty cycle, and $v_L^{off}$ is the voltage across the inductor during the OFF time.

Equations in Table 3-2 are employed to model the DC-DC converters operation. The converter's efficiency is considered to approximately affect only the input-output voltage

relationship ((3.7), (3.10), (3.13), (3.17), (3.21), (3.25), (3.28), (3.31), and (3.34)), that is, the model assumes that the relationship between the input and the output currents is ideal (electromagnetic losses are neglected) [38, 181, 183]:

$$\eta_{pc} = \frac{P_{out}}{P_{in}} = \frac{v_{out} i_{out}}{v_{in} i_{in}} = \frac{v_{out} i_{in} f(D)}{v_{in} i_{in}} = \frac{v_{out} f(D)}{v_{in}} \Rightarrow f(D) = \frac{v_{in} \eta_{pc}}{v_{out}}$$

Notation has been simplified in these equations by eliminating the superscript that identifies the converter to which the variables refer in each case. For example, $v_{in}^{PV}, i_{in}^{PV}, v_{out}^{PV}, i_{out}^{PV}, \eta_{pc}^{PV}, D^{PV}, \Delta B^{PV}, P_{ctrl}^{PV}$ are the variables that characterize PV operation while $v_{in}^{WT}, i_{in}^{WT}, v_{out}^{WT}, i_{out}^{WT}, \eta_{pc}^{WT}, D^{WT}, \Delta B^{WT}, P_{ctrl}^{WT}$ characterize WT operation, and so on for the remaining converters; they are expressed simply as $v_{in}, i_{in}, v_{out}, i_{out}, \eta_{pc}, D, \Delta B, P_{ctrl}$ since left column of Table 3-2 already specifies the converter at which the variables refer to.

The model performs iterative calculation of each converter's efficiency at discrete time $k$, $\eta_{pc}^{i}[k]$, is performed until efficiency error is less than 0.1%. A color code has been used to highlight the different mechanisms originating power losses. The following power losses have been considered, using averaged voltage and current values:

- Conduction losses:
  - $R_L i_L^2$ in the inductors.
  - $t_d^{cond} f_{sw} \left( R_d i_d^{cond\,2} + V_f i_d^{cond} \right)$ in the diodes.
  - $t_S^{on} f_{sw} R_d' i_S^{on\,2}$ in the MOSFETs.
  - $t_S^{on} f_{sw} \left( R_S' i_S^{on\,2} + V_f' i_S^{on} \right)$ in the IGBTs.

  where $i_L$ is the average inductor current; $t_d^{cond}$ and $t_S^{on}$ are, respectively, the times conduction times of the diode and the transistor within each switching period; and $i_d^{cond}$ and $i_S^{on}$ are, respectively, the diode and the transistor current when they are conducting.
- Core losses: $Vol_c K (\Delta B/2)^{\beta} f_{sw}^{\alpha}$

  according to the Steinmetz equation presented above.
- Switching losses: $0.5 v_{block} i_S^{on} t_{sw} f_{sw}$

  which represents the turn-on and turn-off losses. $t_{sw}$ is calculated as $\left( t_{d(on)} + t_r + t_{d(off)} + t_f \right)$, and $v_{block}$ is the voltage blocked by the transistor during the off time: $v_{block}^{PV} = v_{block}^{WT} = v_{block}^{FC} = v_{bus}$, $v_{block}^{LOAD} = (1 + D^{LOAD}) v_{bus}$, $v_{block}^{EZ} = (1 + D^{EZ}) v_{bus}$, $v_{block,S1}^{BESS} = v_{block,S2}^{BESS} = v_{bus}$ both in boost mode and in buck mode, and $v_{block,S1}^{INV} = v_{block,S2}^{INV} = v_{INV(DC)}$ both in boost mode and in buck

mode (where $v_{INV(DC)} \simeq 565\,V$ is the stabilized voltage of the inverter's internal DC bus).

- Constant losses: $P_{ctrl}$

  which represents the power supply of the gate driver controller, modeled as constant.

Table 3-2. Equations utilized to model the converters' power losses.

| Converter | Equations | |
|---|---|---|
| PV converter (Boost) [IGBT] | $D = \frac{v_{bus} - v_{in}\eta_{pc}}{v_{bus}} \Leftrightarrow f(D) = 1 - D$ | (3.7) |
| | $v_L^{on} = v_{in} - R_{L1}i_{in} - \left(V'_{f1} + R'_{S1}\right)i_{in}$ | (3.8) |
| | $P_{loss} = \left\{R_L i_{in}^2 + Vol_c K(\Delta B/2)^{\beta} f_{sw}^{\alpha}\right\}_L + \left\{(1-D)\left(R_d i_{in}^2 + V_f i_{in}\right)\right\}_d + \left\{D\left(R'_S i_{in}^2 + V'_f i_{in}\right) + (0.5 v_{bus} i_{in} t_{sw} f_{sw})\right\}_S + P_{ctrl}$ | (3.9) |
| WT converter (Boost) [MOSFET] | $D = \frac{v_{bus} - v_{in}\eta_{pc}}{v_{bus}} \Leftrightarrow f(D) = 1 - D$ | (3.10) |
| | $v_L^{on} = v_{in} - R_{L1}i_{in} - R'_{S1}i_{in}$ | (3.11) |
| | $P_{loss} = \left\{R_L i_{in}^2 + Vol_c K(\Delta B/2)^{\beta} f_{sw}^{\alpha}\right\}_L + \left\{(1-D)\left(R_d i_{in}^2 + V_f i_{in}\right)\right\}_d + \left\{DR'_S i_{in}^2 + (0.5 v_{bus} i_{in} t_{sw} f_{sw})\right\}_S + P_{ctrl}$ | (3.12) |

| Converter | Equations | |
|---|---|---|
| FC converter (Quad. boost) [MOSFET] | $$D = 1 - \sqrt{\frac{v_{in}\eta_{pc}}{v_{bus}}} \Leftrightarrow f(D) = (1-D)^2$$ | (3.13) |
| | $$v_{L1}^{on} = v_{in} - R_{L1}i_{in} - \left(V_{f2} - R_{d2}i_{in}\right) - \left(V'_{f1} - R'_{S1}(2-D)i_{in}\right)$$ | (3.14) |
| | $$v_{L2}^{on} = \frac{Dv_{bus}}{1-D} - R_{L2}\frac{i_{out}}{1-D}$$ | (3.15) |
| | $$\begin{aligned} P_{loss} = &\left\{R_{L1}i_{in}^2 + Vol_{c1}K(\Delta B_{L1}/2)^{\beta}f_{sw}^{\alpha}\right\}_{L1} \\ &+ \left\{(1-D)^2R_{L2}i_{in}^2 + Vol_{c2}K(\Delta B_{L2}/2)^{\beta}f_{sw}^{\alpha}\right\}_{L2} \\ &+ \left\{(1-D)\left(R_{d1}i_{in}^2 + V_{f1}i_{in}\right)\right\}_{d1} \\ &+ \left\{D\left(R_{d2}i_{in}^2 + V_{f2}i_{in}\right)\right\}_{d2} \\ &+ \left\{(1-D)\left(R_{d3}i_{out}^2 + V_{f3}i_{out}\right)\right\}_{d3} \\ &+ \left\{DR'_S(Di_{in})^2 + (0.5v_{bus}Di_{in}t_{sw}f_{sw})\right\}_S + P_{ctrl} \end{aligned}$$ | (3.16) |
| LOAD converter (Quad. buck) [IGBT] | $$D = \sqrt{\frac{v_{out}}{v_{bus}\eta_{pc}}} \Leftrightarrow f(D) = \frac{1}{D^2}$$ | (3.17) |
| | $$v_{L1}^{on} = (1-D)v_{bus} - R_{L1}Di_{out} + \left(V_{f2} + R_{d2}(1-D)i_{out}\right)$$ | (3.18) |
| | $$v_{L2}^{off} = v_{out} - R_{L2}i_{out} - \left(V_{f3} + R_{d3}i_{out}\right)$$ | (3.19) |
| | $$\begin{aligned} P_{loss} = &\left\{R_{L1}(Di_{out})^2 + Vol_{c1}K(\Delta B_{L1}/2)^{\beta}f_{sw}^{\alpha}\right\}_{L1} \\ &+ \left\{R_{L2}i_{out}^2 + Vol_{c2}K(\Delta B_{L2}/2)^{\beta}f_{sw}^{\alpha}\right\}_{L2} \\ &+ \left\{D\left(R_{d1}(Di_{out})^2 + V_{f1}Di_{out}\right)\right\}_{d1} \\ &+ \left\{(1-D)\left(R_{d2}\left((1-D)i_{out}\right)^2 + V_{f2}(1-D)i_{out}\right)\right\}_{d2} \\ &+ \left\{D\left(R_{d3}i_{out}^2 + V_{f3}i_{out}\right)\right\}_{d3} \\ &+ \left\{D\left(R'_S i_{out}^2 + V'_f i_{out}\right)\right. \\ &\left.+ (0.5(1+D)v_{bus}i_{out}t_{sw}f_{sw})\right\}_S + P_{ctrl} \end{aligned}$$ | (3.20) |

| Converter | | Equations | |
|---|---|---|---|
| EZ converter (Quad. buck) [MOSFET] | | $D = \sqrt{\frac{v_{out}}{v_{bus}\eta_{pc}}} \Leftrightarrow f(D) = \frac{1}{D^2}$ | (3.21) |
| | | $v_{L1}^{on} = (1-D)v_{bus} - R_{L1}Di_{out} + \left(V_{f2} + R_{d2}(1-D)i_{out}\right)$ | (3.22) |
| | | $v_{L2}^{off} = v_{out} - R_{L2}i_{out} - \left(V_{f3} + R_{d3}i_{out}\right)$ | (3.23) |
| | | $P_{loss} = \{R_{L1}(Di_{out})^2 + Vol_{c1}K(\Delta B_{L1}/2)^{\beta}f_{sw}^{\alpha}\}_{L1} + \{R_{L2}i_{out}^2 + Vol_{c2}K(\Delta B_{L2}/2)^{\beta}f_{sw}^{\alpha}\}_{L2} + \{D(R_{d1}(Di_{out})^2 + V_{f1}Di_{out})\}_{d1} + \{(1-D)\left(R_{d2}((1-D)i_{out})^2 + V_{f2}(1-D)i_{out}\right)\}_{d2} + \{D(R_{d3}i_{out}^2 + V_{f3}i_{out})\}_{d3} + \{DR_S'i_{out}^2 + (0.5(1+D)v_{bus}i_{out}t_{sw}f_{sw})\}_S + P_{ctrl}$ | (3.24) |
| BESS converter (Bidirectional) [IGBT] | Boost mode. (in = BESS out = bus) | $D = \frac{v_{bus} - v_{in}\eta_{pc}}{v_{bus}} \Leftrightarrow f(D) = 1 - D$ | (3.25) |
| | | $v_L^{on} = v_{in} - R_{L1}i_{in} - \left(V_{f1}' + R_{S1}'\right)i_{in}$ | (3.26) |
| | | $P_{loss} = \{R_Li_{in}^2 + Vol_cK(\Delta B/2)^{\beta}f_{sw}^{\alpha}\}_L + \{(1-D)(R_{d2}i_{in}^2 + V_{f2}i_{in})\}_{d2} + \{D(R_{S1}'i_{in}^2 + V_{f1}'i_{in}) + (0.5v_{bus}i_{in}t_{sw1}f_{sw})\}_{S1} + P_{ctrl}$ | (3.27) |
| | Buck mode. (in = bus out = BESS) | $D = \frac{v_{out}}{v_{bus}\eta_{pc}} \Leftrightarrow f(D) = \frac{1}{D}$ | (3.28) |
| | | $v_L^{on} = v_{bus} - v_{out} - \left(V_{f2}' + R_{S2}'i_{out}\right) - R_Li_{out}$ | (3.29) |
| | | $P_{loss} = \{R_Li_{out}^2 + Vol_cK(\Delta B/2)^{\beta}f_{sw}^{\alpha}\}_L + \{(1-D)(R_{d1}i_{out}^2 + V_{f1}i_{out})\}_{d1} + \{D(R_{S2}'i_{out}^2 + V_{f2}'i_{out}) + (0.5v_{bus}i_{out}t_{sw2}f_{sw})\}_{S2} + P_{ctrl}$ | (3.30) |

| Converter | | Equations | |
|---|---|---|---|
| INV converter (Bidirectional) [IGBT] | Boost mode. (in = bus out = INV(DC)) | $D = \frac{v_{out} - v_{bus}\eta_{pc}}{v_{out}} \Leftrightarrow f(D) = 1 - D$ | (3.31) |
| | | $v_L^{on} = v_{bus} - R_{L1}i_{in} - \left(V'_{f1} + R'_{S1}\right)i_{in}$ | (3.32) |
| | | $P_{loss} = \left\{R_L i_{in}^2 + Vol_c K(\Delta B/2)^{\beta} f_{sw}^{\alpha}\right\}_L + \left\{(1-D)\left(R_{d2}i_{in}^2 + V_{f2}i_{in}\right)\right\}_{d2} + \left\{D\left(R'_{S1}i_{in}^2 + V'_{f1}i_{in}\right) + \left(0.5 v_{out} i_{in} t_{sw1} f_{sw}\right)\right\}_{S1} + P_{ctrl}$ | (3.33) |
| | Buck mode. (in = INV(DC) out = bus) | $D = \frac{v_{bus}}{v_{in}\eta_{pc}} \Leftrightarrow f(D) = \frac{1}{D}$ | (3.34) |
| | | $v_L^{on} = v_{in} - v_{bus} - \left(V'_{f2} + R'_{S2}i_{out}\right) - R_L i_{out}$ | (3.35) |
| | | $P_{loss} = \left\{R_L i_{out}^2 + Vol_c K(\Delta B/2)^{\beta} f_{sw}^{\alpha}\right\}_L + \left\{(1-D)\left(R_{d1}i_{out}^2 + V_{f1}i_{out}\right)\right\}_{d1} + \left\{D\left(R'_{S2}i_{out}^2 + V'_{f2}i_{out}\right) + \left(0.5 v_{in} i_{out} t_{sw2} f_{sw}\right)\right\}_{S2} + P_{ctrl}$ | (3.36) |

Table 3-2 expresses the power losses of each µG's converter, $P_{loss}^{i}$, as a sum of several curly-bracketed terms. Each curly-bracketed term represents the power loss that occurs in one of the circuit elements, namely: inductors (L), transistors (S), diodes (d) and consumption of power supplies ($P_{ctrl}$). Power losses of input/output capacitors have been considered negligible compared to the other terms [184].

The derivation of the voltage across the inductors ($v_L^{on}$ or $v_L^{off}$), which is necessary to compute $\Delta B$ (to calculate the core losses, see (3.6)), is justified next by applying small-signal analysis:

- In the boost converter, the voltage across the inductor during the on time ((3.8) and (3.11)) is the input voltage, $v_{in}$, minus the voltage drop in the parasitic elements of $L$ and $S$ caused by the current $i_L = i_{in}$:

$$v_L^{on} = v_{in} - R_{L1}i_{in} - \left(V'_{f1} + R'_{S1}\right)i_{in}$$

where $V_{f1} = 0$ when the transistor is a MOSFET, and $V_{f1} > 0$ when it is an IGBT (see Table 3-1).

- In the quadratic-boost converter,
  - $L_1$: the input current flows through $L_1$, $d_2$ and $S_1$ during the on time, while the output current is provided by the output capacitor. Thus, the voltage across $L_1$ during the on time is equal to $v_{in}$ minus the voltage drop in the parasitic elements of $L_1$, $d_2$ and $S_1$ caused by the current $i_{L1} = i_{in}$ and the voltage drop in the $S_1$ caused by the current $i_{S1}^{on} = i_{L1} + i_{L2}$, where $i_{L2} = i_{out}/1 - D$. The calculation of $i_{L2}$ is derived from the fact that the average current through $C_2$ is equal to zero:

$$Di_{C2}^{on} + (1-D)i_{C2}^{off} = 0 \Leftrightarrow D(-i_{out}) + (1-D)(i_{L2} - i_{out}) = 0$$
$$\Rightarrow i_{L2} = \frac{i_{out}}{(1-D)}$$

Taking into account that $i_{out}/i_{in} = (1-D)^2$, $i_{S1}^{on}$ results

$$i_{S1}^{on} = i_{in} + (1-D)i_{in} = (2-D)i_{in}$$

Therefore, the voltage across $L_1$ during the on time (3.14) results:

$$v_{L1}^{on} = v_{in} - R_{L1}i_{in} - \left(V_{f2} - R_{d2}i_{in}\right) - R'_{S1}(2-D)i_{in}$$

  - $L_2$: during the on time, the voltage across $L_2$ is equal to $v_{C1} - v_{out}$ minus the voltage drop in the parasitic resistor of $L_2$ caused by the current $i_{L2}$. The calculation of $v_{C1}$ is derived from the fact that the average voltage through $L_2$ is equal to zero:

$$Dv_{L2}^{on} + (1-D)v_{L2}^{off} = 0 \Leftrightarrow Dv_{C1} + (1-D)(v_{C1} - v_{out}) = 0$$
$$\Rightarrow v_{C1} = \frac{v_{out}}{1-D}$$

With this, the voltage across $L_2$ during the on time (3.15) results:

$$v_{L2}^{on} = \frac{Dv_{out}}{1-D} - R_{L2}\frac{i_{out}}{1-D}$$

- In the quadratic-buck converter,
  - $L_1$: during the on time, the voltage across $L_1$ is $v_{in} - v_{C1}$ minus the voltage drop in the parasitic elements of $L_1$ caused by the current $i_{L1}$ and the voltage drop in $d_2$ caused by the current $i_{C1}^{on}$. The calculation of $v_{C1}$ is derived from the fact that the average voltage through $L_1$ is equal to zero:

$$Dv_{L1}^{on} + (1-D)v_{L1}^{off} = 0 \Leftrightarrow D(v_{in} - v_{C1}) + (1-D)(-v_{C1}) = 0$$
$$\Rightarrow v_{C1} = Dv_{in}$$

The calculation of $i_{L1}$ is derived from the fact that the average current through $C_1$ is equal to zero:

$$Di_{C1}^{on} + (1-D)i_{C1}^{off} = 0 \Leftrightarrow D(i_{L2} - i_{L1}) + (1-D)(-i_{L1}) = 0$$
$$\Rightarrow D(i_{out} - i_{L1}) - (1-D)i_{L1} = 0 \Rightarrow i_{L1} = Di_{out}$$

where the average current $i_{L2}$ has been recognized to be equal to $i_{out}$. With this, the voltage across $L_1$ during the on time ((3.18) and (3.22)) results:

$$v_{L1}^{on} = (1-D)v_{in} - R_{L1}Di_{out} + \left(V_{f2} + R_{d2}(1-D)i_{out}\right)$$

- $L_2$: in this case, it is easier to consider the voltage across the inductor during the off time (instead of the on time), since it is simply $v_{out}$ minus the voltage drop in the parasitic elements of $L_2$ and $d_3$ caused by the current $i_{L2} = i_{out}$ ((3.19) and (3.23)). Thus:

$$v_{L2}^{off} = v_{out} - R_{L2}i_{out} - \left(V_{f3} + R_{d3}i_{out}\right)$$

- In the bidirectional converter, the boost mode is analogous to the boost converter analyzed above. Thus, during the on time of $S_1$ ((3.26) and (3.32)):

$$v_L^{on} = v_{in} - R_{L1}i_{in} - \left(V'_{f1} + R'_{S1}\right)i_{in}$$

In the buck mode, the voltage across $L$ during the on time of $S_2$ is $v_{in} - v_{out}$ minus the voltage drop in the parasitic elements of $S_2$ and $L$ caused by the current $i_L = i_{out}$ ((3.29) and (3.35)):

$$v_L^{on} = v_{in} - v_{out} - \left(V'_{f2} + R'_{S2}i_{out}\right) - R_L i_{out}$$

## 3.2. Optimization strategies

Microgrid (μG) operation controlled by E-BCS is taken as the reference to assess performance of the two proposed efficiency optimization strategies: Bus Voltage Optimization Control (BVOC) and Online Optimization of Switching Frequency (OOSF). In principle, the power that each source/load/bidirectional converter must deliver is determined by E-BCS. But when BVOC is implemented, it controls the BESS converter, substituting E-BCS (only) in this unit. The rest of the converters maintain their VEC and SOCEC control laws, except for the VEC control laws of FC and EZ, which only apply in specific situations, as explained below. Under BVOC, BESS' power is calculated as the power needed for $v_{bus}$ to reach its optimum value. OOSF, in turn, does not affect the power reference of the μG's converters –OOSF locally optimizes the switching frequency of each converter, while their power references remain unaltered. In summary, power references in all the μG converters are imposed by E-BCS, except when BVOC is implemented, in which case, it modifies the BESS converter power reference.

Power of the μG's sources, loads and bidirectional units continuously varies so maximizing the converter's energy efficiency at a single operation point (their rated power, for instance) is not an adequate approach in μG applications. Optimization considering all

possible power sharing arrangements (i.e., all the possible operation points of the converters) is conducted next.

### 3.2.1. Bus Voltage Optimization Control (BVOC)

Bus Voltage Optimization Control (BVOC) adaptively improves the global efficiency of the set of μG's converters, for all possible power flows. This control strategy makes use of the distinctive characteristic of the μG studied of having a varying DC bus voltage. BVOC substitutes BESS' Voltage Event Control (VEC) control law to control BESS' power, while the converters of the PV, WT, LOAD and INV maintain their Events-Based Control System (E-BCS) control laws. The converters of FC and EZ maintain their State-of-Charge Event Control (SOCEC) control laws, but their VEC control laws only apply in case of BVOC controller failure, energy shortage or energy excess.

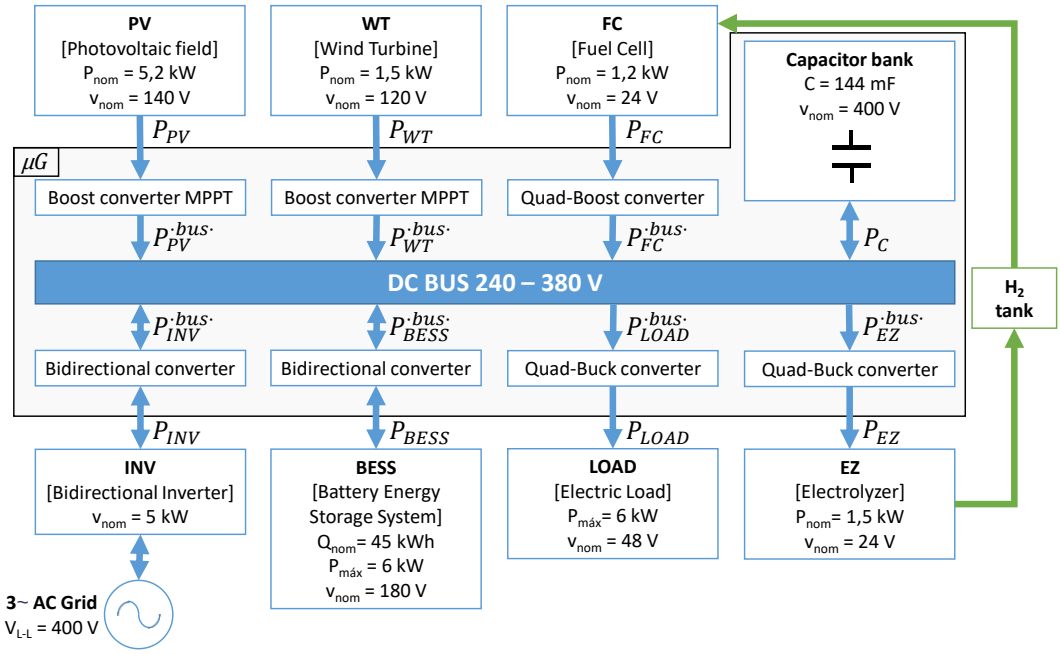


Figure 3-6. Possible power flows in the μG. The shadowed box in the background defines the system $\mu G$.

Bus Voltage Optimization Control is a type of tertiary control applied to the BESS in which the bus-voltage reference is variable (instead of constant) to continually keep $v_{bus}$ at its optimum value in every moment. The optimum bus voltage, $v_{optim}$, is defined in this work as the value of $v_{bus}$ within the interval inside which both loads and energy sources remain

unconstrained, $[250, 370]\,V$, that minimizes the sum of the converters' losses, $P_{loss}^{\boxed{\mu G}}$, given the instantaneous combination of power flows among the μG's units. The system $\boxed{\mu G}$ (shadowed box in Figure 3-6) is defined as that composed of all the μG's DC-DC converters, the DC bus and the capacitor bank.

A centralized Energy Management System (EMS) evaluates the $v_{bus}$–dependent deterministic model of $P_{loss}^{\boxed{\mu G}}$ explained below to find $v_{optim}$ every 100 ms. From this reference voltage, a PI controller determines the power that BESS must perform to make $v_{bus}$ catch up with $v_{optim}$. Note that BVOC only controls BESS' power, while the remaining converters maintain their respective power references determined by E-BCS.

The EMS gathers sensor readings of switching frequencies, and input and output voltages and currents from all the converters. With them, the EMS evaluates online the sum of losses of all the μG's converters as a function of $v_{bus}$. The Matlab function *fminbnd* is used to solve the nonlinear optimization problem formulated in (3.37) and (3.38) in discrete time, with a time step of $100\,ms$. The function *fminbnd* is a one-dimensional minimizer that finds a minimum for a problem specified by $\min f(x)$, where $x_1 < x < x_2$. The algorithm is based on golden section search and parabolic interpolation.

The function *fminbnd* returns the value of the variable $v_{bus}$ that is a minimizer of the sum of the converters' losses, $P_{loss}^{\boxed{\mu G}}$. Variables have been highlighted in blue in the equations to help visualizing the dependencies in the optimization problem:

$$v_{optim}[k+1] = \min_{250\,V \le v_{bus} \le 370\,V} \left[ \tilde{P}_{loss}^{\boxed{\mu G}}(v_{bus}) \Big|_k \right] \tag{3.37}$$

$$\begin{aligned} \tilde{P}_{loss}^{\boxed{\mu G}}(v_{bus}) \Big|_k = {} & \tilde{P}_{loss}^{PV}(v_{bus}) \Big|_k + \tilde{P}_{loss}^{WT}(v_{bus}) \Big|_k + \tilde{P}_{loss}^{FC}(v_{bus}) \Big|_k + \\ & \tilde{P}_{loss}^{LOAD}(v_{bus}) \Big|_k + \tilde{P}_{loss}^{EZ}(v_{bus}) \Big|_k + \tilde{P}_{loss}^{BESS}(v_{bus}) \Big|_k + \tilde{P}_{loss}^{INV}(v_{bus}) \Big|_k, \end{aligned} \tag{3.38}$$

where the accent ~ indicates approximated value, $\tilde{P}_{loss}^{\boxed{\mu G}}(v_{bus}) \Big|_k$ is the (accurately) approximated expression of $P_{loss}^{\boxed{\mu G}}$, calculated as the sum of the approximated $v_{bus}$–dependent expressions of power losses of the converters of all the μG's units $i = \{PV, WT, FC, LOAD, EZ, BESS, INV\}$, $\tilde{P}_{loss}^{i}$, at instant $k$, given their instantaneous switching frequencies, $f_{sw}^{i}[k]$, powers, $P_i[k]$, and voltages, $v^i[k]$ –this is the voltage of the converter's side different from the μG's DC bus in each unit (be it the input or the output). Note that the

functions $\tilde{P}_{loss}^{\boxed{\mu G}}$ and $\tilde{P}_{loss}^{i}$ are in general dependent on $v_{bus}, f_{sw}^{i}, P^{i}$ and $v^{i}$. That is, $\tilde{P}_{loss}^{\mu G}(v_{bus}, f_{sw}^{i}, P^{i}, v^{i})$ and $\tilde{P}_{loss}^{i}(v_{bus}, f_{sw}^{i}, P^{i}, v^{i})$. The notation "$\tilde{P}(v_{bus})\,|_{k}$" indicates here that function $\tilde{P}$ is evaluated at instant $k$, considering dependency on only one variable, $v_{bus}$, and considering the remaining variables ($f_{sw}^{i}, P^{i}$ and $v^{i}$) as constants equal to their instantaneous values within the time step $k$. Thus, $\tilde{P}_{loss}^{\boxed{\mu G}}(v_{bus})\,|_{k} = \tilde{P}_{loss}^{\boxed{\mu G}}(v_{bus}, f_{sw}^{i}[k], P^{i}[k], v^{i}[k])$ and $\tilde{P}_{loss}^{i}(v_{bus})\,|_{k} = \tilde{P}_{loss}^{i}(v_{bus}, f_{sw}^{i}[k], P^{i}[k], v^{i}[k])$. Equations (3.1)–(3.36) are used to solve the BVOC optimization problem stated in (3.37).

In order to clarify how the EMS calculates $v_{optim}$, the first addend of (3.38) is examined. That is, the equations that define the (approximated) power loss of the PV's converter as a function of the bus voltage, $\tilde{P}_{loss}^{PV}(V_{bus})\,|_{k}$. This is calculated every time step $k$ by evaluating (3.39)–(3.42) considering constant values (within the time step) of $f_{sw}^{PV}[k], P^{PV}[k]$ and $v_{in}^{PV}[k]$ and all possible values of bus voltage within the range $[250, 370]\ V$.:

$$\widetilde{\eta_{pc}}^{PV}[k] \simeq \frac{v_{out}^{PV}[k] i_{out}^{PV}[k]}{v_{in}^{PV}[k] i_{in}^{PV}[k]} \tag{3.39}$$

$$\tilde{D}^{PV}(v_{bus})\,|_{k} \simeq \frac{v_{bus} - v_{in}^{PV}[k]\widetilde{\eta_{pc}}^{PV}[k]}{v_{bus}} \tag{3.40}$$

$$\Delta\tilde{B}^{PV}(v_{bus})\,|_{k} = \frac{v_{in}^{PV}[k]\,\tilde{D}^{PV}(v_{bus})\,|_{k}}{N A_C f_{sw}} \tag{3.41}$$

$$\begin{aligned}\tilde{P}_{loss}^{PV}(v_{bus})\,|_{k} \simeq \Bigg\{ & R_L^{PV} {i_{in}^{PV}}^2[k] \\ & + K(f_{sw}^{PV}[k]) \left( \frac{\Delta\tilde{B}^{PV}(v_{bus})\,|_{k}}{2} \right)^{\beta} (f_{sw}^{PV}[k])^{\alpha(f_{sw}^{PV}[k])} \Bigg\}_{inductor} \\ & + \left\{ \left(1 - \tilde{D}^{PV}(v_{bus})\,|_{k}\right) \left( V_f^{PV} i_{in}^{PV}[k] + R_d^{PV} {i_{in}^{PV}}^2[k] \right) \right\}_{diode} \\ & + \Big\{ \tilde{D}^{PV}(v_{bus})\,|_{k} \left( {V_f^{PV}}' i_{in}^{PV}[k] + {R_S^{PV}}' {i_{in}^{PV}}^2[k] \right) \\ & + \left(0.5 v_{bus} i_{in}^{PV}[k] t_{sw}^{PV} f_{sw}^{PV}[k]\right) \Big\}_{IGBT} + P_{ctrl}\end{aligned} \tag{3.42}$$

It is convenient to comment some aspects of the equations defining $\tilde{P}_{loss}^{PV}(V_{bus})\,|_{k}$:

- In the PV's converter, it is always satisfied that $v_{out}^{PV}[k] \equiv v_{bus}[k]$.
- Dependence on $v_{bus}$ appears in the functions $P_{loss}^{PV}$, $\eta_{pc}^{PV}$, $D^{PV}$, and $\Delta B^{PV}$.
- However, the converter's efficiency, $\eta_{pc}^{PV}$, is not considered to be dependent on $v_{bus}$ within each time step but equal to the result obtained from (3.39) with $v_{out}^{PV}[k]$ being the measured value $v_{bus}[k]$. This approximated value is denominated $\widetilde{\eta_{pc}}^{PV}[k]$ (instead of $\eta_{pc}^{PV}(v_{bus})\big|_k = \left(P_{PV}[k] - P_{loss}^{PV}(v_{bus})\big|_k\right)/P_{PV}[k]$) to evidence this approximation.
- This simplifies the subsequent calculations of (3.40), (3.42) and, consequently, (3.38). Indeed, it provides and approximate value $\widetilde{\eta_{pc}}^{PV}[k]$ which is introduced in (3.40) to calculate an approximate value of $D^{PV}(v_{bus})\big|_k = \left(v_{bus} - v_{in}^{PV}[k]\eta_{pc}^{PV}(v_{bus})\big|_k\right)/v_{bus}$ for any possible value of $v_{bus}$, denominated $\tilde{D}^{PV}(v_{bus})\big|_k$. This is, in turn, used to approximate $\Delta\tilde{B}^{PV}(v_{bus})\big|_k$. All these approximations are very accurate and, consequently, they produce a good approximation of the converter's power losses, $\tilde{P}_{loss}^{PV}(v_{bus})\big|_k$.
- The approximated $\widetilde{\eta_{pc}}^{PV}$, $\tilde{D}^{PV}$, $\Delta\tilde{B}^{PV}$ and $\tilde{P}_{loss}^{PV}$ tend to converge to their actual values as the bus voltage approaches $v_{optim}$.

Equation (3.42) is only one of the seven addends in (3.38). The comprehensive expression that estimates all the converters' losses as a function of $v_{bus}$ is certainly long and intricate. Note that solving it considering the exact values of $\eta_{pc}^{i}$, $D^{i}$ and $\Delta B^{i}$ would require complex iterative calculations. The remaining $\tilde{P}_{loss}^{i}(v_{bus})\big|_k$ expressions in (3.38) are analogous ((3.10)–(3.36), substituting the variables $f_{sw}^{i}, P^{i}$ and $v^{i}$ with their values particularized at $k$: $f_{sw}^{i}[k], P^{i}[k]$ and $v^{i}[k]$). They must be added up to $\tilde{P}_{loss}^{PV}(v_{bus})_k$ to obtain $\tilde{P}_{loss}^{\boxed{\mu G}}(v_{bus})\big|_k$, in order to calculate the total power losses as a function of $v_{bus}$ and determine the value $v_{optim}[k]$ that minimizes it.

BVOC achieves two main goals: first, it forces BESS to balance the power of sources, loads and inverter and, second, it controls the bus voltage. Bus voltage dynamics are mainly governed by the capacitors bank, which is the only unregulated μG's unit directly connected to the DC bus. Thus, BVOC controls the bus voltage by injecting / consuming small extra power with respect to the power value that would achieve exact power balance at every moment. This small extra power is consumed (withdrawn) by (from) the capacitor bank, what causes the bus voltage to rise (decrease). Equations (3.43) and (3.44) help to clarify how both BVOC goals are achieved:

$$P_{BESS}^{\cdot bus\cdot}[k] + P_C[k] = -\sum_j P_j^{\cdot bus\cdot}[k], \tag{3.43}$$

$$v_{bus}[k] = v_{bus}[k-1] - \frac{1}{C} i_C[k]\Delta t \simeq v_{bus}[k-1] - \frac{1}{C}\frac{P_C[k]}{v_{bus}[k-1]}\Delta t \tag{3.44}$$

where $P_{BESS}^{\cdot bus\cdot}$ is the BESS power at the bus side of the converter, $P_C$ is the capacitor bank's power, $\sum_j P_j^{\cdot bus\cdot}$ is the resultant power of the remaining μG's units $j = \{\text{PV}, \text{WT}, \text{FC}, \text{LOAD}, \text{EZ}, \text{INV}\}$ at the DC bus side of the converters, and $C$ is the capacity of the capacitor bank. Recall that positive sign is assigned to power flows injected into the DC bus, and negative sign is assigned to power coming out from it.

Explanation of different aspects of BVOC is provided next:

- Power balance.

  Equation (3.43) shows that the sum of powers of BESS and capacitor bank coming into the DC bus always equals the sum of powers of the remaining μG's units coming out from the DC bus. If net power from sources, loads and inverter is positive (power injected into the DC bus), then $P_{BESS}^{\cdot bus\cdot} + P_C$ must be negative and, thus, behave as a load (withdrawing power from the DC bus) to balance the system, and vice versa. BVOC keeps $P_{BESS}^{\cdot bus\cdot}$ very close (or equal) to $\left(-\sum_j P_j^{\cdot bus\cdot}\right)$ at all times. Therefore $P_C$ is forced to be very low (few or zero watts).

- Control of bus voltage.

  Bus voltage is governed according to (3.44):

  - When $v_{bus}[k]$ is (already) equal to $v_{optim}[k]$, $P_{BESS}^{\cdot bus\cdot}[k]$ is, consequently, exactly equal to $(-\sum_j P_j^{\cdot bus\cdot}[k])$, so $P_C[k] = 0$ to maintain that voltage level constant.

  - Otherwise, $P_{BESS}$ will differ from $(-\sum_j P_j^{\cdot bus\cdot})$ in a very small power, $-P_C$. This extra power from the BESS is determined by a PI controller to make $v_{bus}$ catch up with $v_{optim}$. The extra BESS' power is absorbed by the capacitor bank, which regulates bus voltage. Following the abovementioned sign criterion, negative $P_C$ takes power from the DC bus to charge the capacitor bank (thus increasing bus voltage), and positive $P_C$ discharges the capacitor bank (thus reducing voltage) injecting power into the DC bus. $P_C$ must be kept small to avoid too rapid $v_{bus}$ changes that could otherwise cause oscillating behavior.

- Operation in extreme scenarios.

  There are three abnormal operation conditions in which VEC (instead of BVOC) is in charge of achieving power balance:

  - BESS or BVOC controller failure.
  - Energy shortage ⇔ high LOAD + low RES + fully discharged battery + failure in bidirectional inverter (islanded mode).
  - Energy excess ⇔ low LOAD + high RES + fully charged battery + failure in bidirectional inverter (islanded mode).

  In these three cases (and only in these three cases), VEC will trigger FC and EZ. Microgrid (μG) operation in such cases is as follows. When bus voltage descends below $260\,V$ (ascends over $360\,V$), E-BCS activates FC (EZ), providing (consuming) power excess. If this is not enough to keep bus voltage within the interval $[250, 370]\,V$, then VEC performs load shedding or generation shedding, accomplishing power balance and restricting bus voltage within the slightly wider voltage range $[240, 380]\,V$.

### 3.2.2. Online Optimization of Switching Frequency (OOSF)

Online Optimization of Switching Frequencies (OOSF) of the power converters is an alternative or complementary approach to improve converter's efficiency. Application of this optimization concept to specific converters types has been studied in the literature, for instance, buck converters in [19], [35]. In this work, application of OOSF to all the μG's converters is studied to evaluate its overall performance.

When OOSF is run, the μG's converters are allowed to vary their switching frequencies within predefined intervals: $3\,kHz \leq f_{sw} \leq 10\,kHz$ for converter with IGBTs and $20\,kHz \leq f_{sw} \leq 100\,kHz$ for converters with MOSFETs. These values have been chosen accordingly to the inductance of the power converters' inductors (lower minimum switching frequencies would entail oversizing the inductors of the power converters to keep current ripple low), and to avoid excessive switching losses (that would be caused by higher maximum switching frequencies).

Optimum switching frequency of converter $i$, $f_{optim}^{i}$, is calculated every $100\,ms$ as the value of $f_{sw}$ that minimizes its individual (approximated) power loss expression, $\tilde{P}_{loss}^{i}$, given the measured power of the converter $i$, $P^{i}$, and the unit's voltage other than the bus voltage, $v^{i}$. In this case, variables have been highlighted in green in the equations to help visualizing the dependencies in the optimization problem:

$$f_{optim}^{i}[k+1] = \min_{f_{min} \le f_{sw}^{i} \le f_{max}} \left[\tilde{P}_{loss}^{i}\left(f_{sw}^{i}\right)\big|_{k}\right], \quad \text{with } \begin{cases} \text{MOSFETs: } f_{min} = 20\text{kHz}, f_{max} = 100\text{kHz} \\ \text{IGBTs: } f_{min} = 3\text{kHz}, f_{max} = 10\text{kHz} \end{cases} \tag{3.45}$$

note that, here, $\tilde{P}_{loss}^{i}$ is dependent on $f_{sw}^{i}$, and that (unlike in BVOC) bus voltage now is not a calculation variable but a measured value: $\tilde{P}_{loss}^{i}\left(f_{sw}^{i}\right)\big|_{k} \equiv \tilde{P}_{loss}^{i}\left(v_{bus}[k], f_{sw}^{i}, P^{i}[k], v^{i}[k]\right)$.

OOSF of each µG's converter is independent. Optimization Matlab function *fminbnd* is used again to find $f_{optim}^{i}$ values. As an example, statement of the optimization problem of the switching frequency of one of the µG's converters is presented next. PV's converter has been selected again to exemplify the optimization method: $f_{optim}^{PV}$ is calculated by minimizing the power loss expression in (3.48), with $\widetilde{\eta_{pc}}^{PV}[k]$, $\Delta\tilde{B}^{PV}\left(f_{sw}^{PV}\right)\big|_{k}$ and $\tilde{D}^{PV}\left(f_{sw}\right)\big|_{k}$ calculated as in (3.39) and (3.46).

$$\tilde{D}^{PV}\left(f_{sw}^{PV}\right)\big|_{k} \simeq \frac{v_{out}^{PV}[k] - v_{in}^{PV}[k]\widetilde{\eta_{pc}}^{PV}[k]}{v_{out}^{PV}[k]} \tag{3.46}$$

$$\Delta\tilde{B}^{PV}\left(f_{sw}^{PV}\right)\big|_{k} \simeq \frac{v_{in}^{PV}[k]\,\tilde{D}^{PV}\left(f_{sw}^{PV}\right)\big|_{k}}{NA_{C}f_{sw}} \tag{3.47}$$

$$\begin{aligned} \tilde{P}_{loss}^{PV}\left(f_{sw}^{PV}\right)\big|_{k} \simeq & \left\{ R_{L}^{PV} {i_{in}^{PV}}^{2}[k] + K\left(f_{sw}^{PV}\right)\left(\frac{\Delta\tilde{B}^{PV}\left(f_{sw}^{PV}\right)\big|_{k}}{2}\right)^{\beta} {f_{sw}^{PV}}^{\alpha\left(f_{sw}^{PV}\right)} \right\}_{inductor} \\ & + \left\{ \left(1 - \tilde{D}^{PV}\left(f_{sw}^{PV}\right)\big|_{k}\right)\left(V_{f}^{PV} i_{in}^{PV}[k] + R_{d}^{PV} {i_{in}^{PV}}^{2}[k]\right) \right\}_{diode} \\ & + \left\{ \tilde{D}^{PV}\left(f_{sw}^{PV}\right)\big|_{k}\left(V_{f}^{PV\prime} i_{in}^{PV}[k] + R_{S}^{PV\prime} {i_{in}^{PV}}^{2}[k]\right) \right. \\ & \left. + \left(0.5 v_{bus}[k] i_{in}^{PV}[k] t_{sw}^{PV} f_{sw}^{PV}\right) \right\}_{IGBT} + P_{ctrl} \end{aligned} \tag{3.48}$$

note that all $\tilde{P}_{loss}^{i}\left(f_{sw}^{i}\right)\big|_{k}$ are dependent on $f_{sw}^{i}$, while $\tilde{D}^{i}\left(f_{sw}^{i}\right)\big|_{k}$ and $\Delta\tilde{B}^{i}\left(f_{sw}^{i}\right)\big|_{k}$ are not actually functions of $f_{sw}^{i}$ but constants within each time step. The notation "$g\left(f_{sw}^{i}\right)\big|_{k}$" indicates now that function $g$ is evaluated at instant $k$, considering dependency only on $f_{sw}^{i}$, and considering the remaining variables ($v_{bus}, P^{i}$ and $v^{i}$) as constants equal to their instantaneous values within time step $k$: $\tilde{P}_{loss}^{i}\left(f_{sw}^{i}\right)\big|_{k} = \tilde{P}_{loss}^{i}\left(v_{bus}[k], f_{sw}^{i}, P^{i}[k], v^{i}[k]\right)$.

Even with $\widetilde{D}^i(f_{sw}^i)\big|_k$ and $\Delta\widetilde{B}^i(f_{sw}^i)\big|_k$ being not dependent on $f_{sw}^i$, this nomenclature is useful to distinguish between: the variables $D^i$ and $\Delta B^i$; the actual value that these variables take at discrete time $k$, $D^i[k]$ and $\Delta B^i[k]$; the $v_{bus}$-dependent functions employed in BVOC optimization calculations at discrete time $k$, $\widetilde{D}^i(v_{bus})\big|_k$ and $\Delta\widetilde{B}^i(v_{bus})\big|_k$; and the (actually not) $f_{sw}^i$-dependent functions employed in OOSF optimization calculations of converter $i$ at discrete time $k$, $\widetilde{D}^i(f_{sw}^i)\big|_k$ and $\Delta\widetilde{B}^i(f_{sw}^i)\big|_k$.

Unlike in BVOC, bus voltage is considered as a constant here (within each time step), equal to its measured value $v_{bus}[k]$, which gets updated every $100\,ms$. Thus, (3.40) and (3.46) are different because, although they both express the same relation between $D, v_{bus}, v_{in}$ and $\eta_{pc}$: bus voltage is a variable ($v_{bus}$) in (3.40), but it is particularized ($v_{bus}[k]$) in (3.46).

### 3.2.1. Optimization procedure

Figure 3-7 represents the control diagram of E-BCS (blue) optimized by simultaneous BVOC (red) and OOSF (green). Note that E-BCS is the base control layer, and thus must be always active, while BVOC and OOSF can be independently activated or deactivated.

The control variables of E-BCS are represented in blue, those of BVOC are represented in red, and those of OOSF are represented in green. Simultaneous operation of the three control strategies is described next. The E-BCS local controller of each converter $j = \{PV, WT, FC, LOAD, EZ, INV\}$ receives the measured value of $v_{bus}[k]$ and $SOC[k]$ and, from them, determines the correspondent power reference $P_j^{ref}[k+1]$ that the converter $j$ must perform, by applying the control laws in Section 2.1.3. Simultaneously, the BVOC centralized controller (i.e., the controller of the BESS' converter) receives measurements of all the μG's relevant variables and, from them, calculates the optimum bus voltage, $v_{optim}[k]$. This voltage reference is the input to a PI regulator that determines and imposes the power reference $P_{BESS}^{ref}[k+1]$. Parallelly, the OOSF local controller of each converter $i = \{j, BESS\}$ receives the measured value of $v_{in}^i[k]$, $v_{out}^i[k]$ (note that one of these two is invariably equal to $v_{bus}[k]$ for all the converters), $i_{in}^i[k]$, $i_{out}^i[k]$, and $f_{sw}^i[k]$ and, from them, calculates and imposes the optimum switching frequency, $f_{sw\ optim}^i[k+1]$. Note that, since BESS and INV are bidirectional, their input and output are not fixed but dependent on the converters operation mode (buck or boost), thus the subscripts $in$ and $out$ have been avoided for these two units. Instead, $i_{BESS}^{bus}$, $i_{INV}^{bus}$ and $v_{bus}$ represent their DC-bus-side currents and voltage, and $i_{BESS}$, $i_{INV(DC)}$, $v_{BESS}$ and $v_{INV(DC)}$ represent their battery-side and inverter-side currents and voltages. The values of $P_i$ and $f_{sw\ optim}^i$ change in $k+1$ towards $P_i^{ref}$ and $f_{sw\ optim}^{i,ref}$.

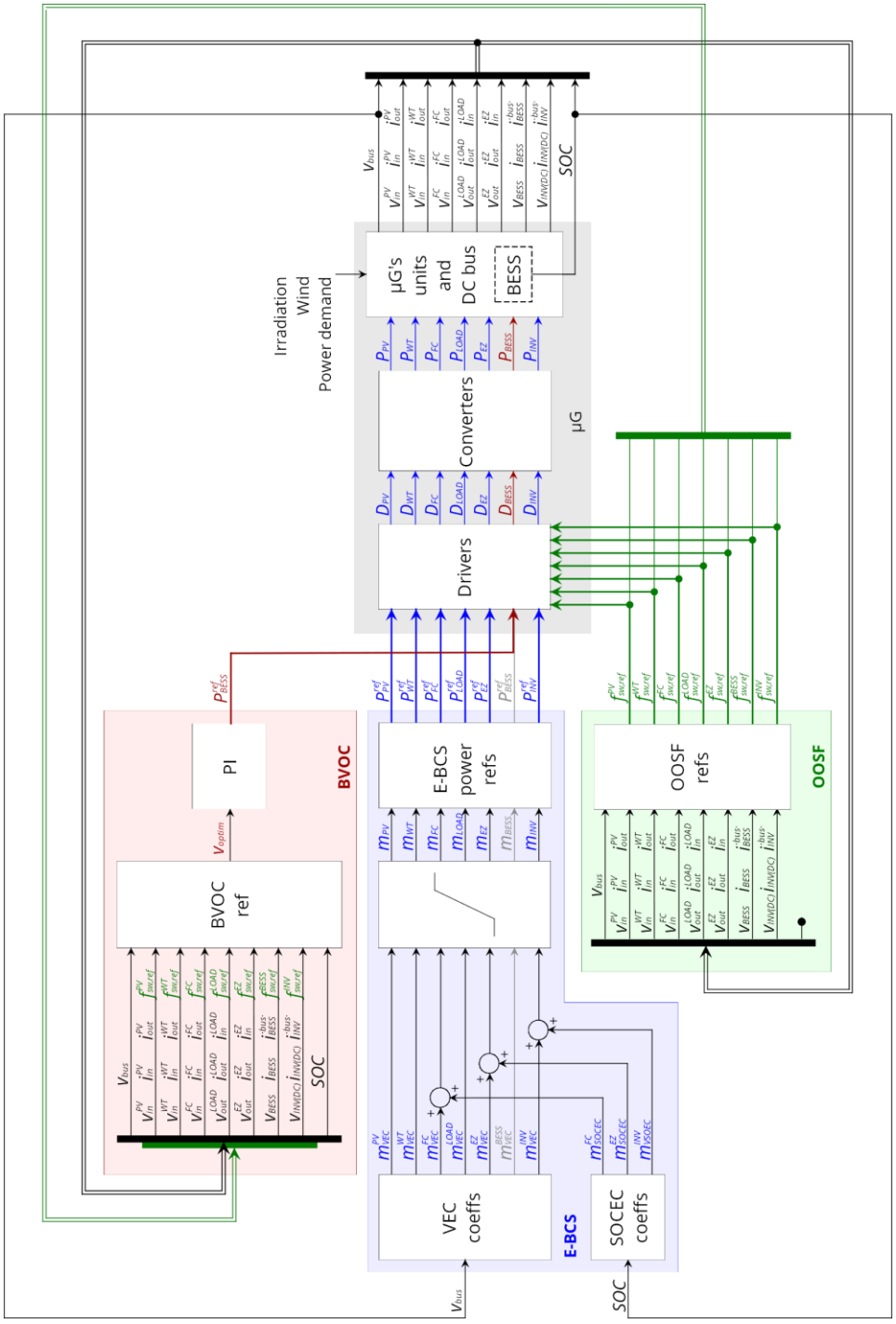


Figure 3-7, Microgrid management flow chart describing the process of simultaneous E-BCS (blue), BVOC (red) and OOSF (green).

The optimization strategies influence the measured values of the converters' currents and voltages, and the battery SOC, which then feed back to the control systems. BVOC and OOSF only interfere with each other in an indirect way (through these feedback signals) to a minor extent.

The greyed out line in Figure 3-7 corresponds to the E-BCS power reference for BESS. BVOC disables that power reference and replaces it with the power reference in red. Similarly, when OOSF is not active, the converters are operated at constant switching frequencies. Only when OOSF is active do the green signals modify the switching frequencies of each μG's converter in real time.

Programming BVOC and OOSF in microcontrollers requires to simplify the complex non-linear optimization problems. An interesting solution is to characterize the converters by testing them in a variety of possible operation points, with diverse input and output currents and voltages, and switching frequencies. The resulting test data would then be used to build lookup tables that would be beneficial for two main reasons. On the one hand, the optimum bus voltage and switching frequencies would be more exact because the models of the converters would be empirical instead of theoretical. On the other hand, the need for computational power would be significantly reduced.

#### 3.2.1.1. Analysis of the energy efficiency of the DC-DC converters

The efficiency curves of the μG's converters predicted by the loss models are analyzed next to anticipate the order of magnitude of the efficiency improvement that the two proposed optimization strategies, BVOC and OOSF, can produce. Figure 3-8 shows the efficiency curves of two representative converters (LOAD's and BESS' converters) operating at a set of different switching frequencies and bus voltage values.

The efficiency curves of the LOAD's and BESS' converters (which are quadratic buck and bidirectional converters, respectively) have been chosen because they serve to illustrate general issues that occur in all the μG's converters, namely:

- First, there is little room for energy-efficiency improvement for both optimization strategies. The efficiency curves reveal small differences within the studied range of possible $v_{bus}$ and $f_{sw}$ values. Efficiency increases are limited to a fraction of a percentage point.
    - The reason for this result might be that the model of the converters' power losses is idealized and the parameters that characterize the parasitic elements are probably too optimistic –although they are actually provided by manufacturers in component datasheets. It is most likely that

experimental testing would reveal higher differences between the curves in the same graph. That is, the impact of modifying the switching frequency and the bus voltage is surely higher in reality than what the models predict.

- Second, the optimum bus voltage is different for individual converters. Thus, a change in $v_{bus}$ leading to catch up with the overall optimum bus voltage, $v_{optim}$, causes some of the µG's converters to operate more efficiently but, also, it causes some other converters to operate less efficiently. The overall effect is that BVOC will achieve limited efficiency improvements for this reason.

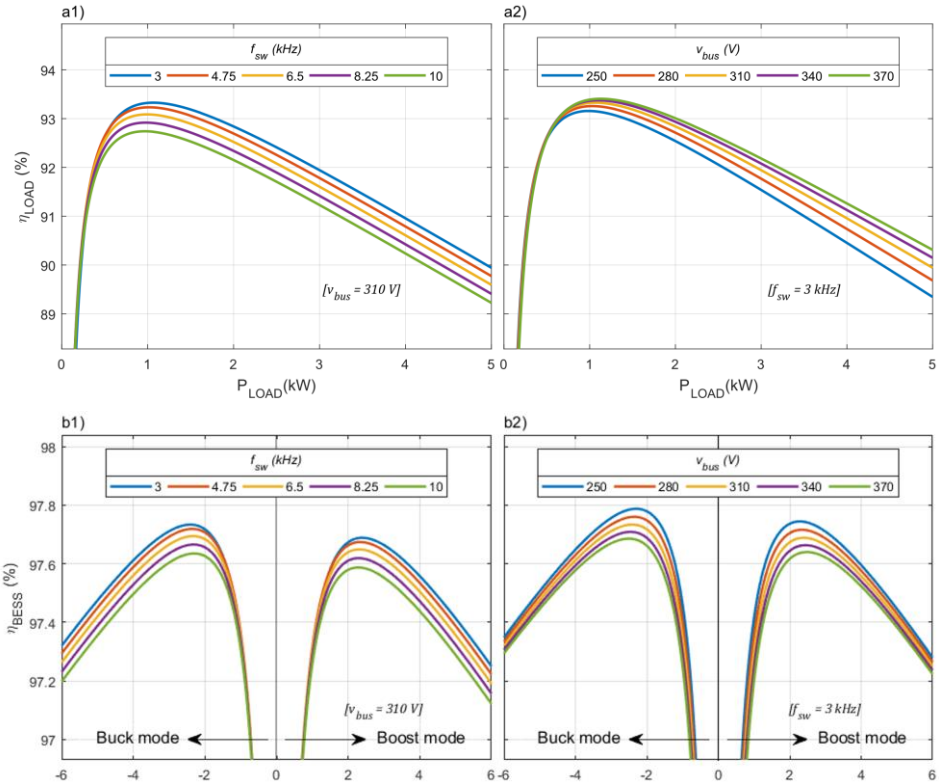


Figure 3-8. Efficiency curves of LOAD's and BESS' converters at different switching frequencies (1) and bus voltages (2): a) LOAD' s quadratic buck converter; b) BESS' bidirectional converter interfacing.

Figure 3-8.a1 shows the efficiency curves of the LOAD's quadratic buck converter at five values of switching frequency linearly distributed within the range $3-10\ kHz$, at constant bus voltage, $v_{bus} = 310\ V$. OOSF applies to each converter individually, so each of the µG's

converters will operate at its optimum switching frequency (the highest curve in the graph). OOSF controls the gate driver of the transistors to impose optimum switching frequency (i.e., $3\ kHz$, blue curve, for most $P_{LOAD}$ values). Efficiency of the LOAD's converter increases steeply from $P_{LOAD} = 0\ kW$ to $1\ kW$ approx. In this first part of the curve, it is possible to obtain significant efficiency improvements in relative terms, but with low impact in absolute terms. In the second part of the curve, from $P_{LOAD} = 1\ kW$ to $5\ kW$ approx., the maximum possible efficiency improvement remains constant with a value of $0.75\%$. Figure 3-8.b1 is essentially the same graph but with the efficiency curves of the BESS' bidirectional DC-DC converter. The left half of the graph ($P_{BESS} < 0\ kW$) represents buck operation mode and the right part represents boost operation mode. The turning points where the slope changes sharply occur at $P_{BESS} = \pm 2\ kW$ approx. The maximum possible efficiency improvement with high $P_{BESS}$ is as low as $0.12\%$ in this case.

Figure 3-8.a2 shows the efficiency curves of the LOAD quadratic buck converter at five bus voltage levels linearly distributed within the range $250 - 370\ V$, considering constant switching frequency $f_{sw}^{LOAD} = 3\ kHz$. BVOC regulates the power performed by BESS in order to achieve the goal of operating the μG at optimum bus voltage. This optimization algorithm is applied globally, so, in general, the global optimum will not coincide with individual optima. In this graph, the efficiency of the LOAD converter increases steeply also from $P_{LOAD} = 0\ kW$ to $1\ kW$ approx. With power greater than $1\ kW$ approx., the maximum possible efficiency improvement in LOAD's converter steadily increases from $0.23\%$ at $1\ kW$ to $0.96\%$ at $5\ kW$. Figure 3-8.b2 is again the same graph but representing the BESS' bidirectional DC-DC converter. The maximum possible efficiency improvement in this converter with high values of $|P_{BESS}|$ is as low as $0.06\%$.

Figure 3-8.a2 and b2 show that, in general, local optima for different μG's units occur at opposed $v_{bus}$ increments: for instance, if $P_{LOAD} > 1\ kW$, raising $v_{bus}$ makes the efficiency of the LOAD's converter increase but, at the same time, it makes the efficiency of the BESS' converter decrease (and vice versa), regardless of the value of $P_{BESS}$. The optimum bus voltage reference, $v_{optim}$, calculated by BVOC is the trade-off that minimizes the sum of power losses in the set of all the μG's DC-DC converters. Hence, in general, not all of them will operate simultaneously at their individual $v_{bus}$ optimum point.

# 3.3. Optimization results.

## 3.3.1. Simulation scenarios

Performance of the proposed optimization strategies is evaluated simulating ten microgrid (μG) operation scenarios, S0 to S9, over a seven-day period. In the first scenario, S0, several μG's units are scheduled to fail with the objective of verifying the robustness of the control system. Simulations S1 to S9, on the contrary, represent different scenarios of regular operation (no failures). In each simulation, different coefficients multiply the base RES generation and the base demand profiles –base profiles are the same in all cases. Table 3-3 summarizes the differences between the simulated scenarios:

Table 3-3. Characteristics of the ten simulation scenarios.

| | Faulty system | No failures | | | | | | | | |
|---|---|---|---|---|---|---|---|---|---|---|
| | | Low power | | | Intermediate power | | | High power | | |
| Energy | S0 | S1 | S2 | S3 | S4 | S5 | S6 | S7 | S8 | S9 |
| $E_{RES\ MPP}[k_{end}]$ (kWh) | 161.2 | 37.7 | | | 113.1 | | | 188.5 | | |
| $\frac{E_{demand}[k_{end}]}{E_{RES\ MPP}[k_{end}]}$ | 1.20 | 0.75 | 1.00 | 1.33 | 0.75 | 1.00 | 1.33 | 0.75 | 1.00 | 1.33 |

S0 represents μG operation with rather high power flows between the μG's units, scheduling failures in RES, BESS and INV. The other nine simulation scenarios differ from each other in the RES available power and in demand data. Base PV and WT generation profiles have been estimated based on meteorological data (solar irradiance, temperature and wind speed) from the Servei Meteorològic de Catalunya (Meteorological Service of Catalonia) [186], and base demand profile corresponds to a residential electricity consumption profile.

## 3.3.2. Microgrid model in Simulink

A simplified model of the μG has been developed in Simulink to evaluate the performance of the proposed control strategies BVOC and OOSF. Figure 3-9 shows the comprehensive (E-BCS+BVOC+OOSF) Simulink model. The model has been divided into six parts that are zoomed in Figure 3-12 to Figure 3-16 and individually analyzed next. But prior to that, some general features of the model should be mentioned:

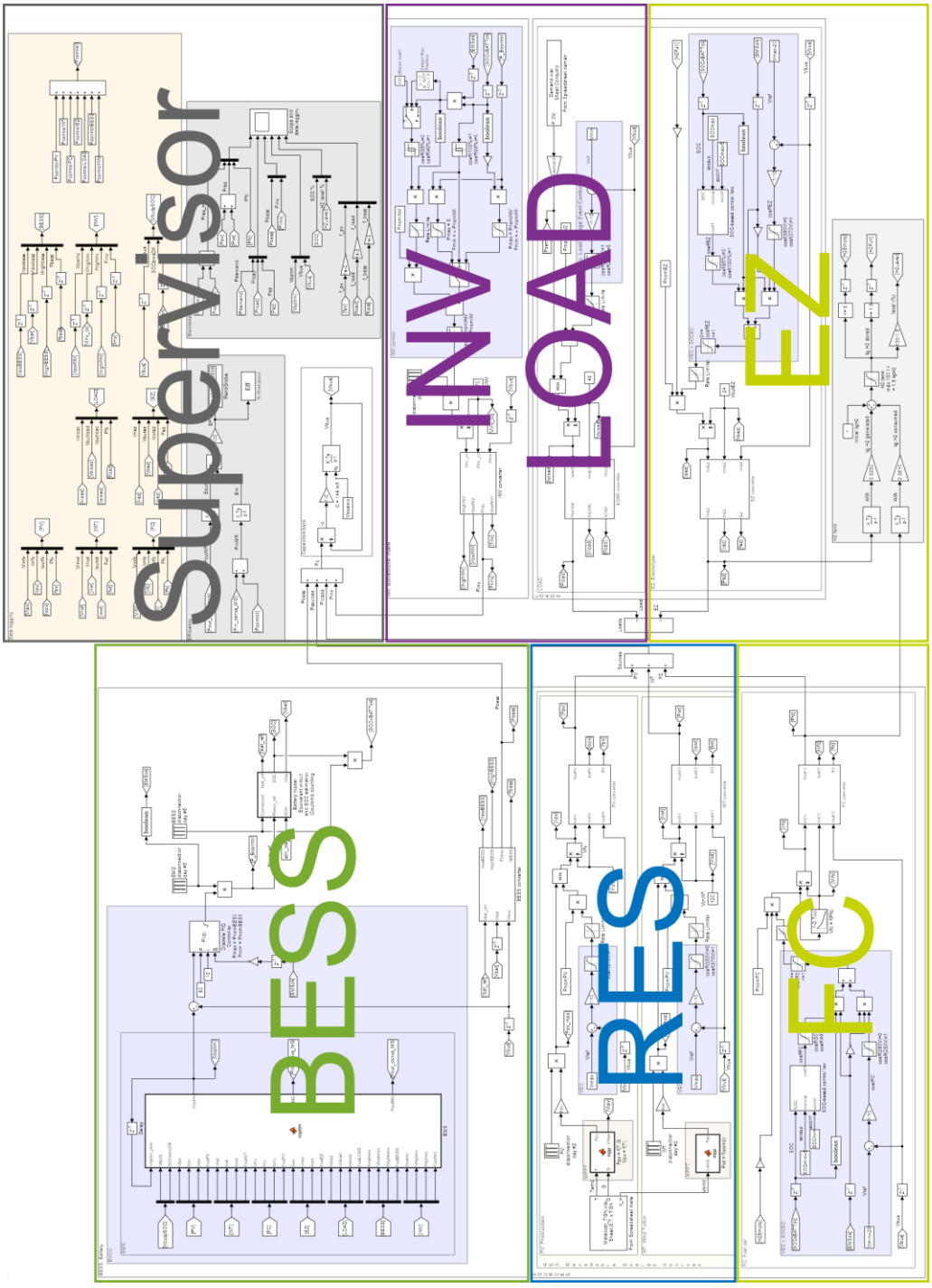


Figure 3-9. General view of the microgrid model in Simulink.

- Events-Based Control System (E-BCS) manages all the μG's units except the BESS, which is controlled applying Bus Voltage Optimization Control (BVOC). In case of BVOC failure, the battery is also self-managed by E-BCS.
- Online Optimization of the Switching Frequency (OOSF) minimizes individual power losses of each μG's converter by adapting its switching frequency to the optimum value. This optimization system is present in all the μG's converters.
- Simulation time step of $\Delta t = 100\,ms$ has been selected, in agreement with the refresh rate of both control schemes BVOC and OOSF. Switching frequency ranges are $20-100\,kHz$ for IGBTs and $3-10\,kHz$ for MOSFETs.

Three additional Simulink models of the microgrid have been built for comparative purposes. There is one model per control strategy: 1. E-BCS only, 2. E-BCS+BVOC+OOSF, 3. E-BCS+BVOC and 4. E-BCS+OOSF

- **Figure 3-12. <u>BESS</u> controlled by BVOC.**

BVOC controls BESS' power, $P_{BESS}$, to make $v_{bus}$ vary towards the instantaneous optimum bus voltage, $v_{optim}$. The optimum bus voltage is calculated as the adaptative value that minimizes power losses in the set of DC-DC converters of the μG. The EMS estimates battery $SOC$ and receives the readings of the input and output currents and voltages from all the converters connected to the DC bus and their switching frequencies. From these data, the EMS runs a $v_{bus}$-dependent open-loop model of the total converters' power losses given the specific power flows, $P_i[k]$, taking place in the moment studied, $k$ (see (3.37)). Iterative calculation leads to finding $v_{optim}[k]$ as the value that minimizes total losses.

The control system BVOC takes $v_{optim}[k]$ as the input to a PI controller that determines the BESS power reference ($-6\,kW \leq P_{BESS}^{ref}[k] \leq 6\,kW$) appropriate to make $v_{bus}$ rapidly approach $v_{optim}$ avoiding excessive voltage oscillations. (Note that Simulink does not allow to utilize superscripts so $P_{BESS}^{ref}$ has been denominated $P_{Bcontrol}$ in the Simulink model.) PI's proportional gain is set in $50$, and integral gain is set in $10$. The PI controller has been tuned experimentally, finding values that achieve fast convergence at the same time that produce limited $v_{bus}$ oscillations. PI's integral error is reset every time the EMS is started from idle. Resetting the integral part avoids accumulation of integral error from previous runs, which allows to correctly restart BVOC in the event of failure or deliberate stop.

The power reference resulting from the PI regulator is imposed to the battery whenever possible –that is, always except when the reference power is negative and the battery is already fully charged, or when the power reference is positive and $SOC \leq SOC_{min}$. The battery is modeled by a Thevenin circuit (Figure 3-10) with a voltage source linearly dependent on $SOC$

between the lower cut-off voltage (for moderate discharge current) and the upper cut-off voltage provided by the manufacturer, and an internal resistance, $R = 15 \cdot 3.5\, m\Omega = 52.5\, m\Omega$ (according to the data sheet of the batteries Lead Crystal $200\, Ah, 12\, V$). This basic model has been selected to elude complicating the model with details out of the scope of the efficiency optimization research. More accurate models are described in Chapter 4 (enhanced equivalent circuit model) and Chapter 5 (simplified physics-based model that accounts for degradation caused by growth of the Solid-Electrolyte Interphase). These more-complex models could easily substitute the Thevenin circuit utilized in the Simulink model of the μG.

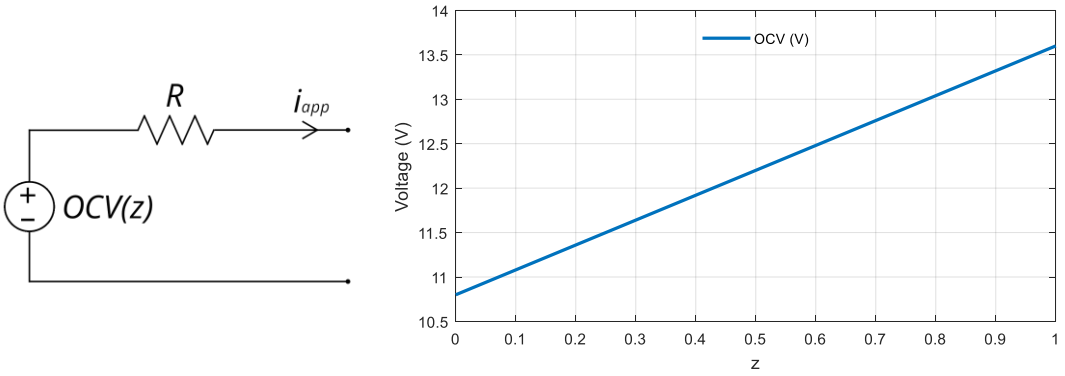


Figure 3-10. Basic battery model employed in the simulation of the microgrid.

The μG's model intentionally schedules disconnection of the battery during the whole fifth day and shutdown of the EMS during the whole sixth day to test the robustness of the system in the face of extreme situations. The logical signal "Battery ok", $BATTok$, is true (one) when BESS work correctly and false (zero) when the battery does not respond, representing failure or disconnection. Therefore, $BATTok$ becomes false during the fifth day. This signal multiplies the SOC estimation in the fused signal $SOC$x$BATTok$, which is transmitted, instead of two separated signals, to FC, EZ and INV to slightly simplify communications between the involved units. Null $SOC$x$BATTok$ deactivates SOCEC control of FC and EZ because $BATTok = 0$ means that the battery is not available and, therefore, it would make no sense to employ FC / EZ power with their intended usages, i.e. to avoid battery overdischarge / overcharge. INV also uses this signal to identify when it must substitute BESS.

Similarly, the signal "EMS ok", $EMSok$, is defined to check when EMS fails to work. This signal is fed to FC, EZ and INV to deactivate their control laws based on $SOC$ in case of EMS failure: if BESS receives no power reference it cannot be charged or discharged.

- **Figure 3-13. Renewable Energy Sources: PV and WT.**

Available power from RES (instantaneous MPP) is modeled by basic models of the generators. RES are controlled by E-BCS based solely on the DC bus voltage value –that is, VEC (see Section 2.1.3.2). VEC limits the power reference imposed to these two units (PV and WT) in case the μG faces generation excess. Otherwise, their controllers maximize energy production thanks to integrated MPPT. Disconnection of both sources is programed the second day as part of the robustness test in scenario S0.

Wind speed data, together with irradiance and temperature data, are read from a pre-stored Excel file that contains actual weather data measured in Tarragona, the location where the GAEI's μG is based in.

- PV

The photovoltaic generator (PV) consists of five paralleled strings of four 260 Wp modules in series each. PV MPP power, $P_{PV\,MPP}$ (in $W$), is modeled as dependent on two variables: irradiance, $G$ (in $W/m^2$), and ambient temperature, $T_{amb}$ (in $K$). The relationship in (3.49) has been obtained by fitting actual MPP generation data from the GAEI's microgrid with irradiation and temperature (R-square $= 0.9996$). PV's input voltage depends linearly on temperature (3.50), as specified by the PV modules manufacturer.

$$P_{PV\,MPP} = G(-0.01903 \cdot T_{amb} + 10.29) \tag{3.49}$$

$$v_{PV\,MPP\,module} = 34.8\left(1 - \frac{0.36}{100}(T_{amb} - 298)\right) \tag{3.50}$$

A gain, $K_{pv}$, has been introduced in the Simulink model to allow to easily shift among the different power profiles of the simulation scenarios.

- WT

The wind turbine (WT) unit models a variable speed generator that performs MPPT. Its voltage is considered to be constant ($120\,V$) in the simplified model, representing a factory-installed front-end rectifier. Wind turbine MPP power, $P_{WT\,MPP}$ (in $W$), is modeled as dependent on only one variable, wind speed, $v_{wind}$ (in $m/s$): $P_{WT\,MPP} = \frac{1}{2} C_p \rho_{air} \pi R_{WT}^2 v_{wind}^3$ (3.51), where $\rho_{air}$ (in $kg/m^3$) is the air density and $R_{WT}$ (in $m$) is the radius of the wind turbine. WT's input voltage is modeled as a constant, $v_{in}^{WT} = 120\,V$.

$$P_{WT\,MPP} = \frac{1}{2} \cdot 0.2442 \cdot 1.225 \cdot \pi \cdot 1.43^2 \cdot v_{wind}^3 \tag{3.51}$$

A gain, $K_{wt}$, has been introduced in the Simulink model to allow to easily shift among the different power profiles of the simulation scenarios.

- **Figure 3-14. Hydrogen storage system: $H_2$ tank, FC and EZ.**

An adapted version of E-BCS regulates the power references of the emergency generator (FC) and the emergency extra load (EZ). E-BCS need to be adapted because FC and EZ should not participate in voltage regulation when BVOC is active. Their VEC laws must be cancelled ($EMSok = 1$ does that), keeping only their SOCEC regulation. Indeed, BVOC optimizes bus voltage within the range $250\,V \leq v_{bus} \leq 370\,V$. Note that this range overlaps the VEC activation regions of FC ($v_{bus} < 260\,V$) and EZ ($v_{bus} > 360\,V$). When BVOC is active, BESS' central controller is in full control of the bus voltage, so $v_{bus}$ being close to these boundaries does not imply the μG experiencing energy shortage / surplus (as was the case with only E-BCS, see Section 2.1.3.2), but just $v_{optim}$ occurring near that boundaries.

Besides, in case of battery or BVOC failure, SOCEC does not make sense, as it is not possible to charge or discharge the battery, so it must be cancelled ($BATTok = 0$ or $EMSok = 0$ do that), activating only VEC during the incidence.

- <u>FC</u>

The power of the fuel cell (FC), $P_{FC}$, is regulated by adapted E-BCS based either on $v_{bus}$ or on $SOC$ –that is, VEC or SOCEC. SOCEC governs $P_{FC}$ under normal operation conditions (EMS operating correctly): FC generation is activated if $SOC$ approaches its lower boundary, providing extra power to the DC bus to help charging the μG's battery. In case of EMS failure, this control scheme is replaced by VEC: then, FC generation is activated if $v_{bus}$ approaches its lower boundary to help avoiding de-energization of the DC bus. Apart from this, $P_{FC}$ is annulled if the $H_2$ storage tank is empty. FC's input voltage, $v_{in}^{FC}$, is a function of $P_{FC}$, modeled by a look-up table according to the datasheet of the fuel cell Ballard Nexa.

- <u>EZ</u>

The power of the electrolyzer (EZ), $P_{EZ}$, is also regulated by adapted E-BCS based either on $v_{bus}$ or on $SOC$ –that is, VEC or SOCEC. SOCEC governs $P_{EZ}$ under normal operation conditions (EMS operating correctly): EZ is activated if $SOC$ approaches its upper boundary, consuming surplus generation to produce hydrogen if that is possible. In case of EMS failure, this control scheme is replaced by VEC: then, EZ consumption is activated if $v_{bus}$ approaches its upper boundary to help avoiding DC-bus over-voltage. Apart from this, $P_{EZ}$ is annulled if

the $H_2$ storage tank is already full. EZ's input voltage is modeled as $v_{out}^{EZ} = 24\,V$, which is a simplification (see the typical voltage curve of an electrolyzer in Figure 3-11).

- Hydrogen storage

Hydrogen is generated by EZ and consumed by FC. It is stored in a metal-hydride tank with a maximum capacity of 1.5 $kg$. This system is used as a secondary energy storage system with a round-efficiency much lower than that of BESS. For this reason, BESS has priority to store energy over the $H_2$ cycle. The $H_2$ tank has sensors to detect when it is full and empty. These sensors produce signals that act to stop $H_2$ generation and consumption, respectively.

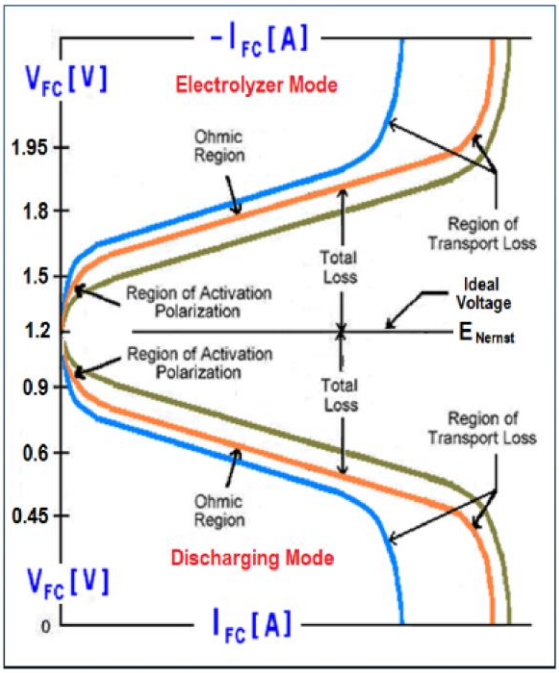


Figure 3-11. Polarization curves and efficiencies of a generic fuel cell (bottom) and an electrolyzer (top) conforming together a regenerative fuel cell.

Note that EZ produces 0.020 $kg$ of $H_2$ per kWh while FC needs 0.061 $kg$ of $H_2$ to generate one kWh. Two conclusions are derived from that. First, FC can produce a maximum of $1.5/0.061 \approx 25\,kWh$ from a full $H_2$ tank. And second, the cycle efficiency of storing energy through hydrogen is only $0.020/0.061 \approx 33\%$. Performance of the fuel cell and the electrolyzer has been considered constant in this study, but in reality is determined by their polarization curves. An example of typical polarization curves is presented in Figure 3-11.

Note that the round-trip efficiency of $H_2$ energy storage results from the product of both the fuel cell and the electrolyzer efficiencies, which tend to decrease as more current is demanded.

- **Figure 3-15. INV and LOAD**
  - INV

The μG control prioritizes cycling the battery over utilizing the bidirectional inverter (INV) to exchange energy with the mains grid during regular operation. However, there are three situations that require the activation of the bidirectional inverter. The first one is in case of BESS failure, while the other two situations correspond to normal operation (EMS functioning and BESS connected) and are based on $SOC$ value, as explained next

- INV is activated in case of BESS failure or disconnection: the EMS calculates the power required to stabilize power flows and to optimize bus voltage, $P_{B_{control}}$; it sends this power reference to both the BESS' and the INV's converters. Under normal operation, BESS is in charge of providing this power but in case BESS fails or is disconnected (BESS provides no current, but the EMS calculates $v_{optim}$ and generates the associated power reference), INV starts assuming this power profile (adequately trimmed to limit maximum power to $\pm 5\ kW$). In this case, the battery cannot be used to store energy, so the grid is used instead as a sort of "infinite capacity energy storage element" in the sense that any amount of surplus energy can be injected into the grid and deferred consumption is always possible.
- When the (faultless) battery is close to full charge state ($SOC \geq 98\%$), INV assumes the BESS' power reference, $P_{Bcontrol}$, to evacuate surplus generation to the mains grid. In this case, INV only performs negative power, saturated to its nominal power: $P_{INV} = \min(0, \max(P_{Bcontrol}, -P_{nom\ INV}))$.
- INV is activated when the μG's battery hits $SOC_{min} = 40\%$. It then executes bulk charge from grid: INV releases full power from the mains grid to the DC bus until $SOC$ above 85% is recovered. A block has been included to reset the coefficient $m_{SOCEC}^{INV}$ when rise of the signal $SOCxBATTok$ from zero to actual $SOC$ or rise of $EMSok$ from zero to one are detected. This avoids INV to immediately start providing full power right after start-up or right after recovering from an EMS failure, in case $40\% \leq SOC < 85\%$ in that moment.

$SOCxBATTok = 0$ or $EMSok = 0$ cancel the last two explained INV triggers –because they are based on the battery SOC, but the battery cannot be (dis)charged while the incidence persists.

In the scenario S0, INV is scheduled to fail the sixth simulated day. Anyway, INV receives no power reference that day because EMS fail is scheduled coincidently, so there is no $P_{Bcontrol}$ available. Thus, the block that disconnects INV the sixth day has no actual effect under control strategies that include BVOC optimization. However, this block has been introduced in all the four Simulink models of the microgrid (there is one per control strategy: 1. E-BCS only, 2. E-BCS+BVOC+OOSF, 3. E-BCS+BVOC and 4. E-BCS+OOSF) to ensure that the simulation scenarios are equivalent, so the efficiency results obtained are comparable.

In case of EMS failure, none of the two bidirectional μG's units (BESS and INV) can generate a power reference. With only the unidirectional units available, distributed autonomous control (based on $v_{bus}$ according to VEC laws) achieves stable operation. In such case, part of the available RES power might be missed, and part of the demand power might not be met.

- LOAD

The demand power profile, $P_{demand}$, is read from a pre-stored Excel file that contains the hourly measured profile of an actual household electric system. A gain block, $K_{demand}$, has been introduced in the Simulink model to scale the demand profile agreeing to the specifications of each of the ten simulation scenarios, S0–S9. Power demand is connected in DC at $v_{out}^{LOAD} = 48\,V$ to the output of the LOAD's converter. This converter is controlled based on $v_{bus}$, according to VEC laws in Section 2.1.3.2. The demand is always supplied unless $v_{bus}$ gets too low in islanded mode due to insufficient energy generation and storage. In that case, VEC limits the power provided to the demand to avoid de-energization of the DC bus.

- **Figure 3-16. Capacitor bank, data logging and supervision.**

The capacitor bank is the only unregulated unit connected to the μG's DC bus. Bus voltage is physically governed mainly by the capacitors' dynamics: $v_{bus}$ solely depends on the power profile experienced by the capacitors, $P_C$. This power $P_C$ is determined by the instantaneous power balance in the microgrid. When BVOC is active, the BESS is controlled to dynamically regulate the bus voltage (to operate the μG at variable optimum bus voltage) by providing / withdrawing the appropriate amount of power to the capacitors –see (3.43), (3.44), and "Control of bus voltage" explanation immediately below.

The Scope block in Simulink model permits to monitor all the relevant variables as the simulation progresses, as well as to log them for ulterior analysis.

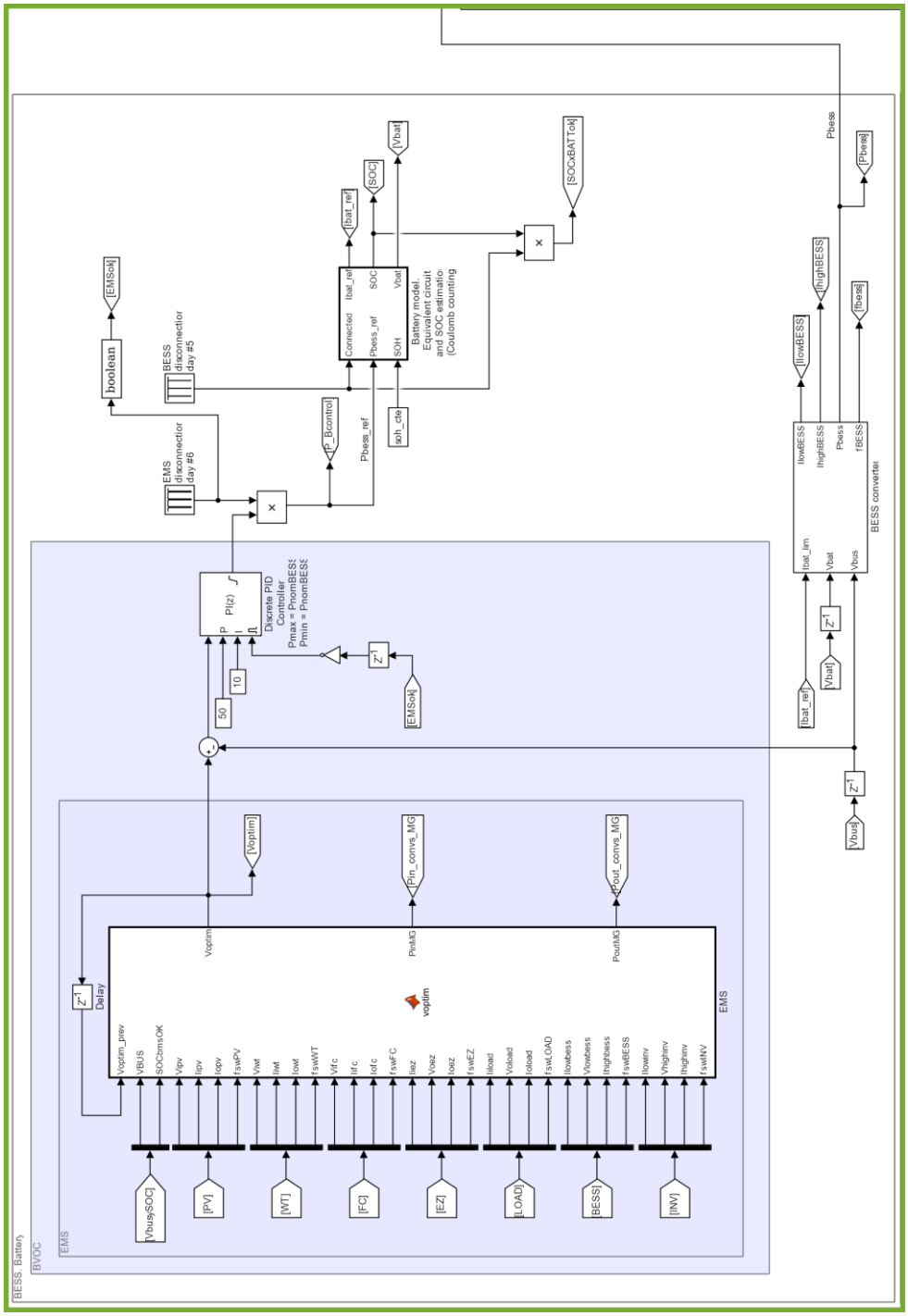


Figure 3-12. Blocks of the µG's Battery Energy Storage System (BESS).

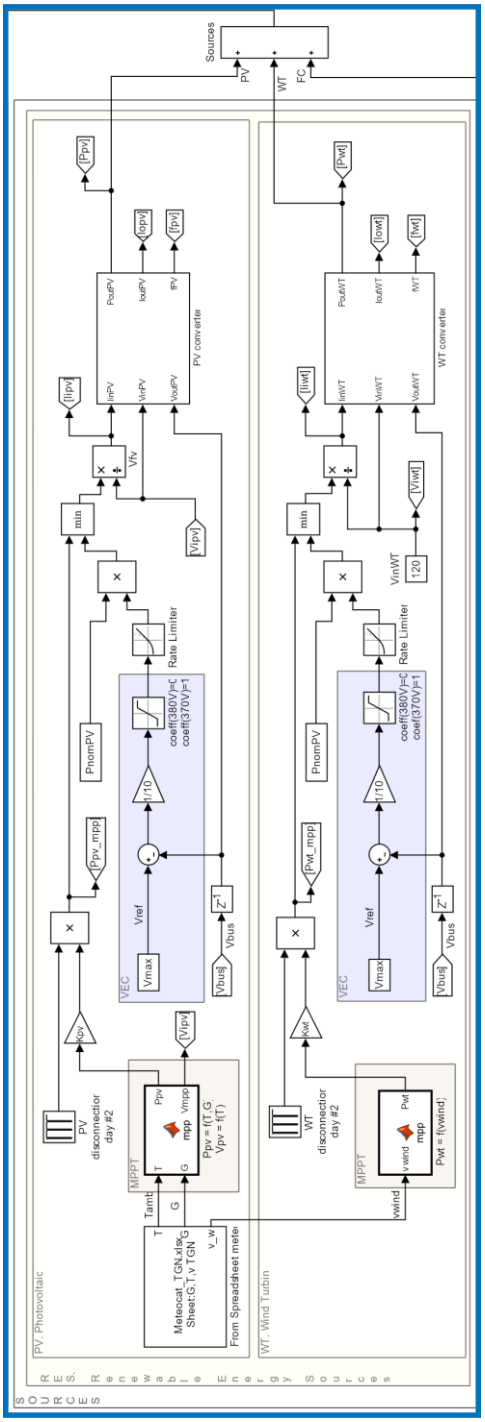


Figure 3-13. Blocks of the µG's renewable energy sources: Phohhtovoltaic (PV) and Wind Turbine (WT).

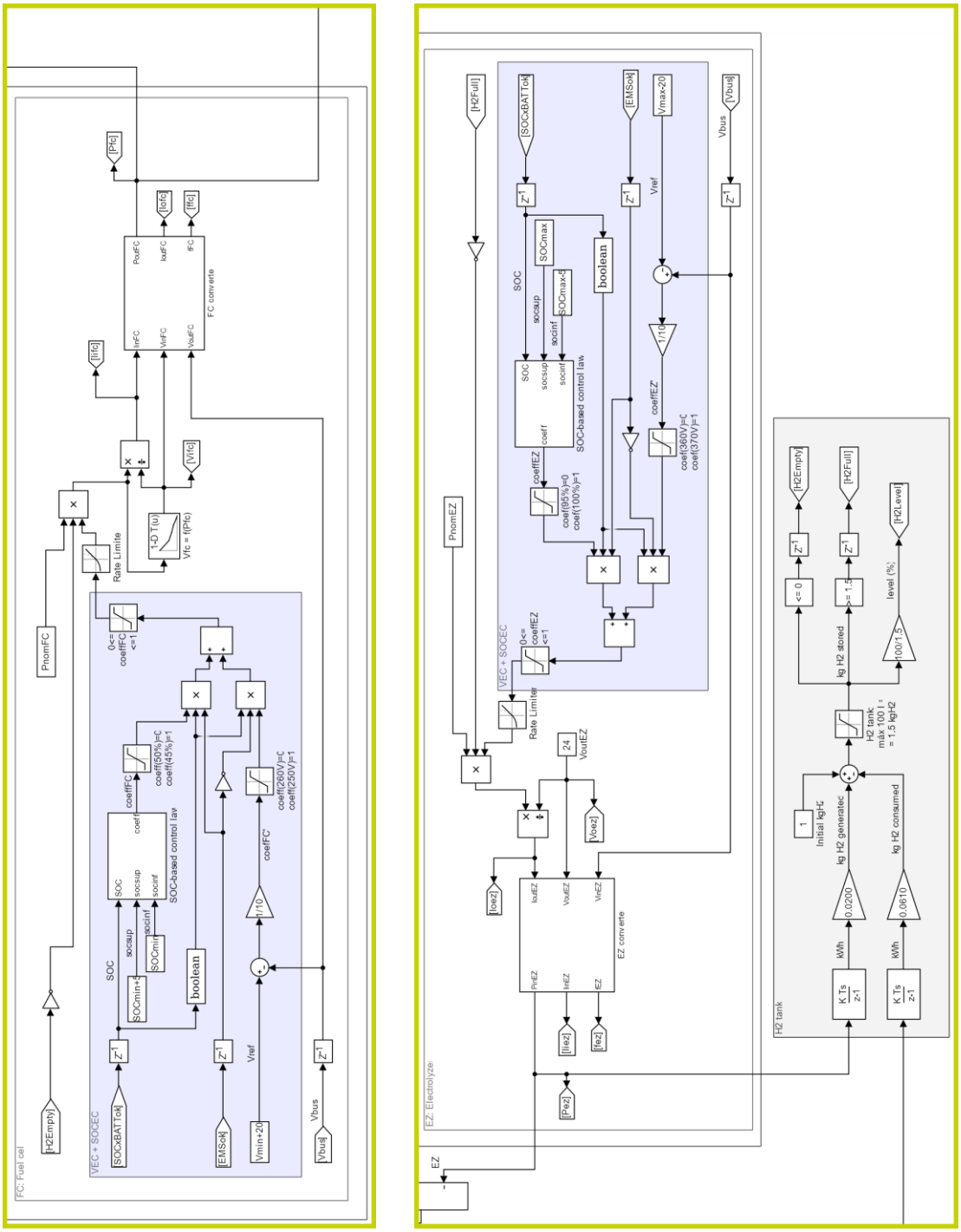


Figure 3-14. Blocks of the μG's Fuel Cell (FC), Electrolyzer (EZ) and $H_2$ tank.

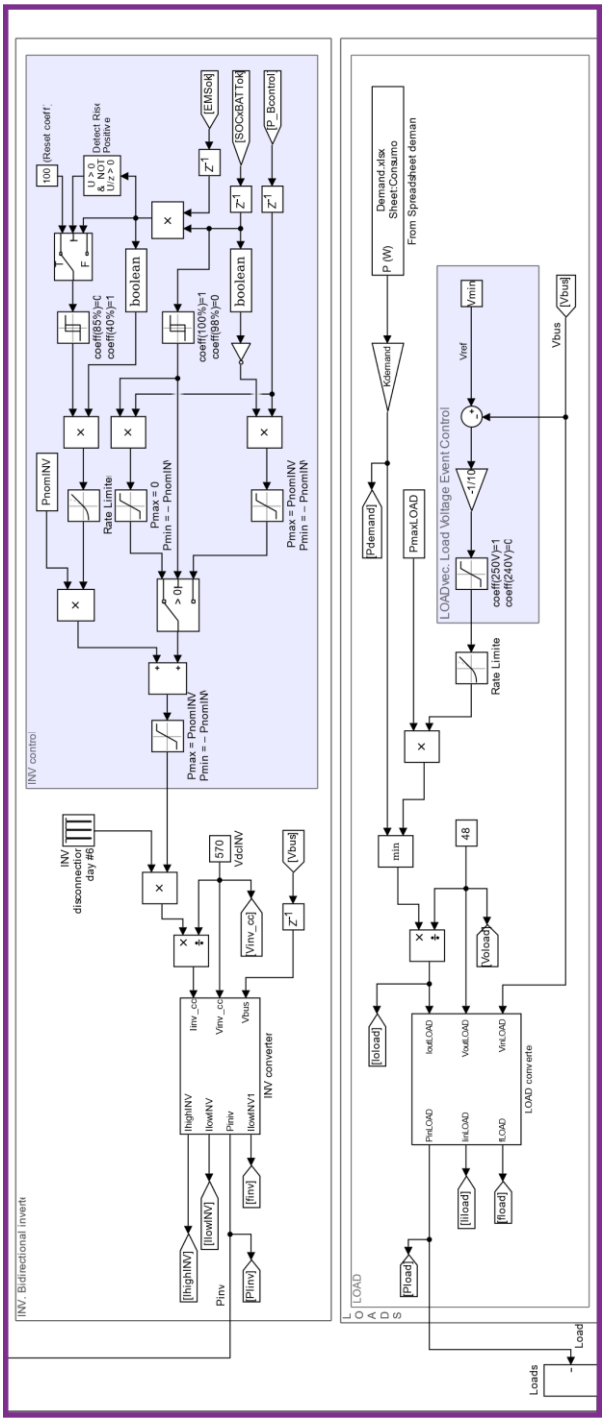


Figure 3-15. Blocks of the μG's.critical demand (LOAD) and bidirectional inverter (INV).

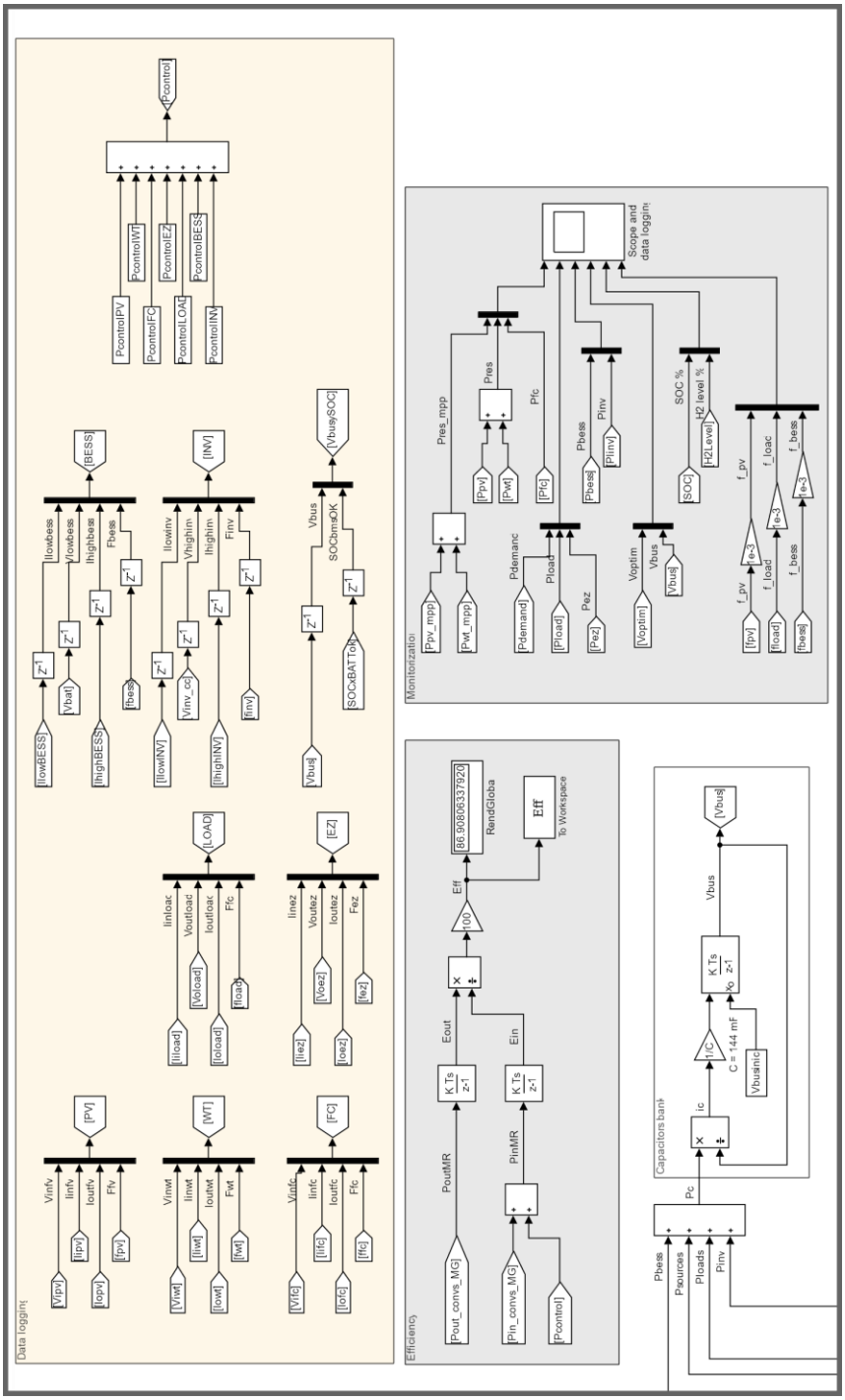


Figure 3-16. Blocks of the μG's capacitor bank and supervision.

### 3.3.3. Dynamic response

To study the dynamic response under the optimization control strategies proposed, microgrid (μG) operation has been simulated implementing base E-BCS together with both BVOC (in the BESS' converter) and OOSF (in all the μG's converters) simultaneously. The dynamic response under simulation scenario S0 is represented in Figure 3-17 and analyzed next. Failures of several elements have been scheduled in the simulation in order to test robustness and verify that operation is sustained even in exceptionally adverse circumstances:

- From $t = 24$ h to $t = 48$ h, all the renewable energy generation (PV and WT) is disconnected.
- From $t = 96$ h to $t = 120$ h, BESS is disconnected.
- From $t = 120$ h to $t = 144$ h, EMS and INV are disconnected.

Figure 3-17 shows that, at the beginning of the first day, generation is higher than consumption and surplus energy is used to charge the BESS until it reaches 100% SOC. EZ and INV are then activated. EZ profits from high generation to produce $H_2$. INV evacuates excess of RES generation into the grid. During the evening, RES generation decreases and LOAD increases, so discharge of BESS starts to supply the demand.

The second day, RES remain disconnected and LOAD is supplied from BESS. Battery SOC descends to low values, triggering the activation of FC and, later, also INV. First, FC delivers emergency power to the DC bus (consuming $H_2$) but this is not enough to recover SOC: it keeps descending and reaches 40%, triggering INV to consume full power from the grid to feed the loads and charge the battery up to 85%.

The third and fourth days, the BESS gets charged when RES power is greater than LOAD and gets discharged when the opposite occurs. BESS' power causes optimum bus voltage reference to be seamlessly followed by $v_{bus}$. All the converters operate at their optimum switching frequencies thanks to OOSF. This is normal operation.

The fifth day, BESS remains disconnected. The control system permits to maintain μG stability, making the INV assume the power profile that would correspond to the BESS if no failure had occurred.

The sixth day, the INV and the BESS' EMS remain disconnected leaving the μG not only operating in islanded mode, but also with no possibility of utilizing any bidirectional unit (apart from the capacitor bank, which energy-storage capacity is insignificant). Thus, generated power must constantly equal consumed power. VEC manages unidirectional units (including FC and EZ) to balance the power being injected to and being consumed from the DC bus. This faulty situation has been scheduled to test control robustness. The result is

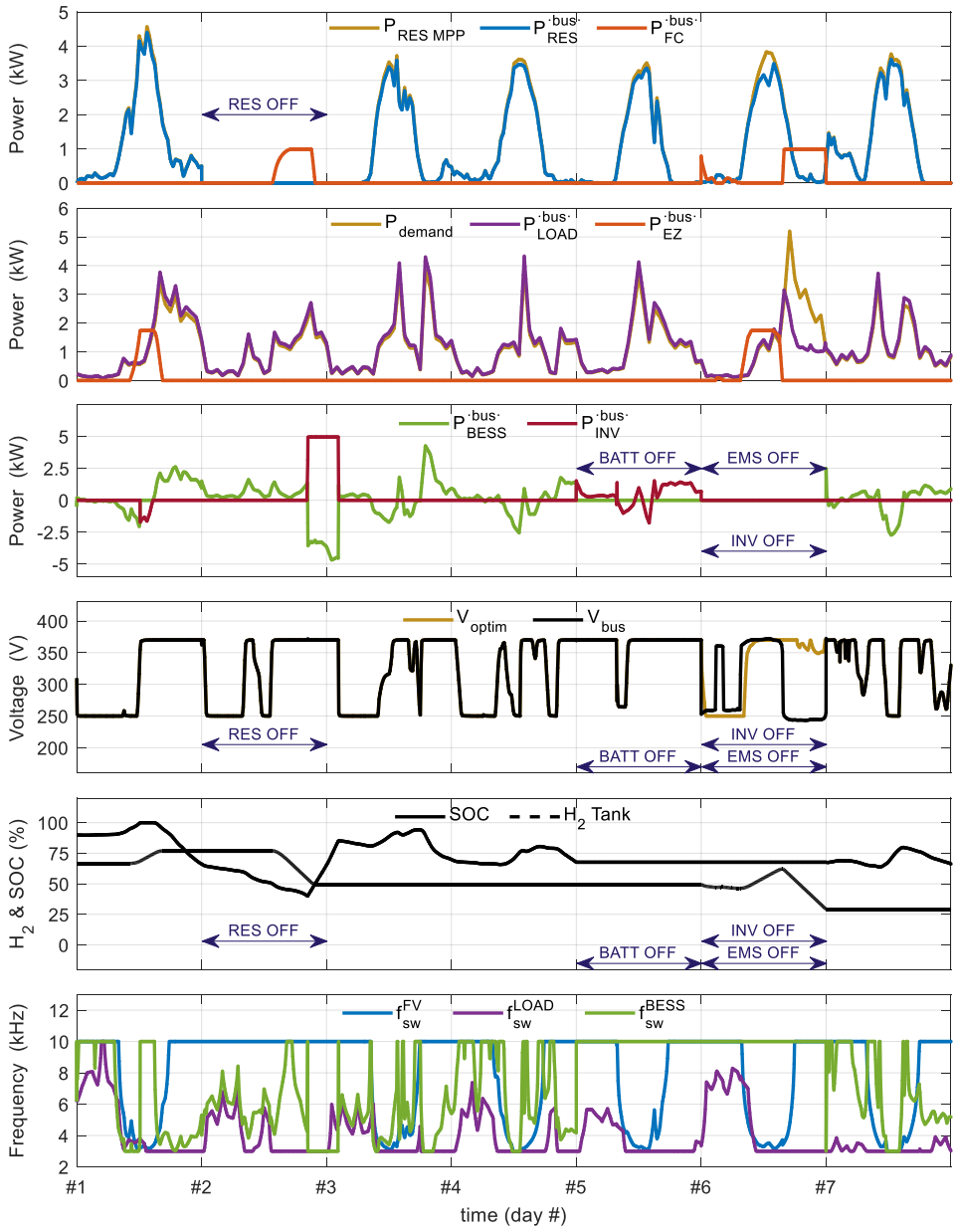


Figure 3-17. Microgrid simulation over 7 days with the optimized control system E-BCS+BVOC+OOSF. From top to bottom: (1) Sources: available RES power, actual RES power injected in the DC bus, and FC power injected in the DC bus; (2) Consumptions: critical loads electricity demand, actual LOAD power consumed from the DC bus, and EZ power consumed from the DC bus; (3) BESS and INV power; (4) Optimum bus voltage reference and actual bus voltage evolution; (5) SOC and hydrogen tank level; (6) Optimized switching frequencies of three µG's converters: PV, LOAD and BESS.

satisfactory: the autonomous control algorithm E-BCS manages the system to supply the loads to greatest extent possible.

On the seventh day, the microgrid returns to normal operation.

The system proves to be robust even in the face of severe failures. No undesired downtimes have occurred. The fourth graph in Figure 3-17 shows bus voltage evolution under BVOC: the optimum voltage reference, $v_{optim}$, is imposed and BESS power is controlled such that bus voltage, $v_{bus}$, follows that reference –except when EMS is down. The bottom graph shows the result of OOSF: switching frequencies constantly vary to match the optimum frequency of every converter. In all cases, optimum switching frequencies turn out to be high for low values of power, that is, when core losses prevail.

### 3.3.4. Efficiency increase

A new variable is defined: μG's global energy efficiency, $\eta_{global}$. Global energy efficiency permit to quantify the efficiency increase, $\Delta\eta_{global}^{control}$, achieved by each control strategy, $control = \{\text{BVOC} + \text{OOSF}, \text{BVOC}, \text{OOSF}\}$, with respect to the reference case, E-BCS. The system $\boxed{\mu G}$ defined in Figure 3-6 is studied now as a black box in which there are energy inputs and outputs. Global efficiency $\eta_{global}$ is defined in (3.52) as the quotient of the energy coming out from the system $\boxed{\mu G}$, $E_{out}^{\boxed{\mu G}}$, divided by the energy coming into, $E_{in}^{\boxed{\mu G}}$:

$$\eta_{global}[k] = \frac{E_{out}^{\boxed{\mu G}}[k]}{E_{in}^{\boxed{\mu G}}[k]} = \frac{\Delta t \sum_k \text{abs}\left(P_{LOAD}^{\cdot bus\cdot}[k] + P_{EZ}^{\cdot bus\cdot}[k] + S_{BESS}^{*}[k] \cdot P_{BESS}^{\cdot bus\cdot}[k] + S_{INV}^{*}[k] \cdot P_{INV}^{\cdot bus\cdot}[k]\right)}{\Delta t \sum_k \left(P_{PV}^{\cdot bus\cdot}[k] + P_{WT}^{\cdot bus\cdot}[k] + P_{FC}^{\cdot bus\cdot}[k] + S_{BESS}[k] \cdot P_{BESS}^{\cdot bus\cdot}[k] + S_{INV}[k] \cdot P_{INV}^{\cdot bus\cdot}[k]\right)} \quad (3.52)$$

where $P_i^{\cdot bus\cdot}[k]$ represents the power injected to ($P_i^{\cdot bus\cdot} > 0$) / withdrawn from ($P_i^{\cdot bus\cdot} < 0$) the DC bus by the converter $i$ in the time step $k$. Recall that the logical variables $S_{BESS}$ and $S_{INV}$ have been defined to distinguish when the BESS' and the INV's converters work as sources ($S_{BESS} = 1$, $S_{INV} = 1$) and when they work as loads ($S_{BESS} = 0$, $S_{INV} = 0$); superscript * indicates negation. Global energy efficiency is evaluated over the total simulation timespan: $\eta_{global}[k_{end}]$.

The μG is simulated with four different control schemes in each of the ten scenarios studied to compare their results:

- E-BCS only (reference case for efficiency comparison)
- E-BCS + BVOC + OOSF
- E-BCS + BVOC
- E-BCS + OOSF

Note that 40 simulations have been performed in total. Four slightly different Simulink models have been employed (one per control strategy) with ten different combinations of coefficients multiplying base meteorological and demand data (according to Table 3-3). Each of the 40 simulations performed takes an average of 15 min to complete using MatlabR2017a–Simulink in Intel® Core™ i7-6700 CPU @ 4.40 GHz, 16 GB RAM. The results of global efficiencies obtained in the simulations are collected in Table 3-4. Figure 3-18 represents graphically the results of Table 3-4:

Table 3-4. Improvement of μG global efficiency (%) with respect to the reference case, E-CBS, with three different control strategies, over seven-day operation in ten different scenarios S0–S9.

| Efficiency at $k_{end}$ (%) | Faulty system | No failures | | | | | | | | |
|---|---|---|---|---|---|---|---|---|---|---|
| | | Low power | | | Intermediate power | | | High power | | |
| | S0 | S1 | S2 | S3 | S4 | S5 | S6 | S7 | S8 | S9 |
| $\eta_{global}^{E-BCS}$ (reference) | 86.328 | 77.985 | 79.540 | 80.874 | 86.236 | 87.101 | 87.374 | 87.447 | 87.261 | 87.468 |
| $\Delta\eta_{global}^{BVOC+OOSF}$ | 0.580 | 0.980 | 0.553 | 0.416 | 0.616 | 0.308 | 0.304 | 0.529 | 0.476 | 0.435 |
| $\Delta\eta_{global}^{BVOC}$ | 0.147 | 0.481 | 0.358 | 0.269 | 0.158 | 0.132 | 0.130 | 0.131 | 0.171 | 0.262 |
| $\Delta\eta_{global}^{OOSF}$ | 0.416 | 0.691 | 0.328 | 0.250 | 0.527 | 0.207 | 0.180 | 0.403 | 0.299 | 0.162 |

The simulation results reveal that simultaneously applying BVOC and OOSF result in an efficiency improvement, $\Delta\eta_{global}^{BVOC+OOSF}[k_{end}]$ (blue in Figure 3-18), ranging from 0.304% in the worst case (scenario S6) to 0.980% in the best case (S1). Applying only BVOC (red) while switching the transistors at fixed frequencies (MOSFETs at 50 kHz and IGBTs at 4 kHz), $\Delta\eta_{global}^{BVOC}$ ranges from 0.130% (S6) to 0.481% (S1). And finally, applying only OOSF

(yellow), letting bus voltage evolve according to VEC and SOCEC, the achieved $\Delta\eta_{global}^{OOSF}$ ranges from 0.162% (S9) to 0.691% (S1).

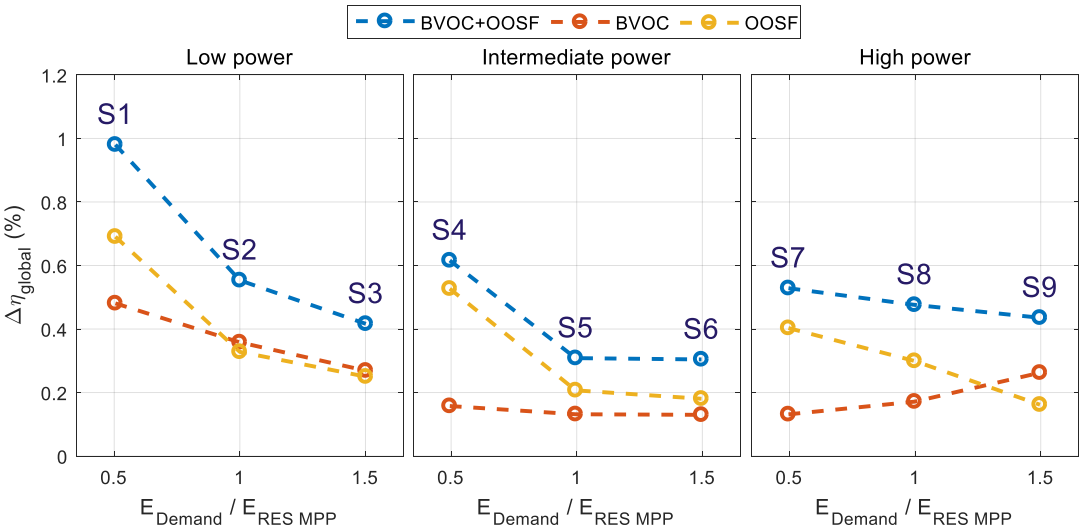


Figure 3-18. Energy efficiency improvement achieved by optimization strategies: simultaneous BVOC+OOSF (blue), only BVOC (red), and only OOSF (yellow) in scenarios S1 to S9.

These results are coherent with the efficiency curves presented in Figure 3-8. There exists a general tendency towards higher $\Delta\eta_{global}$ with lower powers, and vice versa, due to the characteristic shape of the efficiency curves. Higher efficiency improvements are achieved in the steep parts of the efficiency curves, which correspond to low power values, while efficiency optimization performance is limited for powers greater than maximum–efficiency power, due to the existing small efficiency differences for different values of $f_{sw}^{i}$ and $v_{bus}$.

Efficiency improvements accomplished by OOSF strategy consistently show this effect in all the simulated scenarios: in all the cases, $\Delta\eta_{global}^{OOSF}$ is higher with low power flows. Hence, for a given RES profile (each of the threes graphs in Figure 3-18), $\Delta\eta_{global}^{OOSF}$ is higher for low LOAD profiles. Indeed, the optimization performance of OOSF verifies $\Delta\eta_{global}^{OOSF}(\text{S1}) > \Delta\eta_{global}^{OOSF}(\text{S2}) > \Delta\eta_{global}^{OOSF}(\text{S3})$ (left graph in Figure 6; the same occurs in the central and the right graphs).

On the other hand, BVOC performance does not show this regularity as it highly depends on the specific sequence of active converters performing the instantaneous power flows. For

example, $\Delta\eta_{global}^{BVOC}$ would be high in a moment when only WT and LOAD were active (WT directly feeding the LOAD) because the individual optimum bus voltage of both converters coincide (it is $370\ V$), but $\Delta\eta_{global}^{BVOC}$ would be much lower if the same power came from BESS instead of from WT because individual optimum bus voltages of the BESS' converter is $250\ V$ but that of the LOAD's converter is $370\ V$. The global optimum bus voltage in this last case would be the trade-off that minimizes the sum of power losses in both converters.

Different operation scenarios produce different power distribution patterns among the μG's units –for instance, INV provides bulk charge to the battery from grid two times in S9; one time in S0, S6 and S8; and none in the remaining scenarios. Consequently, global efficiency is only comparable between different control strategies applied under the same operation scenario (columns of Table 3-4), but not from one operation scenario to another (rows of Table 3-4) since they yield quite different power share schemes.

The efficiency improvements achieved with the two proposed optimization strategies, BVOC and OOSF, are small but still interesting. Even though μG's efficiency increase with both optimization strategies combined ranges only from 0.3% to 1% (approx.) in the evaluated operation scenarios, it is achieved at virtually no cost: just introducing changes in the discrete control algorithms of the DC-DC converters. Implementing both optimization strategies produces net energy (and economic) savings in all possible operating situations. Nevertheless, BVOC and OOSF are best suited for:

- microgrids applications which require low power flows compared to the nominal power of the converters and/or
- microgrids in which maximum efficiency consistently occurs at the same value of $v_{bus}$ in all the μG's converters –that is, individual optimum bus voltages of all the converters coincide.

Some application examples that meet these requirements might be Uninterruptible Power Supply systems (in which the BESS operates at near zero power to maintain the battery floating), remote Base Transceiver Stations and weather stations. In these applications, the BESS is normally significantly oversized so that it can sustain the operation of the station for several days in case of generation shortage. Thus, the BESS converter normally operates well below its nominal power and can benefit from OOSF high performance at low power. Furthermore, if the individual optimum bus-voltage values of the μG's converters happen to coincide, BVOC performance can be more significant than in the μG studied here.

### 3.3.5. Influence of control parameters in optimization performance

In this last sub-section, some control parameters of BVOC and OOSF are modified to evaluate how they affect the efficiency improvement achieved. The modifications of parameters that have been studied are:

- Varying the refresh rate of the BVOC controller, $\Delta t_{BVOC}$.
- Varying the refresh rate of the OOSF controllers, $\Delta t_{OOSF}$.
- Widening the switching frequency optimization intervals of IGBTs and MOSFETs.

Table 3-5. Influence of control parameters on optimization performance.

| Efficiency | Parameters | E-BCS… | …+BVOC +OOSF | …+BVOC | …+OOSF |
|---|---|---|---|---|---|
| $\eta_{global}[k_{24h}]$ (%) | Reference case Scenario S0 day #1 | (86.300) | 87.283 | 86.518 | 87.020 |
| $\Delta\eta_{global}[k_{24h}]$ (%) | $\Delta t_{BVOC} = 100\ ms$ | – | $3.74 \cdot 10^{-4}$ | $8.13 \cdot 10^{-4}$ | – |
| | $\Delta t_{BVOC} = 5\ s$ | – | $-0.007$ | $-0.010$ | – |
| | $\Delta t_{OOSF} = 10\ ms$ | – | $5.67 \cdot 10^{-5}$ | – | $2.84 \cdot 10^{-5}$ |
| | $\Delta t_{OOSF} = 5\ s$ | – | $-6.12 \cdot 10^{-6}$ | – | $-7.39 \cdot 10^{-7}$ |
| | $f_{sw}^{MOSFET} \in [10, 200]\ kHz$, $f_{sw}^{IGBT} \in [2, 15]\ kHz$ | – | 0.272 | – | 0.246 |

Table 3-5 shows the parameter values that have been tested in this study. Operation of the μG has been simulated over a period of 24 h, which is sufficient to evaluate the influence of the studied parameters. The simulation time step, $\Delta t$, has been reduced from previous $100\ ms$

to 10 $ms$, consistently with the new values of $\Delta t_{BVOC}$ and $\Delta t_{OOSF}$. Each of the executed 24-hour simulations has taken an average of 15 minutes to complete.

Results in Table 3-5 indicate that BVOC and OOSF performance can be further improved to some extent if control parameters are chosen properly:

- $\Delta t_{BVOC}$: Refresh rate of BVOC controller has very limited influence in overall BVOC performance for the studied values. The capacitor bank smooths bus voltage dynamics, so $v_{bus}$ evolution is slow compared to the evaluated $\Delta t_{BVOC}$. Calculating and updating the optimum bus voltage reference, $v_{optim}$, more frequently does not significantly improve the efficiency of BVOC algorithm.
- $\Delta t_{OOSF}$: Variations in OOSF performance when the refresh rate of OOSF is changed are insignificant. Again, the power profiles of all the μG's units evolve very slowly compared to the evaluated $\Delta t_{OOSF}$.
- Switching frequency ranges: Efficiency improvements around 0.25% can be obtained by widening the range of possible switching frequencies of MOSFETs from $[20, 100]\ kHz$ to $[10, 200]\ kHz$ and that of IGBTs from $[3, 10]\ kHz$ to $[2, 15]\ kHz$. However, it is important to mention that a new optimization problem arises here to select the most appropriate frequency limits. The trade-off between OOSF efficiency improvement and passive-filters size and electromagnetic interferences restriction must be established.

Summarizing the results, control parameters were already satisfactory. Changing the refresh rate of BVOC and OOSF controllers produce nearly zero improvements. Only by widening the range of switching frequency window some appreciable efficiency increases might be obtained. Nevertheless, this has important drawbacks (e.g., increased current ripple) that might require re-designing the μG's converters.

## 3.4. Summary

A self–managed DC microgrid (μG) has been described. Events-Based Control System (E-BCS), which is constituted of decentralized Voltage Event Control (VEC) and State of Charge Event Control (SOCEC), has been the starting point to evaluate two strategies to optimize the efficiency of the μG's converters. E-BCS determines the power of each unit based on bus voltage ($v_{bus}$) and on battery SOC. These control laws prevent that $v_{bus}$ and $SOC$ reach extreme values by progressively activating loads and deactivating sources when $v_{bus}$ or $SOC$ get too high, and gradually deactivating loads and activating sources when $v_{bus}$ or $SOC$ get too low.

The two proposed optimization strategies have been described and validated in simulation. Both strategies increase the efficiency of the μG's converters adaptively, responding to changes in the operation point. They utilize two different approaches to minimize power losses of the μG's converters. The non-linear optimization problems that they solve are formulated based on small-signal averaged deterministic loss models of the converters. The two presented optimization strategies can be implemented individually or simultaneously.

- Bus Voltage Optimization Control (BVOC): BESS power is controlled such that it fulfills two purposes: first, balancing the power of sources, loads and inverter and, second, dynamically controlling the (variable) optimum bus voltage, so the system always operates at $v_{optim}$. The value of $v_{optim}$ is calculated online as the minimizer of the sum of power losses in the μG's DC-DC converters. Thus, this optimization applies to the whole set of converters, but only actuates in the BESS' converter, imposing the appropriate power reference.
- Online Optimization of Switching Frequency (OOSF): Switching frequency of every μG's converter $i$, $f_{sw}^{i}$, is individually optimized online to improve its energy efficiency.

A model of the μG studied has been developed in Simulink. Microgrid operation has been simulated over seven days under ten different scenarios that represent different electricity generation and consumption profiles. The comprehensive control system E-BCS+BVOC+OOSF manages the μG in a stable manner and is capable of overcoming abnormal difficulties, such as the simultaneous failure of all bidirectional units. The two optimization strategies result in low (yet interesting) efficiency improvements: $\Delta\eta_{global}^{BVOC+OSF} = 0.304 - 0.980\%$ (depending on the operation scenario considered); $\Delta\eta_{global}^{BVOC} = 0.130 - 0.481\%$; and $\Delta\eta_{global}^{OOSF} = 0.162 - 0.691\%$. Even though these efficiency improvements are low, they are exclusively based in discrete control algorithms, so they involve (almost) no extra investment.

# 4. Active Battery Balancing via a Switched DC-DC Converter

This chapter presents a novel battery balancing system (equalizer) topology and the control strategy designed for it. The equalizer studied is of the active type and it is based in power-multiplexing: it transfers charge (ampere-hours) from the strongest battery (that with the highest SOC) in the battery pack to the weakest (that with the lowest SOC) through a single DC-DC converter. Without balancing, the weakest cell would limit the battery pack's performance, impeding full utilization of the battery pack's capacity, because it reaches cut-off voltages before the other cells do. The following topics have been addressed to design the equalizer's control strategy: modeling the batteries of the battery pack, simulating the battery pack's response without balancing to estimate its natural tendency towards imbalance, calculating the control parameters from the simulation results, modeling the equalizer, and validating the control strategy in simulation. A prototype of the equalizer was built in a previous project and experimental works have started to test its performance. This chapter is divided into two main sections: theoretical study and experimental study.

## 4.1. Theoretical study

This section describes the equalizer topology, presents the simulation model of the equalizer and the battery pack, and shows how the design and tuning of the equalizer's control strategy have been carried out. Simulations validate the equalizer topology and the proposed control method.

### 4.1.1. Equalizer design

The proposed battery balancing system fits in the category of converter-based active balancing arrangements. This equalizer was ideated to balance the battery pack of the GAEI's μG and, thus, it can manage up to fifteen 12 *V* monobloc batteries in series. Nevertheless, the equalizer's topology is validated considering a battery pack comprising only five monoblocs, for the sake of clarity. Figure 4-1 illustrates the equalizer topology and operation principle, which is based on power multiplexing. The equalizer periodically detects the batteries with highest SOC (B4 in the figure) and lowest SOC (B2) and transfers charge among them theough the DC-DC converter to progressively equilibrate the pack. The main advantages of this topology with respect to other converter-based topologies are that only one power converter is utilized [187], instead of one converter per battery cell (Ćuk, buck, boost, quasi-resonant, multi-flyback), and that this topology does not require a transformer, unlike other proposals (those based on the flyback converter) [131].

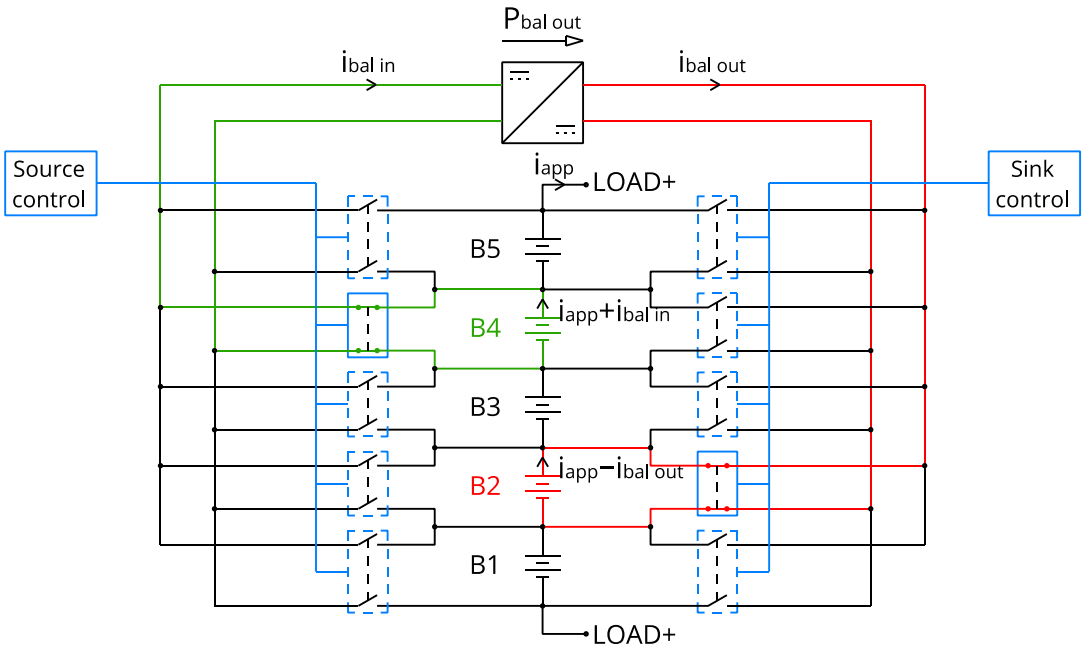


Figure 4-1. Battery balancing system topology. Green color represents the strongest monobloc battery (B4). Red color represents the weakest monobloc battery (B2). The DC-DC converter is transferring charge from B4 to B2. Power routing through the appropriate switches is ruled by the blocks "Source control" and "Sink control".

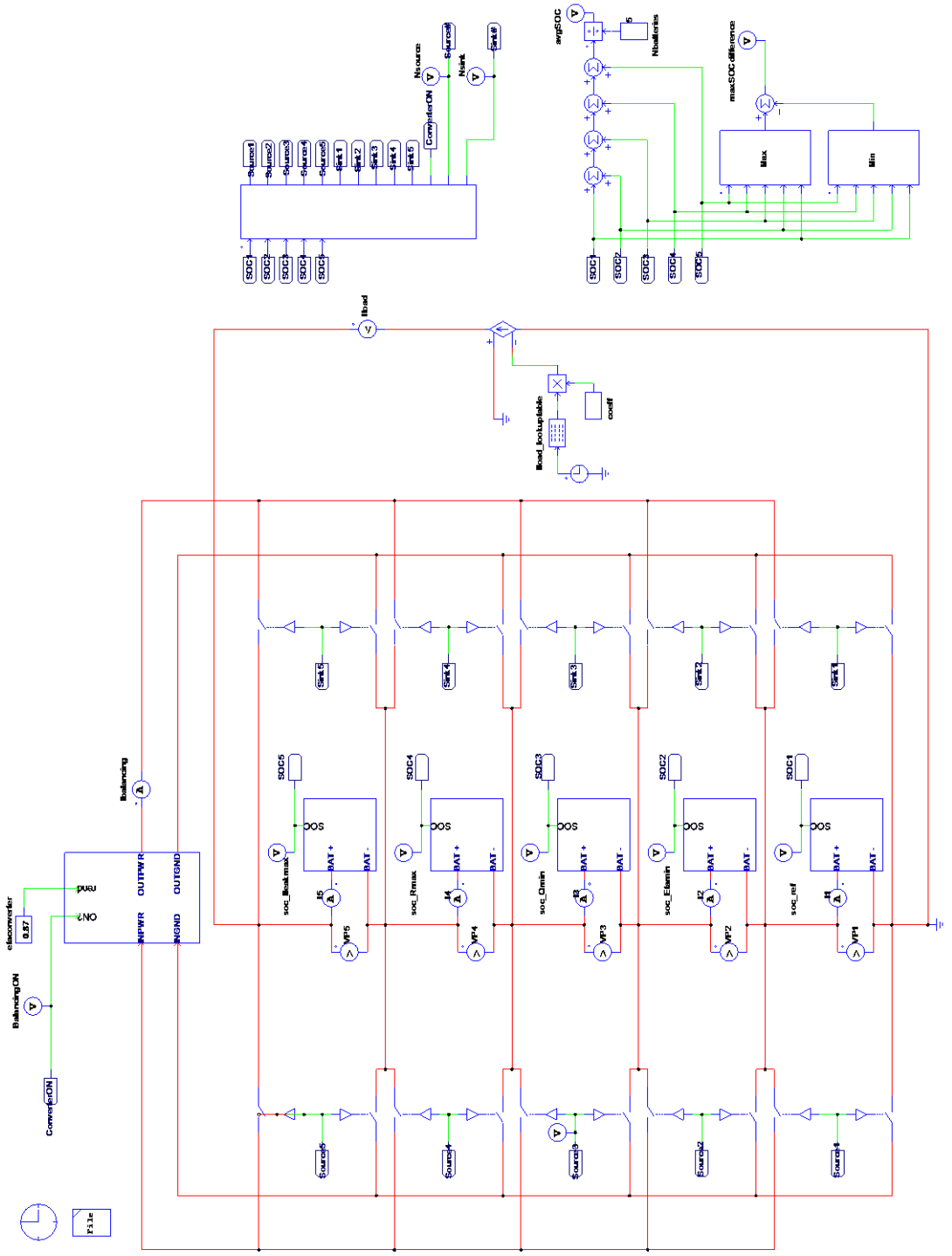


Figure 4-2. Model of the equalizer in PSIM.

A battery pack composed of fifteen Lead Crystal 6-CNFJ-200 (nominal voltage: $12\ V$, nominal capacity: $Q_{nom} = 200\ Ah$) is intended to replace the current BESS (Battery Energy Storage System) of the GAEI's μG. However, only five batteries with lower capacity are considered to test the equalizer, to simplify the testing procedures and to get clearer results. The battery pack analyzed to validate the equalizer design consists of five Lead Crystal 6-CNFJ-40 monobloc batteries ($12\ V$, $40\ Ah$ instead of $200\ Ah$). Each monobloc is a bundle of six lead-acid cells with nearly solid-state electrolyte. Balancing within the monobloc's cells is not possible since the monoblocs are, by definition, sealed. Balancing is performed among monoblocs. Lead-acid batteries can usually handle imbalance to some extent without specific balancing hardware, through controlled overcharging of the stronger cells (which is forbidden for lithium-ion batteries) [188]. Thus, lead-acid batteries do not normally require active balancing –although they *can* be actively balanced.

Lead Crystal batteries have been investigated to gain insight into this rather new technology. The manufacturer, Betta Batteries, claims (perhaps too optimistically) that this technology performs better than any other mainstream battery technology (lead-acid, gel, lithium, and Absorbent Glass Mat) in terms of allowed temperature range, usage life, capacity loss, cycle life at high temperature, cost of ownership, environmental impact, and safety. However, minor modifications would permit using the equalizer with other battery types such as lithium-ion.

One unidirectional buck-boost converter Traco Power TEP 150-2413WI [189], is employed to transfer energy "cell-to-cell" —in fact, monobloc-to-monobloc, as explained above. This converter operates in constant current (CC) mode, delivering an output current $i_{bal\ out} = 10\ A$, until the output voltage reaches $15\ V$. The converter then shifts to constant voltage (CV) mode, fixing the output voltage at the aforementioned value of $15\ V$ and, therefore, reducing the output current. The maximum output voltage value can be adjusted within a $\pm 20\%$ range. In this specific case, the maximum output voltage value must be set in $14.7\ V$, according to Lead Crystal 6-CNFJ-40 specifications.

The equalizer performs SOC balancing by routing charge (ampere-hours) from the strongest monobloc (highest SOC) to the weakest monobloc (lowest SOC) through two controlled strings of switches operated as power multiplexers. The block "Source control" closes the appropriate switches from the string in the left in Figure 4-1 to connect the strongest monobloc battery to the input port of the DC-DC converter, and "Sink control" closes the appropriate switches from the string in the right in Figure 4-1 to connect the output port of the converter to the weakest monobloc battery. During SOC balancing, the weakest monobloc battery (Bweak) experiences a reduced load, $i_{app\ Bweak} = i_{app} - i_{bal\ out}$, while the strongest monobloc (Bstrong) experiences an increased load, $i_{app\ Bstrong} = i_{app} + i_{bal\ in}$, where

$i_{app\ Bweak}$ is the applied current of the weakest battery, $i_{app\ Bstrong}$ is the applied current of strongest battery, $i_{app}$ is the pack current, $i_{bal\ out}$ is the converter's output current, and $i_{bal\ in}$ is the converter's input current. The DC-DC converter's efficiency $\eta_{pc}$ is modelled by a constant value of $\eta_{pc} = 87\%$ at full load. Thus, the converter's input current is $i_{bal\ in} = i_{bal\ out}/\eta_{pc} = 10/0.87 = 11.5\ A$. Note that further precision could be easily introduced into the model by using a look-up table $\eta_{pc}(i_{bal\ out})$ but this has been considered unnecessary at this point as the focus is to design a control strategy and validate the capability of the proposed topology to balance the battery pack.

### 4.1.2. Simulation model

In this theoretical study, a fictitious highly imbalanced battery pack is considered. The parameter values of each monobloc battery have been conceived such that each monobloc is identical to the reference monobloc except for one parameter value. This allows to discern how each parameter affects to balancing. The performance of the proposed battery balancing circuit is evaluated by means of a PSIM simulation. Figure 4-2 represents the equalizer's model.

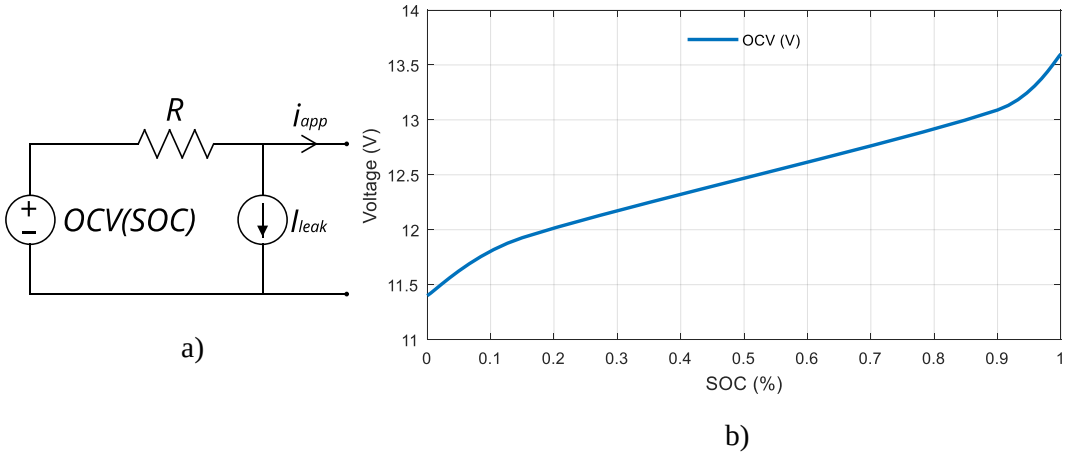


Figure 4-3. a) Equivalent circuit of monobloc batteries, b) Approximate OCV vs. SOC characteristic curve.

The five monobloc batteries that compose the battery pack have been modeled by equivalent Thevenin circuits with current leakage. Each circuit consists of an SOC-dependent Open Circuit Voltage (OCV) source, a constant internal resistance, $R$, and a current source that models leakage current, as shown in Figure 4-3. This is one of the most basic battery

models available but, nevertheless, it is sufficient to capture SOC evolution because battery degradation is negligible over the short simulation period, and the current profile applied, $i_{app}$ (characteristic of a microgrid), varies rather slowly (see Figure 4-5 below), so SOC dynamics (which roughly result from the integration of $i_{app}$) are slow too –fast dynamics are irrelevant in the simulated scenario. This equivalent circuit model could be refined by introducing additional elements. Indeed, works have started to characterize the monobloc batteries with the Enhanced Self-Correcting equivalent model described in [94], as explained in Section 4.2.2.3.

The electrical parameters of the five monobloc batteries are listed in Table 4-1. These made-up parameters present intentionally high values of imbalance (on the order of 10%) with the intention of making the simulation results easily observable. Each battery represents imbalance in a different parameter with respect to the reference battery, B1:

- B2 has lower coulombic efficiency ($\downarrow \eta_Q$)
- B3 has lower capacity ($\downarrow Q$)
- B4 has higher internal resistance ($\uparrow R$)
- B5 has higher leakage current ($\uparrow I_{leak}$)

Table 4-1. Parameters of the monobloc batteries. (Deviations from the reference battery have been highlighted).

| Monobloc battery | $\eta_Q$ | $Q\ (Ah)$ | $R\ (m\Omega)$ | $I_{leak}\ (A)$ |
|---|---|---|---|---|
| B1: reference | 0.90 | 40 | 8 | $2.6 \cdot 10^{-7}$ |
| B2: $\downarrow \eta_Q$ | $\mathbf{0.80}$ | 40 | 8 | $2.6 \cdot 10^{-7}$ |
| B3: $\downarrow Q$ | 0.90 | **35** | 8 | $2.6 \cdot 10^{-7}$ |
| B4: $\uparrow R$ | 0.90 | 40 | **9** | $2.6 \cdot 10^{-7}$ |
| B5: $\uparrow I_{leak}$ | 0.90 | 40 | 8 | $\mathbf{50 \cdot 10^{-3}}$ |

where $\eta_Q$ is the coulombic efficiency, $Q$ is the capacity, $R$ is the internal resistance and $I_{leak}$ is the self-discharge current. In the case of B5, $I_{leak}$ comprises the sum of self-discharge current and current drained to feed external circuitry (this represents the BMS being connected to B5): $I_{leak} = i_{self-discharge} + i_{leakage}$, according to the definition in (2.37).

Battery balancing acts at all times –charging, discharging, and idling. The load profile employed in the simulations, $i_{app}$, is representative of a typical residential microgrid application –renewable energy generation and residential electricity consumption profile.

### 4.1.3. Design of the control strategy

The equalizer's controller periodically evaluates whether the battery pack is balanced or not and, in case it is not, it estimates the existing degree of imbalance and identifies which monobloc batteries to balance. Figure 4-4 represents the activation sequence, which is executed repetitively. If balancing is needed at the beginning of the period, the DC-DC converter is activated during $T_{bal}$, and it rests then during $T_{rest}$ until the end of the period. If balancing is not needed, the converter just stays off (so $i_{bal} = 0$ during the whole period).

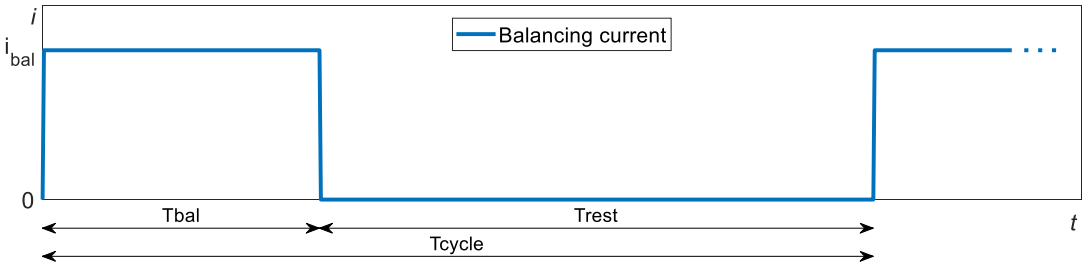


Figure 4-4. Activation of the battery balancing system. Balancing current over one balancing period, $T_{cycle}$.

The central controller receives voltage, current and temperature data from each monobloc battery and processes them to estimate the individual states of charge, $SOC_{Bi}$ (where $i = 1 \dots 5$), at the end of each period, $T_{cycle}$. Then, maximum and minimum $SOC_{Bi}$ are identified. In general, this $SOC_{Bi}$ are the estimated values, not the actual ones (which are not accessible); nevertheless, exact SOC estimation is assumed in this study of balancing for simplicity. The controller determines then the activation of the DC-DC converter during the following period:

- If SOC imbalance (that is, $\max(SOC_{Bi}) - \min(SOC_{Bi})$) is lower than 0.5%, it is considered negligible and the DC-DC converter remains off.
- Otherwise, i.e., $\max(SOC_{Bi}) - \min(SOC_{Bi}) > 0.5\%$, balancing is activated. Then:
    - The "Source control" and the "Sink control" close the appropriate switches.
    - The DC-DC converter is turned on for a certain balancing time, $T_{bal}$, smaller than the period $T_{cycle}$. Charge transfer occurs during this balancing time.
    - Afterwards, the DC-DC converter is turned off and rest time, $T_{rest}$, follows until the end of the period.

The DC-DC converter Traco Power TEP 150-2413WI has been selected because it is suitable for battery applications thanks to its CC-CV output characteristic. In this analysis, only the CC mode is studied for simplicity because it is the prevailing operation mode –CV mode starts when the battery pack's weakest battery is already almost fully charged and so does not accept full CC charge current.

#### 4.1.3.1. Justification of balancing speed. Natural rate of imbalance

The equalizer must transfer charge from the strongest battery to the weakest battery at a rate that simultaneously satisfies two conditions: first, the balancing charge rate must at least be greater than the average rate of natural imbalance and, second, it must be low enough to avoid generating SOC oscillations.

The DC-DC converter delivers a constant output current $i_{bal\,out}$ of $10\,A$ in CC mode ($0.25C$). The equalizer's duty cycle, $T_{bal}/T_{cycle}$, must be selected such that the two conditions mentioned above are met. A period $T_{cycle}$ of $60\,s$ has been selected in this work with the aim of performing frequent updates in order to identify and confront imbalance as soon as it starts to grow. Note that the study presented below could be easily adapted to other values of $T_{cycle}$, though.

The battery pack is simulated with no balancing system to assess the natural rate of imbalance growth. A typical current profile is applied to evaluate the extent of SOC divergence it causes. The current profile applied to the battery pack, $i_{app}$, is typical of a microgrid application, scaled down by the total capacity of the test battery pack. It represents a 24-hour charge-discharge cycle that displays three main stages (see Figure 4-5.a): 1) the battery pack is discharged during night due to some electricity consumption combined with little renewable energy generation (wind energy); 2) around $9{:}00$, the consumption shows a small peak immediately followed by a rise of renewable energy generation (mainly photovoltaic energy), which charges the battery from $10{:}15$ to $17{:}30$ approximately; 3) finally, load demand grows again and the highest load occurs from $19{:}00$ to $23{:}00$ approx.

Figure 4-5 shows the simulation results, which are analyzed next. The effect that parameters dispersion has on SOC, taking the monobloc battery B1 as the reference battery, is examined analyzing Figure 4-5.b and Figure 4-5.c. SOC evolution is modeled according to (4.1) and (4.2) (Coulomb counting in discrete time). Note that coulombic efficiency is ascribed to charging only [71, 190]:

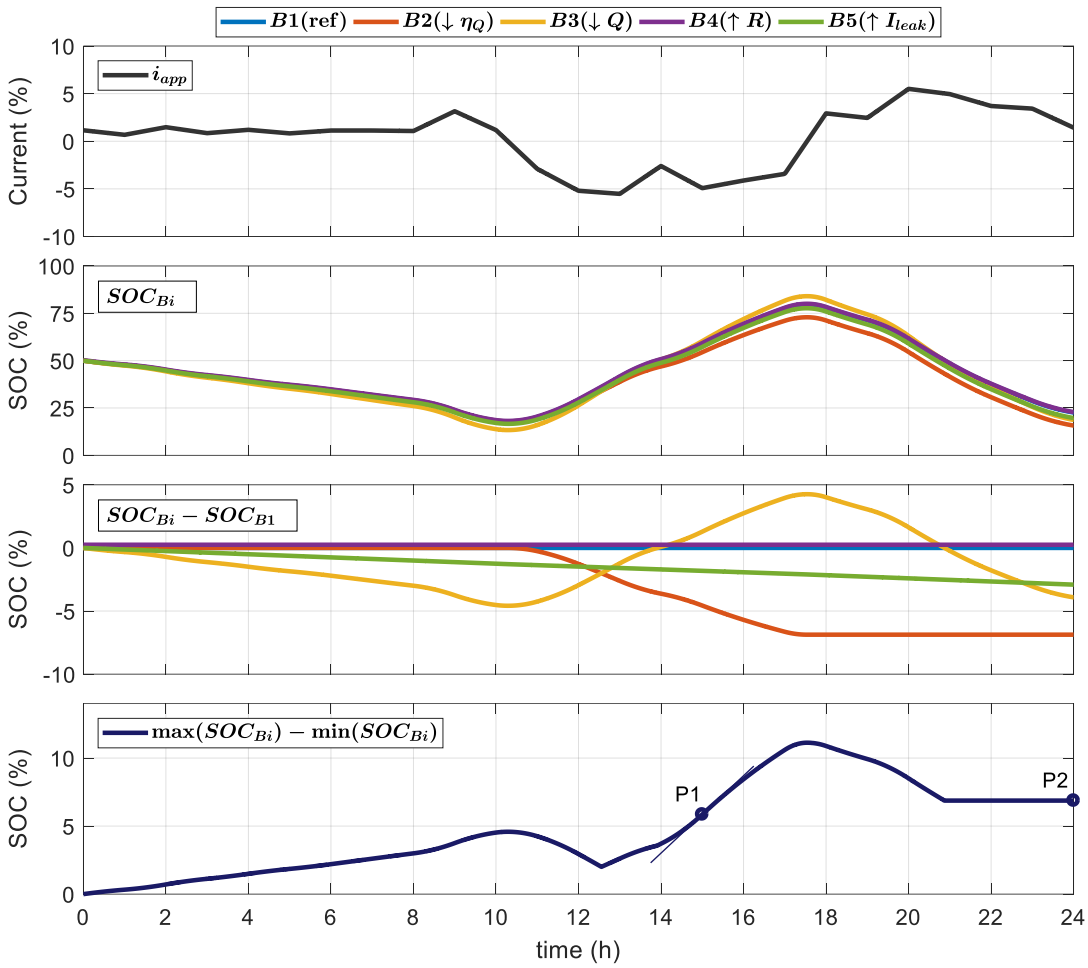


Figure 4-5. Simulation results. Battery pack operating with no balancing system over a typical 24-hour cycle. Top to bottom: a) Current profile applied, b) Individual SOC evolution of the five monobloc batteries, c) Individual SOC deviation from SOC of the reference battery (B1), d) Maximum SOC difference among the five monobloc batteries (P1 and P2 indicate critical points).

$$SOC_{Bi}[k] = SOC_{Bi}[0] - \frac{\Delta t}{3600 \cdot Q_{Bi}} \sum_{0}^{k} \eta_{Q\,Bi}[k]\left(i_{app\,Bi}[k] + I_{leak\,Bi}\right) \tag{4.1}$$

$$\eta_{Q\,Bi}[k] = \begin{cases} 1, & i_{app\,Bi}[k] \geq -I_{leak\,Bi}\ (discharge) \\ \eta_{Q\,Bi}, & i_{app\,Bi}[k] < -I_{leak\,Bi} \quad (charge) \end{cases} \tag{4.2}$$

where the subscript $Bi$ represents that the associated variable or parameter refers to battery $i$, with $i = \{1, 2, 3, 4, 5\}$, $k$ is the index of discrete time ($t = k\Delta t$), $\Delta t$ is the time step (in this case, $\Delta t = 1\ s$), $SOC_{Bi}[k]$ is the state of charge at $k$, $\eta_{Q\,Bi}[k]$ is the coulombic efficiency ($\eta_{Q\,Bi}[k]$ is one during discharge and $\eta_{Q\,Bi} < 1$ during charge), $Q_{Bi}$ is the capacity in Ah, $i_{app\,Bi}[k]$ is the discharge current provided by the battery (defined as in Figure 4-3.a), and $I_{leak\,Bi}$ is the leakage current (also defined as in Figure 4-3.a).

- $\downarrow \eta_Q$: B2's SOC evolves parallel to $SOC_{B1}$ during discharge but, during charging, $SOC_{B2}$ grows more slowly (see $10{:}15 < t < 17{:}30$) because its coulombic efficiency is lower. Thus, given a certain charge of $x$ Ah, B2 gets less charged (i.e., it reaches a lower SOC) than B1.

  Coulombic efficiency imbalance self-amplifies as the battery pack is cycled because it produces SOC differences that accumulate with every charge. If the resultant charge imbalance was not externally compensated, successive charges of the battery pack would eventually leave the pack unusable: B2 would progressively reach lower SOC after each full charge of the battery pack, up to the point of $SOC_{B1}$ hitting 100% when B2 is still at $SOC_{min}$. In this situation, neither charging nor discharging the battery pack would be possible (as in Figure 2.21).

- $\downarrow Q$: B3's reduced capacity causes this monobloc battery to get charged and discharged sooner than the reference battery. The slope of $SOC_{B3}$ is steeper than that of $SOC_{B1}$ both during charging and discharging. B3 hits minimum and maximum SOC before the other monobloc batteries do.

  A monobloc battery having lower capacity causes incomplete use of the capacity stored in the other monobloc batteries: unbalanced operation would result in B3 reaching cut-off (high / low) voltage (corresponding to $SOC_{B3} = 100\%$ / $SOC_{B3} = SOC_{min}$, respectively) before any of the other monobloc batteries in the battery pack. The battery pack's available capacity would thus be reduced to $5 \cdot (100\% - SOC_{min}) \cdot Q_{B3}$. Capacity imbalance also tends to self-amplify because the battery with lowest capacity in the pack is subjected more often to high and low SOC –which instigate accelerated degradation.

- $\uparrow R$: B4's SOC curve is identical to that of B1.

  The difference in internal resistance is not a real cause of imbalance (although it produces voltage differences that could mislead to infer an underlying SOC imbalance). Increased internal resistance causes incomplete use of the battery pack's capacity in an unbalanced pack and reduces the maximum power it can

provide: B4's voltage would reach maximum / minimum voltage boundary before the rest of the batteries get full charged / discharged.

- $\uparrow I_{leak}$: B5 gets charged more slowly and gets discharged faster than B1. The reason is that B5 is extra-loaded: its discharge current is a little higher and its charge current is a little lower compared to the other batteries. This produces steady decline of $SOC_{B5}$ compared to $SOC_{B1}$.

  Increased leakage current can mean two things: battery being extra loaded or experiencing increased self-discharge. On one hand, extra loading of individual monobloc batteries can normally be reduced or avoided by design (feeding small-power circuitry from individual cells or monoblocs is bad practice). On the other hand, increased self-discharge is generally indicative of early degradation. This issue should be examined individually to apply custom solutions.

  If increased leakage current was not eliminated or compensated by means of an equalizer, it would lead to B5 always reaching $SOC_{min}$ before B1 and it would also impede B5 to reach full-charge SOC. It would tend to self-amplification analogously to the case of reduced coulombic efficiency.

Figure 4-5.d shows the battery pack's natural tendency towards imbalance. Critical points, P1 and P2, have been identified –note that local/global maximums are not relevant because what matters is not the absolute value of accumulated imbalance at a specific point, but the rate at which imbalance grows instead. Denominating $NCIR$ to the Natural Charge Imbalance Rate of the battery pack subjected to typical current profile,

$$NCIR(t) \coloneqq \frac{d}{dt}\left[max\left(SOC_{Bi}(t)\right) - min\left(SOC_{Bi}(t)\right)\right]$$

P1 is the point of maximum instantaneous rate of imbalance, i.e. maximum positive slope in the graph, and P2 corresponds to the accumulated SOC imbalance over 24 hours. Therefore, P1 relates to max($NCIR$) and P2 relates to avg($NCIR$):

- P1. Maximum instantaneous rate of imbalance:

$$\max(NCIR) = NCIR(t_{P1}) = 2.844\%/h$$

- P2. Average rate of imbalance over one cycle:

$$\text{avg}(NCIR) = \frac{\max\left(SOC_{Bi}(t_{P2})\right) - \min\left(SOC_{Bi}(t_{P2})\right)}{t_{P2}} = \frac{6.873\%}{24h} = 0.286\%/h$$

Defining Balancing Charge Per Period ($BCPP$) as in (4.3) will help to calculate the design limits of $T_{bal}$. $BCPP$ represents the amount of charge (ampere-hours) devoted to generating SOC balancing during one period, that is, the charge withdrawn from the strongest battery

plus the charge absorbed by the weakest cell. Note that $BCPP$ is proportional to the equalizer's duty cycle, $T_{bal}/T_{cycle}$.

$$BCPP = \frac{(i_{bal\ out} + i_{bal\ in})T_{bal}}{T_{cycle}} \tag{4.3}$$

#### 4.1.3.2. Minimum balancing charge per period ($BCPP_{min}$)

The equalizer must transfer enough charge to compensate natural imbalance. Minimum balancing charge per period is denoted $BCPP_{min}$. Following [97], natural imbalance is assessed simulating the equalizer model over 24 hours (typical discharge-charge period). The following initial and operation conditions have been considered:

- The battery pack is balanced at the beginning of the simulation. The initial state of charge is $SOC[0] = SOC_{Bi}[0] = 0.50$.
- There is no balancing.
- The battery pack's current, $i_{app}$, is representative of a residential microgrid application, with renewable energy generation and a typical residential electricity consumption profile.

Under these assumptions, the states of charge of the five monobloc batteries tend to diverge as Figure 4-5 demonstrates. Different design criteria can be followed to determine the minimum Balancing Charge Per Period, $BCPP_{min}$, depending on what goal the equalizer is meant to achieve:

- To compensate instantaneous imbalance rate at every moment, P1 should be considered: $BCPP$ should then be greater than $\max(NCIR) \cdot Q_{nom}$. This would produce ultra-fast compensation of imbalances, but it would also entail the risk of overcompensating them in moments when rate of imbalance is small.

  $$\max(NCIR) \cdot Q_{nom} = 2.844\%/h \cdot 40\ Ah = 1.138\ Ah/h = 1.138\ As/s$$

  Expressing the result in $As/s$ (ampere second per second) is more convenient because $T_{bal}$ and $T_{cycle}$ are expressed in seconds too.

- To ensure balancing the battery pack within one cycle (24-hour period in this case), P2 should be considered instead: $BCPP$ should then be greater than $\text{avg}(NCIR) \cdot Q_{nom}$. This condition is much less demanding than compensating instantaneous imbalance at all times. Designing the equalizer's duty cycle such that $BCPP = \text{avg}(NCIR) \cdot Q_{nom}$ would cause imbalance to rise faster than what the equalizer can compensate at some moments (for example, at P1) thus allowing (to some extent) accumulation of SOC differences over time. Nevertheless, charge transfer

calculated this way would be, by definition, sufficient to compensate them before the 24-hour cycle period ends.

$$\text{avg}(NCIR) \cdot Q_{nom} = 0.286\%/h \cdot 40\ Ah = 0.114\ As/s$$

In a strict sense, $BCPP_{min}$ is equal to $\text{avg}(NCIR) \cdot Q_{nom}$ because this is the actual *minimum* charge that must be transferred to exactly compensate imbalance (no more, no less). Nevertheless, faster balancing can be imposed by design by selecting a higher value of $BCPP_{min}$. This value is selected in principle, pending to confirm that $BCPP \geq \max(NCIR) \cdot Q_{nom}$ does not produce SOC oscillations (see next section).

$$BCPP_{min} = max(NCIR) \cdot Q_{nom} = 1.138\ As/s \tag{4.4}$$

#### 4.1.3.3. Maximum balancing charge per period ($BCPP_{max}$)

Excess of balancing power would produce undesired SOC oscillations. To illustrate this, suppose that the battery pack is imbalanced by an SOC difference just above the 0.5% threshold established to activate the balancing system. Figure 4-6 shows an initially slightly imbalanced battery pack where $\max(SOC_{Bi}) - \min(SOC_{Bi}) = 0.58\%$, equalized by a balancing system in which $T_{bal}$ has not been optimized: $T_{bal}$ has been set to span the whole balancing period $T_{cycle}$. B1 is the strongest battery and B2 is the weakest, so transfer of charge is performed between these two batteries. The balancing system starts to firmly compensate the existing imbalance and charge transfer is kept over the whole cycle. That happens to be too long: a point is reached where imbalance gets overcompensated. At the end of the period, imbalance has not only been compensated but inverted, leaving B1 being the weakest battery and B2 being the strongest. Note that imbalance is again greater than 0.5% at the beginning of the next balancing period so balancing is activated once again. The equalizer would repeat this scheme indefinitely.

To avoid generating SOC oscillations, balancing charge must be limited such that it does not overcompensate SOC imbalance. Taking into consideration that the SOC-imbalance threshold to activate the equalizer has been set in 0.5%, the maximum Balancing Charge Per Period, $BCPP_{max}$, results:

$$\begin{aligned} BCPP_{max} &= 0.5\% \cdot \frac{3600 \cdot Q_{nom}}{T_{cycle}} + avg(NCIR) \\ &= 0.005 \cdot \frac{40\ Ah}{60\ s} \cdot \frac{3600\ s}{1\ h} + 0.114\ As/s = 12.114\ As/s \end{aligned} \tag{4.5}$$

The fact that $BCPP_{max} > \max(NCIR) \cdot Q_{nom}$ confirms that, in the case studied here, it is possible not only to compensate average imbalance accumulated over one cycle, but also to instantaneously compensate imbalance within every balancing period, $T_{bal}$, without causing SOC oscillations.

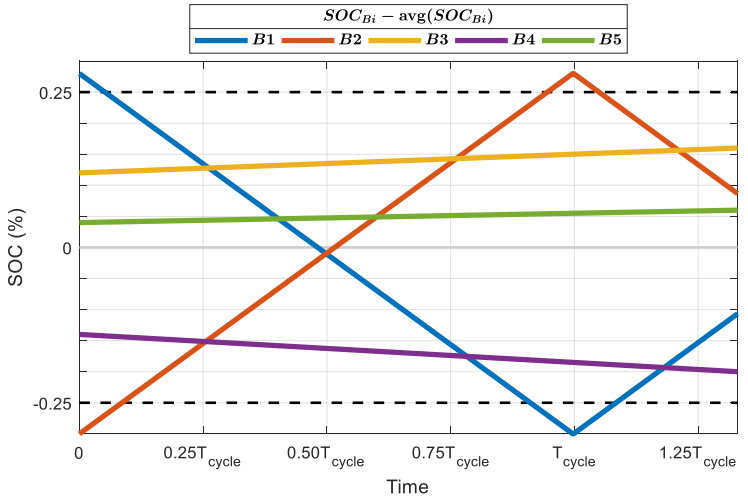


Figure 4-6. State of Charge deviation of battery $Bi$ from the average SOC in a battery pack with overcompensation of imbalance due to $T_{bal}$ set too long: $T_{bal}$ spans the whole balancing period $T_{cycle}$. This produces excessive transfer of charge from the strongest (B1) to the weakest battery (B2): SOC imbalance is overcompensated leading to imbalance again but with B1 and B2 having switched roles.

#### 4.1.3.4. Choice of balancing time ($T_{bal}$)

The equalizer's duty cycle must be chosen such that it complies with the restrictions: $BCPP_{min} \leq BCPP \leq BCPP_{max}$. Solving for $T_{bal}$ in (4.3) and applying the mentioned restrictions, the lower and upper $T_{bal}$ boundaries are obtained in (4.6) and (4.7):

$$T_{bal} > \frac{BCPP_{min} T_{cycle}}{i_{bal\,out} + i_{bal\,in}} = \frac{1.138 \cdot 60}{10 + 11.5} \approx 3.2\ s \tag{4.6}$$

$$T_{bal} < \frac{BCPP_{max} T_{cycle}}{i_{bal\,out} + i_{bal\,in}} = \frac{12.114 \cdot 60}{10 + 11.5} \approx 34\ s \tag{4.7}$$

Pushing $T_{bal}$ towards the upper boundary leads to faster (yet stable) battery balancing process. That means longer but less frequent charge transfers among the monoblocs. On the

contrary, selecting a rather low value of $T_{bal}$ produces shorter, but more frequent, charge transfers. Given these two conditions, a $T_{bal}$ of $20\ s$ is chosen as a trade-off.

The lower boundary of $T_{bal}$ results extremely small and the upper boundary is perhaps too low (roughly half of $T_{cycle}$ is unproductive, reserved for idling). This happens because the battery pack chosen to study the equalizer prototype is not well suited to the balancing capability of the equalizer, which was designed to balance a much larger battery pack –fifteen $200\ Ah$, instead of just five $40\ Ah$, monobloc batteries. For experimental testing, it is suggested to downsize the DC-DC converter in favor of one with smaller output current, consistent with the test battery pack's capacity.

The higher the equalizer's duty cycle, the lower the balancing current that needs to be used. Lower balancing current translates into the monoblocs performing less aggressive partial charge-discharge cycles, which redounds to reduced battery degradation, especially in lead-acid batteries –not so much in li-ion batteries because they can handle partial cycling much better [191].

### 4.1.4. Validation of the control strategy. Simulation results

Performance of the equalizer, controlled with the control strategy designed above, is verified in simulation. The battery pack is simulated over 24-hour operation with the battery parameters specified in Table 4-1, adding initial SOC dispersion: SOCs at the beginning of the simulation, $SOC_{Bi}[0]$, are evenly distributed between 45% and 55%, as shown in Table 4-2.

Table 4-2. Initial States of Charge.

| Monobloc battery | B1 | B2 | B3 | B4 | B5 |
|---|---|---|---|---|---|
| $SOC[0]$ | 55% | 52.5% | 50% | 47.5% | 45% |

Figure 4-7 shows the simulation results. Figure 4-7.a represents the load current $i_{app}$ and the balancing current performed by each of the five monobloc batteries when balancing is activated. The (severely imbalanced) simulated battery pack needs intense balancing at the beginning of the simulation. After that, it only needs balancing occasionally. Some trends can be identified, as analyzed below: balancing is required more often with high (absolute value of) load current, more often when charging than when discharging, and less often right after the sign of $i_{app}$ changes.

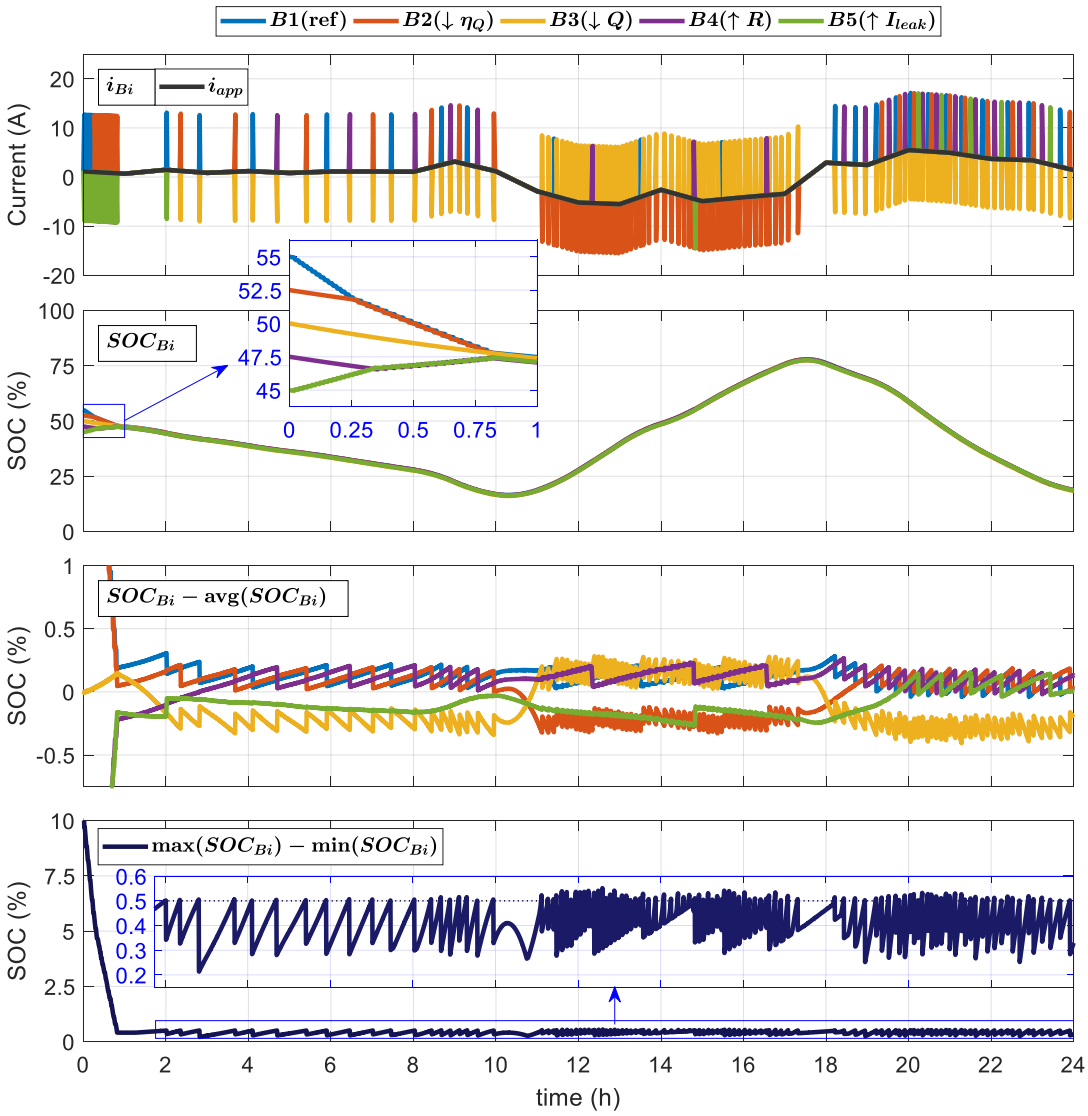


Figure 4-7. Performance of active balancing the simulated battery pack under load. Each monobloc battery represents a different parameter deviation with respect to B1, the reference battery (B2: ↓ $\eta_Q$, B3: ↓ $Q$, B4: ↑ $R$, B5: ↑ $I_{leak}$). a) Current of the five monobloc batteries, which is the sum of the battery pack's discharge current, $i_{app}$, and balancing currents, $i_{bal\ in}$ and $i_{bal\ out}$, b) SOC convergence, c) SOC deviation of battery $Bi$ from the average SOC, d) Maximum SOC difference among the five monobloc batteries.

Figure 4-7.b shows the overall result, which is excellent. SOC convergence is achieved, proving that the balancing control parameters have been selected adequately as they are sufficient to correct the battery pack's natural tendency towards imbalance, while the

transference of charge is not excessive –SOCs do not oscillate. The balancing system rapidly compensates the (large) initial SOC deviations, i.e., the five batteries reach the same SOC (within a 0.5% tolerance window) in approximately 48 minutes (0.80 h). And from then on, the equalizer keeps the battery pack balanced, with only occasional interventions. The zoomed part of Figure 4-7.b shows that the rate of balancing of battery $B_i$, $r_{bal\,B_i}$, during stages when $n$ batteries are being balanced at the same time is proportional to $1/n$:

$$r_{bal\,B_i}(t) = d\left(SOC_{Bi}(t) - avg\big(SOC_{Bi}(t)\big)\right)/dt$$
$$\simeq r_{bal\,B_i}[k] = \Delta\big(SOC_{Bi}[k] - avg(SOC_{Bi}[k])\big)/\Delta t$$

- During $0\ h < t < 0.27\ h$, only B1 and B5 are balanced, at a rate of $|r_{bal}|_{B1,B5} \approx 2.5\%/0.27\ h = 9.3\%/h$ each.
- During $0.27\ h < t < 0.80\ h$, B2 and B4 are also balanced, together with B1 and B5, at a rate of $|r_{bal}|_{B1,B2,B4,B5} \approx 2.5\%/0.53\ h \approx 0.5 \cdot 9.30\%/h = 4.65\ \%/h$ each.

Figure 4-7.c shows SOC deviation of the individual monoblocs, defined as the difference between $SOC_{Bi}$ and the average SOC, avg($SOC_{Bi}$). This graph illustrates how the equalizer continuously corrects the imbalance caused by discrepancy in the batteries' parameters. Some operation conditions trigger activation of the balancing system more often than others:

- High current (in absolute value) cause SOC to vary faster than low current (see (4.1)). Consequently, SOC differences also grow faster when the batteries are subjected to high current values. Note that the more $i_{app}$ departs from zero, the more often balancing is activated.
- Charging instigates $SOC_{B2}$ to rise more slowly than $SOC_{B1}$ due to lower coulombic efficiency. Discharging, on the other hand, does not make $SOC_{B2}$ deviate from $SOC_{B1}$ –both curves run parallel when no external balancing is used (see Figure 4-5.c also). Thus, charging causes more activation of the balancing system than discharging.
- Around $i_{app}$ sign changes ($10{:}00 < t < 11{:}05$ and $17{:}20 < t < 18{:}15$), the SOC tendencies of B2 and B3 swap: $SOC_{B2}$ and $SOC_{B3}$ graphs naturally tend to intertwine, so they get enclosed inside the 0.5% SOC threshold without external balancing, i.e., with the equalizer being off.

Figure 4-7.d reveals the overall outcome of the equalizer's operation: the balancing system rapidly compensates the extreme imbalance existing at the beginning of the simulation. To do so, the equalizer gets activated every balancing period for the first 48

minutes of simulation; at this point, the battery pack is considered balanced ($\max(SOC_{Bi}) - \min(SOC_{Bi}) < 0.5\%$). From then on, activation of the equalizer follows the natural tendency of the pack towards imbalance, so the equalizer works less frequently with low absolute values of $i_{app}$ and it works more frequently whit high positive values of $i_{app}$, restituting SOC balance straightaway each time the maximum SOC difference among the five monobloc batteries surpass the stablished threshold of 0.5%.

### 4.1.5. Secondary observations

Once the performance of the balancing system has been verified and analyzed, some secondary observations are made:

#### 4.1.5.1. Efficiency of the balancing process

The efficiency of the balancing process is obviously less than 100% because:

- Power converter's efficiency, $\eta_{pc}$, is not perfect.
- The monoblocs' round-trip energy efficiency is not perfect because the cell's internal resistance causes power loss in the form of heat generation.
- The monoblocs' coulombic efficiency, $\eta_{Q\,Bi}$, is not perfect because part of the charge does not cause SOC increase in the battery. Instead, this part of the charge is used in side-reactions or in the self-discharge process.

Consequently, not all the charge transferred from the strongest to the weakest battery is devoted to SOC balancing. However, this short-term loss of charge is a cost worth paying in exchange of avoiding a weak cell to limit the performance of the whole battery pack in the short-term, and of extending the battery pack's life in the long-term.

#### 4.1.5.2. Importance of having a good battery model

In the presented simulation, the estimated States of Charge are assumed to be known (exact $SOC_{Bi}$ estimations). Thus, in the simulation, the equalizer acts exactly when needed: it does not perform wrong charge transfers –note that they could take place if SOC estimations were inaccurate. Wrong balancing is a common drawback of simple balancing algorithms that estimate SOC based exclusively on voltage [97], given that voltage is not a good indicator of SOC. For example, differences in internal resistances cause voltage differences that are not related to SOC.

Furthermore, the four inconsistencies in the battery parameters that have been studied here ($\eta_Q$, $Q$, $R$, and $I_{leak}$), as well as others, can operate simultaneously in reality and to diverse extents in the different cells/monobloc batteries of a battery pack. Discerning the specific

influence on the individual cell/battery SOC caused by each inconsistent parameter is, consequently, challenging. Battery models and parameters estimation must be highly precise to estimate SOC accurately. Only with proficient battery models will the equalizer be able to effectively diagnose when and what to balance.

Exact SOC estimation (as has been assumed in this paper) is an unrealistic assumption, although practical and reasonable to analyze operation of the balancing system within the scope of this work. Use of a refined battery model is planned for the experimental study of the equalizer prototype.

## 4.2. Experimental study

The theoretical study is a pre-requisite to put into operation the equalizer prototype. After completing the theoretical analysis of the balancing system, the next scheduled works were: to model and characterize the actual battery pack, to tune the control algorithm parameters accordingly, to program the control scheme in the equalizer's controller and, finally, to perform experimental tests to validate the equalizer prototype. These works got started, but irruption of coronavirus altered the intended itinerary of research works.

The prototype (Figure 4-8) was originally ideated with a voltage-based balancing strategy. It would periodically transfer charge from the battery with the highest voltage to the one with the lowest. This is a poor control strategy because voltage-based balancing is imprecise: external voltage does not faithfully represent battery SOC. This method is regarded as ineffective [132] and its use is relegated to low-end equalizers. For this reason, an improved control algorithm based on SOC is proposed in this work.

This second part of the present chapter presents the finished and future works related with experimental testing and validation of the equalizer prototype.

### 4.2.1. Description of the equalizer prototype

The front printed circuit board (Figure 4-9) contains the power supply connections, the dsPIC microcontroller (dsPIC33EV256GM106), four user interface buttons programmable to perform certain basic commands, one reset button, one button to manually operate the DC-DC converter, a liquid-crystal display (Fordata FDCC4004A) and its controller (Sunplus SPLC780D), two red leds, and fifteen analog-to-digital converters that, together with fifteen operational amplifiers (Texas Instruments MC33078P), adapt the voltage signals of the (up to) fifteen series-connected batteries that can conform the battery pack.

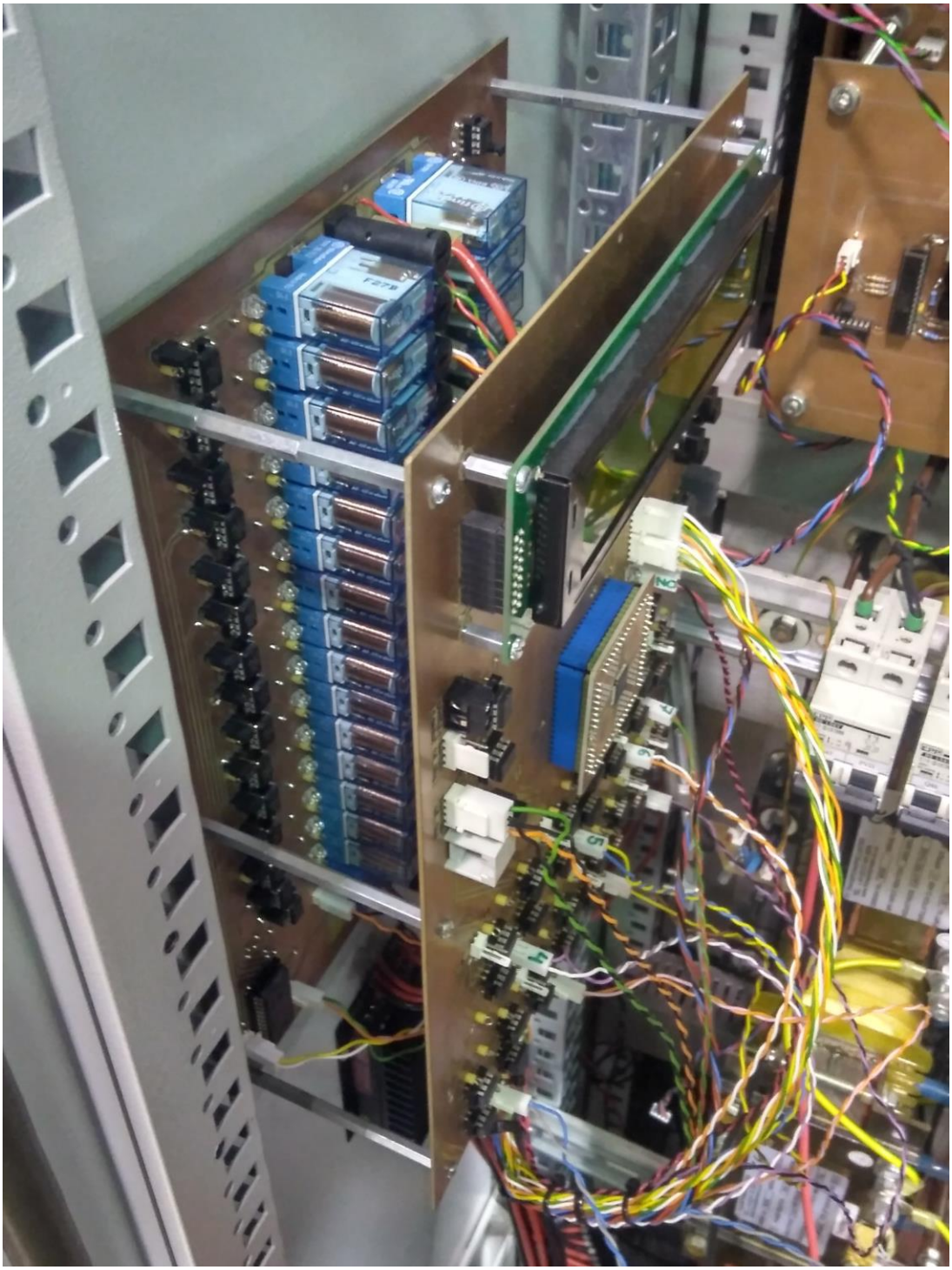

Figure 4-8. Equalizer prototype, with elements of the GAEI's microgrid in the background.

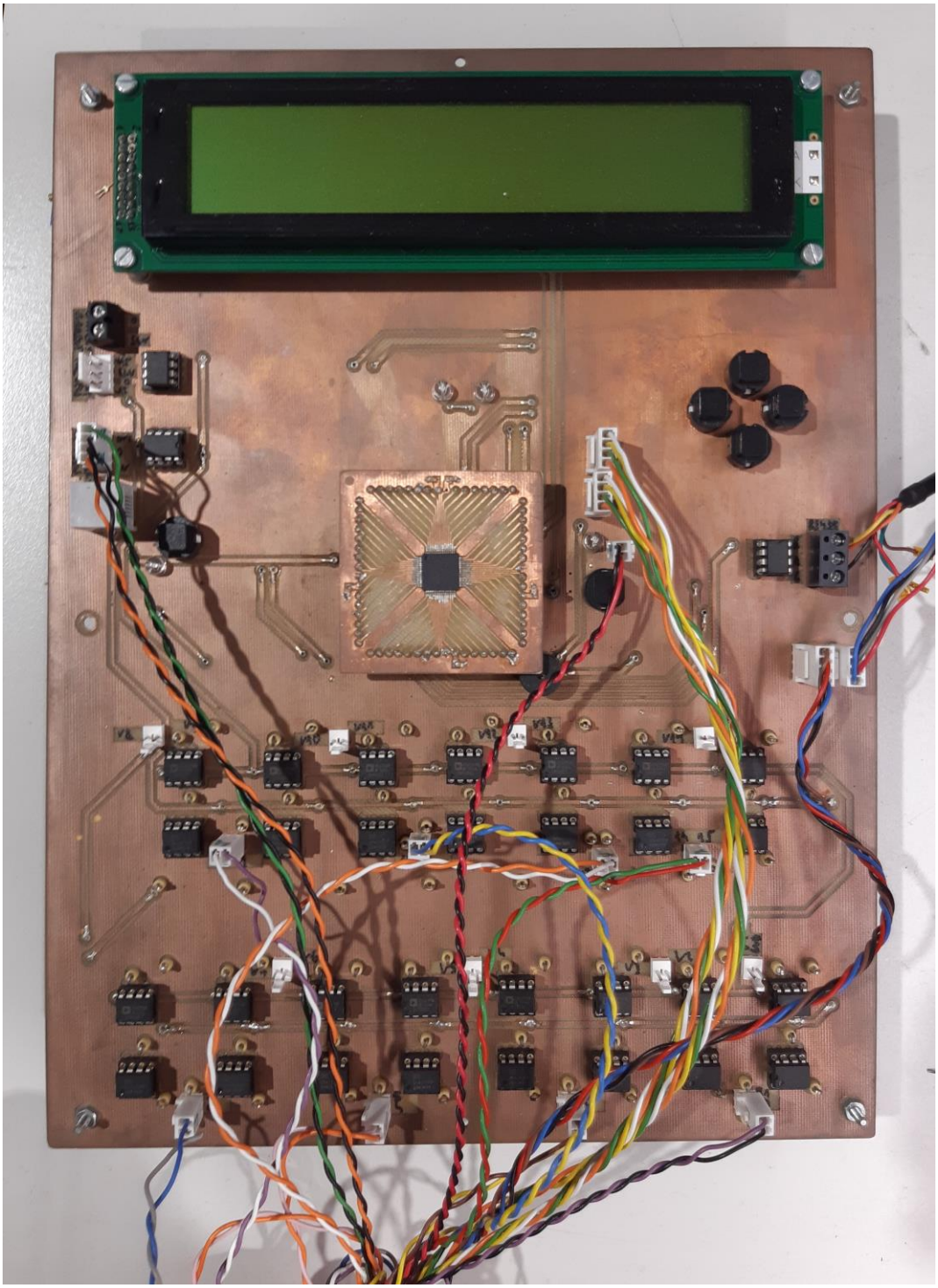

Figure 4-9. Front board of the equalizer prototype.

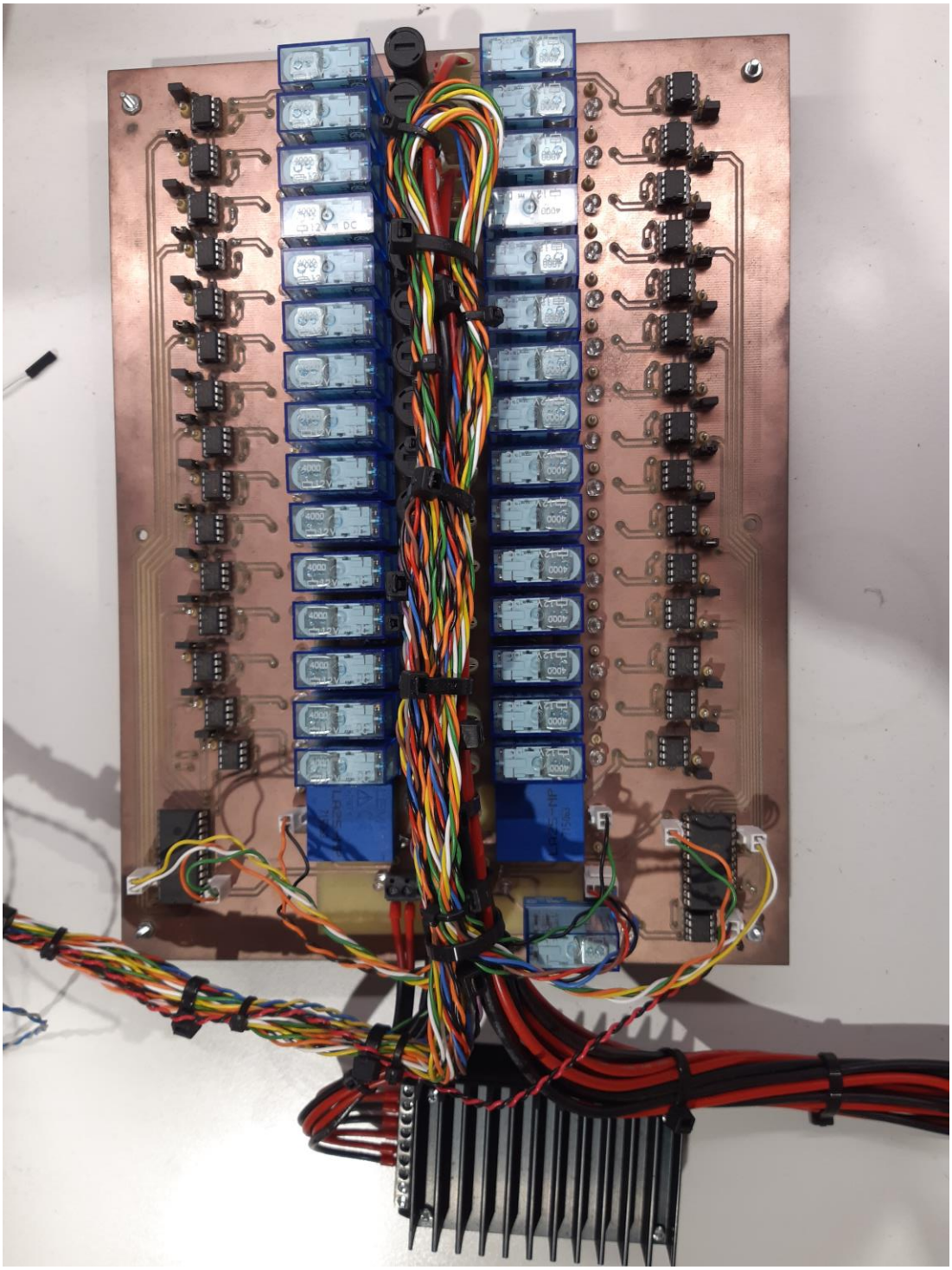

Figure 4-10. Back board of the equalizer prototype.

The back printed circuit board (Figure 4-10) contains two arrays of fifteen $16\,A$ relays (Finder 40.61.9.012.4000), one led per relay, two decoders (Texas Instruments CD4514BE), fifteen $16\,A$ fuses, thirty MOSFETs drivers (Microchip MCP1407), two $36\,A$ hall-effect current sensors (for the DC-DC converter's input and output currents, LEM LA 25-NP), the DC-DC converter (Traco Power TEP 150-2413WI), and an alarm buzzer. Serial communication among both boards is possible thanks to a Universal Asynchronous Receiver-Transmitter (Maxim Integrated MAX 485) configured for RS-485 protocol.

### 4.2.2. Battery modeling

The battery pack used for experimental testing is composed of five Lead Crystal batteries, in which differential aging was artificially caused. The batteries were (differently) abused to induce imbalance. An aging platform was created to help subjecting the batteries to abusive conditions. The platform design and control are described below.

After artificially unbalancing the battery pack, the monobloc batteries needed to be characterized to parametrize the equalizer's control, which basic operation, based on SOC estimations, has been explained above. Precise SOC estimation is thus a key part of the equalizer's control but, at the same time, the SOC estimation algorithm should be kept simple. Indeed, accuracy and simplicity must go together since the model will be coded into the equalizer's microcontroller, which has limited memory and calculation capability. The Thevenin model used in simulations (Section 4.1) is too basic to fully capture voltage dynamics and, although coulomb counting (4.1) is a reasonably good SOC estimation method, integration of current can cause small measurement errors to accumulate over time. To solve both issues, it is planned to use the Enhanced Self-Correcting (ESC) equivalent model presented in [94] and to periodically correct the coulomb-counting SOC estimation by means of an $OCV$ vs. $SOC$ look-up table.

#### 4.2.2.1. Aging platform. Description

A simple cycling test platform has been designed to automatically perform battery charge-discharge cycles to cause accelerated aging. Figure 4-11 shows the electrical plan of the aging platform. Different cycling schemes were to be applied to each of the monobloc batteries, with the objective of generating imbalance among them. A battery pack with a high imbalance level is useful in the experimental-testing stage because it permits to discern the effects of imbalance and to evaluate the performance of the equalizer.

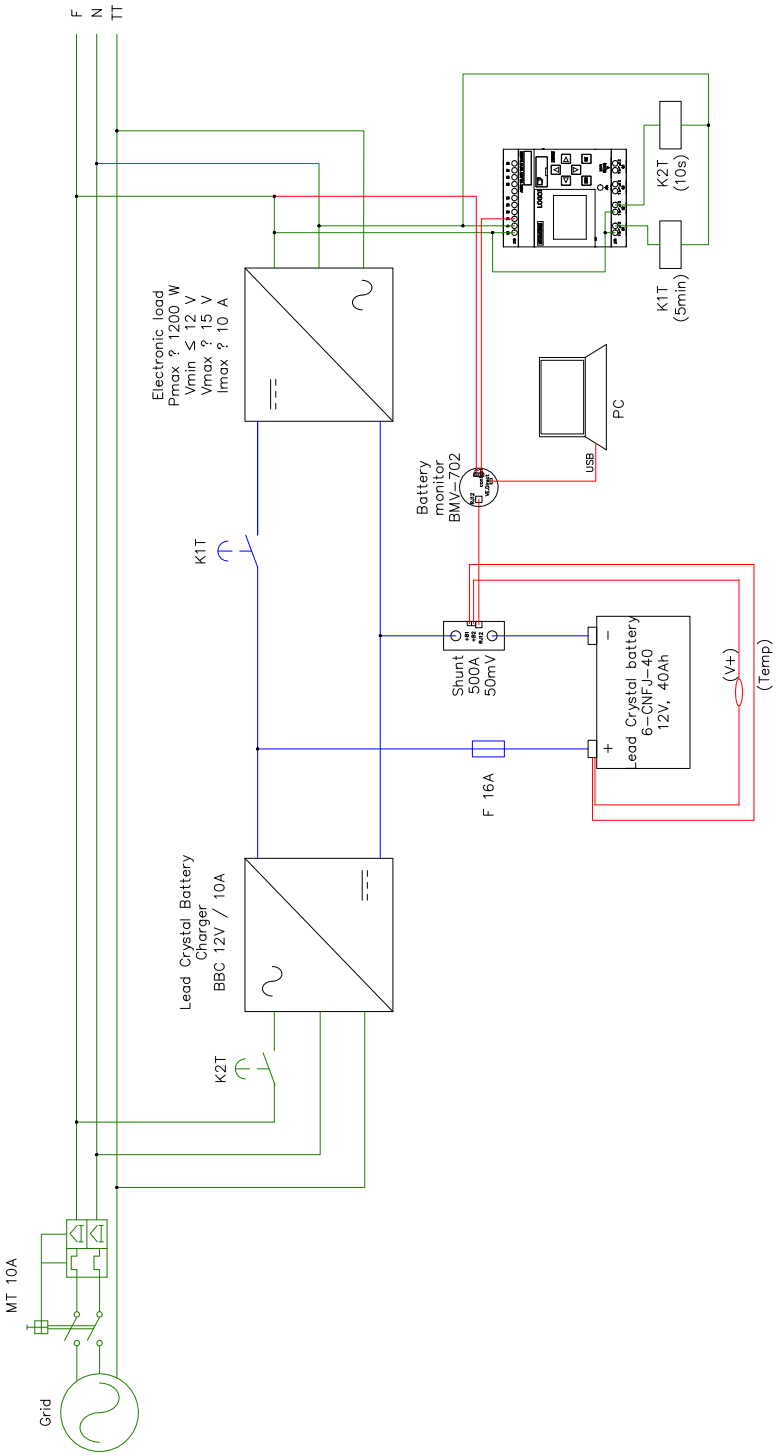


Figure 4-11. Electrical plan of the aging (cycling) platform

The main elements of the cycling platform are:

- Battery: Five monobloc batteries Lead Crystal 6-CNFJ-40, $12\,V$, $40\,Ah$, were cycled and abused in the platform.
- Charge-discharge elements: Cycling is carried out by a Lead Crystal BBC 12V/10A battery charger and a Hewlett-Packard 6060b electronic load set in CC/CV mode.

  During the CC stage, the electronic load withdraws $10\,A$ from the connected battery. The end of discharge was established by different cut-off voltages for some of the batteries (to overdischarge them), while for others it was set by a certain level of DOD (performing different DOD cycles leads to dissimilarly degrade the five batteries). In some occasions, the charger was substituted by an Elektro-Automatik PSI 9750-40, ($0\ldots10\,kW$, $0\ldots750\,Vdc$, $0\ldots40\,A$) to subject the batteries to overcharging.
- Thermal chamber: Temperature was kept constant throughout the tests thanks to a 35-liter thermal chamber Mytron KPK 35.
- Protection elements: The platform is protected against overcurrent in AC and DC. A $10\,A$ thermomagnetic circuit breaker protects the AC connections, and a $16\,A$ fuse protects the positive cable of the battery –the fuse rating proved to be too low to withstand the current peak produced when connecting the electronic load, so it should be replaced by a $16\,A$ or $25\,A$ fuse.
- Control elements: Control logic is implemented through several elements, namely, a Victron Energy BMV 702 battery monitor (thanks to its programmable dry contact); two RS Pro 144-1600 single pole-double throw relays ($12\,A$, $230\,V$ coil); and a logic module Siemens LOGO! 6ED1052-1FB08-0BA0.
- Monitoring elements: Battery current and voltage are measured by the battery monitor Victron Energy BMV 702 and a BMV $500\,A$ / $50\,mV$ current shunt. Data can be logged into an excel file if the battery monitor is connected to a computer.

Figure 4-12 shows the platform being used to cycle one of the batteries at high temperature. In the picture, the battery under test is inside the thermal chamber, which is located on the left, programmed to sustain $60\,°C$ constant temperature with unregulated humidity. On the bottom right, there is the electronic load, idling at that moment. Just above it, on the right, there is the cycling platform, controlling the cycling. The battery charger is to the left of the platform; it was performing a $0.99\,A$ at the moment when the picture was taken. Just above the battery charger, there is the current shunt that communicates with the battery monitor (on the top right), which (blurry) reads a terminal temperature of $61.3\,°C$.


Figure 4-12. Cycling platform used to abuse the monobloc batteries to induce accelerated aging.

#### 4.2.2.2. Aging platform. Control

The control scheme implemented into the cycling platform controller is very simple: it will indefinitely perform repetitive cycles of a pre-defined DOD:

- The electronic load is configured to discharge the battery at a $C/4$ rate ($10\ A$). The DC relay switches the connection between the electronic load and the battery.
- The battery monitor senses the battery current and voltage and estimates battery SOC applying coulomb counting corrected with the Peukert's law to account for reduced deliverable capacity at higher discharge current:

$$i_{app}^{\lambda} t_{fd} = C_{1A} = cnt$$

where $C_{1A}$ represents the ampere-hours discharged at a $1\ A$ rate, $i_{app}$ is the discharge current, $\lambda$ is the Peukert constant (normally $\lambda \in [1.09, 1.25]$ in sealed Pb-acid batteries), and $t_{fd}$ is the full-discharge time.

The cycling platform can be controlled either based on voltage or on SOC. The battery monitor is programmed to close the dry contact when the battery reaches a certain voltage or SOC value. $SOC = 100\%$ and it remains closed until the discharge reaches the pre-defined DOD. Figure 4-13 shows the dry contact signal configured to activate cycles of $DOD = 60\%$.

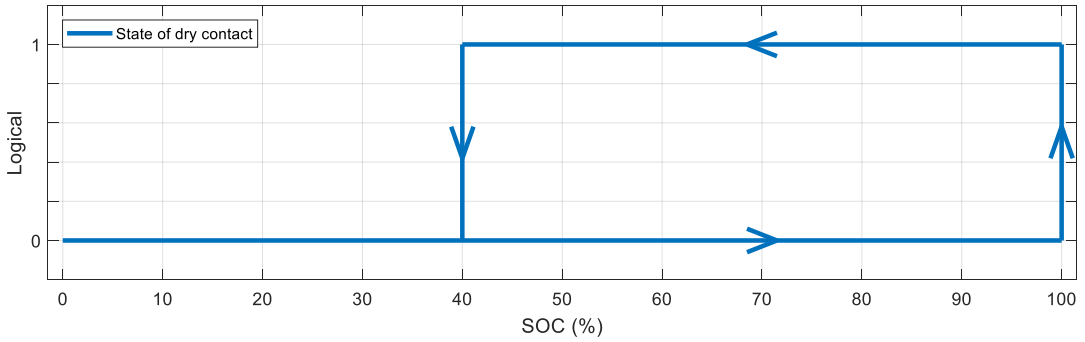


Figure 4-13. Activation of the battery monitor's dry contact, configured with DOD= 60% hysteresis.

- The logic module LOGO! is programmed to open/close the AC/DC relays depending on whether the dry contact of the battery monitor is on or off.
- The electronic load's DC relay gets closed after the battery has reached 100% SOC and stayed for 5 minutes. The relay remains closed until the battery monitor's dry contact switches off.
- The battery charger's AC relay gets closed ten seconds after the battery monitor's dry contact switches off. Having both relays (the AC and the DC ones) closed at the same time is not allowed by design. In addition to their dependency on the dry contact state, which already makes that situation implicitly impossible, electrical interlock is explicitly introduced into the control scheme of the logical module (see Figure 4-14).

Figure 4-14 illustrates the control logic programmed into the logical module LOGO! (using the software LOGO! Soft Comfort). There is only one digital input (*I1*), which is equal to the state of the battery monitor's dry contact. This signal is dependent on the battery SOC and exhibits sharp hysteresis, as represented in Figure 4-13. The upper line of the diagram in Figure 4-14, which controls the activation of the electronic load, is examined first. The delay block *B006* is an on-delay that keeps the electronic load from getting activated for ten minutes after *I1* becomes 1 (SOC reaches 100%). The *AND* block *B001* warrantees that the battery

charger is off to activate the electronic load (*Q1*). As soon as the battery SOC drops by a 60% (or any other DOD value, previously programmed in the dry contact controller), *I1* becomes 0, which instantaneously switches off *Q1*. Parallelly, the lower line of the diagram controls the activation of the battery charger. The delay block *B007* is an on-delay that keeps the battery charger from getting activated for five seconds after *I1* becomes 0 (SOC reaches 40%). The *AND* block *B005* warrantees that the electronic load is off to activate the battery charger (*Q2*). As soon as the battery SOC rises up to 100% again, *I1* becomes 1, which instantaneously switches off *Q2*.

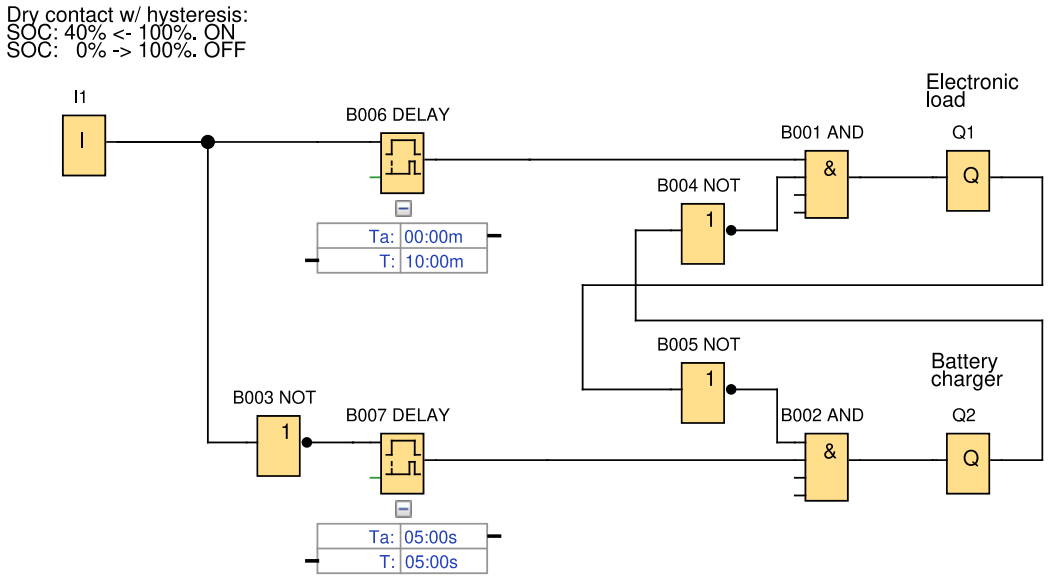


Figure 4-14. Control diagram programmed in the logical module LOGO! to perform cycles of 60% DOD.

The platform was used to cycle the monobloc batteries under abusive conditions to generate accelerated degradation. The batteries were subjected to overdischarge (as low as $6\,V$ in some cases) at high temperature (from $60\,°C$ to $70\,°C$) over extended periods of time (up to three weeks under abusive conditions, and stored for several months afterwards). Overcharge (as high as $15\,V$ in some cases) was also applied utilizing the power supply which provides more flexibility to mistreat the batteries within a wider voltage range. In addition, adequately modifying the control logic allowed to dispense with cycling in some cases, in favor of sustaining high or low voltage over a predefined period of time. All four employed conditions (extreme high and low voltages, overheating and prolonged storage times) are causes of severe damage to the batteries [60].

DISCHARGE CURRENT AND END VOLTAGE

| Discharge current (A) | End voltage (V) |
|---|---|
| 0.05C or below or Intermittent discharge | 11.4 |
| 0.05C of current close to it | 11.1 |
| 0.1C of current close to it | 10.8 |
| 0.2C of current close to it | 10.5 |
| From 0.2C to 0.5C | 10.2 |
| From 0.5C to 1C | 9.6 |
| From 1C to 3C | 9.0 |
| Current in excess of 3C | 7.8 |

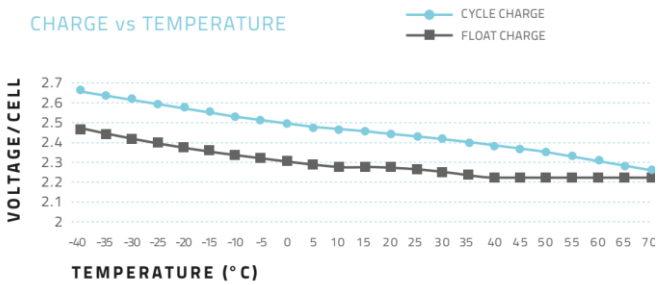


Figure 4-15. Charge and discharge characteristics of the Lead Crystal 6-CNFJ-40. Reproduced from the datasheet form the manufacturer, Betta Batteries.

The five Lead Crystal 6-CNFJ-40, $12\,V$, $40\,Ah$ batteries (see characteristics in Figure 4-15) were assigned names Batt1 to Batt5, analogously to the theoretical study. Batt2 to Batt5 were cycled under abusive operating conditions to induce accelerated aging. Batt1 was left untouched, to serve as the reference against which the other four can be compared to evaluate the degree of induced degradation / imbalance achieved. Specifically, these were the abuse tests performed:

- Batt1 was not abused to keep it as the reference.
- Batt2 performed twelve 100% DOD cycles at $60\,°C$ and it got ultra-deep discharged once, down to $6\,V$.
- Batt3 was left at 0% SOC over 18 days, 75% of the time at ambient temperature and the last 25% at $70\,°C$.
- Batt4 was overheated at $70\,°C$, 80% SOC, over 20 days, and then overcharged at $15\,V$, $70\,°C$, over 48 hours –the latter produced venting inside the sealed monobloc, causing the battery case to swell slightly.

- Batt5 was already the oldest battery, having six more months of shelf-storage time than the rest. When tested, it performed seven 40% DOD cycles at 60 °$C$ and seven voltage-limited cycles between 8.5 $V$ (overdischarge) and 14.7 $V$, also at 60 °$C$

After performing the abuse tests the batteries were stored, at intermediate SOC.

#### 4.2.2.3. Battery model

The battery model must be simple and allow accurate SOC estimation. On one hand, simplicity is required to program the model equations in the equalizer's microcontroller, which has limited computational capability. On the other hand, accurate SOC estimation is essential for the balancing system to adequately identify imbalance. Wrong imbalance assessment would cause the equalizer to not transfer enough charge among the imbalanced monoblocs or, what is worse, to transfer charge among the wrong monoblocs –thus causing imbalance rather than compensating it.

Taking these requirements into account, the ESC model [94] is selected. This model, represented in Figure 4-16, consists of an equivalent electrical circuit that contains an SOC-dependent voltage source $OCV(z)$ (where $z$ represents per unit SOC), a hysteresis element ($hyst$), two parallel resistor-capacitor pairs, ($R_1C_1 + R_2C_2$), which represent the dynamic response of the cell due to diffusion processes, and a series resistance, $R_0$, which represents the instantaneous drop in the cell voltage when current is applied.

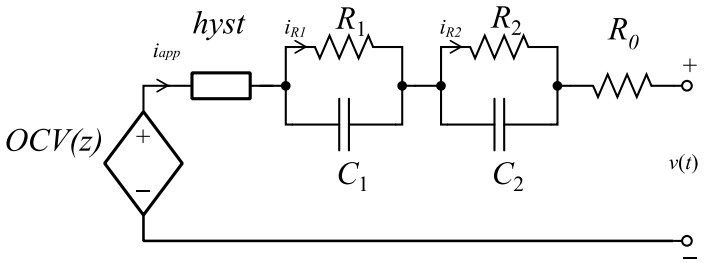


Figure 4-16. ESC equivalent circuit model.

The discrete time equation that describes the cell's response when a current $i_{app}$ is applied is:

$$v[k] = OCV(z[k]) + (M_0 s[k] + Mh[k]) - \left(R_1 i_{R_1}[k] + R_2 i_{R_2}[k]\right) - R_0 i_{app}[k] \quad (4.8)$$

where $k$ represents the discrete time, $v$ is the terminal voltage, which is the result of adding four terms: an open-circuit voltage term, $OCV(z)$, a hysteresis term, $(M_0 s + Mh)$, a diffusion term, $-\left(R_1 i_{R_1} + R_2 i_{R_2}\right)$, and an internal resistance term, $-R_0 i_{app}$. The variables in (4.8) are calculated as follows:

$$i_{R_j}[k] = exp\left(\frac{-\Delta t}{R_j C_j}\right) i_{R_j}[k-1] + \left(1 - exp\left(\frac{-\Delta t}{R_j C_j}\right)\right) i_{app}[k-1] \tag{4.9}$$

$$h[k] = A_H[k-1]h[k-1] + (A_H[k-1] - 1)sgn\left(i_{app}[k-1]\right) \tag{4.10}$$

$$A_H[k] = exp\left(-\left|\frac{\eta_Q[k] i_{app}[k] \gamma \Delta t}{Q}\right|\right) \tag{4.11}$$

$$\eta_Q[k] = \begin{cases} 1, & i_{app}[k] \geq 0 \\ \eta_Q, & i_{app}[k] < 0 \end{cases} \tag{4.12}$$

$$z[k] = z[k-1] - \frac{\eta_Q[k]\Delta t}{Q} i_{app}[k] \tag{4.13}$$

$$s[k] = \begin{cases} sgn\left(i_{app[k]}\right), & i_{app}[k] \neq 0 \\ s[k-1], & i_{app}[k] = 0 \end{cases} \tag{4.14}$$

where $j = \{1,2\}$, $R_j$ is the resistance of the $j$ RC parallel pair, $C_j$ is the capacitance of the $j$ RC parallel branch, $i_{R_j}$ are the currents graphically defined in Figure 4-16, $i_{app}$ is the battery discharge current (note that self-discharge and leakage currents are considered insignificant, thus $i_{net} \simeq i_{app}$, see (2.8)), $h$ is the unitless hysteresis state $-1 \leq h \leq 1$, sgn$(x)$ is the sign function of $x$, $\eta_Q$ is the coulombic efficiency during charging, $\gamma$ is the hysteresis time constant, $\Delta t$ is the sampling time, $Q$ is the battery capacity, and $z$ is the per-unit battery SOC. Note that the original formulation of the model uses coulomb counting to estimate battery SOC (4.13). Nevertheless, it is planned to calibrate the SOC estimation through (4.8) solved for $OCV$ (with $v$, the measured cell voltage, being an input), and the look-up tables $OCV$ vs. $SOC$ to achieve improved accuracy. The sampling time, $\Delta t$, must be chosen in accordance with the rate at which the current profile $i_{app}$ varies. In this case, $\Delta t = 1\ s$ has been selected.

These equations will be reviewed in Chapter 5, where this equivalent circuit model is complemented with the effects of degradation.

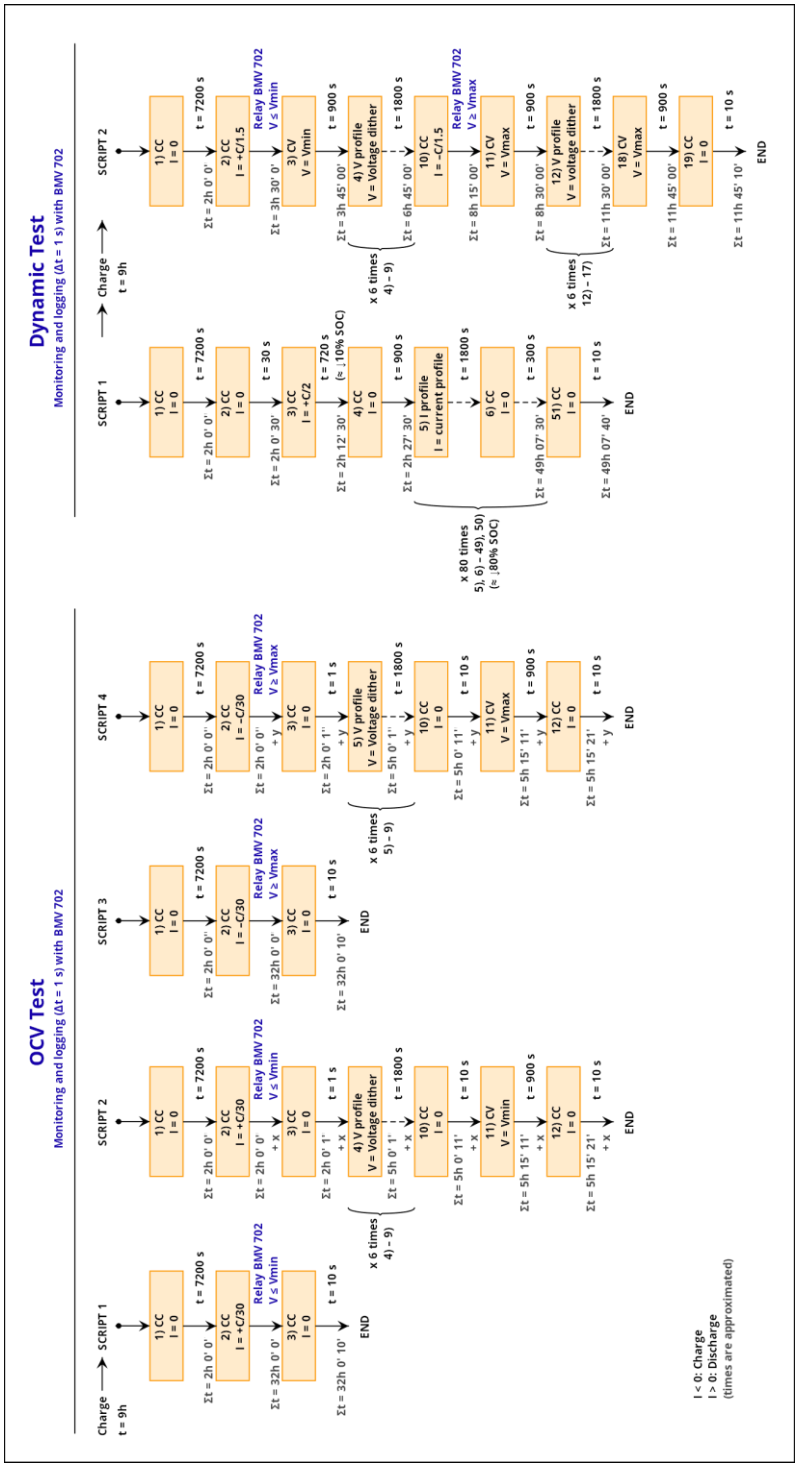


Figure 4-17. Procedure to perform the OCV and the dynamic tests to identify the parameters of the ESC model.

#### 4.2.2.4. Characterization tests

The testing procedure for parameter estimation was adapted from [94]. The procedure was originally described for small-capacity lithium-ion cells used in battery packs of electric vehicles. Voltage boundaries and current profiles have been adapted to characterize large-capacity lead-acid monoblocs used for testing the equalizer, with a typical microgrid load profile, instead. Two characterization tests were carried out, both at $25\,°C$: "OCV test", utilized to identify the batteries' $OCV$ vs. $SOC$ curves, their actual capacity, $Q$, and their coulombic efficiency, $\eta_Q$; and "dynamic test", utilized to estimate the other parameters of the ESC model. The OCV and dynamic tests are schematized in Figure 4-17. They are described next, together with the procedure followed to estimate the model parameters.

- OCV test. Script #1: Slow CC discharge:
    1) Soak the cell at $25\,°C$ for two hours.
    2) Discharge the battery at a constant-current rate of $C/30$ until terminal voltage reaches $V_{min} = 10.2\,V$, the low cut-off voltage indicated by the manufaturer (see Figure 4-15).
    3) Let the battery rest for some $10\,s$ to finish the first script.

- OCV test. Scrip #2. Slow CV discharge and hysteresis reduction:
    1) Soak the cell at $25\,°C$ for two hours.
    2) At this point, voltage should be greater than $V_{min}$. Discharge the battery at a $C/30$ rate until the voltage is equal to $V_{min}$.
    3) Idle for at least $1\,s$ to facilitate identification of step progress in the results.
    4) – 9) Apply a 30-minute dither cycle to eliminate hysteresis. Repeat six times in total.
    10) Let the battery rest for some $10\,s$.
    11) Perform constant-voltage discharge at $V_{min}$ for 15 minutes.
    12) Let the battery rest for some $10\,s$ to finish the second script.

- OCV test. Script #3: Slow CC charge:
    4) Soak the cell at $25\,°C$ for two hours.
    5) Charge the battery at a constant-current rate of $C/30$ until terminal voltage reaches $V_{max} = 14.7\,V$, the high cut-off voltage indicated by the manufaturer (see Figure 4-15).
    6) Let the battery rest for some $10\,s$ to finish the third script.

- OCV test. Scrip #4. Slow CV charge and hysteresis reduction:
    1) Soak the cell at $25\,°C$ for two hours.
    2) At this point, voltage should be smaller than $V_{max}$. Charge the battery at a $C/30$ rate until the voltage is equal to $V_{max}$.

3) Idle for at least $1\ s$ to facilitate identification of step progress in the results.
4) – 9) Apply a 30-minute dither cycle to eliminate hysteresis. Repeat six times in total.
10) Let the battery rest for some $10\ s$.
11) Perform constant-voltage charge at $V_{max}$ for 15 minutes.
12) Let the battery rest for some $10\ s$ to finish the fourth script.

(Note that subjecting five monobloc batteries to the OCV test takes over $372.5\ h = 15.5$ days.) Now, the dynamic test is described:

- Dynamic test. Script #1. Apply dynamic current profile:
  1) Soak the cell at $25\ °C$ for two hours.
  2) Let the battery rest for 30 extra seconds.
  3) Discharge the battery at a (rather high) constant-current rate of $C/2$ for 12 minutes to reduce the battery $SOC$ from 100% to 90% approximately.
  4) Idle for 15 minutes.
  5) – 50)Cycle the battery over the SOC range of interest, nominally from 90% down to 10%, with a current profile that produces enough dynamic behavior followed by five minutes of idling. The number of repetitions is determined by $(10\% - 90\%)/\Delta SOC_{1cycle}(\%)$; in this case, the overall battery SOC decay in one cycle is $\Delta SOC_{1cycle} = -1\%$, so 80 cycles must be performed.
  51) Let the battery rest for some $10\ s$ to finish the first script.

- Dynamic test. Scrip #2. CC charge-discharge cycling and hysteresis reduction:
  0) Fully charge the battery.
  1) Soak the cell at $25\ °C$ for two hours.
  2) Discharge the battery at a (rather high) constant-current rate of $C/1.5$ until terminal voltage reaches $V'_{min} = 9.6\ V$, as indicated by the manufaturer (see Figure 4-15).
  3) At this point, stabilized voltage should be greater than $V'_{min}$. Perform constant-voltage discharge at $V'_{min}$ for 15 minutes to fully discharge the battery.
  4) – 9) Apply a 30-minute dither cycle to eliminate hysteresis. Repeat six times in total.
  10) Charge the battery at a (rather high) constant-current rate of $C/1.5$ until terminal voltage reaches $V_{max} = 14.7\ V$, as indicated by the manufacturer (see Figure 4-15).

11) At this point, stabilized voltage should be smaller than $V_{max}$. Perform constant-voltage charge at $V_{max}$ for 15 minutes to fully charge the battery.
12) – 17) Apply a 30-minute dither cycle to eliminate hysteresis. Repeat six times in total
18) Keep the battery at constant-voltage $V_{max}$ for 15 minutes again.
19) Let the battery rest for some 10 $s$ to finish the second script.

(Note that subjecting five monobloc batteries to the dynamic test takes over $304.3\ h = 12.7$ days.)

Battery tests were started but had to be interrupted because of the lockdown decreed as a consequence of coronavirus. Some preliminary results were indeed obtained throughout the first attempts but, unfortunately, they were not satisfactory –see explanation below. Improvements to the test scripts are suggested in this section for future consideration. It is expected that such improvements will lead to successful parametrization of the battery models. The test results are critically reviewed in the following sub-sections, and comments are provided to make testing more effective.

The testing setup used in the first attempt was adequate and will be used again in the future. It consists of:

- Controllable power supply, Elektro-Automatik PSI 9750-40, $0\ldots10\ kW$, $0\ldots750\ Vdc$, $0\ldots40\ A$, used to perform negative parts of the current profile (charging).
- Controllable electronic load with energy recovery, Elektro-Automatik ELR 9750-44, $0\ldots7\ kW$, $0\ldots750\ Vdc$, $0\ldots44\ A$, used to perform positive parts of the current profile (discharging).
- Battery monitor, Victron Energy BMV 702, used to sense voltage and current every one second, and to communicate data to the computer.
- A computer, used to log and analyze the test data.

The power supply and the electronic load were initially used to transfer test data to the computer, but the battery monitor proved better performance because it provides three significant decimal places for voltage instead of the two offered by the power devices' logging system.

#### 4.2.2.5. OCV test

The OCV test consists in slowly charging and discharging the batteries to identify their characteristic $OCV$ vs. $SOC$ curves. Voltage and current are logged during the test with a sampling time $\Delta t = 1\ s$.

These data are used to calculate the battery capacity, $Q$, and its coulombic efficiency, $\eta_Q$. The total capacity is equal to the net ampere-hours discharged over scripts #1 and #2. The net ampere-hours charged over scripts #3 and #4, however, result slightly higher than $Q$ since the coulombic efficiency of the battery is not perfect. The value of $\eta_Q$ is computed applying the following definitions:

$$\begin{cases} i_{OCV}^{+} \coloneqq i_{OCV} \geq 0\ (discharge) \\ i_{OCV}^{-} \coloneqq i_{OCV} \leq 0\ (charge) \end{cases} \tag{4.15}$$

$$Q = \Delta t \cdot \Sigma_0^{k_{end}^{+}} i_{OCV}^{+} \tag{4.16}$$

$$\eta_Q = \frac{Q}{\Delta t \cdot \Sigma_{k_{end}^{+}}^{k_{end}^{-}} i_{OCV}^{-}} \tag{4.17}$$

where $i_{OCV}$ is the current measured throughout the whole test, $i_{OCV}^{+}$ and $i_{OCV}^{-}$ are defined from it as the non-negative (discharge) and the non-positive (charge) values, $k_{end}^{+}$ is the discrete time at the end of script #2, and $k_{end}^{-}$ is the discrete time at the end of script #4.

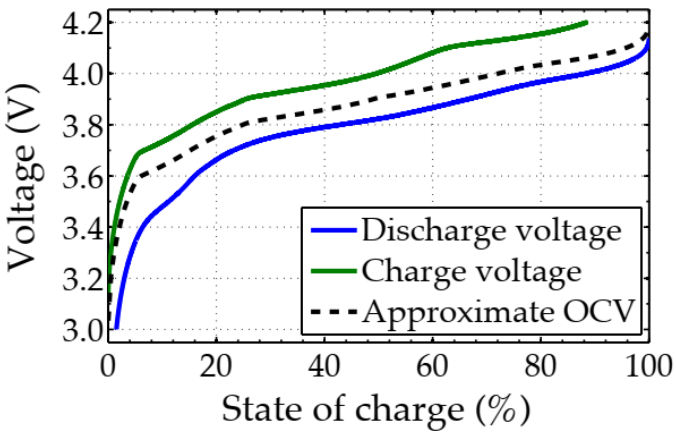


Figure 4-18. Example of OCV vs. SOC curves obtained in the OCV test of a lithium-ion cell tested at low temperature. Reproduced from [94].

Once $Q$ and $\eta_Q$ have been obtained, the evolution of $z[k]$ over the charge and discharge tests can be estimated from the logged current through (4.13). For each SOC value, there will be two voltage readings: one measured during charging and the other one during discharging, as Figure 4-18 illustrates. This graph represents a lithium-ion cell.

Note that the "approximate OCV" curve could be obtained as the average between the charging and the discharging voltage curves for most SOC values, but there is no discharge-voltage curve at low SOCs and there is no charge-voltage curve at high SOCs. Since the OCV curve must be continuous and without abrupt changes, the estimation method must deal adequately with incomplete information near the extremes. To do so, a Thevenin model with SOC-dependent voltage source, $OCV(z)$, and SOC-dependent series, $R_z(z)$, resistance is employed (this SOC-dependent Thevenin model is used only here, just to deal with this specific issue) to calculate OCV as a function of SOC over the whole SOC range. The process is as follows:

- The SOC-dependent series resistance is supposed to vary linearly with SOC. There are three easily calculable values of $R_z$:
    - $R_z(1)$ is computed dividing the instantaneous voltage drop when the test moves from Script #1 step 1 to step 2 by the applied current.
    - $R_z(0)$ is computed the same way, using the data around the transition from Script #3 step 1 to step 2.
    - $R_z(0.5)$ is computed considering that the correct OCV value at this point, $OCV(z = 0.5)$, is the average between the charge-voltage and the discharge-voltage curves.
- $R_z$ is defined as a piecewise function:

$$R_z(z) = \begin{cases} R_z(0) + 2z\big(R_z(0.5) - R_z(0)\big), & \text{if } 0 \le z \le 0.5 \\ R_z(0.5) + 2(z - 0.5)\big(R_z(1) - R_z(0.5)\big), & \text{if } 0.5 < z \le 1 \end{cases}$$

- $OCV(z)$ is also defined as a piecewise function:

$$OCV(z) = \begin{cases} v_{OCV}^{+}(z) + R_z(z) \cdot |i_{OCV}^{+}|, & \text{if } 0 \le z \le 0.5 \\ v_{OCV}^{-}(z) - R_z(z) \cdot |i_{OCV}^{-}|, & \text{if } 0.5 < z \le 1 \end{cases}$$

  where $v_{OCV}^{+}$ and $v_{OCV}^{-}$ are defined from the voltage measured throughout the whole test, $v_{OCV}$, as the discharge-voltage and the charge-voltage, respectively. In the definition above, $v_{OCV}^{+}$ and $v_{OCV}^{-}$ appear expressed already as a function of $z$ rather than as a function of time.

After, these calculations, the auxiliary parameter $R_z$ is discarded, while $OCV(z)$ is kept as the characteristic voltage curve of the studied battery. This curve, together with the values of $Q$ and $\eta_Q$ are the results of the OCV test.

- **Experimental results**

Test results of Batt3 are examined next to illustrate the attempts made to estimate the model parameters of the monobloc batteries. Sadly, the characterization attempts resulted unsatisfactory, probably due to wrong choice of the test voltages and currents applied to the batteries.

The results of capacity and coulombic efficiency estimation for Batt3 yield very poor results: $Q_{Batt3} \stackrel{?}{=} 29.90\ Ah$ and $\eta_{Q\ Batt3} \neq 116.97\%$. The coulombic efficiency estimation is obviously wrong, probably due to a wrong election of the upper cut-off voltage. The float charge voltage, $2.27\ V$ per cell (i.e., $13.62\ V$), was used instead of the cycle charge voltage, $2.45\ V$ per cell (i.e., $14.7\ V$, see Figure 4-15), what caused the script 3 (charging) to end prematurely. Therefore, the discharge-charge cycle would be incomplete. The SOC at the beginning of the test was indeed $100\%$ (because it was initially fully charged with the Lead Crystal BBC 12V/10A charger) but the end of the charging stage did not correspond to $SOC = 100\%$ again. The estimated capacity results from accumulated ampere-hours during discharge only, so in principle this result might be correct (although $29.90\ Ah$ seems fairly low for a cell with nominal cell capacity of $40\ Ah$, even after subjecting it to a little abuse). Unfortunately, the lockdown due to the coronavirus crisis impeded to redo the testing to get more accurate results.

Figure 4-19 and Figure 4-20 show the data logged during the OCV test of Batt3.

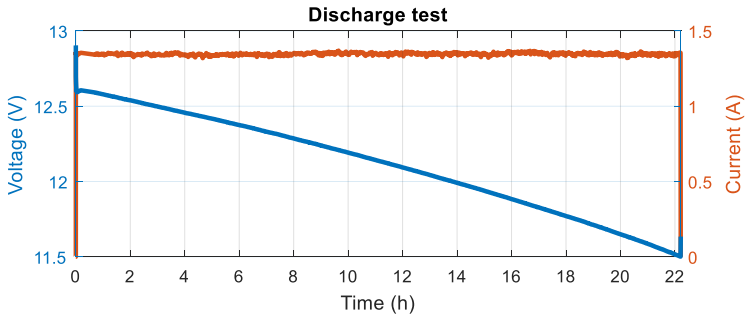


Figure 4-19. Measured voltage and current in the OCV discharge test (script 1).

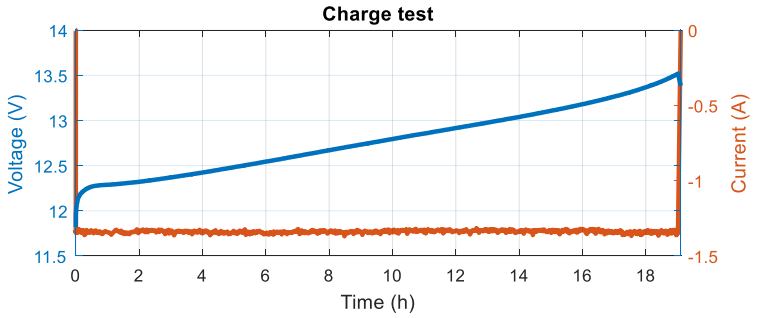


Figure 4-20. Measured voltage and current in the OCV charge test (script 3).

Figure 4-21 represents the $OCV$ vs. $SOC$ fit estimation obtained from the Lead Crystal experimental test results. Note that the graph does not exhibit the characteristic described above of having incomplete data near 0% and 100% SOC. Indeed, both measured curves cover the whole x axis. This is probably due to the mentioned wrong selection of the cut-off voltages, what would have leaded to incorrectly assign the whole SOC range to the x axis while, in reality, the battery did not actually reach all the SOC values during the tests. Furthermore, the obtained $OCV$ vs. $SOC$ relationship is non-monotonous near 100% SOC which, in principle, should not occur. The tests should be repeated to obtain better results.

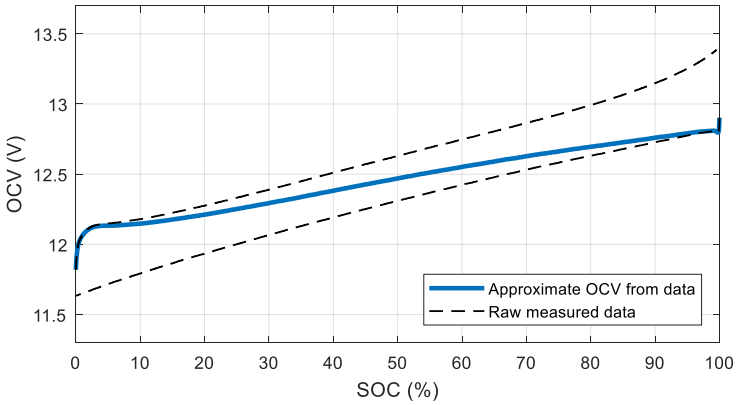


Figure 4-21. Measured and adjusted OCV vs. SOC curves obtained in the OCV test.

#### 4.2.2.6. Dynamic test

The dynamic test consists in applying a current profile to the battery that produces a diversity of voltage transients. This current profile is applied repeatedly over the entire SOC range while the battery's voltage response is logged. The parameters $\{M, M_0, R_0, R_1, R_2\}$ are

then estimated by fitting the voltage response resulting from simulating the ESC model under the applied current profile to the actual response measured in the test. That is, the parameters are chosen such that they minimize the simulation's voltage error.

Figure 4-22 shows the current profile, $i_{DYN}$, employed to estimate the model parameters. This training current profile is representative of the battery pack's final application (a small microgrid). The current profile was sampled at a rate of one second in an existing the microgrid, in the Ngarenanyuki (Tanzania) school [192]. This is a $10\,kW$ stand-alone microgrid, with a $70\,kWh$ lead-acid Battery Energy Storage System (BESS). The current profile corresponds to one-day operation of the microgrid with high photovoltaics generation during the daytime. The profile was scaled by the ratio of the capacity of the batteries under test ($40\,Ah$) with respect to the capacity of the actual microgrid's BESS ($202\,Ah$). Operation data of the Ngarenanyuki's microgrid was generously provided by the research group Energy4Growing, Politecnico di Milano, under an open-source license.

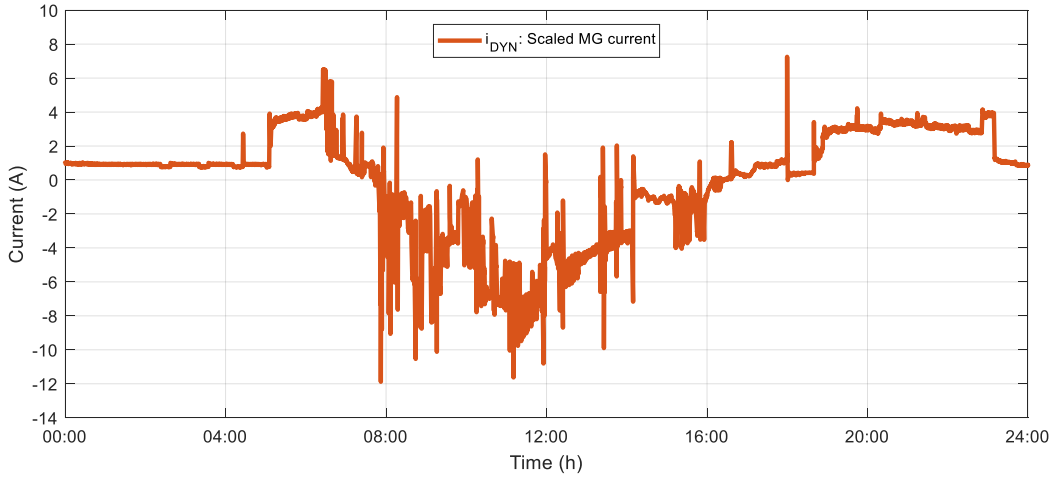


Figure 4-22. Scaled 24-hour current profile in the Ngarenanyuki school's microgrid [192].

Since the power supply and the electronic load used for testing are unidirectional, the data of the current profile applied to the batteries had to be processed a little to assign positive and negative current separately to each device. The current profile was split into non-negative, $i^{+}_{DYN}$, and non-positive, $i^{-}_{DYN}$, to generate the input references: the power supply performs negative current ($i^{-}_{DYN}$, charging) and the electronic load performs positive current ($i^{+}_{DYN}$, discharging). Both devices must operate coordinately in parallel for the combination of their current profiles to actually reassemble the original (un-split) one.

The Matlab code used to process the dynamic test data and to analyze them is part of the supplementary material of [94, 193]. Parameters are estimated by finding the least-square solution to the set of equations (4.19) (built from (4.8), through the derivation in (4.18)).

$$\hat{v}[k] = v[k] - OCV(z[k]) = Mh[k] + M_0 s[k] - \left(R_1 i_{R_1}[k] + R_2 i_{R_2}[k]\right) - R_0 i_{app}[k] \quad (4.18)$$

$$\underbrace{\begin{bmatrix} \hat{v}_{DYN}[0] \\ \hat{v}_{DYN}[1] \\ \dots \\ \hat{v}_{DYN}[k] \\ \dots \\ \hat{v}_{DYN}[k_{end}] \end{bmatrix}}_{Y} = \underbrace{\begin{bmatrix} h[0] & s[0] & -i_{DYN}[0] & -i_{R_1}[0] & -i_{R_2}[0] \\ h[1] & s[1] & -i_{DYN}[1] & -i_{R_1}[1] & -i_{R_2}[1] \\ \dots & \dots & \dots & \dots & \dots \\ h[k] & s[k] & -i_{DYN}[k] & -i_{R_1}[k] & -i_{R_2}[k] \\ \dots & \dots & \dots & \dots & \dots \\ h[k_{end}] & s[k_{end}] & -i_{DYN}[k_{end}] & -i_{R_1}[k_{end}] & -i_{R_2}[k_{end}] \end{bmatrix}}_{B} \underbrace{\begin{bmatrix} M \\ M_0 \\ R_0 \\ R_1 \\ R_2 \end{bmatrix}}_{X} \quad (4.19)$$

where $\hat{v}$ is the voltage component not explained by OCV, and $v_{DYN}$ is the terminal voltage measured in the dynamic test. The best solution is found by minimizing the error between true and predicted $\hat{v}_{DYN}$, i.e., minimizing $||Bx - Y||$. First, $z[k]$ is calculated using equation (4.13), with the $\eta_Q$ and $Q$ calculated in the OCV test. Then, $OCV(z[k])$ is calculated thanks to the OCV vs. SOC curve also obtained in the OCV test. Then $\hat{v}_{DYN}$ is calculated from the vectors $v_{DYN}[k]$ and $OCV(z[k])$, to be used in the left-hand side of the optimization problem in (4.19). The discrete-time state-space matrix $B$ is built applying subspace identification for linear systems following [194]. Parameter estimation is carried out in Matlab by computing $X = B^{\dagger}Y$, where the dagger symbol (†) represents a matrix pseudo-inverse. The value of $\gamma$ is recursively updated to minimize the root mean square error –$\gamma$ is not included in (4.19) to keep the problem linear, since dependency on $\gamma$ is non-linear (see (4.11)).

It was expected that the selected current profile, $i_{DYN}$ (Figure 4-22), would produce accurate results to populate the ESC model. Unfortunately, this was not the case: the parameter values found are out of range and, consequently, they produce a voltage response in simulation that does not reproduce the actual cell transients (measured during the 24-hour charge-discharge cycle). Thus, the dynamic tests need to be repeated too. Unsuccessful results are thought to be consequence of training the model with a current profile with relatively few and slow transients: the training profile is not very dynamic, so the parameter estimation algorithm might have difficulty fitting time constants of the two RC pairs in the model.

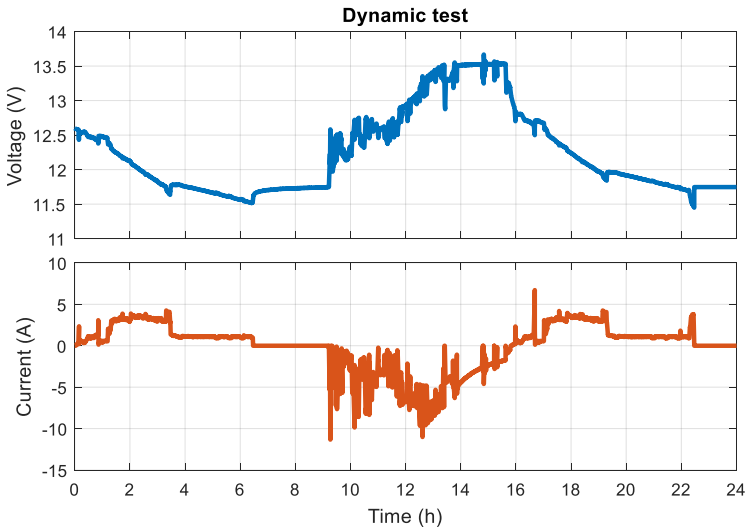


Figure 4-23. Measured voltage and current during DYN test (scripts 1 and 2).

A more dynamic current profile is proposed to repeat the dynamic tests: the normalized current for the Urban Dynamometer Drive Schedule (UDDS) profile, $i_{UDDS}$, typical of automotive applications. This profile contains a much greater number of transients per unit of time, with current varying much more steeply, compared to the profile employed in the first attempt. Comparing Figure 4-24 with Figure 4-22 reveals the very different time scale between both training current profiles (note that the x-axis limits differ in a factor × 48).

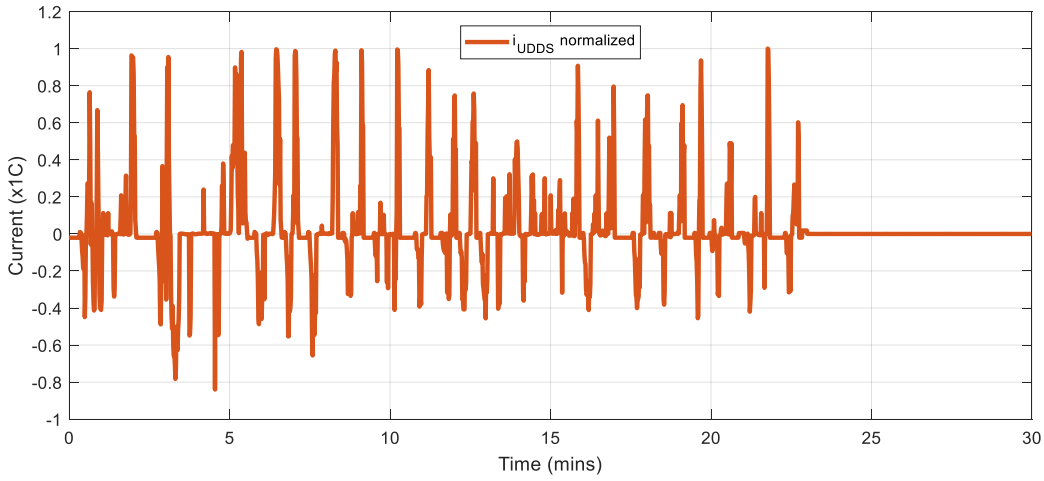


Figure 4-24. Normalized current for the Urban Dynamometer Drive Schedule (UDDS) profile.

It is predicted that, this time, the UDDS current profile will generate enough dynamic behavior to allow tuning of the parameter values of the batteries' ESC models.

## 4.3. Summary

A converter-based equalizer topology has been proposed in this chapter to perform active balancing in battery packs with up to 15 series-connected $12\,V$ monobloc batteries. Active balancing recursively transfers charge (ampere-hours) from the strongest monobloc battery to the weakest one. The central element of the equalizer is a (single) DC-DC converter which gets activated when SOC imbalance among the monoblocs is greater than $0.5\%$. The converter's input and output are adequately routed via controlled switches to perform cell-to-cell charge transfer –that is, power multiplexing.

A particularly imbalanced battery pack of five Lead Crystal $12\,V$, $40\,Ah$ monobloc batteries has been conceived as the case study to evaluate the performance of the balancing system by means of PSIM simulations. Each monobloc battery models imbalance in a different parameter with respect to a reference battery: reduced coulombic efficiency ($\downarrow \eta_Q$), reduced capacity ($\downarrow Q$), increased internal resistance ($\uparrow R$), and increased leakage current ($\uparrow I_{leak}$). An equivalent circuit model has been selected to model the monobloc batteries response. The battery pack's natural tendency towards imbalance has been evaluated by simulating typical operation with no external balancing. The studied battery pack represents the energy storage system of a microgrid, so the current profile utilized in the simulation is typical of this application. The parameters of the equalizer's control strategy have been tuned based on this study. Specifically, minimum and maximum boundaries have been found for the equalizer's duty cycle in order to, on one hand, compensate natural imbalance and, on the other hand, prevent SOC oscillations –by avoiding excessive charge transfer (overcompensation of imbalance).

The control strategy has been validated in simulation. For this study, a $10\%$ initial SOC imbalance has been considered in addition to the parameter discrepancy mentioned above. The simulation covers $24$ hours of operation, with the battery pack loaded again with a typical microgrid current profile. The equalizer demonstrates excellent performance, as it compensates the (large) initial SOC deviations in $0.75$ hours and keeps the pack balanced (within a $0.5\%$ SOC window) from then on. The influence of the four inconsistent parameters ($\eta_Q$, $Q$, $R$, and $I_{leak}$) in SOC divergence has been thoroughly analyzed.

The prototype of the equalizer has been described and works have started to validate its performance in experimental tests. Prior to that, the battery pack employed in such validation

experiments (five Lead Crystal $12\,V$, $40\,Ah$ monoblocs) has to be modeled. Imbalance has been artificially induced in this battery pack by subjecting it to cycling under abusive conditions, which causes accelerated aging. Different abuse tests have been inflicted to each battery, to produce differential degradation. An aging platform has been built to facilitate this process. Its design and possible operation schemes have been described.

Ongoing battery-testing works have been described. Open Circuit Voltage (OCV) and dynamic tests permit to estimate the model parameters. Preliminary results have been presented and possible improvements to the battery testing procedure have been suggested.

# 5. Battery degradation modeling

Experimental battery models (equivalent circuits) have been used in Chapter 3 and Chapter 4. Utilization of equivalent-circuit models is widespread nowadays because they reunite a series of characteristics that facilitate their implementation. Primarily, this type of model is easy to parametrize from non-destructive tests, and require low computational resources. Thus, they are suitable for BMS applications. The drawbacks of equivalent-circuit models are that they do not provide insight on the physicochemical processes that take place in the cell, neither do they account for capacity depletion as the cell ages. Physic-based models, in contrast, are much more complex because they are derived from the examination of the processes that take place inside the cells but, in return, they are more versatile and provide long-term prediction capability.

In this chapter, a novel battery model is proposed combining an equivalent circuit with a physics-based model. The comprehensive model predicts the fast dynamics response thanks to the equivalent model, and the long-term capacity fade and resistance increase thanks to the degradation model. The base of the comprehensive model is the ESC model, in which time dependency has been introduced into some of the parameters to account for degradation. These time-dependent parameters are updated by incorporating changes in capacity and internal resistance, which are estimated employing a reduced-order zero-dimensional physics-based model of the Solid-Electrolyte Interphase (SEI) side reaction. This degradation mechanism causes loss of cyclable lithium and is one of the most important causes of

degradation during most of the cell's life, as illustrated in Figure 5-1 [195]. The proposed model produces State of Health (SOH) estimations, which is essential to optimize battery operation and extend its lifetime.

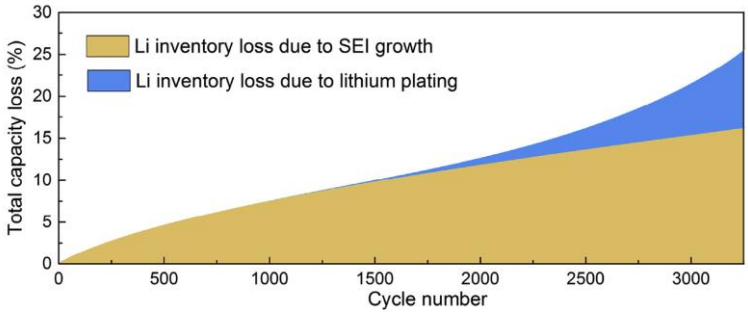


Figure 5-1. Loss of capacity due to SEI growth and lithium plating throughout battery life. Reproduced from [195].

This modeling work is mainly based on:

- G. L. Plett's technical lessons on battery modeling and control [94].
- P. Ramadass' paper on modeling SEI degradation mechanism [126].
- A. V. Randall's paper on reducing the computational complexity of Ramadass' model [125].
- G. L. Plett's paper on algebraically solving Randall's implicit equation of the current density of the SEI side reaction [196].
- R. Machado's self-discharge tests data [197].

Apart from the main contribution of coupling the ESC model with the SEI growth model, this chapter includes several improvements that have been developed with respect to the original formulation of the employed models:

- Modeling secondary capacity recovery (which was not addressed in [125, 126]) to fine-tune the capacity fade estimation.
- Estimating SOC from the degree of lithiation of the electrodes (electrochemical model) rather than from coulomb counting.
- Reducing computational time by pre-storing the degradation model results, obtained for a variety of operation conditions.

The cells studied in this work were manufactured by Panasonic. They have prismatic form factor, an NMC positive electrode and graphite negative electrode, and were used in the

battery packs of the Ford C-MAX Energi and Ford Fusion Energi plug-in hybrid vehicles (PEVs) between 2013 and 2018. Their nominal voltage is 3.7 $V$ and their nominal capacity is 25 $Ah$.

## 5.1. Cell model. Part 1: Equivalent circuit

The basis of the proposed model is an empirical equivalent electrical circuit: the Enhanced Self Correcting (ESC) model described in [94]. Originally, the ESC model is characterized by constant parameters, so it cannot account for degradation. The proposed model, in contrast, converts some of the parameters into time-dependent variables. Figure 5-2 shows the circuit with black letters representing constant parameters and blue letters representing time-dependent parameters (affected by degradation).

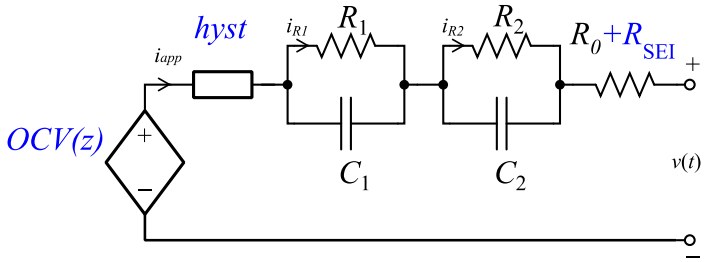


Figure 5-2. ESC equivalent circuit model

Specifically, capacity, $Q$, internal resistance, $R_0 + R_{SEI}$, and the Open Circuit Voltage (OCV) curve as a function of State of Charge (SOC), $OCV(z)$, and the hysteresis term, $hyst$, are updated every time step.

The Panasonic-cell parameter values were obtained empirically from cell response to the test scripts described in [94] and reproduced in Section 4.2.2.4. Table 5-1 collects the nomenclature of the ESC model parameters and the values of the constant parameters.

The ESC model equations (presented above, in Section 4.2.2.3) are reviewed next, highlighting in blue the variables affected by degradation. The discrete time equation that describes the cell's response when a current $i_{app}$ is applied is:

$$v[k] = OCV(z[k])\big|_k + (M_0 s[k] + M h[k]) - \left(R_1 i_{R_1}[k] + R_2 i_{R_2}[k]\right) - (R_0 + R_{SEI}[k]) i_{app}[k], \quad (5.1)$$

Table 5-1. ESC model parameters and variables. In the column "Value/Variable", ✓ indicates variable.

| | Parameter / Variable | Value / Variable | Unit |
|---|---|---|---|
| $C_1$ | RC # 1 Capacitance | 26467 | $F$ |
| $C_2$ | RC # 2 Capacitance | 52082 | $F$ |
| $h$ | SOC-dependent hysteresis state | ✓ | – |
| $i_{app}$ | Discharge current | ✓ | $A$ |
| $k$ | Discrete time index | ✓ | – |
| $M$ | SOC-dependent hysteresis coefficient | 0.0012 | $V$ |
| $M_0$ | Instantaneous hysteresis coefficient | $4.4782 \cdot 10^{-4}$ | $V$ |
| $Q$ | Cell capacity | ✓ | $Ah$ |
| $R_0$ | Initial equivalent series resistance | 1.3164 | $m\Omega$ |
| $R_1$ | RC # 1 resistance | 0.1866 | $m\Omega$ |
| $R_2$ | RC # 2 resistance | 0.9492 | $m\Omega$ |
| $R_{SEI}$ | SEI layer resistance | ✓ | $\Omega$ |
| $z$ | State of charge (SOC) | ✓ | – |
| $\Delta t$ | Time interval used in discretization | 60 | $s$ |
| $\eta_Q$ | Coulombic efficiency during charging | 99.87 | % |
| $\gamma$ | Hysteresis time constant | 523.8311 | – |
| $\theta_p$, $\theta_n$ | Degree of lithiation of the positive and the negative electrodes (PE and NE) | ✓ | – |
| $\theta_p^0$, $\theta_n^0$ | $z = 0$ degree of lithiation of the PE and the NE | ✓ | – |
| $\theta_p^{100}$, $\theta_n^{100}$ | $z = 1$ degree of lithiation of the PE and the NE | ✓ | – |

where the nomenclature $f(x)\,|_k$ symbolizes the dependency of the function or variable $f$ with the variable $x$ at instant $k$. Overall, (5.1) states that cell voltage $v$ is the result of adding four terms: an open-circuit voltage term, $OCV(z)\,|_k$, a hysteresis term, $(M_0 s + Mh)$, a diffusion term, $-\left(R_1 i_{R_1} + R_2 i_{R_2}\right)$, and an internal resistance term, $-(R_0 + R_{SEI}) i_{app}$. The elements of (5.1) are calculated as follows:

$$i_{R_j}[k] = exp\left(\frac{-\Delta t}{R_j C_j}\right) i_{R_j}[k-1] + \left(1 - exp\left(\frac{-\Delta t}{R_j C_j}\right)\right) i_{app}[k-1] \tag{5.2}$$

$$h[k] = A_H[k-1]h[k-1] + (A_H[k-1] - 1)sgn\left(i_{app}[k-1]\right) \tag{5.3}$$

$$A_H[k] = exp\left(-\left|\frac{\eta_Q[k] i_{app}[k] \gamma \Delta t}{Q[k]}\right|\right) \tag{5.4}$$

$$\eta_Q[k] = \begin{cases} 1, & i_{app}[k] \geq 0 \\ \eta_Q, & i_{app}[k] < 0 \end{cases} \tag{5.5}$$

$$z[k] = \frac{\theta_n[k] - \theta_n^0[k]}{\theta_n^{100}[k] - \theta_n^0[k]} \tag{5.6}$$

$$s[k] = \begin{cases} sgn\left(i_{app}[k]\right), & i_{app}[k] \neq 0 \\ s[k-1], & i_{app}[k] = 0 \end{cases} \tag{5.7}$$

where $j = \{1,2\}$; $h$ is the unitless hysteresis state $-1 \leq h \leq 1$; $\mathrm{sgn}(x)$ is the sign function of $x$; and $\theta_n$ is the negative electrode's stoichiometry ($\mathrm{Li}_{\theta_n}\mathrm{C}_6$), which is calculated in equation (5.18). The sampling time, $\Delta t$, must be chosen in accordance to the rate at which the current profile $i_{app}$ varies. In this case, $\Delta t = 60\ s$ has been selected for the simulation of Section **¡Error! No se encuentra el origen de la referencia.**. This precision is more than sufficient t o simulate the cell response to the applied current profile, where current is mostly zero corresponding to self-discharge tests, as described further below.

Sections 5.2 and 5.3 show how (time-varying) cell capacity, $Q$, and SEI film resistance, $R_{SEI}$, are calculated using the degradation model. These two results are incorporated into the ESC equivalent circuit, converting some of the ESC model's constant parameters into time-dependent parameters (blue letters in Figure 5-2). Capacity variations affects the calculation of the hysteresis coefficient, $A_H$ (defined in (5.4), used in (5.3), (5.1)), and the definition of the variable $z$ (≡SOC, defined in (5.6), used in (5.1)) and, thus, the $OCV(z)$ curve (defined in (5.28), used in (5.1)), while the resistance of the SEI layer, $R_{SEI}$, is added to the initial series resistance $R_0$, so the total series resistance results $R_0 + R_{SEI}$ (used in (5.1)). From now on, only black characters will be used to refer to all the model variables and parameters.

## 5.2. Cell model. Part 2: SEI degradation

Energy transfer to (from) the battery cell is due to the primary reaction, that is, the reversible reaction of lithium (de-)intercalation. The electrochemical potential favors that, when closing the external circuit, the atomic lithium stored in the porous space of the negative electrode (NE) loses electrons. These electrons circulate through the external circuit, supplying the load, and return into the cell at the positive electrode (PE), while the

corresponding $Li^+$ ions are internally released from the NE to the electrolyte, which carries them through the separator to the PE, as well. There, the electrons and $Li^+$ ions combine with the PE's de-lithiated compound, in this case NMC. Charging process is inverse: flow of electrons is externally forced by applying a voltage higher than that of the cell.

But the reaction of (de-)intercalation is not the only one that takes place. There are also undesired side reactions that degrade the cell. This work models the irreversible SEI layer growth reaction, which is one of the main cause of battery degradation (Figure 5-1). This side-reaction consumes part of the inventory of cyclable lithium causing the cell capacity to decrease and the internal resistance to increase [118]. The SEI layer growth is caused by the reduction of the organic solvent on the surface of the NE, as schematically shown in Figure 5-3 [195]. A large variety of compounds have been observed in the SEI layer. The composition, morphology and stability of the SEI depend on many factors such as the type and morphology of graphite, electrolyte composition, electrochemical conditions and cell temperature [118, 198].

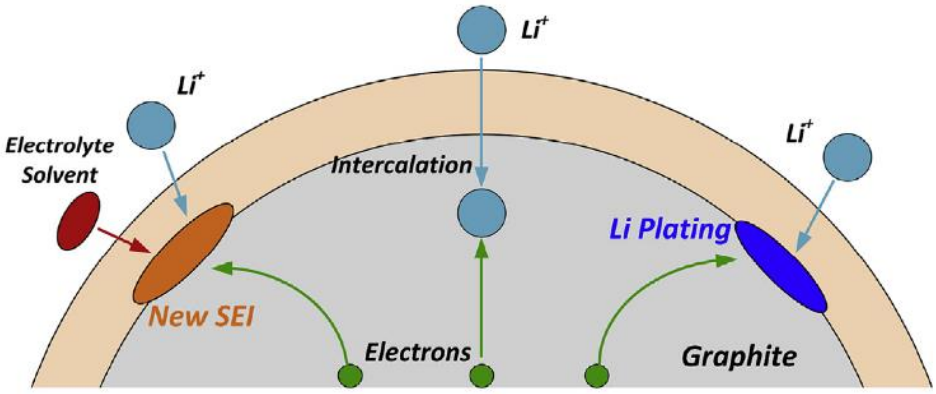


Figure 5-3. Main competing reactions in the negative electrode: intercalation, SEI layer growth and lithium plating. Reproduced from [195].

### 5.2.1. Solid-Electrolyte Interphase (SEI)

In this work, degradation is modeled utilizing the reduced-order model of the SEI reaction proposed by Randall et al. in [125], which is derived from the system of partial differential equations presented by Ramadass et al. in [199]. Two of the starting hypotheses has been reconsidered regarding [125]:

- The SEI reaction has been considered to occur not only during cell charging, but also during discharging. For example, [200] and [110] confirm that the SEI layer also grows during discharge (although at a slower rate).
- The value of the internal resistance rise coefficient, $k_R$ (defined below), has been selected to produce a plausible increase of resistance at cell's End of Life (EOL), instead of calculating it from averaged SEI film properties (density, molecular weight and conductivity), which is difficult and uncertain due to the extreme diversity of components and complex configurations that can appear in the SEI layer [118].

Also, the values of the cell's parameters have been adapted to model the 25 Ah Panasonic NMC cell, instead of the 1.8 Ah Sony 18650 Li-CoO2 cell originally modeled in [125]. The nomenclature used in the SEI layer growth model is presented in Table 5-2.

The SEI layer growth process is modeled for lithium-ion cells with electrolyte containing ethylene carbonate organic solvent, where the solvent reduction reaction is irreversible ($\text{Solvent} + 2\text{Li}^+ + 2\text{e}^- \Leftrightarrow \text{Products}$, where multiple different solvent reduction reactions are represented by the average equilibrium potential), solvent-diffusion through the SEI is the rate-limiting step, rates of charge and discharge are moderate (the studied range of C-rates is $|i_{app}| \leq 3C$ [125] and quasi-equilibrium state is assumed, neglecting local variations in electrolyte and solid surface concentration), disregarding of mobile electrons and inserted lithium ions on the exchange-current density, uniform intercalation and side reactions over the anode, and with anodic and cathodic charge-transfer coefficients $\alpha_a = \alpha_c = 0.5$. The model applies for post-formation SEI growth.

### 5.2.2. SEI growth model equations

The set of equations employed to calculate the current density of the SEI side reaction, $J_{side}$ ((5.8) and (5.17)) is presented next. $J_{side}$ represents the flux of lithium from the SEI layer. Since the sign of $J_{side}$ is always negative, the magnitude of $J_{side}$ represents the rate of lithium loss due to the side reaction that grows the SEI layer. Capacity loss and internal resistance increase are directly proportional to $J_{side}$ ((5.21) and (5.22)). Table 5-2. Degradation model parameters and variables. The symbol ✓ indicates variable.

| Name | Description | Is a variable | Unit |
|---|---|---|---|
| $a$ | Specific area of porous electrode | | $m^{-1}$ |
| $A$ | Area of the electrode | | $m^2$ |
| $c$ | Lithium concentration | ✓ | $mol/m^3$ |
| $c^{max}$ | Maximum lithium concentration in the material | | $mol/m^3$ |
| $F$ | Faraday's constant, 96 485 | | $A\,s/mol$ |
| $i_0$ | Exchange-current density | ✓ | $A/m^2$ |
| $J$ | Local volumetric current density | ✓ | $A/m^3$ |
| $k_n$ | Rate of electrochemical reaction | | $A\,m^{2.5}/\,mol^{1.5}$ |
| $k_R$ | SEI resistance increase coefficient | | $\Omega\,m^3\,/\,A\,s$ |
| $OCP$ | Open Circuit Potential | ✓ | $V$ |
| $n$ | Absolute number of lithium moles | ✓ | $mol$ |
| $R_s$ | Average radius of the negative electrode's particles | | $m$ |
| $R_{SEI}$ | SEI layer resistance | ✓ | $\Omega$ |
| $R_g$ | Universal gas constant, 8.314 | | $J/mol\,K$ |
| $T$ | Temperature | ✓ | $K$ |
| $U^{ref}$ | Local equilibrium potential | | $V$ |
| $Vol$ | Volume of the electrode | | $m^3$ |
| $\alpha_a$, $\alpha_c$ | Anodic and cathodic charge transfer coefficients of the electrochemical reaction | | $-$ |
| $\varepsilon$ | Volume fraction of solid phase in the electrode | | $-$ |
| $\eta$ | Local overpotential driving electrochemical reaction | ✓ | $V$ |
| $\phi$ | Local potential of a phase | ✓ | $V$ |
| Subscripts | | | |
| $e$ | Pertaining to electrolyte | | |
| $I$ | Relating to intercalation reaction | | |
| $n$ | Pertaining to negative electrode (NE) | | |
| $p$ | Pertaining to positive electrode (PE) | | |
| $s$ | Pertaining to solid | | |
| $side$ | Relating to side reaction (SEI) | | |

At every spatial location in the NE, it is satisfied that $J_{total} = J_I + J_{side}$, where $J_{total}$ and $J_I$ are the total current density and the intercalation current density. Making the simplifying assumption that these are uniform over the thickness of the NE, it is possible to write:

$$J_{total} = J_I + J_{side} = \frac{i_{app}}{Vol_n} \tag{5.8}$$

The sign criteria in the NE are as follows: $J_{total}$ and $J_I$ are positive when $Li^+$ ions leave the electrode and $J_{side}$ is always negative (see (5.14)) because $Li^+$ ions always enter the SEI layer –lithium recovery from the SEI is not possible. The sign criterion for the applied current $i_{app}$ is that it is positive when discharging the cell. Figure 5-4 represents the lithium fluxes and volumetric current densities, $J_{total}$, $J_I$ and $J_{side}$, under three scenarios: cell discharge, inactivity and charge.

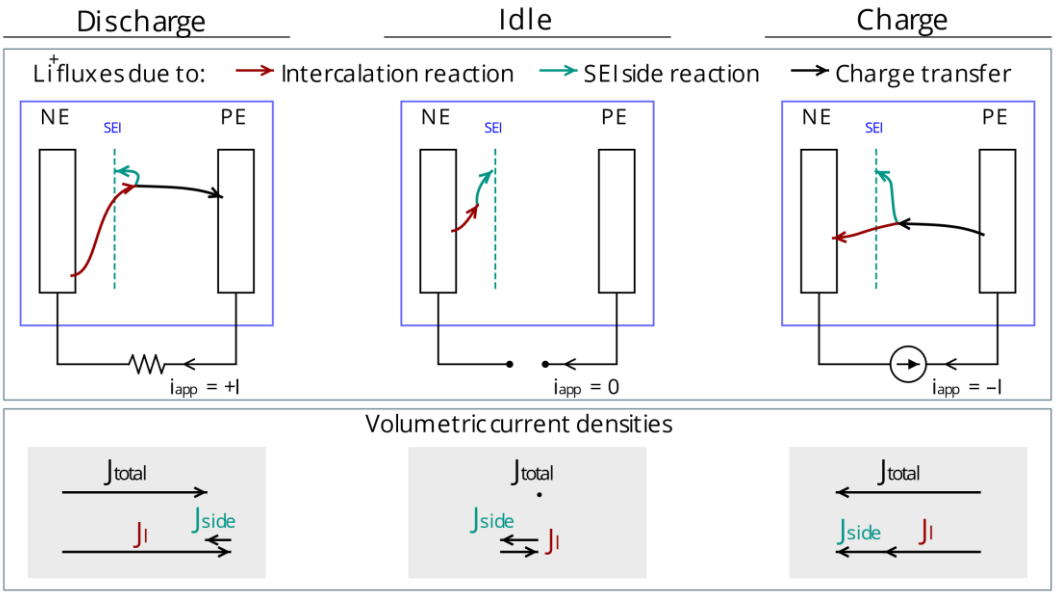


Figure 5-4. Direction of lithium fluxes and volumetric current densities during discharge, inactivity and charge. (NE = Negative Electrode, PE = Positive Electrode.)

First, the Butler-Volmer equation (5.9) models the reversible (primary) intercalation reaction.

$$J_I = a_n i_{0,n} \left[ exp\left(\frac{\alpha_{a,n} F}{R_g T} \eta_n\right) - exp\left(-\frac{\alpha_{c,n} F}{R_g T} \eta_n\right) \right], \tag{5.9}$$

where the specific area of the electrode, $a_n$, the exchange current density, $i_{0,n}$, and the intercalation reaction overpotential, $\eta_n$, are calculated as follows:

$$a_n = \frac{3\varepsilon_{s,n}}{R_s} \tag{5.10}$$

$$i_{0,n} = k_n\left((1-\theta_n)c_s^{max}\right)^{\alpha_{a,n}}(\theta_n c_s^{max})^{\alpha_{c,n}}c_e^{\alpha_{a,n}} \tag{5.11}$$

$$\eta_n = \phi_s - \phi_e - OCP_n - \frac{J_{total}}{a_n}R_{SEI}A_n \tag{5.12}$$

Considering $\alpha_{a,n} = \alpha_{c,n} = 0.5$ [126] and acknowledging that $\sinh(x) = (e^x - e^{-x})/2$, the next expression can be derived from (5.9):

$$\eta_n = \frac{2R_gT}{F}asinh\left(\frac{J_I}{2a_n i_{0,n}}\right) \tag{5.13}$$

The irreversible side reaction is modeled as a function of the SEI reaction overpotential, $\eta_{side}$, using the Tafel equation (5.14):

$$J_{side} = -a_n i_{0,side}\,exp\left(-\frac{\alpha_{a,side}F}{R_gT}\eta_{side}\right) \tag{5.14}$$

$$\eta_{side} = \phi_s - \phi_e - U_{side}^{ref} - \frac{J_{total}}{a_n}R_{SEI}A_n \tag{5.15}$$

Note that the value of $J_{side}$ is, by definition, always negative. Combining (5.12) and (5.15), $\eta_{side}$ can be expressed in terms of $\eta_n$:

$$\eta_{side} = \eta_n + OCP_n - U_{side}^{ref} \tag{5.16}$$

Finally, considering $\alpha_{c,side} = 0.5$ [125] and combining (5.16) with (5.13), allows to transform (5.14) into:

$$J_{side} = -a_n i_{0,side}\,exp\left(-\frac{F\left(OCP_n - U_{side}^{ref}\right)}{2R_gT}\right)exp\left(-asinh\left(\frac{\frac{i_{app}}{Vol_n} - J_{side}}{2a_n i_{0,n}}\right)\right) \tag{5.17}$$

Here, $J_{side}$ appears expressed implicitly but its value can be algebraically found by applying the resolution method proposed in [196]. Equation (5.17) shows that the rate of cyclable lithium loss depends on three variables: the degree of lithiation of the NE, $\theta_n$ ($OCP_n$ and $i_{0,n}$ are functions of $\theta_n$), the applied current, $i_{app}$, and the temperature, $T$.

The degree of lithiation of the electrode, $\theta_{el}$ (where $el = \{n, p\}$), represents the instantaneous concentration of stored lithium in that electrode with respect to the maximum concentration that the electrode's material can store: $\theta_{el} = c_{s,el}/c_{s,el}^{max}$. In the incremental degradation model, the values of the variables $\theta_n$ and $\theta_p$ are calculated counting the input and output flows of Li+ ions to/from each electrode, as (5.18) and (5.19) show:

$$\theta_n[k] = \theta_n[k-1] - \frac{J_I[k]}{\varepsilon_{s,n} F c_{s,n}^{max}} \Delta t \tag{5.18}$$

$$\theta_p[k] = \theta_p[k-1] + \frac{i_{app}[k]/Vol_p}{\varepsilon_{s,p} F c_{s,p}^{max}} \Delta t \tag{5.19}$$

Equation (5.18) can be expressed splitting the $\theta_n$ increment in two terms: the first one corresponding to the lithium flux caused by external current and the second one corresponding to the lithium flux caused by degradation.

$$\begin{aligned} \theta_n[k] &= \theta_n[k-1] - \frac{i_{app}[k]/Vol_n}{\varepsilon_{s,n} F c_{s,n}^{max}} \Delta t + \frac{J_{side}[k]}{\varepsilon_{s,n} F c_{s,n}^{max}} \Delta t \\ &= \theta_n[k-1] - \frac{i_{app}[k]/Vol_n}{\varepsilon_{s,n} F c_{s,n}^{max}} \Delta t - \Delta\theta_n^{loss}[k] \end{aligned} \tag{5.20}$$

Note that the first term is proportional to the increment of $\theta_p$ (5.19) and that the degradation term has been denoted $\Delta\theta_n^{loss}[k]$, which is a positive quantity.

Incremental capacity loss, $\Delta Q_{side}^{loss}$ (in Ah), and resistance increase, $\Delta R_{SEI}$ (in Ω), caused by growth of the SEI layer can be estimated from the current density $J_{side}$:

$$\Delta Q_{side}^{loss}[k] = -k_Q \Delta t \, J_{side}[k] \tag{5.21}$$

$$\Delta R_{SEI}[k] = -k_R \Delta t \, J_{side}[k], \tag{5.22}$$

where $k_R$ and $k_Q$ are, respectively, the (positive) coefficients of SEI resistance increase and capacity loss. Note that $\Delta Q_{side}^{loss}$ and $\Delta R_{SEI}$ are both positive because the value of $J_{side}$ is always negative. Equation (5.1) of the ESC model is updated with (5.22), and (5.4) is updated with

(5.21). The NE's degree of lithiation $\theta_n[k]$ and lithiation boundaries $\{\theta_n^0[k], \theta_n^{100}[k]\}$ (used in (5.6)) are also affected by $\Delta Q_{side}^{loss}$, as explained in Section 5.3.3 below.

There are two possible expressions that are equal to $\Delta\theta_n^{loss}[k]$:

$$\Delta\theta_n^{loss}[k] = -\frac{J_{side}[k]}{\varepsilon_{s,n}\, Fc_{s,n}^{max}}\Delta t = \frac{3600\,\Delta Q_{side}^{loss}[k]}{Vol_n \varepsilon_{s,n}\, Fc_{s,n}^{max}} \tag{5.23}$$

This leads to deriving $k_Q$:

$$-\frac{J_{side}[k]}{\varepsilon_{s,n}\, Fc_{s,n}^{max}}\Delta t = -\frac{3600\, k_Q\, J_{side}[k]}{Vol_n \varepsilon_{s,n}\, Fc_{s,n}^{max}}\Delta t \Rightarrow k_Q = \frac{Vol_n}{3600} \tag{5.24}$$

The parameter $k_R$ can in theory be calculated from the average molecular weight, density and conductivity of the SEI's components, according to [125]. Nevertheless, those values are hard to estimate since the composition of the SEI layer is complex and remains largely unknown. Pulse Tests results from [67] (presented below, in Section 5.4) could be used instead to estimate $k_R$, but that results are not consistent with the expected continuous rise of the internal resistance (see Figure 5-22), as explained below. Thus, estimating $k_R$ from Pulse Test data was discarded and, instead, is estimated based on literature, considering that the EOL internal resistance is double the Beginning Of Life's (BOL):

$$k_R = \frac{k_Q R_0}{0.2 \cdot Q[0]} \tag{5.25}$$

This expression comes from (5.21) and (5.22), simultaneously satisfying that $R_{SEI}[k] = \sum_0^{k_{EOL}} \Delta R_{SEI}[k] = R_0$ when 20% of the initial capacity $Q[0]$ has faded away due to degradation: $Q_{side}^{loss}[k_{EOL}] = \sum_0^{k_{EOL}} \Delta Q_{side}^{loss}[k] = 0.2 \cdot Q[0]$ (this is a common definition of EOL for automotive batteries, although it is worth to mention that batteries can get a second life after surpassing this conventional EOL criterion: they can then be used in less demanding applications in terms of energy density and power density, such as storage elements in renewable energy systems). The result is $k_R = 5.5827 \cdot 10^{-12}\ \Omega\, m^3/A\, s$.

Finally, since independent estimates of $i_{0,side}$ and $U_{side}^{ref}$ are not available, the lumped parameter $k_{SEI}$ has been defined to group both. Estimation of the parameter $k_{SEI}$ is explained in Section 5.1.

$$k_{SEI} = a_n i_{0,side}\, exp\left(F\frac{U_{side}^{ref}}{2R_gT}\right) \tag{5.26}$$

With this, (5.17) particularized at discrete time $k$ results:

$$J_{side}[k] = -k_{SEI}\, exp\left(-\frac{F\, OCP_n(\theta_n[k])}{2R_gT}\right) exp\left(-asinh\left(\frac{\frac{i_{app}[k]}{Vol_n} - J_{side}[k]}{2a_n i_{0,n}(\theta_n[k])}\right)\right) \tag{5.27}$$

Table 5-3 collects the values of the parameters used in the formulation of the model. Some values were obtained in the study of the Panasonic cell [201], others have been estimated from literature review [126, 202–208] and the rest of them have been estimated.

Table 5-3. Parameters of the Panasonic cell.

| | Value | Unit | Source |
|---|---|---|---|
| $\alpha_n$, $\alpha_p$ | 0.5 | – | [126] |
| $\alpha_{c,side}$ | 0.5 | – | [125] |
| $A_n$ | 1.2152 | $m^2$ | [201] |
| $c_e$ | 2000 | $mol\, m^{-3}$ | [208] |
| $c_s^{max}$ | 32000 | $mol\, m^{-3}$ | [207] |
| $\varepsilon_{s,n}$ | 0.81 | – | estimated |
| $k_n$ | $2.6473 \cdot 10^{-6}$ | $A\, m^{2.5}\, mol^{-1.5}$ | averaged [126, 201–207] |
| $R_s$ | $5 \cdot 10^{-6}$ | $m$ | [201] |
| $\theta_n^0[0]$ | 0.0093 | – | estimated |
| $\theta_n^{100}[0]$ | 0.5262 | – | estimated |
| $\theta_p^0[0]$ | 0.8089 | – | estimated |
| $\theta_p^{100}[0]$ | 0.4280 | – | estimated |
| $Vol_n$ | $7.29 \cdot 10^{-5}$ | $m^3$ | [201] |

The initial electrode's lithiation boundaries of the Panasonic cell, $\{\theta_p^0[0], \theta_p^{100}[0], \theta_n^0[0], \theta_n^{100}[0]\}$, have been found based on data obtained from characterization tests of the electrodes' Open Circuit Potential (OCP) [201] and on the initial cell's OCV [197]. The initial lithiation boundaries are calculated by fitting the difference

$OCP_p(\theta_p)$ minus $OCP_n(\theta_n)$, to the initial OCV curve $OCV(z)\big|_0$ referring the variables $\theta_p$, $\theta_n$ and $z$ to a common reference [209]. This optimization is described in Section 5.3.2. The volume fraction of solid in the NE, $\varepsilon_{s,n}$, is calculated such that it is consistent with the rest of the cell parameters:

$$\varepsilon_{s,n} = \frac{3600 \cdot Q[0]}{Vol_n c_{s,n}^{max} F(\theta_n^{100}[0] - \theta_n^0[0])}$$

where this expression is derived from (5.50). Microscopic analysis of the NE in [201] validates the result.

## 5.3. Cell model. Part 3: Secondary capacity recovery

Together with the capacity loss caused by the SEI side reaction, a secondary process takes place leading the cell to recover a small fraction of the lost capacity. This is caused by the relative displacement of the NE's OCP curve with respect to the PE's OCP curve, and the resulting variation of the Open Circuit Voltage (OCV) curve. A small extension of the range of allowed degrees of lithiation, $(\theta_n^{100} - \theta_n^0)$, corresponding to $OCV \in [V_{min}, V_{max}]$, takes place and, therefore, a fraction of the capacity lost in the SEI reaction, $Q_{side}^{loss}[k] = \sum_k \Delta Q_{side}^{loss}[k]$, is recovered in this secondary process, $\left(Q_{\theta_0}^{gain}[k] + Q_{\theta_{100}}^{gain}[k]\right) = \sum_k (\Delta Q_{\theta_0}^{gain}[k] + \Delta Q_{\theta_{100}}^{gain}[k])$.

### 5.3.1. Relationship between the curves $OCP_p$, $OCP_n$ and $OCV$

The variables $\theta_p$ and $\theta_n$ are the degrees of lithiation of the PE and the NE, respectively. These two variables have values between 0 and 1 and represent the stoichiometry of lithium in the PE: $Li_{\theta p}Ni_xMn_yCo_zO_2$ (the exact x-y-z composition of the studied cell is unknown, but it is probably the NMC 532 or the NMC 622 type, based on the technology available by the year of production), and the NE: $Li_{\theta n}C_6$. In other words, they represent the instantaneous concentration of stored lithium in that electrode with respect to the maximum concentration that the electrode's material can hold, as mentioned above.

Figure 5-5 provides an intuitive representation of the variables $\theta_p$ and $\theta_n$ as lithiation levels. Bold letters and the green horizontal line represent cell's state at a given instant $k$. Regular letters indicate other known states in the three represented axes: $\theta_p$ (blue),

$\theta_n$ (orange) and $z$ (green). Note that not all $\theta_p$ and $\theta_n$ values are allowed. Practical cells do not use the electrodes' entire capacity in order to stay away from boundaries which would lead to rapid cell degradation and to power depletion [94]. Therefore, lithium cycling is practically restricted to a limited range: $0 < \theta_p^{100} \leq \theta_p \leq \theta_p^0 < 1$ and $0 < \theta_n^0 \leq \theta_n \leq \theta_n^{100} < 1$, where $\theta_p^0$ and $\theta_n^0$ are the degrees of lithiation of the PE and the NE when the cell is at $z = 0$ (defined for this cell by $OCV = V_{min} = 2.1\ V$), and $\theta_p^{100}$ and $\theta_n^{100}$ are the degrees of lithiation of the PE and the NE when the cell is at $z = 1$ (defined for this cell by $OCV = V_{max} = 4.1\ V$). Cell's capacity is consequently proportional to the extension of the range $(\theta_n^{100} - \theta_n^0)$ –as indicated by double-arrowed black line in Figure 5-5.

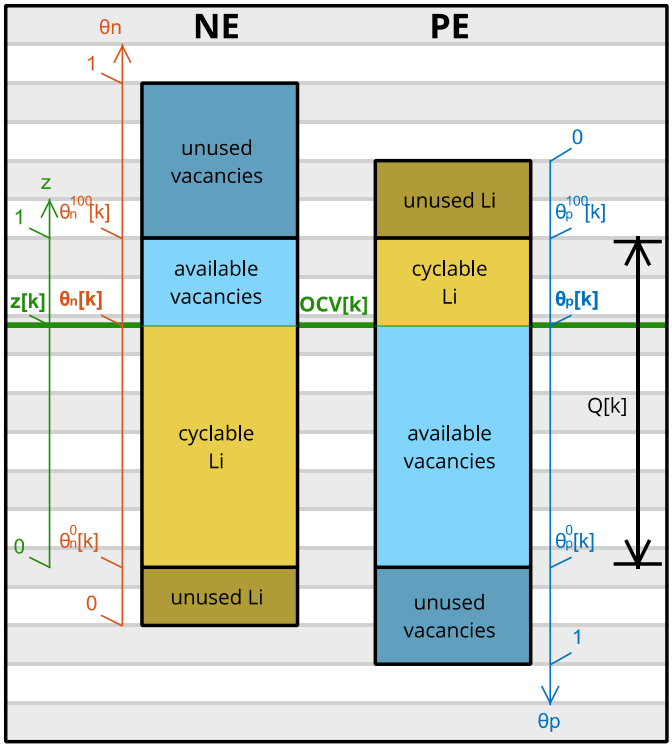


Figure 5-5. Intuitive representation of PE's and NE's degrees of lithiation, $\theta_p$ and $\theta_n$, as lithiation levels.

Logically, the degrees of lithiation of PE and NE are complementary: when charging the cell, $\theta_n$ increases and $\theta_p$ decreases, and vice-versa when discharging. For example, $\theta_n^{100}$ is a high value, meaning that the NE is rather full of inserted lithium when the cell is fully charged, while $\theta_p^{100}$ is a low value, meaning that the PE is concurrently rather empty of lithium.

The electrodes' lithiation boundaries $\{\theta_p^0, \theta_p^{100}, \theta_n^0, \theta_n^{100}\}$ are not fixed but vary with degradation. The relationship between three curves: the Open Circuit Potential (OCP) of the positive electrode, $OCP_p$, that of the negative electrode, $OCP_n$, and the cell's Open Circuit voltage, $OCV$, must be studied to find the values of the electrodes' lithiation boundaries at any instant $k$, $\{\theta_p^0[k], \theta_p^{100}[k], \theta_n^0[k], \theta_n^{100}[k]\}$, as the cell ages. This enables calculation of the remaining cell capacity $Q[k]$ as explained in Section 5.3.3.1.

The curve $OCV$ is calculated as the difference between $OCP_p$ and $OCP_n$ (see (5.28)). These three curves are defined dependent on three different variables: $OCV(z)\big|_k$, $OCP_p(\theta_p)$ and $OCP_n(\theta_n)$. Therefore, a common reference must be selected to study how they interrelate. Since the SEI reaction consumes lithium from the NE, the NE's degree of lithiation, $\theta_n$, has been selected as the reference in this work. With this, the relationship between $OCV(z)\big|_k$, $OCP_p(\theta_p)$ and $OCP_n(\theta_n)$ can be expressed as:

$$OCV\big(z(\theta_n)\big|_k\big)\big|_k = OCP_p\big(\theta_p(\theta_n)\big|_k\big) - OCP_n(\theta_n) \tag{5.28}$$

The curves $OCP_p(\theta_p)$ and $OCP_n(\theta_n)$ remain valid throughout the whole cell's lifetime, while the function $OCV(z)\big|_k$, as well as the relationships $\theta_p(\theta_n)\big|_k$ and $z(\theta_n)\big|_k$ vary over time, as explained below. The nomenclature "$\big|_k$" represents this fact: $f(\theta_n)\big|_k$ symbolizes the dependency of the function or variable $f$ with the variable $\theta_n$ (the common reference) at $k$. Equations (5.29) and (5.30) relate the three variables: $\theta_p$, $\theta_n$ and $z$, at any instant $k$:

$$z(\theta_n)\big|_k = \frac{\theta_n - \theta_n^0[k]}{\theta_n^{100}[k] - \theta_n^0[k]} \tag{5.29}$$

$$z(\theta_p)\big|_k = \frac{\theta_p^0[k] - \theta_p}{\theta_p^0[k] - \theta_p^{100}[k]} \tag{5.30}$$

Equaling the right hand sides of (5.29) and (5.30) and solving for $\theta_p$ results in the function:

$$\begin{aligned}\theta_p(\theta_n)\big|_k &= \theta_p^0[k] - \frac{\theta_p^0[k] - \theta_p^{100}[k]}{\theta_n^{100}[k] - \theta_n^0[k]}(\theta_n - \theta_n^0[k]) \\ &= \theta_p^0[k] - C_{pn}(\theta_n - \theta_n^0[k])\end{aligned} \tag{5.31}$$

The coefficient $C_{pn}$, which relates $\theta_n$ to $\theta_p$, is proven to be constant next. The demonstration is derived from the fact that the total amount of cyclable lithium at any given instant, $n_{Li}^{cyclable}[k]$ (in $mol$), is exactly the same for both the PE and the NE –in fact,

$n_{Li}^{cyclable}[k]$ is shared between both electrodes. From the definition of $\theta_p$ and $\theta_n$, $\left(\theta_p^0[k] - \theta_p^{100}[k]\right) = \frac{n_{Li}^{cyclable}[k]}{c_{s,p}^{max}\varepsilon_{s,p}Vol_p}$, and $(\theta_n^{100}[k] - \theta_n^0[k]) = \frac{n_{Li}^{cyclable}[k]}{c_{s,n}^{max}\varepsilon_{s,n}Vol_n}$. Therefore:

$$\begin{aligned} n_{Li}^{cyclable}[k] &= \varepsilon_{s,p}Vol_p c_{s,p}^{max}\left(\theta_p^0[k] - \theta_p^{100}[k]\right) \\ &= \varepsilon_{s,n}Vol_n c_{s,n}^{max}(\theta_n^{100}[k] - \theta_n^0[k]), \end{aligned} \tag{5.32}$$

from where $C_{pn}$ is calculated:

$$C_{pn} = \frac{\theta_p^0[k] - \theta_p^{100}[k]}{\theta_n^{100}[k] - \theta_n^0[k]} = \frac{\varepsilon_{s,n}Vol_n c_{s,n}^{max}}{\varepsilon_{s,p}Vol_p c_{s,p}^{max}} \qquad \forall\, k \tag{5.33}$$

### 5.3.2. Study of initial $OCP_p$, $OCP_n$ and $OCV$

Prior to studying how $OCV(z|_k)\,\big|_k$ varies with degradation, the initial conditions ($k = 0$) are examined. The initial electrodes' lithiation boundaries, $\{\theta_p^0[0], \theta_p^{100}[0], \theta_n^0[0], \theta_n^{100}[0]\}$, have been found for the Panasonic cell based on data obtained from characterization tests of the electrodes' OCP and on the cell's OCV curve at BOL [201]. The lithiation boundaries are calculated by fitting the difference $OCP_p$ (Figure 5-6.a) minus $OCP_n$ (Figure 5-6.b) to the measured $OCV$ curve (Figure 5-6.c). As stated above, these $OCP_p$ and $OCP_n$ curves are valid during the whole cell's lifetime, while the represented $OCV$ curve is only valid at the cell's BOL.

Unfortunately, the measured curves $OCP_p$ (Figure 5-6.b) and $OCP_n$ (Figure 5-6.c) [201] do not cover their whole degrees of lithiation ranges (which, by definition, are $0 \leq \theta_n \leq 1$ and $0 \leq \theta_p \leq 1$) and their x-axes ($\theta_n^{rel}$ and $\theta_p^{rel}$) are not calibrated. Indeed:

$$\theta_n = k_{cv}^n \theta_n^{rel} + \theta_n^{shift}$$
$$\theta_p = k_{cv}^p \theta_p^{rel} + \theta_p^{shift},$$

with all the four constants $k_{cv}^p, k_{cv}^n, \theta_n^{rel}, \theta_p^{rel} \in (0,1)$. The proportionality constants have been found by fitting the measured $OCP_p$ and $OCP_n$ curves to their theoretical values. Theoretical expressions of NMC [210] and graphite [211] OCP curves have been selected to fit the measured $OCP_p$ and $OCP_n$ curves, respectively. Their expressions are reproduced next:

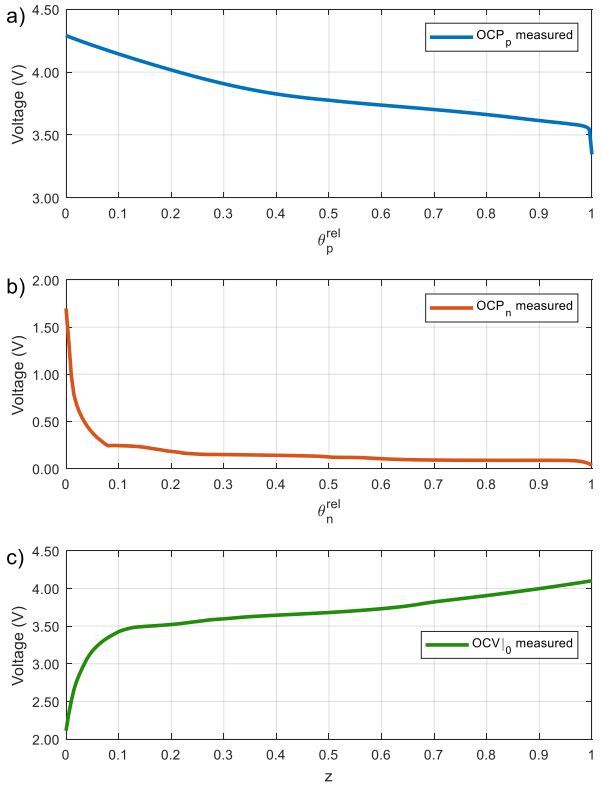


Figure 5-6. Measured OCP curves of the (a) positive and (b) negative electrodes with respect to their relative degrees of lithiation, and (c) measured $OCV$ vs. SOC curve at BOL.

$$OCP_p^{theor}(\theta_p) = 6.0826 - 6.9922\theta_p + 7.1062\theta_p^2 - 0.54549 \cdot 10^{-4}\, exp(124.23\theta_p - 114.2593) - 2.5947\theta_p^3 \quad (5.34)$$

$$OCP_n^{theor}(\theta_n) = 0.7222 + 0.13868\theta_n + 0.028952\theta_n^{0.5} - 0.017189\theta_n^{-1} + 0.0019144\theta_n^{-1.5} + 0.28082\, exp(15(0.06-\theta_n)) - 0.78944\, exp(0.44649(\theta_n - 0.92)) \quad (5.35)$$

Fitting the curves measured at $T = 25\,°C$ to (5.34) and (5.35) using the custom Matlab functions *FitOCPp.m* and *FitOCPn.m* (see Section 5.1.1.1) yields the following results: $k_{cv}^p = 0.5928$, $\theta_p^{shift} = 0.3934$, and $k_{cv}^n = 0.8505$, $\theta_n^{shift} = 0.0081$. This is graphically represented in Figure 5-7.a and Figure 5-7.b.

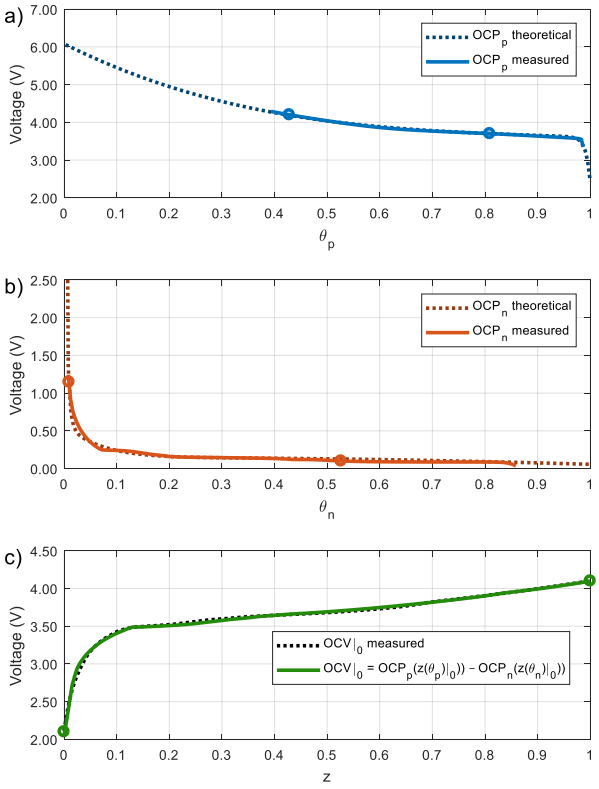


Figure 5-7. Fitting of the measured OCP curves of (a) Positive and (b) Negative electrodes (solid lines) to their theoretical OCP curves (dotted lines), the electrodes' lithiation boundaries are indicated by circled markers, (c) Result of $OCP_p - OCP_n$ best fit to $OCV|_0$.

From this result, the initial electrodes' lithiation boundaries are calculated by minimizing the error between the curve resulting from the subtraction $OCP_p\left(\theta_p(\theta_n)\,\middle|_{\,0}\right) - OCP_n(\theta_n)$ and $OCV\left(z(\theta_n)\,\middle|_{\,0}\right)\middle|_{\,0}$, being the range of $\theta_n$ and $\theta_p$ the variables to optimize. The fit is best when the appropriate ranges $\theta_n \in \left[\theta_n^0[0], \theta_n^{100}[0]\right]$ and $\theta_p \in \left[\theta_p^0[0], \theta_p^{100}[0]\right]$ are considered. This fitting has been performed using the custom Matlab function *FitOCV.m* (see Section 5.1.1.1) considering a temperature $T = 25°C$. The result of this fitting is graphically shown in Figure 5-7.c and yields the following results: $\theta_0^{p,rel}[0] = 0.7008$, $\theta_{100}^{p,rel}[0] = 0.0583$, $\theta_0^{n,rel}[0] = 0.0015$, $\theta_{100}^{n,rel}[0] = 0.6092$ or, in absolute terms, $\theta_0^{p}[0] = 0.8089$, $\theta_{100}^{p}[0] = 0.4280$, $\theta_0^{n}[0] = 0.0093$, $\theta_{100}^{n}[0] = 0.5262$ (circled markers in Figure 5-7.a and Figure 5-7.b). These values delimit the initial relative position between the PE's and the NE's stoichiometry windows as shown in Figure 5-8.

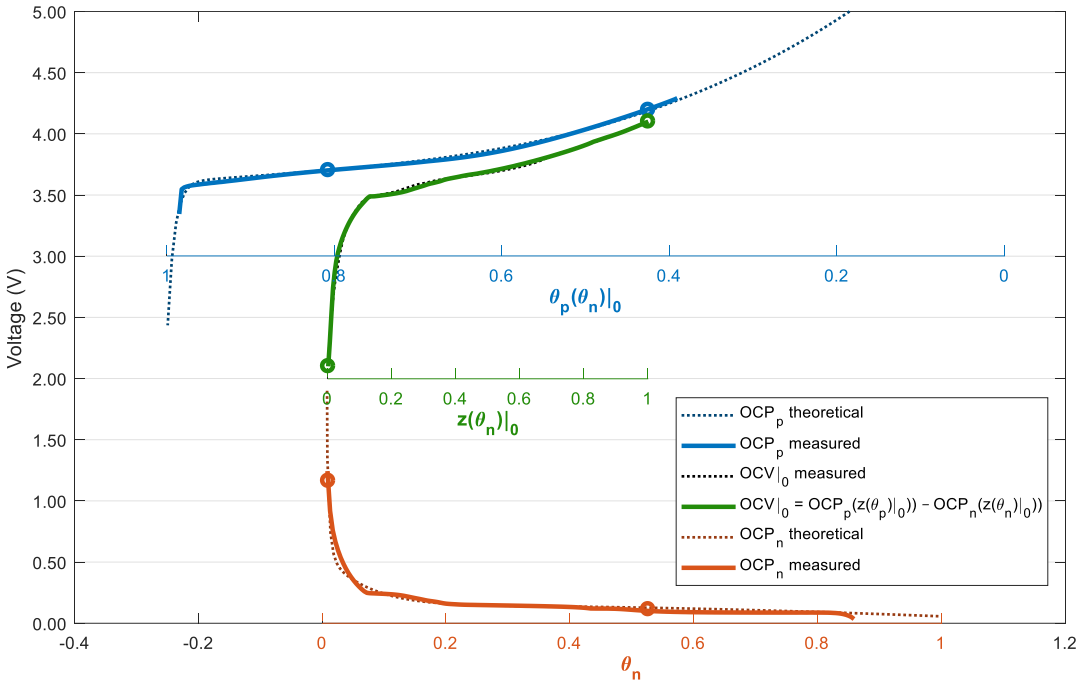


Figure 5-8. Relative position of the PE's and the NE's stoichiometric windows and resulting initial OCV curve.

The SEI reaction causes the initial lithium inventory of the NE to decrease. Thus, as the cell degrades, the NE's stoichiometry window shifts with respect to that of the PE [107] and, consequently, the OCV curve changes (it gets shrank). Next section studies how the relationships $\theta_p(\theta_n)\big|_k$ and $z(\theta_n)\big|_k$ change with degradation and the subsequent evolution of the curve $OCV\big(z(\theta_n)\big|_k\big)\big|_k$.

### 5.3.3. Relative displacement between the OCP curves with degradation

The lithium loss caused by the SEI reaction produces a relative displacement between the OCP curves: the NE's degree of lithiation $\theta_n$ corresponding to a given PE's degree of lithiation $\theta_p$ decreases as the SEI layer consumes cyclable lithium. The displacement of the $\theta_n$ axis between Figure 5-9.A and $B_{1,}$ or in Figure 5-10, exemplify this process. Figure 5-9 and Figure 5-10 are two graphical representations that complement each other as they show different aspects of the degradation process of a cell over a prolonged self-discharge period. Figure 5-9 illustrates the changes in the electrodes' lithiation boundaries produced by SEI

degradation, while Figure 5-10 represents the corresponding displacement between the OCP curves of both electrodes and the consequent recalculation of the OCV curve.

- Figure 5-9.A is the initial stage: the cell is fully charged.
- Figure 5-9.$B_1$ represents the cell after a long self-discharge time. A large capacity loss $Q_{side}^{loss}\left|{}_{A}^{B}\right. = \sum_{k_A}^{k_B} \Delta Q_{side}^{loss}\,[k]$ occurs between the initial stage and the degraded stage. Equation (5.20) shows that the NE loses Li due to the SEI side reaction. Thus, $\theta_n$ decreases by an amount $\theta_n^{loss}\left|{}_{A}^{B}\right. = \sum_{k_A}^{k_B} \Delta\theta_n^{loss}\,[k]$ (5.23). Meanwhile, the PE's degree of lithiation ($\theta_p$) remains the same according to (5.19) because the cell is unloaded during self-discharge (see also Figure 5-4 - Idle). To be consistent with the extra loss of lithium in the NE, the NE's stoichiometry window gets shifted by an offset equal to $\theta_n^{loss}\left|{}_{A}^{B}\right.$ with respect to the PE's stoichiometry window (see Figure 5-9.$B_1$). Note that $\theta_n^{loss}\left|{}_{A}^{B}\right.$ reduces the amount of cyclable lithium but, in principle, does not affect the unused Li reserves.

  Figure 5-9.$B_2$ and Figure 5-9.$B_3$ represent the thought experiment of fully discharging ($B_2$) and recharging ($B_3$) the cell that, if performed experimentally, would lead to reach the updated electrodes' lithiation boundaries at $k_B$. Since $B_2$ and $B_3$ are just a thought experiment, there is no capacity variation in these two stages. Hence, all Bi stages represent the same cell's state (B) in terms of capacity. $B_2$ and $B_3$ have been included for didactic purposes only, to show the change in the electrodes' lithiation boundaries ($\theta_p^0, \theta_n^0$ and $\theta_p^{100}, \theta_n^{100}$) and the associated capacity recoveries, $Q_{\theta_0}^{gain}\left|{}_{A}^{B}\right. = \sum_{k_A}^{k_B} \Delta Q_{\theta_0}^{gain}\,[k]$ and $Q_{\theta_{100}}^{gain}\left|{}_{A}^{B}\right. = \sum_{k_A}^{k_B} \Delta Q_{\theta_{100}}^{gain}[k]$, caused by the incorporation of Li from the NE's and the PE's previously unused Li reserves into the cyclable Li range. Although it is possible to theoretically compute the post-degradation electrodes' lithiation boundaries already as in the stage $B_1$, in practice, the post-degradation $\theta_p^0[k_B]$ and $\theta_n^0[k_B]$ are unknown until the cell is fully discharged and, similarly, the post-degradation $\theta_p^{100}[k_B]$ and $\theta_n^{100}[k_B]$ are unknown until the cell is fully charged again. In practical applications, this means that it is not possible to exactly predict when $z|_{k_B}$ will reach 0 and 1 using simple SOC estimation strategies such as coulomb counting.

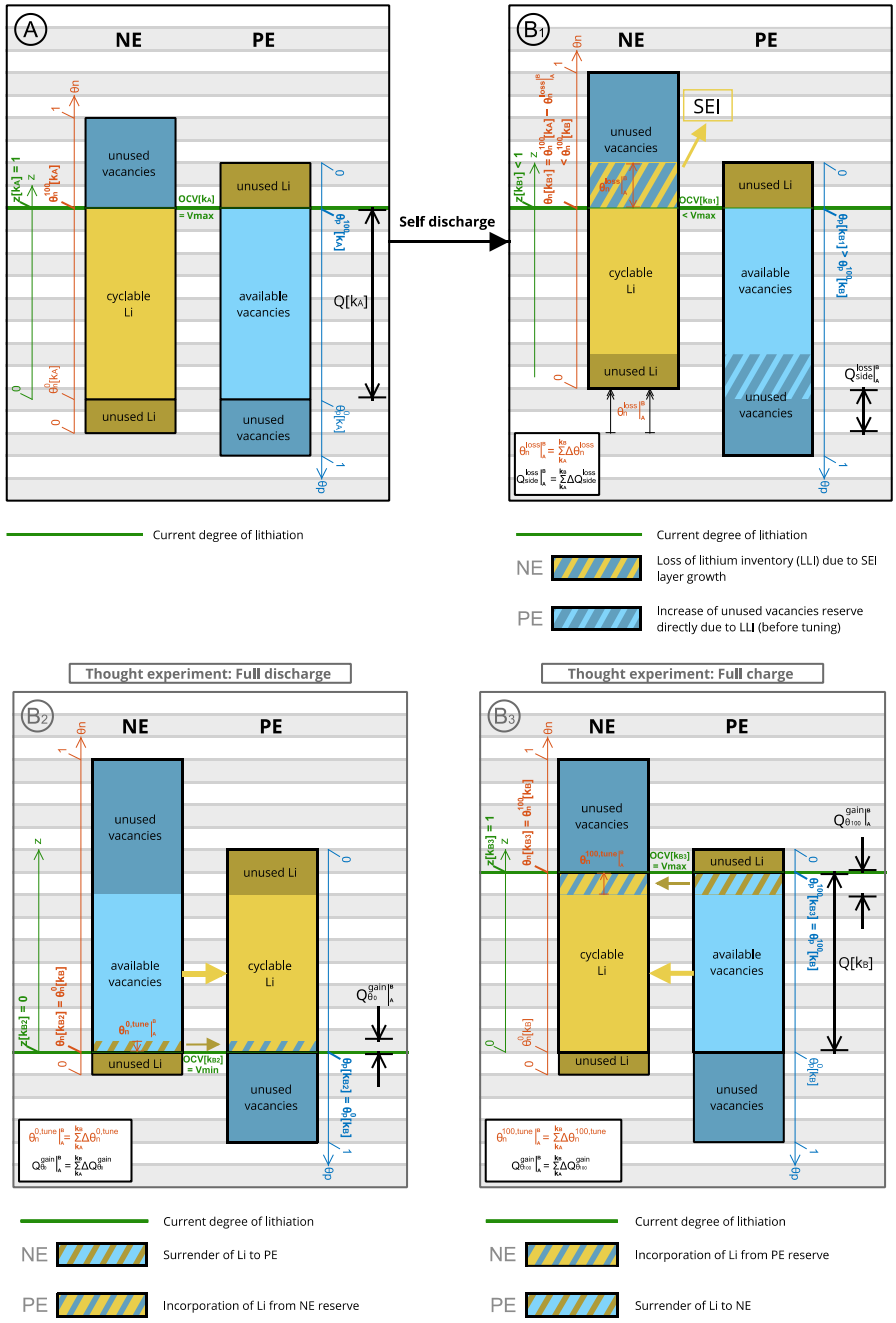


Figure 5-9. Cell's stages: (A) Initally fully charged cell →[Self-discharge]→ ($B_1$) Loss of cyclable lithium $\theta_n^{loss}|_A^B$ after a prolonged self-discharge time (capacity loss $Q_{side}^{loss}|_A^B$) →[Full discharge]→ ($B_2$) Update of $\theta_p^0$ and $\theta_n^0$ (capacity recover $Q_{\theta_0}^{gain}|_A^B$) →[Full charge]→ ($B_3$) Update of $\theta_p^{100}$ and $\theta_n^{100}$ (capacity recover $Q_{\theta_{100}}^{gain}|_A^B$)

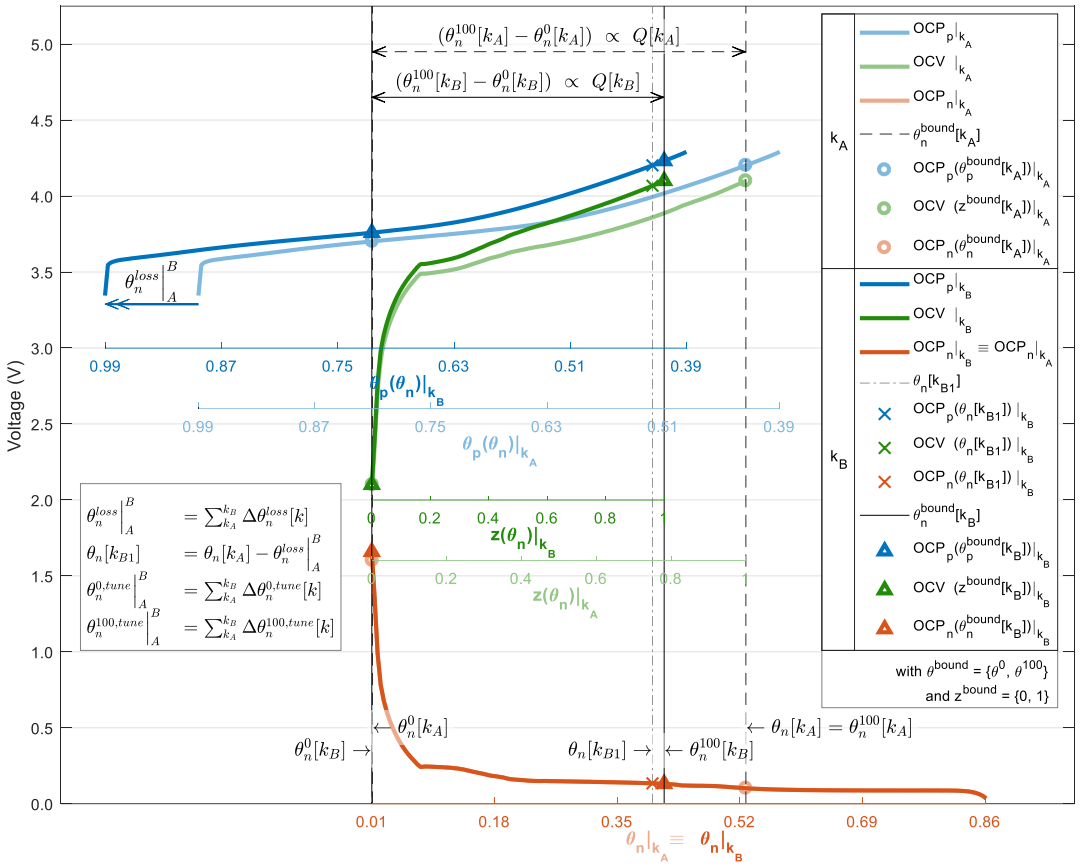


Figure 5-10. Main figure: Relative displacement $\theta_n^{loss}\big|_A^B$ between the PE's stoichiometric window $\theta_p$ (blue x axis) with respect the NE's stoichiometric window $\theta_n$ (orange x axis, the common reference), after an extended period of degradation ($k_A \rightarrow k_B$). The pastel color curves correspond to the initial instant, $k_A$ (pre-degradation), and the solid color curves correspond to the final instant, $k_B$ (post-degradation). The $OCP_p$ curve (blue) gets displaced with respect to $OCP_n$ (orange) and, consequently, $OCV$ (green) gets horizontally shrank

Figure 5-10 shows the effect of the relative shift between the NE's and PE's stoichiometry windows $\theta_n$ (orange x-axis, taken as the reference for all the represented graphs) and $\theta_p$ (blue x-axes) after a long self-discharge period. $OCP_p$ (blue) gets shifted with respect to $OCP_n$ (orange) and, consequently, $OCV$ (green) gets shrank. Pale lines represent the cell at the pre-degradation stage, $k_A$, and solid lines represent the cell at the post-degradation stage, $k_B$. The recalculation of $\theta_n^0$ and $\theta_n^{100}$ is also represented. Zoomed graphs in Figure 5-11 show how those limits get tuned with respect to the $\theta_n$ values that correspond to the unused Li reserves as in $k_{B_1}$ (see Figure 5-9.B1).

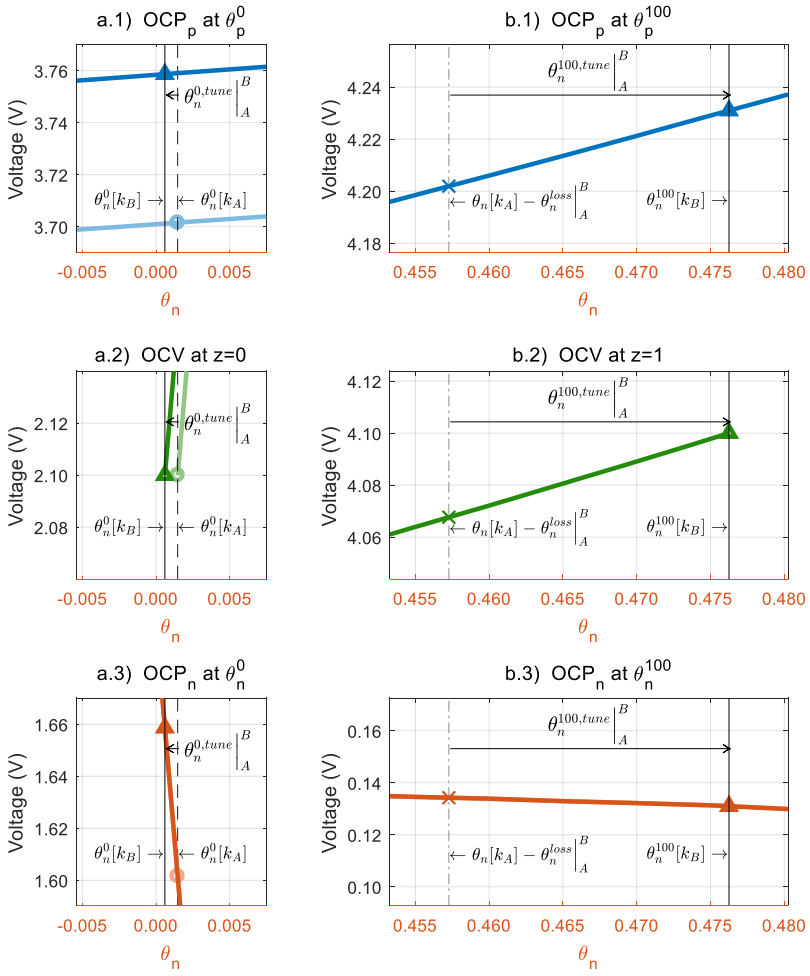


Figure 5-11. Zooms of Figure 5-10: (a) Recalculation of $\theta_n^0$ such that $OCV(\theta_n^0[k_B])\,|_{k_B} = V_{min}$; (b) Recalculation of $\theta_n^{100}$ such that $OCV(\theta_n^{100}[k_B])\,|_{k_B} = V_{max}$.

The displacement between the $OCP_p$ and $OCP_n$ curves due to SEI reaction affects the OCV curve. The latter changes because it is constrained by the relationship (5.28). If $\theta_n$ is taken as the common reference (i.e. the fixed axis), $\theta_p$ and, together with it, $OCP_p\big(\theta_p(\theta_n)\,|_k\big)$, undergo a relative displacement [107] (see Figure 5-10). While (5.31) remains valid, $\theta_p(\theta_n)\,|_k$ can also be calculated from the translation in (5.36):

$$\theta_p(\theta_n)\,|_k = \theta_p\big(\theta_n + \Delta\theta_n^{loss}[k]\big)\,|_{k-1} \tag{5.36}$$

Equation (5.36) is derived next from examination of (5.19) and (5.20) together with (5.31). Equations (5.19), (5.20) and (5.31) are reproduced here for clarity:

$$\theta_p[k] = \theta_p[k-1] + \frac{i_{app}[k]/Vol_p}{\varepsilon_{s,p}\, Fc_{s,p}^{max}}\Delta t$$

$$\theta_n[k] = \theta_n[k-1] - \frac{i_{app}[k]/Vol_n}{\varepsilon_{s,n}\, Fc_{s,n}^{max}}\Delta t - \Delta\theta_n^{loss}[k]$$

$$\theta_p(\theta_n)\big|_k = \theta_p^0[k] - C_{pn}(\theta_n - \theta_n^0[k])$$

Substituting the term $\theta_p[k-1]$ in (5.19) with (5.31) specialized at $k-1$ results:

$$\theta_p(\theta_n[k])\big|_k = (\theta_p^0[k-1] - C_{pn}(\theta_n[k-1] - \theta_n^0[k-1])) + \frac{i_{app}[k]/Vol_p}{\varepsilon_{s,p}\, Fc_{s,p}^{max}}\Delta t$$

where the term $\frac{i_{app}[k]/Vol_p}{\varepsilon_{s,p}\, Fc_{s,p}^{max}}\Delta t$, which is equal to $C_{pn}\left(\frac{i_{app}[k]/Vol_n}{\varepsilon_{s,n}\, Fc_{s,n}^{max}}\Delta t\right)$, can be expressed in terms of (5.20):

$$\theta_p(\theta_n[k])\big|_k = (\theta_p^0[k-1] - C_{pn}(\theta_n[k-1] - \theta_n^0[k-1])) + C_{pn}(\theta_n[k-1] - \theta_n[k] - \Delta\theta_n^{loss}[k]),$$

which, rearranged, is:

$$\theta_p(\theta_n[k])\big|_k = \theta_p^0[k-1] - C_{pn}\big(\theta_n[k] + \Delta\theta_n^{loss}[k] - \theta_n^0[k-1]\big),$$

which, according to (5.31) is $\theta_p\big(\theta_n[k] + \Delta\theta_n^{loss}[k]\big)\big|_{k-1}$. Therefore:

$$\theta_p(\theta_n[k])\big|_k = \theta_p\big(\theta_n[k] + \Delta\theta_n^{loss}[k]\big)\big|_{k-1} \tag{5.37}$$

Generalizing this expression for any value of $\theta_n$, (5.36) is finally obtained:

$$\theta_p(\theta_n)\big|_k = \theta_p\big(\theta_n + \Delta\theta_n^{loss}[k]\big)\big|_{k-1},$$

where the domain is such that $\theta_p \in [0,1]$.

The $OCV$ curve is updated by combining this result with (5.28):

$$OCV\big(z(\theta_n)\big|_k\big)\big|_k = OCP_p\big(\theta_p\big(\theta_n + \Delta\theta_n^{loss}[k]\big)\big|_{k-1}\big) - OCP_n(\theta_n) \tag{5.38}$$

The result of (5.38) is used to generate a lookup table that links $OCV$ directly to $\theta_n$. The domain of the function $OCV(z)\big|_k$ is $z \in [0,1]$ or, equivalently, the domain of $OCV\big(z(\theta_n)\big|_k\big)\big|_k$ is $\theta_n \in \left[\theta_n^0[k], \theta_n^{100}[k]\right]$. Boundary values of $\theta_n$ are defined by $V_{min}$ and

$V_{max}$ (see Figure 5-11.a.2) and b.2), respectively), and are calculated using the lookup table generated from (5.38) inversely:

$$V_{min} = OCV\big(z(\theta_n^0[k])\,\big|_k\big)\,\big|_k \Leftrightarrow \theta_n^0[k] = z^{-1}\big(OCV^{-1}(V_{min})\,\big|_k\big)\,\big|_k \tag{5.39}$$

$$V_{max} = OCV\big(z(\theta_n^{100}[k])\,\big|_k\big)\,\big|_k \Leftrightarrow \theta_n^{100}[k] = z^{-1}\big(OCV^{-1}(V_{max})\,\big|_k\big)\,\big|_k \tag{5.40}$$

Equations (5.1) and (5.6) of the ESC model described in Section 5.1 are updated with the recalculated values of $\theta_n^0[k]$ and $\theta_n^{100}[k]$ and the updated curve $OCV\big(z(\theta_n)\,\big|_k\big)\,\big|_k$.

It is useful to introduce two new variables to calculate the capacity recovery associated to the extension of the minimum and maximum degrees of lithiation. New variables $\theta_n^{0,tune}$ and $\theta_n^{100,tune}$ are introduced to track the change in the NE's lithiation boundaries ($\theta_n^0, \theta_n^{100}$) from one time step to the next. $\Delta\theta_n^{0,tune}[k]$ is the small change in $\theta_n^0[k]$ after the SEI lithium loss and $\Delta\theta_n^{100,tune}[k]$ is the (not so) small change in $\theta_n^{100}[k]$ after subtracting $\Delta\theta_n^{loss}[k]$ from $\theta_n^{100}[k-1]$ due to SE lithium loss (see Figure 5-9 and Figure 5-10 for graphical clarification).

The variables $\theta_n^{0,tune}$ and $\theta_n^{100,tune}$ represent the amount of previously unused lithium that becomes cyclable after degradation (see Figure 5-9.$B_2$ and $B_3$). This is the reason why $\Delta\theta_n^{0,tune}[k]$ is referred to the unused Li NE's reserve degree of lithiation at the previous time step $\theta_n^0[k-1]$ in (5.41), while $\Delta\theta_n^{100,tune}[k]$ is referred to the new $\theta_n$ value corresponding to the unused Li PE's reserve degree of lithiation at the previous time step $\big(\theta_n^{100}[k-1] - \Delta\theta_n^{loss}[k]\big)$ in (5.42).

$$\Delta\theta_n^{0,tune}[k] = \theta_n^0[k] - \theta_n^0[k-1] \tag{5.41}$$

$$\Delta\theta_n^{100,tune}[k] = \theta_n^{100}[k] - \big(\theta_n^{100}[k-1] - \Delta\theta_n^{loss}[k]\big) \tag{5.42}$$

Note that $\theta_n^{0,tune}[k] = \sum_k \Delta\theta_n^{0,tune}[k] < 0$ and $0 < \theta_n^{100,tune}[k] = \sum_k \Delta\theta_n^{100,tune}[k] < \theta_n^{loss}$ for all $k$ because both curves $OCP_p\big(\theta_p\big)$ and $OCP_n(\theta_n)$ are monotonically decreasing. The variable $\theta_n^{loss}$ has been intentionally defined positive to represent a loss (of lithium).

With these three variables, the time-varying relationship $z(\theta_n)\,\big|_k$ (5.29) can be tracked, relating it either to the current time step ($k$) or to the initial ($k = 0$) stages:

$$z(\theta_n)\big|_k = \frac{\theta_n - \theta_n^0[k]}{\theta_n^{100}[k] - \theta_n^0[k]} = \frac{\theta_n - \left(\theta_n^0[0] + \sum_k \Delta\theta_n^{0,tune}[k]\right)}{\left(\theta_n^{100}[0] - \sum_k \Delta\theta_n^{loss}[k] + \sum_k \Delta\theta_n^{100,tune}[k]\right) - \left(\theta_n^0[0] + \sum_k \Delta\theta_n^{0,tune}[k]\right)} \quad (5.43)$$

Conversely, the projection of $z|_k$ onto $\theta_n$ can be calculated using:

$$\begin{aligned}\theta_n(z|_k) &= \theta_n^0[k] + z|_k(\theta_n^{100}[k] - \theta_n^0[k]) \\ &= \left(\theta_n^0[0] + \sum_k \Delta\theta_n^{0,tune}[k]\right) + z|_k \Big(\left(\theta_n^{100}[0] - \sum_k \Delta\theta_n^{loss}[k] + \right. \\ &\quad \left. \sum_k \Delta\theta_n^{100,tune}[k]\right) - \left(\theta_n^0[0] + \sum_k \Delta\theta_n^{0,tune}[k]\right)\Big)\end{aligned} \quad (5.44)$$

Equations (5.31) and (5.36), which link $\theta_p$ to $\theta_n$, are revised here to relate them to the current and initial stages. The inverse function is also provided:

$$\begin{aligned}\theta_p(\theta_n)\big|_k &= \theta_p^0[k] - C_{pn}(\theta_n - \theta_n^0[k]) = \\ &\theta_p^0[0] - C_{pn}\left(\theta_n + \sum_k \Delta\theta_n^{loss}[k] - \theta_n^0[0]\right)\end{aligned} \quad (5.45)$$

$$\begin{aligned}\theta_n\left(\theta_p|_k\right) &= \theta_n^0[k] + \frac{1}{C_{pn}}\left(\theta_p^0[k] - \theta_p|_k\right) = \\ &\theta_n^0[0] + \tfrac{1}{C_{pn}}\left(\theta_p^0[0] - \theta_p|_0\right) - \sum_k \Delta\theta_n^{loss}[k]\end{aligned} \quad (5.46)$$

#### 5.3.3.1. Secondary capacity recovery

Modification of the OCV curve because of the relative displacement between $OCP_p$ and $OCP_n$ has a welcome side-effect. The (small) extension of the range of allowed degrees of lithiation $\left(\theta_n^{100,tune} - \theta_n^{0,tune}\right)$ produces a (small) capacity recovery $\left(Q_{\theta_{100}}^{gain} + Q_{\theta_0}^{gain}\right)$.

The SEI side reaction causes degradation in the form of cyclable lithium loss, $\Delta\theta_n^{loss}$. This has been quantified as a capacity loss $\Delta Q_{side}^{loss}$ in (5.21). Subsequent to degradation, one might expect to have a remaining capacity $Q[k]$ equal to $\left(Q[k-1] - \Delta Q_{side}^{loss}[k]\right)$, but this is not the case. The definition of $z = 0$ and $z = 1$ based on open-circuit voltage levels leads to a small capacity recovery. After the displacement between the curves $OCP_p$ and $OCP_n$ (instant $k_B$ in Figure 5-9 and Figure 5-10), $OCV[k_B]$ is lower than $V_{max}$ (see the green cross in Figure 5-10). Therefore, the cell SOC at this point is no longer 100% but lower. The reason is that $V_{max}$ does not correspond to $\left(\theta_n^{100}[k_A] - \theta_n^{loss}\big|_A^B\right)$ and, similarly, $V_{min}$ does not correspond to

$\theta_n^0[k_A]$. This process extends the range of allowed degrees of lithiation causing a small secondary capacity recovery $\left(\Delta Q_{\theta_0}^{gain} + \Delta Q_{\theta_{100}}^{gain}\right)$:

$$\Delta Q_{\theta_0}^{gain}[k] = \frac{\varepsilon_{s,n} Vol_n c_{s,n}^{max} F}{3600}\left(-\Delta\theta_n^{0,tune}[k]\right) \tag{5.47}$$

$$\Delta Q_{\theta_{100}}^{gain}[k] = \frac{\varepsilon_{s,n} Vol_n c_{s,n}^{max} F}{3600}\Delta\theta_n^{100,tune}[k] \tag{5.48}$$

The result of adding the three contributions to capacity change is a net capacity loss $\Delta Q_{tot}^{loss}[k]$. Figure 5-11 contains several zooms of Figure 5-10 that illustrate the post-degradation recalculation of the electrodes' lithiation boundaries. Figure 5-11 reveals that $\theta_n^{0,tune}$ is almost insignificant (Figure 5-12) and, thus, so is $Q_{\theta_0}^{gain}$ too (Figure 5-13), while $\theta_n^{100,tune}$ (Figure 5-12) accounts for nearly all the NE's stoichiometric window extension and (consistently) $Q_{\theta_{100}}^{gain}$ accounts for nearly all the capacity recovery (Figure 5-13).

$$\begin{aligned}\Delta Q_{tot}^{loss}[k] &= \Delta Q_{side}^{loss}[k] - \left(\Delta Q_{\theta_0}^{gain}[k] + \Delta Q_{\theta_{100}}^{gain}[k]\right) \\ &= \frac{\varepsilon_{s,n} Vol_n c_{s,n}^{max} F}{3600}\left(\Delta\theta_{100}^{n}[k] - \Delta\theta_0^{n}[k]\right)\end{aligned} \tag{5.49}$$

$$Q[k] = Q[k-1] - \Delta Q_{tot}^{loss}[k] = \frac{\varepsilon_{s,n} Vol_n c_{s,n}^{max} F}{3600}\left(\theta_n^{100}[k] - \theta_n^{0}[k]\right) \tag{5.50}$$

Figure 5-12, Figure 5-13 and Figure 5-14 are the result of running the code *QgainsVsQloss.m* (see Section 5.1.1.1). They show $\theta_n^{0,tune}$ and $\theta_n^{100,tune}$ vs. $\theta_n^{loss}$ as the cell ages (Figure 5-12), the contribution of $Q_{side}^{loss}$, $Q_{\theta_0}^{gain}$ and $Q_{\theta_{100}}^{gain}$ to the total capacity loss $Q_{tot}^{loss} = \sum_k \Delta Q_{tot}^{loss}[k]$ (Figure 5-13) and the ratio of capacity recovery $\left(Q_{\theta_0}^{gain}[k] + Q_{\theta_{100}}^{gain}[k]\right) = \sum_k \left(\Delta Q_{\theta_0}^{gain}[k] + \Delta Q_{\theta_{100}}^{gain}[k]\right)$ to the capacity loss caused by the SEI reaction $Q_{side}^{loss}[k] = \sum_k \Delta Q_{side}^{loss}[k]$ as the cell ages (Figure 5-14). The represented x-axis ranges in these three figures correspond to the whole lifespan of the cell, considering that its EOL corresponds to a 20% total capacity loss

Figure 5-12 shows that $\theta_n^{0,tune}$ is very small (under 1% of $\theta_n^{loss}$), while $\theta_n^{100,tune}$ is significantly larger (over 10% of $\theta_n^{loss}$). Figure 5-14 shows that both contributions add up to recover a fraction of $Q_{side}^{loss}$. This capacity recovery is non-linear with $Q_{side}^{loss}$ and ranges between 11% and 17.5% of $Q_{side}^{loss}$, approximately.

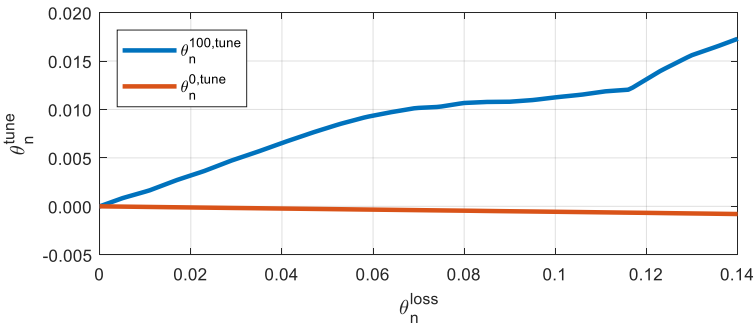


Figure 5-12. $\theta_n^{0,tweak}$ and $\theta_n^{100,tweak}$ vs. $\theta_n^{loss}$

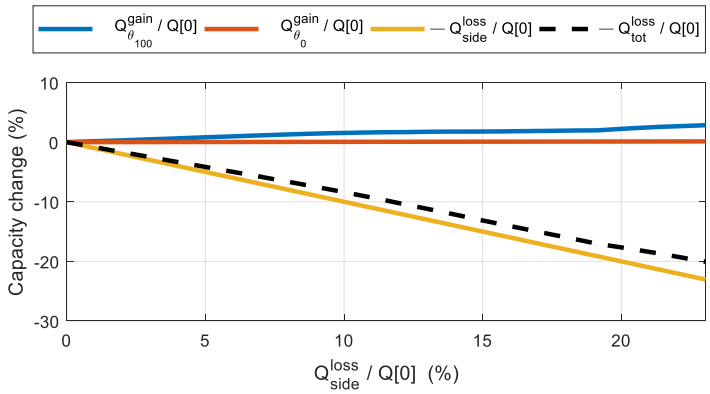


Figure 5-13. Capacity gains $Q_{\theta_{100}}^{gain}$ and $Q_{\theta_0}^{gain}$ and total capacity loss $Q_{tot}^{loss}$

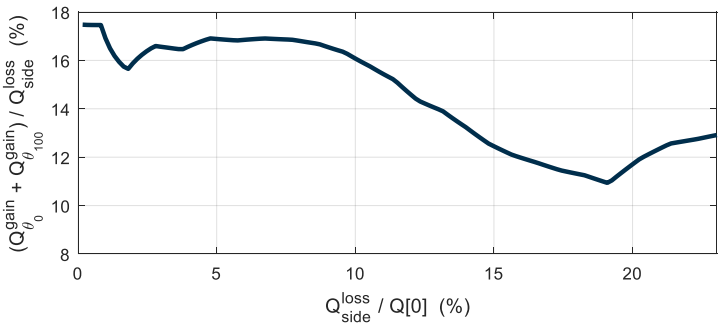


Figure 5-14. Relative capacity recovery with respect to $Q_{side}^{loss}$

## 5.4. Characterization tests of battery cells

The experimental data of the studied cells were obtained in [197]. Nine Panasonic NMC cells with graphite negative electrode were subjected to a diversity of tests, including long-term self-discharge tests. This specific cell type was used in the plug-in hybrid electric vehicles Ford C-Max Energi and Ford Fusion Energi from 2013 to 2018 and is currently under thorough study at the University of Colorado Colorado Springs. They have a nominal voltage of 3.7 $V$ and a nominal capacity of 25 $Ah$.

The nine tested cells (FP07 to FP15) were divided into three groups of three, corresponding to different test temperatures. Three two-months-each Self-Discharge Tests were performed at 0 °$C$ (cells FP07, FP08, FP09), 25 °$C$ (cells FP13, FP14, FP15) and 50 °$C$ (cells FP10, FP11, FP12). The main objective of the tests was to observe battery degradation during self-discharge. Four different test types were used to characterize cell degradation:

- 2 × Four-steps OCV Test (OCVT)
- 4 × Pulse Test (PT)
- 3 × Self-Discharge Test (SDT)
- 2 × Capacity Single Loop Test (CSLT)

Table 5-4 and Figure 5-15 describe the test flowchart followed over the accumulated period of seven and a half months. A brief description of each individual test is provided next.

Table 5-4. Tests flowchart

| # | Test | Description | Duration |
|---|---|---|---|
| 1. | OCVT1 | Initial accurate capacity estimation | 15 days |
| 2. | PT1 | Initial internal resistance measurement | 3 days |
| 3. | SDT1 | Observation of self-discharge | 2 months |
| 4. | PT2 | Intermediate internal resistance measurement | 3 days |
| 5. | CSLT1 | First intermediate approximate capacity estimation | 3 days |
| 6. | SDT2 | Observation of self-discharge | 2 months |
| 7. | PT3 | Intermediate internal resistance measurement | 3 days |
| 8. | CSLT2 | Second intermediate approximate capacity estimation | 3 days |
| 9. | SDT3 | Observation of self-discharge | 2 months |
| 10. | PT4 | Final internal resistance measurement | 3 days |
| 11. | OCVT2 | Final accurate capacity estimation | 15 days |
| | | Total | 7 ½ months |

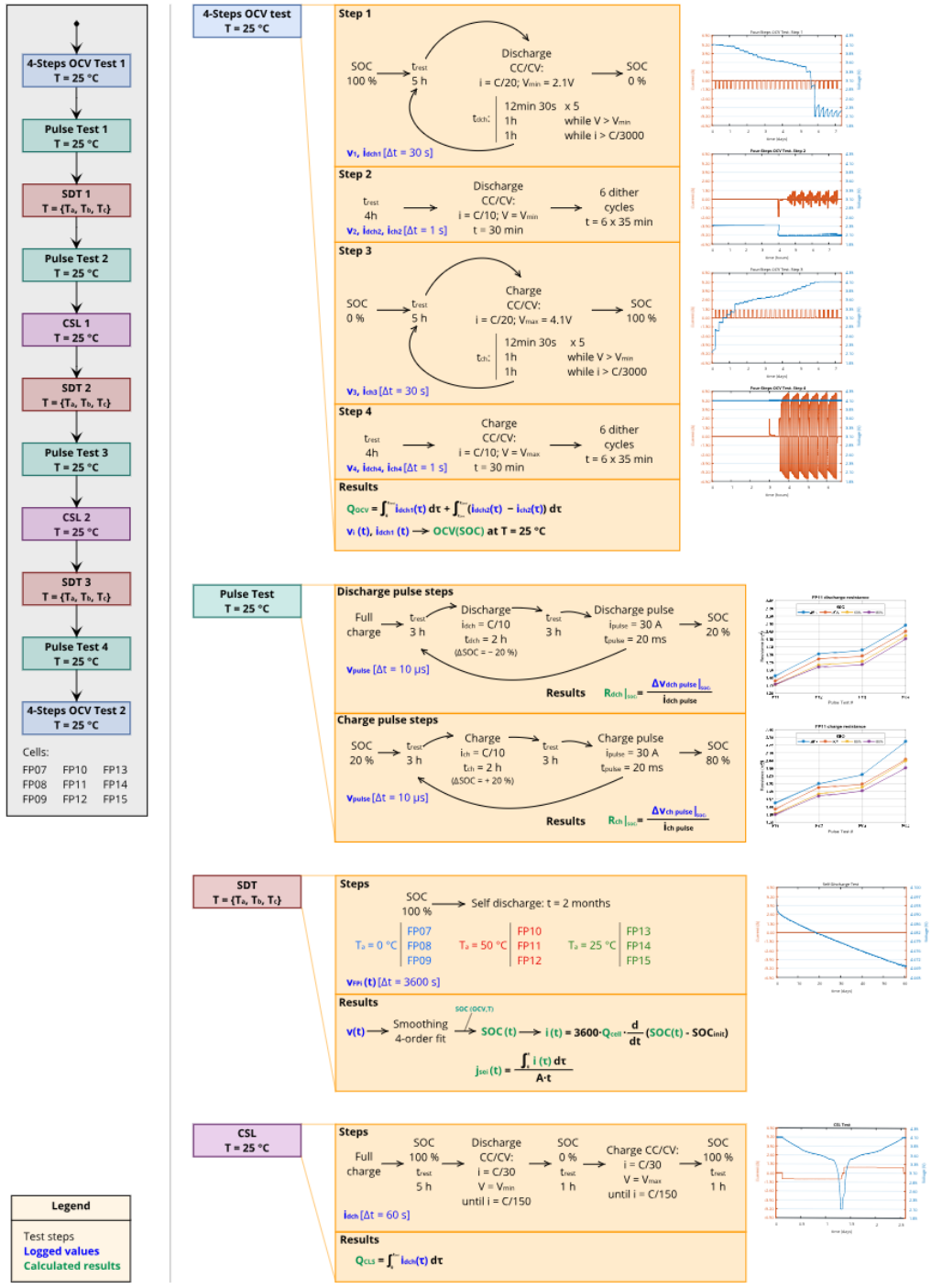


Figure 5-15. Tests procedures

### 5.4.1. Capacity estimation: Four-Steps OCV Test (OCVT)

Accurate capacity estimations were performed at the beginning and the end of the experiment. The cells were discharged from a 100% State of Charge (SOC) to 0% applying a scheme similar to CC/CV (constant current / constant voltage) but including periodic interruptions of prolonged rest periods to let the cell stabilize at OCV. The current used was $1.25\ A\ (C/20)$. The voltage limits were established in $V_{max} = 4.1\ V$ and $V_{min} = 2.1\ V$ [201] (it is considered that OCV equaling this limits corresponds to $z = 1$ and $z = 0$, respectively). These are the Four-Steps OCV Tests (OCVTs).

This test is divided into four steps:

- Step 1 (Figure 5-16)

The cell is initially fully charged ($z = 1$, $v = 4.1\ V$,where $v$ is the cell terminal voltage). It remains unloaded for 5 hours to guarantee equilibrium. Then, a 12.5-minute discharge is performed followed by a 5-hour rest period. This is repeated five times. Afterwards, the same discharge–rest scheme is repeated but extending the discharge period to one hour. Discharge current is set at $C/20$ while $v > V_{min}$ (constant current stage). The constant voltage stage starts when the cell voltage reaches the lower limit. Then, constant current discharge periods are substituted by constant voltage ($V_{min}$) periods. Rest periods of 5 hours follow every discharge period. This continues while $i_{app} > C/3000$. At this point, the cell is considered to be at $z = 0$.

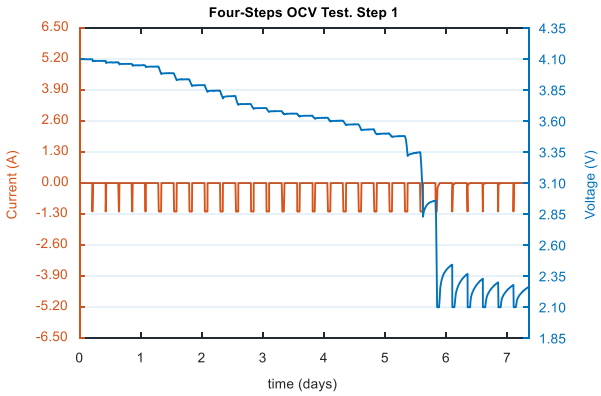


Figure 5-16. Four-Steps OCV Test applied to FP14. Discharge.

- Step 2 (Figure 5-17)

The cell then rests for 4 hours to let its voltage stabilize–at a value higher than $V_{min}$. A 30-minute CC/CV discharge is performed next with a 2.5 $A$ ($C/10$) current so the cell voltage reaches exactly $V_{min}$. Afterwards, six low-current ($|i_{app}| < C/25$) dither cycles of 35 minutes each are executed to minimize the hysteresis.

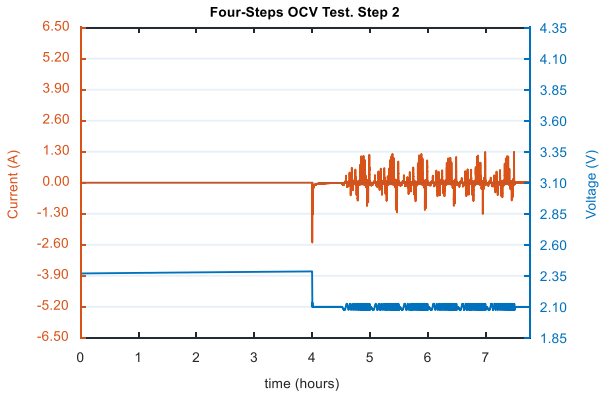


Figure 5-17. Four-Steps OCV Test applied to FP14. Hysteresis minimization after discharge.

- Step 3 (Figure 5-18)

The battery cell is charged from $z = 0$ to $z = 1$ following the same process as in step 1 but now charging instead of discharging.

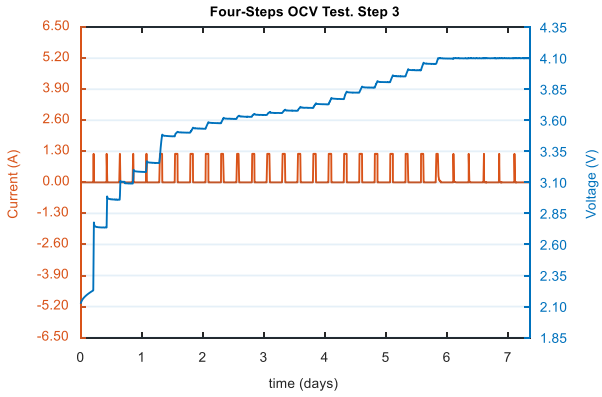


Figure 5-18. Four-Steps OCV Test applied to FP14. Charge.

- Step 4 (Figure 5-19)

The hysteresis is minimized following the Step 2 procedure with higher current: $|i_{app}| < C/4$. Initial charge (instead of discharge) is required in this case prior to the six dither cycles.

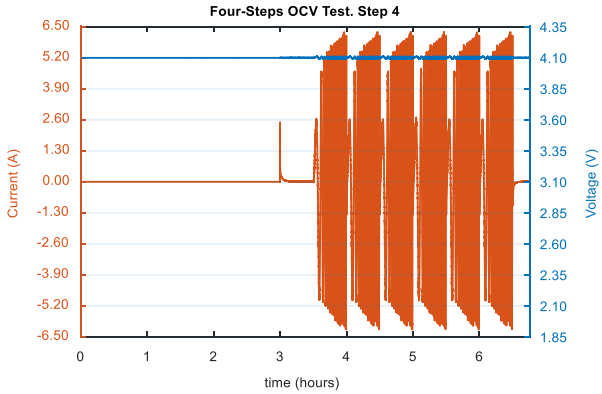


Figure 5-19. Four-Steps OCV Test applied to FP14. Hysteresis minimization after charge.

Cell capacity is estimated by integrating the discharge current over the discharge time. Capacity estimates prior to and after the three Self-Discharge Tests are shown in Figure 5-20:

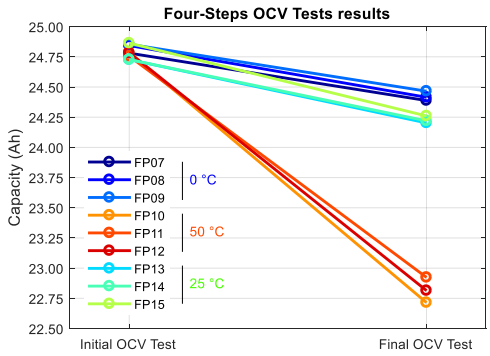


Figure 5-20. Results of the initial and final Four-Steps OCV Tests.

### 5.4.2. Internal resistance estimation: Pulse Test (PT)

Cell's internal resistance is estimated by means of pulse tests at four different states of charge: 80%, 60%, 40% and 20%, both charging and discharging. One pulse test is performed after the initial Four-Step OCV Test and then one after each Self-Discharge Test. Pulse Test procedure is carried out as explained next, starting with fully charged cell:

- Discharge pulse steps

The cell rests for 3 hours, then a 2.5 $A$ ($C/10$) discharge current is applied for 2 hours, i.e. the SOC falls by 20%. A new 3 hours rest period follows and then a 20 $ms$, 30 $A$ ($1.20C$) discharge pulse is applied. Cell voltage is sampled at high frequency over a certain time window around the pulse. Cell internal resistance can thus be calculated by dividing the voltage increment by the pulse current (Ohm's law). This process is repeated at $SOC = \{80\%, 60\%, 40\%, 20\%\}$.

- Charge pulse steps

The same procedure is repeated while charging the battery from $SOC = 20\ \%$ to 80 %. Current pulses are now charging pulses.

The results are graphically represented in Figure 5-21.

The overall expected behavior of the cell's internal resistance is to increase as the cell ages. However, it deviates from this general tendency at some points, probably due to cracking of the (rather rigid) SEI layer caused by rapid volume changes of the negative electrode when charging or discharging the cell [110]. When the SEI layer cracks, a new conductive path is opened for the lithium ions to flow, so average cell's internal resistance decreases temporarily. As the cell degrades, new SEI will grow over the crack surface thus causing new increase of the resistance of the SEI layer and, consequently, of the cell's internal resistance, $R_0 + R_{SEI}$ [124, 212].

This might be the reason that explains some cells' internal resistance erratic tendency over time. As Figure 5-22 shows, FP14's internal resistance both increases and decreases at some point within the tests period. Although FP14's internal resistance does not exhibit a clear tendency up or down from PT1 to PT4, it is expected that internal resistance will grow in the long term. This is actually the tendency that other cells' internal resistance shows already over the 7 ½ months tests period. For example, FP11 (see Figure 5-23).

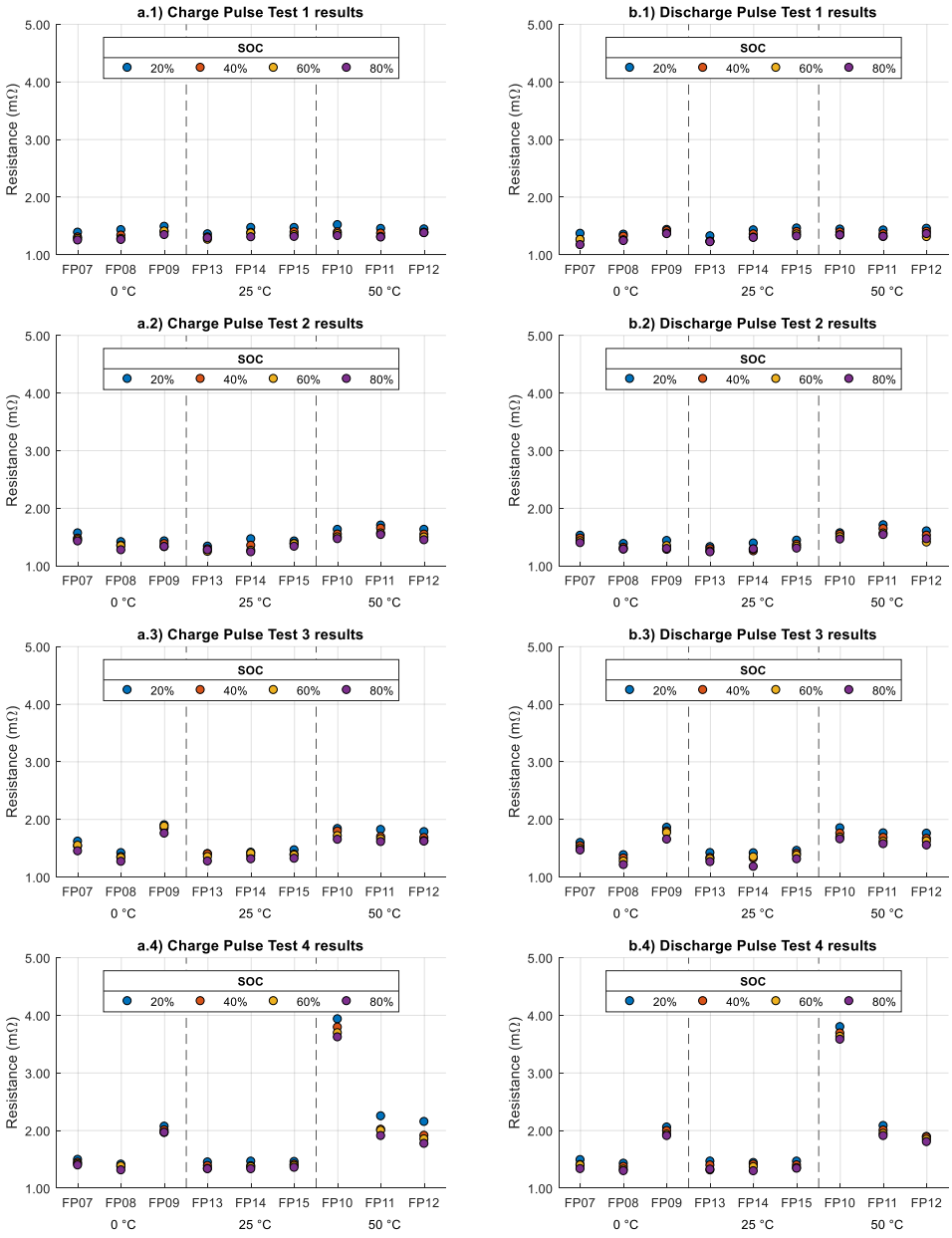


Figure 5-21. Results of Pulse Tests 1 to 4. Internal resistance is calculated at four different states of charge $SOC = \{20\%, 40\%, 60\%, 80\%\}$: (a.i) Charge Pulse Test #i, (b.i) Discharge Pulse Test #i

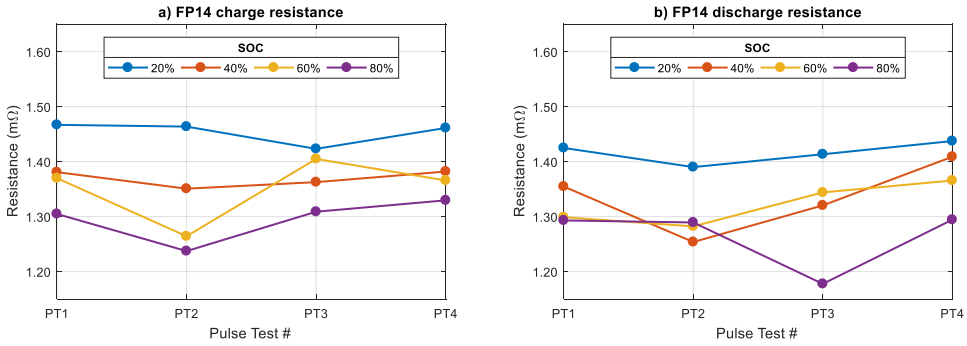


Figure 5-22. Individual cell results: (a) FP14 Charge Pulse Tests, (b) FP14 Discharge Pulse Tests

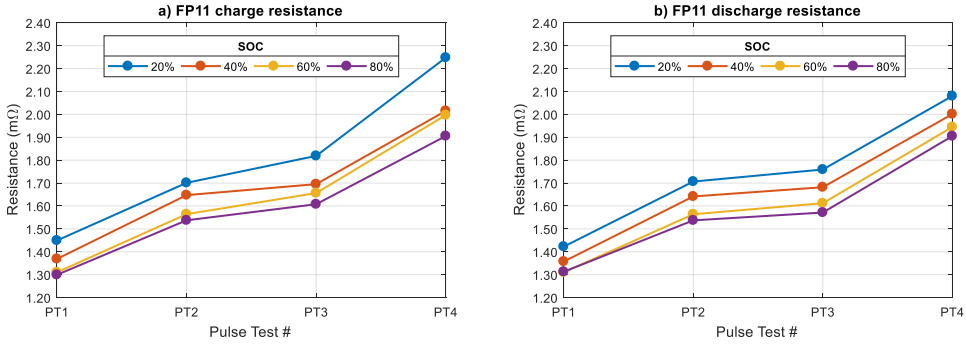


Figure 5-23. Individual cell results: (a) FP11 Charge Pulse Tests, (b) FP11 Discharge Pulse Tests.

### 5.4.1. Self-Discharge Test (SDT)

The cells are charged up to $z = 1$ and then stored for 2 months at constant temperature while continuously monitoring their voltages (see Figure 5-24). This is the Self-Discharge Test (SDT). Cells are divided into three groups, according to the temperature at which the SDTs test are performed: 0 °$C$ (cells FP07, FP08, FP09), 25 °$C$ (cells FP13, FP14, FP15) and 50 °$C$ (cells FP10, FP11, FP12).

Voltage drop is shallow at the three tested temperatures, but it gets noticeably deeper at higher temperatures. Indeed, voltage drop over two-months SDT1 is approximately 6 $mV$ at 0 °$C$, 24 $mV$ at 25 °$C$ and 110 $mV$ at 50 °$C$. Voltage drop in successive SDTs is less deep. In principle, this is coherent with the model's prediction since $\theta_n^{100}$ decreases with degradation; therefore, $\theta_n$ starts at $\theta_n^{100}[0]$ (the initial state at the beginning of each SDT) and gets progressively smaller, and $J_{side}$ decreases pronouncedly as $\theta_n$ decreases.

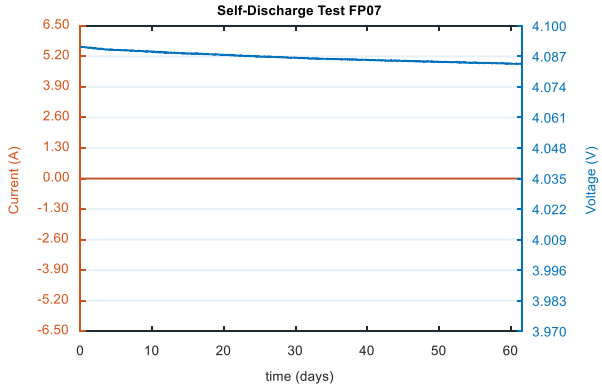


(a)

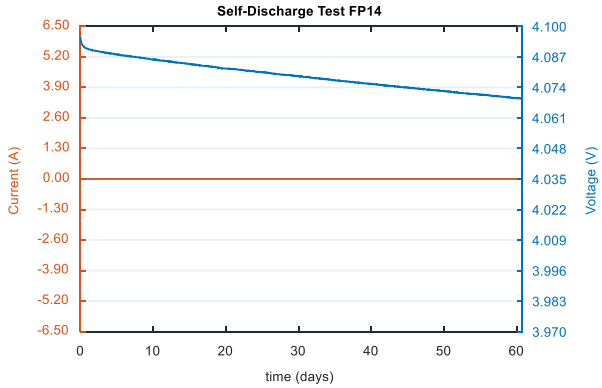


(b)

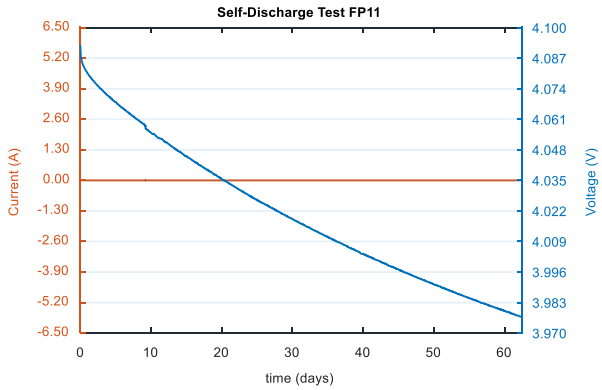


(c)

Figure 5-24. OCV evolution during SDT1 of (a) FP07 (0 °C), (b) FP14 (25 °C), (c) FP11 (50 °C)

### 5.4.2. Capacity estimation: Capacity Single Loop Test (CSLT)

Capacity Single Loop Tests (CSLT) consist in performing intermediate estimations of capacity after SDT1 and SDT2. Unfortunately, CSLT is different from the Four-Steps OCV Test so their results are not comparable to each other: CSLT is simpler, faster (see the x-axis in Figure 5-25) and less accurate test than OCVT. The cells are charged up to $z = 1$ and stabilized at this SOC for 5 hours, afterwards a CC/CV discharge is performed with a $C/30$ discharge current. The CV (at $V_{min}$) stage ends when the current descends below $C/150$. Afterwards, the battery cells rest at $z = 0$ for 1 hour and then they are charged following the inverse procedure. The cells' capacities are estimated by integrating the discharge currents.

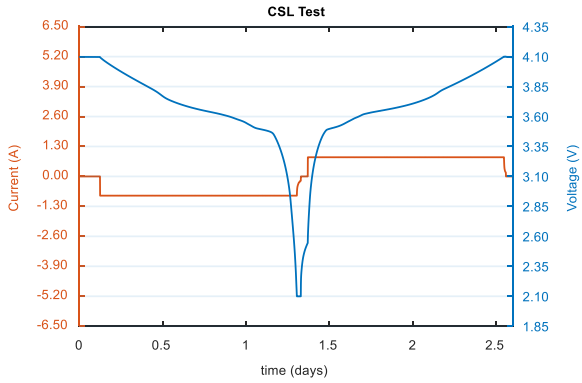


Figure 5-25. Capacity Single Loop Test applied to FP14

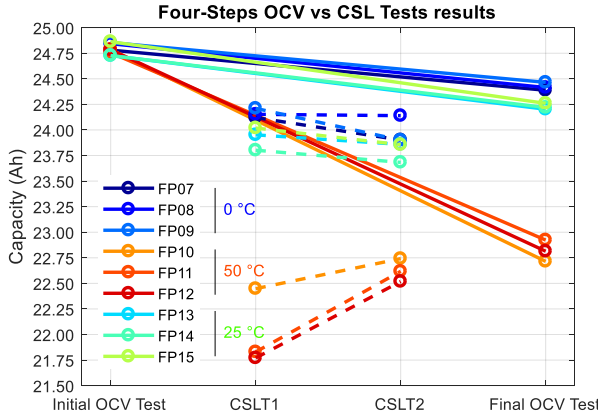


Figure 5-26. Four-Steps OCV Tests and CSL Tests results

The results of CSLTs are shown in Figure 5-26 superposed to those of the Four-Steps OCV Test. It is evident that the capacity estimations from these two different test types are incomparable and, what is worse, CSLTs results seem wrong in some cases, as some cell capacities grow from CSLT1 to CSLT2, which makes no physical sense.

### 5.4.3. Self-Discharge Tests data

The most relevant numerical results from these tests have been gathered in Table 5-5. Some of the results have been used to develop the proposed degradation model. The following list connects the tests with the results they produce:

- Initial and final Four-Steps OCV Tests → Capacity estimation $Q_{ocv}$
- Pulse Tests 1–4 → Discharge and charge internal resistance estimations $R_{dch}$ and $R\_ch$, at $SOC = \{20\%, 40\%, 60\%, 80\%\}$
- Self-Discharge Tests 1–3 → Voltage curve, Final OCV
- Capacity Single Loop Tests 1–2 → Capacity estimation $Q_{csl}$

All the tests were performed at 25 °C, except some of the SDTs, as explained above.

## 5.1. Simulation of cell operation

Cell response is simulated using the ESC equivalent circuit cell model presented in section 5.1 complemented with the degradation model explained in Sections 5.2 and 5.3. The comprehensive model has been implemented in a system of Matlab functions.

### 5.1.1. Model implementation in Matlab

Several programs have been created to model cell response in Matlab. They are reviewed next. The Matlab functions *SimCell.m* and *SimCell_lookuptables.m* compute the cell response to any current profile input. The latter is a bit faster as it uses lookup tables to save time and computational resources. Both functions rely on a package of other functions to work; this system of functions is explained next.

Table 5-5. Summary of Machado's tests results. Table cell's background indicates the temperature at which the test was performed: blue 0 °C, green 25 °C, red 50 °C.

| # | Test | Result | | FP07 | FP08 | FP09 | FP10 | FP11 | FP12 | FP13 | FP14 | FP15 |
|---|---|---|---|---|---|---|---|---|---|---|---|---|
| 1 | OCVT1 | $Q_{ocv1}$ $(Ah)$ | | 24.781 | 24.843 | 24.854 | 24.786 | 24.755 | 24.784 | 24.727 | 24.727 | 24.863 |
| 2 | PT 1 | $R_{dch1}$ (mΩ) | 20% | 1.365 | 1.350 | 1.432 | 1.439 | 1.423 | 1.452 | 1.322 | 1.425 | 1.457 |
| | | | 40% | 1.257 | 1.316 | 1.410 | 1.388 | 1.357 | 1.399 | 1.225 | 1.355 | 1.396 |
| | | | 60% | 1.259 | 1.252 | 1.368 | 1.338 | 1.310 | 1.308 | 1.229 | 1.299 | 1.353 |
| | | | 80% | 1.168 | 1.239 | 1.359 | 1.338 | 1.313 | 1.360 | 1.219 | 1.293 | 1.319 |
| | | $R_{ch1}$ (mΩ) | 20% | 1.385 | 1.428 | 1.486 | 1.515 | 1.449 | 1.441 | 1.356 | 1.467 | 1.466 |
| | | | 40% | 1.303 | 1.334 | 1.393 | 1.390 | 1.369 | 1.380 | 1.303 | 1.381 | 1.392 |
| | | | 60% | 1.276 | 1.276 | 1.406 | 1.358 | 1.310 | 1.384 | 1.261 | 1.370 | 1.341 |
| | | | 80% | 1.249 | 1.258 | 1.343 | 1.326 | 1.299 | 1.376 | 1.287 | 1.305 | 1.311 |
| 3 | SDT 1 | $OCV_{end1}$ $(V)$ | | 4.084 | 4.070 | 4.084 | 3.979 | 3.977 | 3.977 | 4.070 | 4.069 | 4.069 |
| 4 | PT 2 | $R_{dch1}$ $(m\Omega)$ | 20% | 1.524 | 1.381 | 1.434 | 1.567 | 1.707 | 1.600 | 1.327 | 1.390 | 1.439 |
| | | | 40% | 1.476 | 1.317 | 1.280 | 1.541 | 1.642 | 1.526 | 1.293 | 1.254 | 1.369 |
| | | | 60% | 1.430 | 1.286 | 1.345 | 1.499 | 1.564 | 1.407 | 1.251 | 1.282 | 1.335 |
| | | | 80% | 1.396 | 1.285 | 1.295 | 1.459 | 1.537 | 1.465 | 1.237 | 1.289 | 1.301 |
| | | $R_{ch1}$ $(m\Omega)$ | 20% | 1.566 | 1.413 | 1.427 | 1.627 | 1.701 | 1.627 | 1.336 | 1.464 | 1.425 |
| | | | 40% | 1.475 | 1.353 | 1.380 | 1.546 | 1.647 | 1.544 | 1.289 | 1.351 | 1.385 |
| | | | 60% | 1.449 | 1.343 | 1.326 | 1.496 | 1.564 | 1.494 | 1.245 | 1.264 | 1.378 |
| | | | 80% | 1.425 | 1.273 | 1.330 | 1.465 | 1.537 | 1.446 | 1.272 | 1.237 | 1.334 |
| 5 | CSL Test 1 | $Q_{csl1}$ $(Ah)$ | | 24.121 | 24.153 | 24.211 | 22.448 | 21.830 | 21.771 | 23.952 | 23.802 | 24.019 |
| 6 | SDT 2 | $OCV_{end2}$ $(V)$ | | 4.088 | 4.088 | 4.087 | 3.993 | 3.989 | 3.994 | 4.069 | 4.069 | 4.069 |
| 7 | PT 3 | $R_{dch3}$ $(m\Omega)$ | 20% | 1.592 | 1.380 | 1.856 | 1.848 | 1.759 | 1.753 | 1.417 | 1.413 | 1.455 |
| | | | 40% | 1.538 | 1.323 | 1.791 | 1.755 | 1.682 | 1.664 | 1.333 | 1.320 | 1.405 |
| | | | 60% | 1.490 | 1.270 | 1.766 | 1.687 | 1.612 | 1.619 | 1.310 | 1.344 | 1.373 |
| | | | 80% | 1.462 | 1.208 | 1.651 | 1.655 | 1.571 | 1.549 | 1.260 | 1.178 | 1.309 |
| | | $R_{ch3}$ $(m\Omega)$ | 20% | 1.615 | 1.416 | 1.899 | 1.835 | 1.819 | 1.780 | 1.400 | 1.423 | 1.465 |
| | | | 40% | 1.531 | 1.348 | 1.841 | 1.791 | 1.695 | 1.678 | 1.394 | 1.363 | 1.390 |
| | | | 60% | 1.544 | 1.331 | 1.877 | 1.712 | 1.656 | 1.625 | 1.347 | 1.405 | 1.375 |
| | | | 80% | 1.447 | 1.265 | 1.754 | 1.648 | 1.608 | 1.616 | 1.271 | 1.309 | 1.318 |
| 8 | CSL Test 2 | $Q_{csl2}$ $(Ah)$ | | 23.902 | 24.140 | 23.900 | 22.742 | 22.618 | 22.518 | 23.859 | 23.683 | 23.856 |
| 9 | SDT 3 | $OCV_{end3}$ $(V)$ | | 4.094 | 4.095 | 4.094 | 4.003 | 4.006 | 4.007 | 4.068 | 4.068 | 4.068 |
| 10 | PT 4 | $R_{dch4}$ $(m\Omega)$ | 20% | 1.488 | 1.425 | 2.053 | 3.796 | 2.080 | 1.891 | 1.463 | 1.437 | 1.462 |
| | | | 40% | 1.403 | 1.371 | 1.992 | 3.687 | 2.001 | 1.879 | 1.395 | 1.409 | 1.397 |
| | | | 60% | 1.395 | 1.322 | 1.930 | 3.628 | 1.945 | 1.842 | 1.309 | 1.366 | 1.348 |
| | | | 80% | 1.332 | 1.296 | 1.905 | 3.578 | 1.905 | 1.800 | 1.323 | 1.294 | 1.338 |
| | | $R_{ch4}$ $(m\Omega)$ | 20% | 1.492 | 1.410 | 2.068 | 3.932 | 2.248 | 2.150 | 1.447 | 1.461 | 1.456 |
| | | | 40% | 1.444 | 1.369 | 2.004 | 3.789 | 2.015 | 1.910 | 1.385 | 1.382 | 1.410 |
| | | | 60% | 1.418 | 1.378 | 1.958 | 3.691 | 1.997 | 1.848 | 1.334 | 1.366 | 1.385 |
| | | | 80% | 1.395 | 1.309 | 1.963 | 3.618 | 1.905 | 1.769 | 1.330 | 1.330 | 1.354 |
| 11 | OCVT2 | $Q_{ocv2}$ $(Ah)$ | | 24.388 | 24.415 | 24.465 | 22.715 | 22.923 | 22.814 | 24.202 | 24.220 | 24.260 |

#### 5.1.1.1. Structure of the simulation programs

Figure 5-27 shows the program dependence graph. It shows all the custom Matlab functions that play a role either in analyzing the data generated from the battery tests in Section 5.4 or in simulating cell's operation, and their dependencies. Matlab functions are represented by white-background boxes, pre-stored lookup tables data (.mat files) are represented by green-background boxes, generation of that data is represented by green arrows, parent-children dependencies are represented by blue lines (parent function being the upper one and children function the lower one), and requirement of pre-stored lookup table data is represented by green dashed lines.

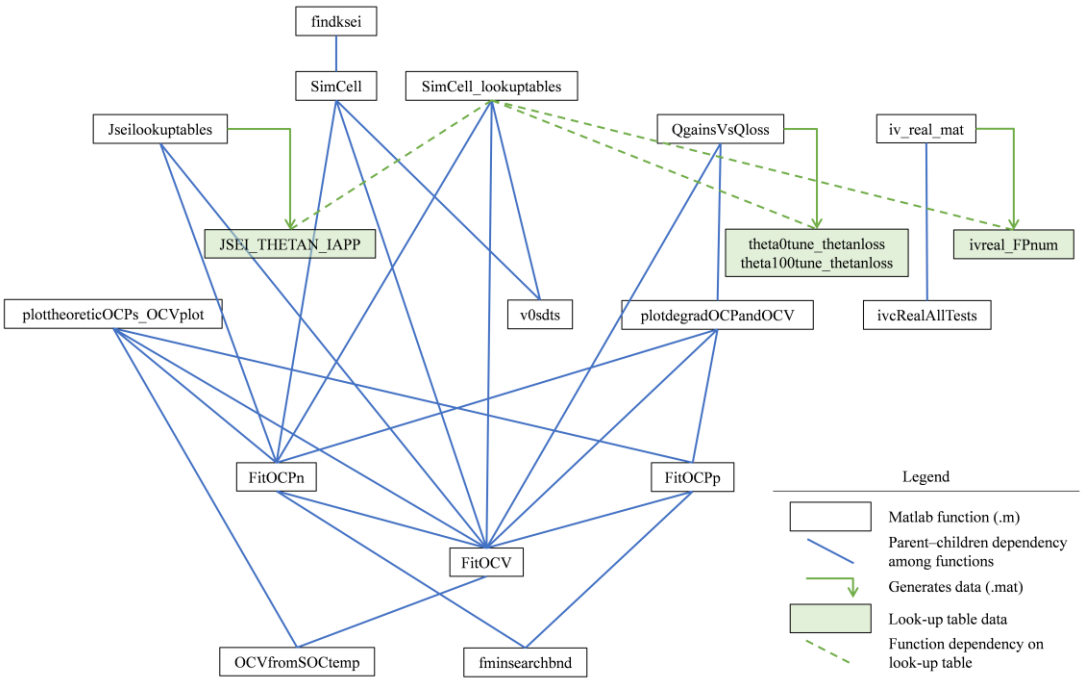


Figure 5-27. Program dependence graph

A brief explanation of individual functions is provided next:

- *findksei.m*: Performs iterative search of the parameter $k_{SEI}$ for each of the nine tested cells. It calls *SimCell.m* with two initial guessed $k_{SEI}$ values to simulate cell operation with an input current profile equal to the one applied through the whole set of tests between OCVT1 and OCVT2 (that is, PT1 →… → OCVT2, as in Section 5.1.2). The guessed $k_{SEI}$ parameters produce a capacity loss in simulation

that is compared to the real one. The $k_{SEI}$-dependent total capacity loss resulting from the simulations are then compared to the real value, ($Q_{ocv1} - Q_{ocv2}$, from Table 5-5). A new plausible $k_{SEI}$ value is then generated by fitting the resulting errors to a linear tendency line "error vs. $k_{SEI}$". The $k_{SEI}$ value correspondent to this tendency line equaling zero (null error) is taken as the next candidate. This value is used as the input to run *SimCell.m* once again. Applying this process iteratively leads to finding successive $k_{SEI}$ values that converge to the best estimate. Achieving a sufficiently small error (relative error lower than $0.01\%$ and absolute error lower than $2.5 \cdot 10^{-3}\ Ah$) stops the search process. The last evaluated $k_{SEI}$ is accepted. Once $k_{SEI}$ values are obtained for the first time, they are hard-coded in the other functions that need them, specifically, *findksei.m* itself (to avoid unnecessary evaluations if it is run again), *SimCell*, *SimCell_lookuptables* and *Jseilookuptables*.

- *SimCell.m*: Executes cell simulation performing all the calculations described in Sections 5.1, 5.2 and 5.3.
- *SimCell_lookuptables.m*: Executes cell simulation (is an alternative to *SimCell.m*) profiting from pre-stored data generated by *Jseilookuptables.m*, *QgainsVsQloss.m* and *iv_real_mat.m*. This saves time and computational effort.
- *Jseilookuptables.m*: Pre-computes $J_{side}$ resulting from all possible combinations of inputs $i = \{-125, -124, \dots, 125\}\ (A)$, $\theta_n = \{0, 0.005, \dots, 1\}$, $FP\# = \{07, 08, \dots, 15\}$. Produces the multidimensional arrays (251 x 201 x 9 each) JSEI, THETAN and IAPP and stores them in *JSEI_THETAN_IAPP.mat*.
- *QgainsVsQloss.m*: Calls *plotdegradOCPandOCV.m* with different input values of $\theta_n^{loss} = \{0, 0.001, \dots, (\theta_n^{100}[0] - \theta_n^{0}[0])\}$. It stores the resulting $\theta_n^{0,tune}$ and $\theta_n^{100,tune}$ corresponding to each $\theta_n^{loss}$ value and creates Figure 5-12, Figure 5-13 and Figure 5-14.
- *iv_real_mat.m*: Calls *ivcRealAllTests.m* for all FP07…15 and creates *ivreal_FPnum.mat* with the resulting data.
- *plottheoreticOCPs_OCV.m*: Creates Figure 5-7.
- *v0sdts.m*: Cell's voltage at the beginning of the SDTs is not exactly $4.1\ V$ but slightly lower (see Figure 5-24). This function finds the voltage value at the beginning of each SDT interpolating a fourth-degree polynomial fit of the measured voltage (the logged voltage curves are smoothed with this fit to neglect measurement inaccuracies). The obtained voltage values are used as the maximum

charge voltages for the simulation in Section 5.1.2 so simulation and measurements are comparable to each other.

- *plotdegradOCPandOCV.m*: Calculates $\theta_n^{0,tune}$ and $\theta_n^{100,tune}$ corresponding to any given $\theta_n^{loss}$ input. It also creates Figure 5-10 and Figure 5-11.
- *ivcRealAllTests.m*: Reads the logged values of (input) current and (output) voltage profiles from the Excel files (.xlsm) resulting from each individual test, and merges them in the appropriate sequence. It generates current and voltage vectors containing this information.
- *FitOCPn.m*: Fits the (incomplete) NE's OCP curve measured in [201] to the theoretical curve $OCP_n^{theor}$ of (5.35) to obtain the parameters $k_{cv}^n$ and $\theta_n^{shift}$. It generates Figure 5-7.b and provides data of the lookup tables $OCP_n^{theor}(\theta_n)$ and $OCP_n(\theta_n^{rel})$ as well.
- *FitOCPp.m*: Fits the (incomplete) PE's OCP curve measured in [201] to the theoretical curve $OCP_p^{theor}$ of (5.34) to obtain the parameters $k_{cv}^p$ and $\theta_p^{shift}$. It generates Figure 5-7.a and provides data for the lookup tables $OCP_p^{theor}(\theta_p)$ and $OCP_p(\theta_p^{rel})$ as well.
- *FitOCV.m*: Fits the subtraction $OCP_p$ minus $OCP_n$ to the initial OCV curve to obtain the initial electrodes' lithiation boundaries $\{\theta_p^0[0], \theta_p^{100}[0], \theta_n^0[0], \theta_n^{100}[0]\}$. It generates Figure 5-7.c and provides data for the lookup tables $OCP_p(\theta_p^{rel})$, $OCP_n(\theta_n^{rel})$ and $OCV(z)|_0$ as well.
- *OCVfromSOCtemp.m*: Interpolates OCV value from SOC and temperature values (code from [94]).
- *fminsearchbnd.m*: Finds minimum of constrained multivariable functions using derivative-free method (code from Matlab File Exchange). It is a variant of *fminsearch.m*, the Matlab solver of unconstrained multivariable functions.

The obtained $k_{SEI}$ values resulting from *findksei.m* are:

Table 5-6. Estimates of $k_{SEI}$ obtained by fitting capacity loss

| FP # | FP07 | FP08 | FP09 | FP10 | FP11 | FP12 | FP13 | FP14 | FP15 |
|---|---|---|---|---|---|---|---|---|---|
| $T$ | 0 °C | | | 50 °C | | | 25 °C | | |
| $k_{SEI}(A/m^3) \cdot 10^3$ | 1.4201 | 1.6961 | 1.5145 | 2.7772 | 2.2497 | 2.3435 | 1.1924 | 1.0283 | 1.2327 |
| $\overline{k_{SEI}}(A/m^3) \cdot 10^3$ | 1.5436 | | | 2.4568 | | | 1.1511 | | |

It is important to comment that the $k_{SEI}$ values obtained here are noticeably smaller than those obtained in [197], where this lumped parameter was calculated by fitting voltage drop over SDTs, disregarding recalculation of OCV with degradation. In this work, on the contrary, $k_{SEI}$ has been fitted to produce a capacity loss in simulation (considering secondary capacity recovery) equal to the observed one over the whole set of tests, but voltage drop over SDTs has not been fitted. It does not seem to be possible to fit both capacity loss and voltage drop at the same time by just tuning the lumped parameter $k_{SEI}$. Presently, it is not certain what may be the main cause: the strategy used to optimize $k_{SEI}$ or the model used.

#### 5.1.1.2. Lookup tables of the degradation model

The simulation codes (both *SimCell.m* and *SimCell_lookuptables.m*) require some lookup tables to work. They are divided into three categories:

- Initial cell characterization lookup tables
  - $OCV(z)\big|_0$ from [201]
  - $OCP_p(\theta_p)$ from [201]
  - $OCP_n(\theta_n)$ from [201]
- Recalculation of OCV curve every time step:
  - $OCV\left(\theta_n, \Delta\theta_n^{loss}\right)\big|_k$ from (5.38)
- Three extra lookup tables are pre-computed to simplify and accelerate calculations only in *SimCell_lookuptables.m*:
  - $J_{side}\left(i_{app}, OCP_n, T\right)$ from (5.17) solved algebraically applying [196]
  - $\theta_n^0\left(\Delta\theta_n^{loss}\right)$ and $\theta_n^{100}\left(\Delta\theta_n^{loss}\right)$ from (5.39) and (5.40)

Generating lookup tables of the intermediate variables $\Delta Q_{side}^{loss}(J_{side})$, $\Delta\theta_n^{loss}(\Delta Q_{side}^{loss})$, $\Delta\theta_n^{0,tune}\left(\Delta\theta_n^{loss}\right)$, $\Delta\theta_n^{100,tune}\left(\Delta\theta_n^{loss}\right)$, $\Delta Q_{\theta_0}^{gain}\left(\Delta\theta_n^{0,tune}\right)$ and $\Delta Q_{\theta_{100}}^{gain}\left(\Delta\theta_n^{100,tune}\right)$ has been discarded because there is no need for simplification as their calculations only involve one basic mathematical operation (multiplication or subtraction) each: see (5.21), (5.23), (5.41), (5.42), (5.47) and (5.48).

### 5.1.2. Simulation results

The Matlab code *SimCell_lookuptables.m* has been utilized to simulate cell response with an input current profile coincident with the set of tests performed between initial and final capacity estimations (i.e. PT1 → SDT1 → PT2 → CSL1 → SDT2 → PT3 → CSL2 → SDT3 → PT4 → OCVT2). Cell FP15 has been simulated, so the temperature is $T = 25\ °C$. The time

step used in discretization is $\Delta t = 60\ s$, which is considerably smaller than needed to capture cell dynamics with the cell subjected to the mentioned current profile. Figure 5-28 shows the simulation results. Blue and red curves are the simulation results, while yellow curves are the real values of some of the variables that were logged during testing.

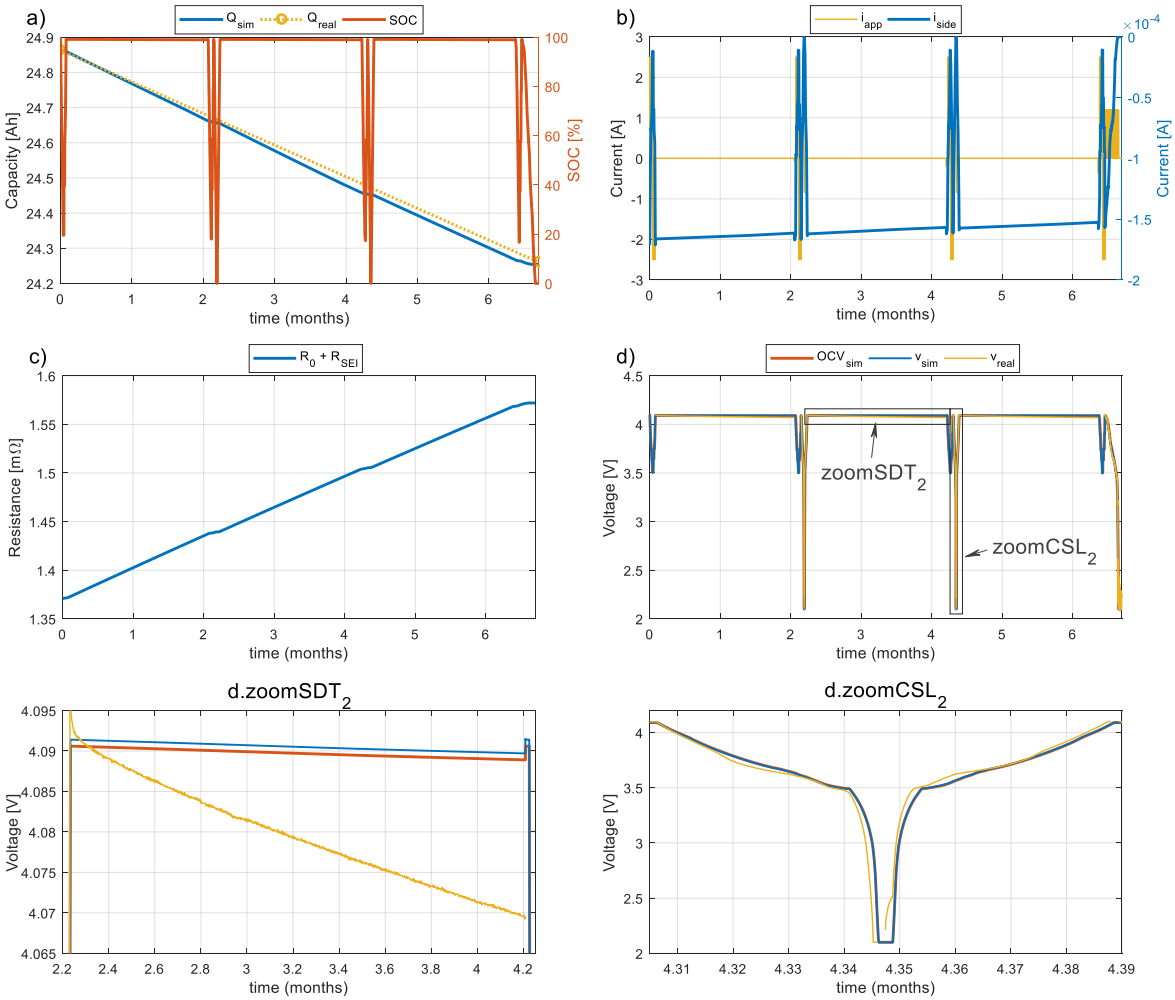


Figure 5-28. Simulation results: cell response under the application of a current profile coincident with the set of tests described in Section 5.4: (a) Capacity and SOC, (b) Applied current and SEI side-reaction current, (c) Series resistance, (d) OCV and cell voltage. Blue and red curves are the simulation results; yellow curves are the real values, measured during testing. The $SDT_2$ and $CSL_2$ regions of (d) have been zoomed-in to make small disagreement between the model results and real measurements visible.

Figure 5-28 graphs are individually described next:

- Figure 5-28.a represents the simulated cell capacity $Q_{sim}$ (blue) and the evolution of the simulated state of charge $SOC_{sim}$ (red). The capacity loss in simulation coincides with the real value $Q_{real}$ (yellow circles) in that points where the latter is available. This was expected given that $k_{SEI}$ has been estimated precisely to fit this result. Note that the actual capacity is only known at the beginning and end of the test; the yellow dashed line only connects both points, but the actual path between them is unknown.
- Figure 5-28.b shows the applied current $i_{app}$ (yellow) and the current associated to cyclable lithium loss $i_{side} = J_{side} Vol_n$ (blue). Coherently with Randall's model, $J_{side}$ is high when so too are charge current and cell SOC (or, equivalently, $\theta_n$).
- Figure 5-28.c represents the cell's internal resistance increase. The SEI film resistance rises at a rate determined by the parameter $k_R$ estimated above.
- Figure 5-28.d shows the evolution of the open circuit voltage $OCV_{sim}$ (red), the simulated cell voltage $v_{sim}$ (blue), and the measured cell voltage $v_{real}$ (yellow). $OCV_{sim}$ and $v_{sim}$ are almost undistinguishable because current is either zero or very low during the whole set of tests, so diffusion voltage $-\left(R_1 i_{R_1}[k] + R_2 i_{R_2}[k]\right)$ and instantaneous voltage drop $-(R_0 + R_{SEI}[k]) i_{app}[k]$ are consequently small, while hysteresis voltage $(M_0 s[k] + Mh[k])$ is typically small too in Li-NMC batteries.
    - Figure 5-28.d.zoomSDT2 shows that cell's voltage decreases over self-discharge because of the relative shift between the NE's and the PE's stoichiometric windows (see Figure 5-9.$B_1$ or green cross in Figure 5-10). This is, indeed, qualitatively predicted by the model, although quantitatively, the model predicts a voltage drop smaller than the one observed in the experimental test.
    - Figure 5-28.d.zoomCSL2 show that the agreement between $v_{sim}$ and $v_{real}$ is fairly good (although not perfect) under operation scenarios with non-zero current, such as cell charge and discharge.

Overall, the simulation results presented above show good performance predicting capacity loss and voltage response under the simulated scenario. On one hand, since the model parameter $k_{SEI}$ has been estimated adjusting the simulated capacity loss to the actual capacity lost between OCVT1 and OCVT2, it is evidently satisfied that $Q_{sim}$ coincides with $Q_{real}$ at the points when the latter is known. On the other hand, the ESC parameters were estimated in dissimilar tests, in which a much faster current profile (the Urban Dynamometer Driving

Schedule for electric vehicles, which represents city driving conditions) was used to characterize the cells. Therefore, the good agreement between $v_{sim}$ and $v_{real}$ exhibited in Figure 5-28.d was not trivially expected. On the contrary, such agreement is noteworthy as it validates the performance of the model.

The minor differences observed in Figure 5-28 zooms are topics of future research. On one hand, voltage differences observed in Figure 5-28.d.zoom$CSL_2$ are most likely due to insignificant inaccuracies in the employed electrodes' OCP curves $OCP_p(\theta_p)$ and $OCP_n(\theta_n)$ and/or the initial OCV curve $OCV(z)\big|_0$ or to wrong estimation of the initial lithiation boundaries. On the other hand, the voltage drop over self-discharge degradation in Figure 5-28.d.zoom$SDT_2$ is not fully captured by the proposed model, and capacity decay in Figure 5-28.a seems rather linear (which is correct in long-term degradation [213], but fails to show the expected square-root-of-time initial tendency [214]); there are three possible causes that can explain these issues:

- Hypothesis 1. The initial lithiation boundaries of the negative electrode might be inaccurate:

  $J_{side}$ depends mainly on the current rate and on the open circuit potential of the negative electrode, $OCP_n(\theta_n)$. Thus, wrong initialization of $\theta_n^{100}[0]$ could have led to imprecise $J_{side}$ estimations.

  The voltage fit performed (minimizing voltage error between the measured initial OCV curve and equation (5.28) at $k = 0$) might have yielded initial negative electrode's lithiation boundaries, $\{\theta_n^0[0], \theta_n^{100}[0]\}$, that differ from the actual values. Indeed, $\theta_n[0] = \theta_n^{100}[0] = 0.5262$ results in a plateau of the curve $J_{side}(i_{app}, \theta_n, T = 25\,°C)$ for any value of $i_{app}$ (see Figure 5-29). This locally produces linear capacity decay, as $J_{side}$ is almost constant for immediately lower $\theta_n$ values. Since a reduction of $\theta_n$ does not significantly modify $J_{side}$, the tendencies of $Q_{side}^{loss}$ and $R_{SEI}$ result rather linear locally –recall that $Q_{side}^{loss}$, and $R_{SEI}$ are proportional to the integral of $J_{side}$.

  A higher value of $\theta_n^{100}[0]$ (which is probably more accurate) would produce faster decline of $J_{side}$ as $\theta_n$ decreases, because $\mathrm{d}J_{side}/\mathrm{d}\theta_n$ is steeper in that region of the $J_{side}$ curves.
- Hypothesis 2. The fitting strategy used to estimate $k_{SEI}$ or the proposed model might be insufficiently accurate:

  If this was the case, other SEI models, more complex than that of Ramadass–Randall would be required to capture the voltage drop. Such models should be simplified to reduce their computational complexity, so that they can be

implemented on a battery management system. Two options are suggested: Fu–Fergus' model of SEI growth [215], and Safari's model [216] in one of its reduced-order forms [217].

- Hypothesis 3. There are other processes apart from SEI growth having influence on cell voltage during self-discharge:

  The last hypothesis assumes that the problem might arise not from the model itself but from more basics assumptions. If this was the case, the proposed model might be correct but incomplete, so it should be complemented by modeling other mechanism(s) capable of producing a voltage drop in an unloaded cell. Thus, SEI layer growth would not be the dominant mechanism determining cell voltage during self-discharge, but other reversible process instead –at least at high SOC. It does not seem feasible that the voltage drop in Figure 5-28.d.zoomSDT2 was totally caused by loss of lithium inventory. Indeed, the capacity loss associated to $\mathbf{20}\ \boldsymbol{mV}$ voltage drop (over two months) would be much higher than the observed value –according to the model proposed here, $\boldsymbol{Q_{tot}^{loss}}$ would be greater than $\mathbf{10}\%\ \boldsymbol{Q}[\mathbf{0}]$. The fact is that the cells did not lose that much capacity permanently, so there seems to exist a second mechanism driving voltage down during self-discharge. Such mechanism would cause loss of charge without causing loss of lithium inventory, since the process does not cause degradation (it is a reversible process). Considering all the reasoning above, self-discharge caused by a small-magnitude electrochemical internal short circuit is an obvious candidate to explain the observed voltage drop. Developing a model for this mechanism and combining it with the SEI growth could yield valuable results to verify this hypothesis.

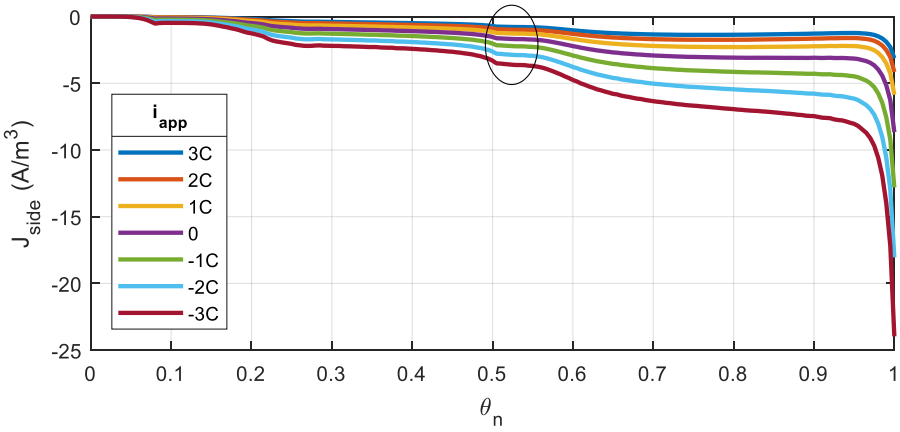


Figure 5-29. $\boldsymbol{J_{side}}$ dependency on $\boldsymbol{\theta_n}$ at various current rates.

## 5.2. Summary

This chapter describes a degradation model of lithium-ion cells with graphite negative electrodes that harmonizes the simplicity of the equivalent-circuit model from [94] with the prediction of capacity loss and internal resistance increase due to SEI degradation provided by the reduced-order physics-based model presented in [125]. A single degradation mechanism has been modeled; specifically, SEI layer growth, one of the dominant mechanisms of capacity loss. The proposed discrete model computes the shrinkage of the negative electrode's stoichiometric window (by definition, proportional to the remaining capacity) caused by loss of cyclable lithium consumed in the SEI side reaction.

Defining $\boldsymbol{SOC = 100\%}$ and $\boldsymbol{SOC = 0\%}$ by voltage levels $\boldsymbol{V_{max}}$ and $\boldsymbol{V_{min}}$ leads to recovering a fraction of the capacity loss in the SEI reaction (roughly, between 11% and 17.5%, see Figure 5-14) because part of the previously unused lithium reserve from both electrodes starts to be cycled. This secondary capacity recovery process has been quantified by modeling the displacement of the electrodes' OCP curves caused by loss of cyclable lithium, the recalculation of the cell's OCV curve, and the resulting recalibration of the electrodes' lithiation boundaries.

Modeling battery degradation is of the uttermost importance to solve a bigger problem: performing predictive control of batteries oriented toward extending their life. With this aim, it is interesting to simplify calculations by pre-computing the degradation caused by a set of combinations of variables (current, SOC and temperature) representative of realistic operation conditions. Lookup tables of the most relevant variables have been generated from that results to accelerate the computation time required by the model.

# 6. Conclusions

This dissertation presents research works that lay the basis for optimizing the operation of a DC microgrid. The GAEI's microgrid has been taken as the case study. This DC microgrid consists of renewable energy generation (PV and WT), controllable generation (FC), uncontrolled loads (LOAD), controllable load (EZ), energy storage in batteries (BESS) and bidirectional inverter (INV). All the microgrid's power units are connected to a DC bus through DC-DC converters. On one hand, research has been conducted towards improving the energy efficiency of the converters interfacing between the power units and the DC bus. On the other hand, BESS has been recognized as the central element of the microgrid (μG) in terms of cost and fragility, and research has been developed aimed at prolonging the BESS lifetime. A single-converter topology for active battery balancing has been developed to achieve SOC balancing at all moments, which can significantly extend battery life. Moreover, a simplified battery degradation model has been developed to perform preventive control of the battery pack, which can potentially reduce the BESS amortization cost significantly with limited implementation cost.

The initial self-managed droop control scheme of the μG, called Events-Based Control System (E-BCS), determines the power performed by each unit based on the bus voltage (decentralized control) and, additionally, determines the power reference of FC, EZ, and INV based also on the battery SOC (distributed control). E-BCS prevents $\boldsymbol{v_{bus}}$ and $\boldsymbol{SOC}$ from reaching extreme values and minimizes energy consumption from the mains grid. This basic

control layer has been complemented with two control strategies with the objective of minimizing power losses of the μG's converters:

- Bus Voltage Optimization Control (BVOC): BESS power is managed such that it fulfills two purposes: first, achieving power balance and, second, making the system work at the instantaneous (varying) optimum bus voltage, $v_{optim}$. The value of $v_{optim}$ is calculated online as the minimizer of the sum of power losses in the μG's DC-DC converters. Thus, this optimization applies to the whole set of converters, but only actuates over the BESS' converter, imposing the appropriate power reference.
- Online Optimization of Switching Frequency (OOSF): the switching frequency of every μG's converter $i$, $f_{sw}^{i}$, is individually optimized in real time to improve its energy efficiency (that is, to minimize its power losses).

A model of the GAEI's DC microgrid has been built in Simulink, including basic models of all the power units, and small–signal averaged loss models of the converters. The basic model configuration includes E-BCS governing all units. The microgrid model allows to test different control strategies in simulation to assess how they cooperate with E-BCS to achieve stable operation and how they influence the μG's energy efficiency. The two proposed optimization strategies have been tested in this simulation environment. Both can be implemented together with E-BCS, individually or simultaneously. Simulation under a residential current profile typical of the μG application has proven that both strategies succeed at increasing the efficiency of the μG's converters adaptively, that is, responding to changes of the operation point.

The two optimization strategies result in modest efficiency improvements: $\Delta\eta_{global}^{BVOC+OSF} = 0.304\% - 0.980\%$ (depending on the operation scenario considered); $\Delta\eta_{global}^{BVOC} = 0.130\% - 0.481\%$; $\Delta\eta_{global}^{OOSF} = 0.162\% - 0.691\%$. Even though these efficiency improvements are limited, they are exclusively based in discrete control algorithms, so they involve (almost) no extra investment. Two main reasons explain those results. First and foremost, the converter models employed are too optimistic and leave small room for efficiency improvement. Indeed, the converters' efficiency curves reveal small variations within the studied ranges of $v_{bus}$ and $f_{sw}^{i}$. Second, the optimum bus voltage is usually opposite for individual converters causing BVOC to calculate $v_{optim}$ as the trade-off that minimizes the overall power losses. Both causes were anticipated by analyzing the efficiency curves of the μG's converters.

Efficiency improvement is higher when the power flows among the μG's units are low. Thus, BVOC and OOSF optimization strategies are appropriate for microgrids applications

that require low power flows compared to the nominal power of the converters. BVOC would achieve better results if all the μG's converters had coincident optimum bus voltages.

Regarding battery preservation, a converter-based active balancing topology has been proposed. Active balancing recursively transfers charge (ampere hours) from the strongest (highest SOC) battery to the weakest (lowest SOC) one in the battery pack using power multiplexing. The central element of the equalizer is a single DC-DC converter that is activated when SOC imbalance among the batteries is greater than 0.5%. The converter's input and output are adequately routed via two strings of controlled switches to perform cell-to-cell charge transfer.

A particularly imbalanced battery pack of five Lead Crystal $12\,V$, $40\,Ah$ monobloc batteries has been conceived as the case study to evaluate the performance of the balancing system by means of PSIM simulations. Each monobloc battery models imbalance in a different parameter with respect to a reference battery: reduced coulombic charge efficiency ($\downarrow \eta_Q$), reduced capacity ($\downarrow Q$), increased internal resistance ($\uparrow R$), and increased leakage current ($\uparrow I_{leak}$). An equivalent circuit model has been employed to model the monobloc batteries response. It models OCV, internal resistance, voltage hysteresis, and dynamic response through two RC pairs. The battery-pack's natural tendency towards imbalance has been evaluated by simulating typical battery operation (as part of the residential μG) with no external balancing. The equalizer's minimum and maximum duty-cycle boundaries have been tuned based on this study, such that the rate of charge transfer is sufficient to compensate natural imbalance but not excessive, to prevent SOC oscillations (overcompensation of imbalance).

The control strategy has been validated in simulation. For this study, a 10% initial SOC imbalance has been considered in addition to the parameter discrepancy mentioned above. The simulation covers 24 hours of operation, with the battery pack loaded (once again) with a typical microgrid current profile. The equalizer demonstrates excellent performance, as it compensates the (large) initial SOC deviations in 0.75 hours and keeps the pack balanced from then on.

Experimental works have begun but completing them has not been possible yet, mainly as a consequence of the coronavirus pandemics. Finished works include the creation of an aging platform, that has been employed to abuse five monobloc batteries, artificially inducing (accelerated) imbalance among them. Ongoing works include performing characterization tests of the imbalanced batteries to parametrize their equivalent circuit models and programming the equalizer's microcontroller. Future works related to experimental validation of the prototype include using the battery models to assess the real battery pack's need for balancing in simulation.

The second approach to battery preservation addressed in this dissertation is to model one of the dominant degradation mechanisms. A model that accounts for SEI layer growth in lithium-ion cells with graphite negative electrodes has been developed. The (novel) proposed model harmonizes the simplicity of an equivalent-circuit model that captures the cell dynamic response with the capability of predicting capacity fade and internal resistance increase due to SEI layer growth provided by a reduced-order physics-based model of the SEI side reaction. The proposed discrete model computes the shrinkage of the NE's stoichiometric window (which is proportional to the remaining capacity) caused by loss of cyclable lithium consumed in the SEI side reaction.

The definition of the SOC levels $SOC = 100\%$ and $SOC = 0\%$ of the cell studied is based on cut-off voltage levels, $V_{max}$ and $V_{min}$. This leads to recovering a fraction of the capacity lost in the SEI reaction (roughly, between 11% and 17.5%) because part of the formerly unused lithium reserves from both electrodes starts to be cycled. This secondary capacity recovery process has been quantified by modeling the displacement of the electrodes' Open Circuit Potential curves caused by loss of cyclable lithium, the subsequent modification of the cell's Open Circuit Voltage curve, and the recalibration of the electrodes' lithiation boundaries.

# 7. Contributions, future works, and other activities

## 7.1. Most relevant contributions

The following contributions have been made:

- A comprehensive model of the GAEI's μG has been developed in Simulink, including models of every μG's power unit and of the converters' losses. Power profiles representative of typical renewable generation and residential electricity consumption are used. The μG model includes a basic control layer based on decentralized interpretation of bus voltage and SOC events. The model allows to evaluate:
    - Dynamics of the DC bus voltage.
    - Energy efficiency of the DC-DC converters.
    - Power sharing among the sources to feed the loads.
    - Response of the μG faced with perturbations, such as BESS failure or loss of connection to the mains grid.
- Two enhanced control strategies have been proposed and validated in simulations to improve the μG's energy efficiency. The two strategies can be applied together or alone, with E-BCS as the basic control managing the power profiles of all the μG's units (except the BESS' when BVOC is applied).

  - Bus Voltage Optimization Control (BVOC) is a centralized control that manages the BESS' power to stabilize μG operation at the optimum DC bus voltage, which is not fixed but continuously varies within the range of allowed voltage values. The optimum voltage is calculated as the voltage value at which the losses in all the μG's DC-DC converters are minimized.
  - Online Optimization of Switching Frequency (OOSF) is a control strategy that optimizes the frequency at which each DC-DC converter in the μG is operated, to minimize their power losses online.

- A new equalizer's topology has been presented. It is an active battery balancing system that recursively transfers charge cell-to-cell using a single DC-DC converter that performs power multiplexing. The converter operates in CC-CV mode, adequate for battery charging. Its input and output are connected to the battery pack's cells with the highest and the lowest SOC, respectively, thanks to two strings of controlled switches.
- The equalizer's control scheme has been designed and tuned to balance a battery pack presenting inconsistency in four parameters ($\eta_Q$, $Q$, $R$, and $I_{leak}$). The battery pack's natural tendency towards SOC imbalance has been evaluated by simulating operation with no external balancing under a typical current profile. The parameters of the control strategy have been tuned based on this study. Specifically, the minimum and maximum boundaries for the equalizer's duty cycle, defined to effectively compensate natural imbalance avoiding excessive charge transfer (overcompensation of imbalance), have been found. The control strategy has been validated in simulation.
- An aging platform has been designed and assembled. This platform has been employed to abuse five monobloc batteries with the objective of artificially inducing (accelerated) aging. The platform permits to subject the batteries to high temperatures and deep charge-discharge cycles, even surpassing the recommended cut-off voltages.
- A battery degradation model has been developed to allow prediction of capacity fade in lithium-ion cells caused by any possible operation conditions. One of the dominant degradation mechanisms has been considered: Solid-Electrolyte Interphase (SEI) layer growth.
  - The model harmonizes the simplicity of an equivalent-circuit model with the capability of predicting capacity loss and internal resistance increase (caused by the SEI side reaction) provided by a physics-based model.
  - The process of secondary capacity recovery has been described and modeled. Capacity loss due to the SEI side reaction causes a relative shift

between the negative electrode's and the positive electrode's stoichiometric windows, which, in turn, entails relative displacement of their OCP curves. The characteristic $OCV$ vs $SOC$ curve of the cell is recursively updated to recalibrate the electrodes' lithiation boundaries, which are proportional to the remaining cell's capacity.

## 7.2. Future lines of research

- The microgrid (μG) model in Simulink includes some simplifications that accelerate its execution. Yet, these simplifications imply reduced accuracy and versatility. Possible improvements include:
    - More precise battery model, with more realistic characterization of the OCV curve, better and more reliable SOC estimation algorithm, and physics-based estimation of capacity fade caused by degradation. The battery model presented in Chapter 5 can be introduced in the μG model to predict capacity fade under any possible power profile applied to the battery pack.
    - The voltage characteristics of the μG 's wind turbine, electrolyzer, and load have been considered as constants to simplify the model. However, the actual WT's and EZ's voltage curves depend on the generated current. This characteristic could be implemented in the model using lookup tables. Furthermore, allowing the connection of loads indifferent to voltage (apart from $48\,V$ constant-voltage loads) would increase flexibility. Permitting these voltage values to vary within a wider and more realistic range could lead to increased performance of the optimization strategy BVOC, as there would be more room for improvement.
    - Economic optimization. Having the capacity fade estimations resulting from the degradation model, a control software would be able to make intelligent decisions on what energy source (utility grid, renewable generation, fuel cell, or battery) to utilize at each moment to maximize benefits / to minimize operation cost, considering the amortization of the BESS. This would make possible to predict the impact of economic optimization in battery life extension and the associated savings produced by BESS replacement deferral.
    - Creation of more accurate models of the DC-DC converters, either by including more mechanisms that cause power loss or by creating lookup

tables from experimental tests of the converters under a diverse range of operation conditions.

- The battery model presented in Chapter 5 can also be introduced as part of the equalizer's program to improve the balancing performance in long-term use. While the ESC model should be sufficiently good to assess imbalance in the short-term, the parameter dispersion causes differential aging that is not captured by this model. Using the SEI degradation model to fine-tune the cells' parameters recursively as they age would provide better SOC estimations, thus reducing the risk of transferring charge between wrong cells.
- Performance of the proposed equalizer has been assessed in simulations. Experimental validation of the prototype and its control strategy entails the following works:
    - Performing characterization tests to the artificially imbalanced Lead-Crystal monobloc batteries.
    - Using the resulting battery models to assess the actual battery pack's need for balancing in simulations.
    - Tuning the parameters of the control algorithm in accordance with the results, to effectively compensate the real battery pack's tendency towards imbalance.
    - Experimentally validating the equalizer's performance by tracking the SOCs of the monoblocs under actual operation conditions.
- The battery model employed to study the equalizer's operation uses coulomb counting to estimate the batteries' SOCs. This method can be improved by periodically calibrating SOC using the $OCV$ vs. $SOC$ lookup tables obtained in the characterization tests. This method works better near $0\%$ and $100\%$ SOC because the slope of the curve is steeper in that areas.
- Currently, the topology of the equalizer can only be used to balance $12\ V$ monobloc batteries. Therefore, it is well suited to balance lead-acid batteries, but this type of battery does not always require such precise active balancing because it can temporarily withstand controlled overcharging ("equalization charge"), which naturally tends to balance the (lead-acid) battery pack to some extent. Moreover, the equalizer prototype can neither balance the battery cells inside the monoblocs, nor be used to balance other type of batteries (such as lithium-ion) because of its input and output voltage ranges. A more flexible design with different DC-DC converter options would increase the relevance of the proposed topology.

Specifically, replacing the current DC-DC converter in favor of one suitable for lower input and output voltages would allow to use the prototype to balance cells of other battery types, such as lithium-ion. This would potentially multiply the number of applications suitable for the balancing system.

- The proposed model of the SEI degradation mechanism is a promising first step towards the creation of a more complete degradation model. Possible improvements may inspire future research works:
    - The model is unsuccessful at estimating the voltage drop experienced by the lithium-ion cell during self-discharge storage periods. This needs to be researched to gain insight on the physical processes inside the cell, and to improve the degradation model accordingly to the findings. Two hypothesis have been formulated in an attempt to explain this phenomenon, namely, the proposed model is insufficiently accurate or there is a second mechanism (probably self-discharge through a soft short circuit) causing reversible loss of charge. Both options can inspire research works aimed at verifying hypothesis and, ultimately, to improving the degradation model.
    - Additional degradation mechanisms, such as lithium plating, could be incorporated to the model. Implementing the model in a BMS requires real-time calculations and decision-making, so some simplifications would be required (as in the case of the SEI degradation model): pre-storing lookup tables with the capacity loss and resistance increase results from the physics-based model, and using the lookup-table evaluations to update the equivalent circuit model parameters

## 7.3. Publications and divulgation

The following publications are an outcome of the research conducted for this dissertation.

Congresses:

- D. García Elvira, H. Valderrama Blavi, À. Cid Pastor, J. M. Bosque Moncusí, and L. Martínez Salamero, “Optimización del rendimiento de una microrred CC con tensión de bus variable,” in Seminario Anual de Automática, Electrónica Industrial e Instrumentación (SAAEI), 2018.
- D. G. Elvira, H. Valderrama Blavi, J. M. Bosque Moncusi, A. Cid Pastor, J. A. Garriga Castillo, and L. Martinez Salamero, “Active battery balancing via a switched DC/DC Converter: Description and performance analysis,” 2019 16th

Conf. Electr. Mach. Drives Power Syst. ELMA 2019 - Proc., no. June, pp. 6–8, 2019, https://doi.org/10.1109/ELMA.2019.8771697.

- J. A. Garriga, H. Valderrama-Blavi, D. Garcia-Elvira, J. A. Barrado, and A. Cid-Pastor, "Impedance matching for an inductive harvesting transducer," 2019 16th Conf. Electr. Mach. Drives Power Syst. ELMA 2019 - Proc., no. June, pp. 6–8, 2019, https://doi.org/10.1109/ELMA.2019.8771485.
- D. García Elvira, G. L. Plett, R. Machado, H. Valderrama Blavi, À. Cid Pastor, and L. Martínez Salamero, "Modelo de degradación por crecimiento de la capa Interfase Sólido-Electrolito en una batería Li-NMC," in Seminario Anual de Automática, Electrónica Industrial e Instrumentación (SAAEI) 2020, 2020.

Journals

- D. G. Elvira, H. V. Blavi, À. C. Pastor, and L. M. Salamero, "Efficiency Optimization of a Variable Bus Voltage DC Microgrid," Energies, vol. 11, no. 11, p. 3090, Nov. 2018, https://doi.org/10.3390/en11113090.

Additionally, a manuscript has been submitted to Journal of Energy Source and is expected to be published soon:

- "Simplified Li-ion cell model for Battery Management Systems, combining equivalent-circuit dynamic model and zero-dimensional physics-based Solid-Electrolyte Interphase model".

## 7.4. Other activities

### 7.4.1. International stage

The author got a research internship at the University of Colorado Colorado Springs to study lithium-ion battery modeling in depth. The short-term stay took place from September 1, 2019, until December 17, 2019.

### 7.4.2. Teaching

The author has collaborated in the teaching tasks of two courses of the Degree in Electrical Engineering and the Degree in Industrial Electronics and Automation Engineering:

- Renewable energies. Course 2019/20.
- Power management of the electric vehicle. Courses 2018/19 and 2019/20.

# Bibliography

[1] V. Smil, Energy Transitions: Global and National Perspectives, 2nd Edition, Second edi. Santa Barbara, California: Praeger, 2017.

[2] BP, "Statistical Review of World Energy globally consistent data on world energy markets . and authoritative publications in the field of energy The Statistical Review world of World Energy and data on world energy markets from is The Review has been providing," p. 66, 2020, [Online]. Available: https://www.bp.com/content/dam/bp/business-sites/en/global/corporate/pdfs/energy-economics/statistical-review/bp-stats-review-2020-full-report.pdf.

[3] I. H. Thompson, "The ethics of sustainability," Landsc. Sustain., pp. 12–32, 2005, https://doi.org/10.5840/du1998811/126.

[4] Bloomberg NFE, "New Energy Outlook 2020," no. October, 2020, [Online]. Available: https://bnef.turtl.co/story/neo2018?teaser=true.

[5] S. Alexander and P. Yacoumis, "Degrowth, energy descent, and 'low-tech' living: Potential pathways for increased resilience in times of crisis," J. Clean. Prod., vol. 197, pp. 1840–1848, Oct. 2018, https://doi.org/10.1016/j.jclepro.2016.09.100.

[6] J. M. Bosque Moncusi, "Ampliación, mejora e integración en la red de un sistema fotovoltaico," PhD thesis. Universitat Rovira i Virgili, 2014.

[7] X. Fang, S. Misra, G. Xue, and D. Yang, "Smart grid - The new and improved power grid: A survey," IEEE Commun. Surv. Tutorials, vol. 14, no. 4, pp. 944–980, 2012, https://doi.org/10.1109/SURV.2011.101911.00087.

[8] A. Hirsch, Y. Parag, and J. Guerrero, "Microgrids: A review of technologies, key drivers, and outstanding issues," Renew. Sustain. Energy Rev., vol. 90, pp. 402–411, Jul. 2018, https://doi.org/10.1016/j.rser.2018.03.040.

[9] I. Alotaibi, M. A. Abido, M. Khalid, and A. V. Savkin, "A Comprehensive Review of Recent Advances in Smart Grids: A Sustainable Future with Renewable Energy Resources," Energies, vol. 13, no. 23, p. 6269, 2020, https://doi.org/10.3390/en13236269.

[10] M. D. Galus, F. Wietor, and G. Andersson, "Incorporating valley filling and peak shaving in a utility function based management of an electric vehicle aggregator," IEEE PES Innov. Smart Grid Technol. Conf. Eur., pp. 1–8, 2012, https://doi.org/10.1109/ISGTEurope.2012.6465894.

[11] S. Li, J. Li, C. Su, and Q. Yang, "Optimization of Bi-Directional V2G Behavior with Active Battery Anti-Aging Scheduling," IEEE Access, vol. 8, pp. 11186–11196, 2020, https://doi.org/10.1109/ACCESS.2020.2964699.

[12] Z. Wang and S. Wang, "Grid power peak shaving and valley filling using vehicle-to-grid systems," IEEE Trans. Power Deliv., vol. 28, no. 3, pp. 1822–1829, 2013, https://doi.org/10.1109/TPWRD.2013.2264497.

[13] S. Pullins, "Why microgrids are becoming an important part of the energy infrastructure," Electr. J., vol. 32, no. 5, pp. 17–21, 2019, https://doi.org/10.1016/j.tej.2019.05.003.

[14] B. Luis and E. Zubieta, "Are Microgrids the Future of Energy ?," IEEE Electrif. Mag., vol. 4, no. 2, pp. 37–44, 2016.

[15] M. L. Di Silvestre, S. Favuzza, E. Riva Sanseverino, and G. Zizzo, "How Decarbonization, Digitalization and Decentralization are changing key power infrastructures," Renew. Sustain. Energy Rev., vol. 93, no. February, pp. 483–498, 2018, https://doi.org/10.1016/j.rser.2018.05.068.

[16] S. B. Qamar and I. Janajreh, "Renewable Energy Sources for Isolated Self-sufficient Microgrids: Comparison of Solar and Wind Energy for UAE," Energy Procedia, vol. 103, no. April, pp. 413–418, 2016, https://doi.org/10.1016/j.egypro.2016.11.308.

[17] A. Hirsch, Y. Parag, and J. Guerrero, "Microgrids : A review of technologies , key drivers , and outstanding issues," Renew. Sustain. Energy Rev., vol. 90, no. March, pp. 402–411, 2018, https://doi.org/10.1016/j.rser.2018.03.040.

[18] X. Liu, M. Shahidehpour, Z. Li, X. Liu, Y. Cao, and Z. Bie, "Microgrids for Enhancing the Power Grid Resilience in Extreme Conditions," IEEE Trans. Smart Grid, vol. 8, no. 2, pp. 589–597, 2017, https://doi.org/10.1109/TSG.2016.2579999.

[19] J. B. Cabrera, M. F. Veiga, D. X. Morales, and R. Medina, "Reducing Power Losses in Smart Grids with Cooperative Game Theory," Adv. Commun. Control Methods Futur. Smartgrids, 2019, https://doi.org/10.5772/intechopen.88568.

[20] M. Nurunnabi, N. K. Roy, E. Hossain, and H. R. Pota, "Size optimization and

sensitivity analysis of hybrid wind/PV micro-grids- A case study for Bangladesh," IEEE Access, vol. 7, pp. 150120–150140, 2019, https://doi.org/10.1109/ACCESS.2019.2945937.

[21] M. Li, X. Zhang, G. Li, and C. Jiang, "A feasibility study of microgrids for reducing energy use and GHG emissions in an industrial application," Appl. Energy, vol. 176, no. 2016, pp. 138–148, 2016, https://doi.org/10.1016/j.apenergy.2016.05.070.

[22] G. Pepermans, J. Driesen, D. Haeseldonckx, R. Belmans, and W. D'haeseleer, "Distributed generation: Definition, benefits and issues," Energy Policy, vol. 33, no. 6, pp. 787–798, 2005, https://doi.org/10.1016/j.enpol.2003.10.004.

[23] T. Dragicevic, X. Lu, J. C. Vasquez, and J. M. Guerrero, "DC Microgrids - Part I: A Review of Control Strategies and Stabilization Techniques," IEEE Trans. Power Electron., vol. 31, no. 7, pp. 4876–4891, 2016, https://doi.org/10.1109/TPEL.2015.2478859.

[24] J. M. Guerrero, J. C. Vasquez, J. Matas, L. G. De Vicuña, and M. Castilla, "Hierarchical control of droop-controlled AC and DC microgrids - A general approach toward standardization," IEEE Trans. Ind. Electron., vol. 58, no. 1, pp. 158–172, 2011, https://doi.org/10.1109/TIE.2010.2066534.

[25] T. Dragicevic, X. Lu, J. C. Vasquez, and J. M. Guerrero, "DC Microgrids - Part I: A Review of Control Strategies and Stabilization Techniques," IEEE Trans. Power Electron., vol. 31, no. 7, pp. 4876–4891, 2016, https://doi.org/10.1109/TPEL.2015.2478859.

[26] J. Zhao and F. Dörfler, "Distributed control and optimization in DC microgrids," Automatica, vol. 61, no. March, pp. 18–26, Nov. 2015, https://doi.org/10.1016/j.automatica.2015.07.015.

[27] D. T. Nguyen and L. B. Le, "Optimal energy trading for building microgrid with electric vehicles and renewable energy resources," in Proceedings of the ISGT 2014, 2014, pp. 1–5, https://doi.org/10.1109/ISGT.2014.6816461.

[28] C. Li, F. de Bosio, S. K. Chaudhary, M. Graells, J. C. Vasquez, and J. M. Guerrero, "Operation cost minimization of droop-controlled DC microgrids based on real-time pricing and optimal power flow," in Proceedings of the IECON 2015–41st Annual Conference of the IEEE Industrial Electronics Society, 2015, pp. 003905–003909, https://doi.org/10.1109/IECON.2015.7392709.

[29] J. M. Lujano-Rojas, R. Dufo-Lopez, J. L. Bernal-Agustin, and J. P. S. Catalao, "Optimizing Daily Operation of Battery Energy Storage Systems Under Real-Time Pricing Schemes," IEEE Trans. Smart Grid, vol. 8, no. 1, pp. 316–330, Jan. 2017, https://doi.org/10.1109/TSG.2016.2602268.

[30] Y. Wang, Y. Huang, Y. Wang, F. Li, Y. Zhang, and C. Tian, "Operation Optimization in a Smart Micro-Grid in the Presence of Distributed Generation and Demand Response," Sustainability, vol. 10, no. 3, p. 847, Mar. 2018, https://doi.org/10.3390/su10030847.

[31] A. Gonzalez-Garrido, A. Saez-de-Ibarra, H. Gaztanaga, A. Milo, and P. Eguia, "Annual Optimized Bidding and Operation Strategy in Energy and Secondary Reserve Markets for Solar Plants with Storage Systems," IEEE Trans. Power Syst., vol. 8950, no. c, pp. 1–10, 2018, https://doi.org/10.1109/TPWRS.2018.2869626.

[32] S. Anand and B. G. Fernandes, "Optimal voltage level for DC microgrids," IECON Proc. (Industrial Electron. Conf., pp. 3034–3039, 2010, https://doi.org/10.1109/IECON.2010.5674947.

[33] Z. Zhao, J. Hu, and H. Chen, "Bus Voltage Control Strategy for Low Voltage DC Microgrid Based on AC Power Grid and Battery," Proc. - 1st IEEE Int. Conf. Energy Internet, ICEI 2017, pp. 349–354, 2017, https://doi.org/10.1109/ICEI.2017.68.

[34] R. Dahiya, "Voltage regulation and enhance load sharing in DC microgrid based on Particle Swarm Optimization in marine applications," vol. 46, no. October, pp. 2105–2113, 2017.

[35] J. M. Liu, C. J. Yu, Y. C. Kuo, and T. H. Kuo, "Optimizing the efficiency of DC-DC converters with an analog variable-frequency controller," IEEE Asia-Pacific Conf. Circuits Syst. Proceedings, APCCAS, pp. 910–913, 2008, https://doi.org/10.1109/APCCAS.2008.4746171.

[36] G. Sizikov, A. Kolodny, E. G. Fridman, and M. Zelikson, "Frequency dependent efficiency model of on-chip DC-DC buck converters," 2010 IEEE 26th Conv. Electr. Electron. Eng. Isr. IEEEI 2010, pp. 651–654, 2010, https://doi.org/10.1109/EEEI.2010.5662132.

[37] F. Jauch and J. Biela, "Generalized modeling and optimization of a bidirectional dual active bridge DC-DC converter including frequency variation," 2014 Int. Power Electron. Conf. IPEC-Hiroshima - ECCE Asia 2014, pp. 1788–1795, 2014, https://doi.org/10.1109/IPEC.2014.6869826.

[38] M. Çelebi, "Efficiency optimization of a conventional boost DC/DC converter," Electr. Eng., vol. 100, no. 2, pp. 803–809, 2018, https://doi.org/10.1007/s00202-017-0552-0.

[39] W. Al-Hoor, J. A. Abu-Qahouq, L. Huang, W. B. Mikhael, and I. Batarseh, "Adaptive digital controller and design considerations for a variable switching frequency voltage regulator," IEEE Trans. Power Electron., vol. 24, no. 11, pp. 2589–2602, 2009, https://doi.org/10.1109/TPEL.2009.2031439.

[40] J. M. Liu, P. Y. Wang, and T. H. Kuo, "A current-mode DC-DC buck converter with efficiency-optimized frequency control and reconfigurable compensation," IEEE Trans. Power Electron., vol. 27, no. 2, pp. 869–880, 2012, https://doi.org/10.1109/TPEL.2011.2162079.

[41] L. Zhao, H. Li, Y. Liu, and Z. Li, "High efficiency variable-frequency full-bridge converter with a load adaptive control method based on the loss model," Energies, vol. 8, no. 4, pp. 2647–2673, 2015, https://doi.org/10.3390/en8042647.

[42] A. Leon Masich and H. Valderrama Blavi, "Circuit adaptador per incorporar fonts d '

energia renovable a una planta fotovoltaica connectada a la xarxa elèctrica .," Final Year Dissertation. Universitat Rovira i Virgili, 2009.

[43] H. Valderrama-Blavi, J. M. Bosque-Moncusi, L. Marroyo, F. Guinjoan, J. A. Barrado, and L. Martinez-Salamero, "Adapting a low voltage PEM fuel-cell to domestic grid-connected PV system," in 2009 35th Annual Conference of IEEE Industrial Electronics, Nov. 2009, pp. 160–165, https://doi.org/10.1109/IECON.2009.5414768.

[44] F. Flores-Bahamonde, H. Valderrama-Blavi, J. M. Bosque, and L. Martinez-Salamero, "Modular-based PFC for low power three-phase wind generator," in 2011 7th International Conference-Workshop Compatibility and Power Electronics (CPE), Jun. 2011, pp. 125–130, https://doi.org/10.1109/CPE.2011.5942219.

[45] F. Flores-Bahamonde, H. Valderrama-Blavi, J. M. Bosque, A. Leon-Masich, and L. Martinez-Salamero, "Grid-connected boost inverter for small-wind urban integration: Analysis and design," in IECON 2012 - 38th Annual Conference on IEEE Industrial Electronics Society, Oct. 2012, pp. 433–439, https://doi.org/10.1109/IECON.2012.6388783.

[46] O. Aviñó, "Realització d'una Càrrega Activa Programable Sense Pèrdues per a una Plataforma de Generació Distribuïda," Final Year Dissertation. Universitat Rovira i Virgili, 2012.

[47] O. Puigcerver Quixal, "Monitorització d ' una Planta Distribuïda de Generació d ' Energia Renovable," Final Year Dissertation. Universitat Rovira i Virgili, 2012.

[48] J. A. Garriga Castillo, "Estudio , Diseño y montaje de un convertidor CC / CC , compuesto por 2 boost en cascada .," Master Thesis, Universitat Rovira i Virgili, 2013.

[49] J. M. Bosque Moncusi, "Estructuras Eléctricas Para La Integración De Un Sistema De Generación Eólica a La Red Eléctrica," PhD Thesis. Universitat Rovira i Virgili, 2014.

[50] F. Flores-Bahamonde, L. Martínez-Salamero, H. Valderrama-Blavi, J. Maixé-Altés, and G. García, "Control of a three-phase AC/DC VIENNA converter based on the sliding mode loss-free resistor approach," IET Power Electron., vol. 7, no. 5, pp. 1073–1082, May 2014, https://doi.org/10.1049/iet-pel.2013.0405.

[51] H. Valderrama-Blavi, J. M. Bosque, F. Guinjoan, L. Marroyo, and L. Martínez-Salamero, "Power adaptor device for domestic DC microgrids based on commercial MPPT inverters," IEEE Trans. Ind. Electron., vol. 60, no. 3, pp. 1191–1203, 2013, https://doi.org/10.1109/TIE.2012.2198038.

[52] M. Alamgir, "Lithium Has Transformed Vehicle Technology," IEEE Electrif. Mag., vol. 5, no. 1, pp. 43–52, 2017.

[53] K. Uddin, M. Dubarry, and M. B. Glick, "The viability of vehicle-to-grid operations from a battery technology and policy perspective," Energy Policy, vol. 113, no. August 2017, pp. 342–347, 2018, https://doi.org/10.1016/j.enpol.2017.11.015.

[54] B. C. Restrepo, A. Salazar, H. Schweizer, and A. Ginart, "Residential Battery Storage. Is the timing right?," no. SEPTEMBER, 2015.

[55] T. Aquino, M. Roling, C. Baker, and L. Rowland, "Battery Energy Storage Technology Assessment," p. 27, 2017, [Online]. Available: https://www.prpa.org/wp-content/uploads/2017/10/HDR-Battery-Energy-Storage-Assessment.pdf.

[56] R. H. Byrne and C. A. Silva-Monroy, "Estimating the Maximum Potential Revenue for Grid Connected Electricity Storage: Arbitrage and Regulation," Sand2012-3863, no. December, p. 64, 2012, [Online]. Available: http://www.sandia.gov/ess/publications/SAND2012-3863.pdf.

[57] G. He, Q. Chen, C. Kang, P. Pinson, and Q. Xia, "Optimal Bidding Strategy of Battery Storage in Power Markets Considering Performance-Based Regulation and Battery Cycle Life," IEEE Trans. Smart Grid, vol. 7, no. 5, pp. 2359–2367, 2016, https://doi.org/10.1109/TSG.2015.2424314.

[58] X. Fan *et al.*, "Battery Technologies for Grid-Level Large-Scale Electrical Energy Storage," Trans. Tianjin Univ., vol. 26, no. 2, pp. 92–103, Apr. 2020, https://doi.org/10.1007/s12209-019-00231-w.

[59] M. Stecca, L. Ramirez Elizondo, T. Batista Soeiro, P. Bauer, and P. Palensky, "A Comprehensive Review of the Integration of Battery Energy Storage Systems into Distribution Networks," IEEE Open J. Ind. Electron. Soc., vol. 1, no. January, pp. 1–1, 2020, https://doi.org/10.1109/ojies.2020.2981832.

[60] T. B. Reddy and D. Linden, Linden's Handbook of Batteries 4th ed. New York: McGraw-Hill, 2011.

[61] A. Chen and P. K. Sen, "Advancement in battery technology: A state-of-the-art review," IEEE Ind. Appl. Soc. 52nd Annu. Meet. IAS 2016, pp. 1–10, 2016, https://doi.org/10.1109/IAS.2016.7731812.

[62] C. Zhang, Y. L. Wei, P. F. Cao, and M. C. Lin, "Energy storage system: Current studies on batteries and power condition system," Renew. Sustain. Energy Rev., vol. 82, no. October 2017, pp. 3091–3106, 2018, https://doi.org/10.1016/j.rser.2017.10.030.

[63] B. Pruthvija and P. K. P. Lakshmi, "Review on Battery Technology and its Challenges," vol. 11, no. 9, pp. 1706–1713, 2020.

[64] G. L. Soloveichik, "Battery technologies for large-scale stationary energy storage," Annu. Rev. Chem. Biomol. Eng., vol. 2, pp. 503–527, 2011, https://doi.org/10.1146/annurev-chembioeng-061010-114116.

[65] A. Ulvestad, "A Brief Review of Current Lithium Ion Battery Technology and Potential Solid State Battery Technologies," arXiv, 2018.

[66] J. Asenbauer, T. Eisenmann, M. Kuenzel, A. Kazzazi, Z. Chen, and D. Bresser, "The success story of graphite as a lithium-ion anode material-fundamentals, remaining challenges, and recent developments including silicon (oxide) composites," Sustain. Energy Fuels, vol. 4, no. 11, pp. 5387–5416, 2020, https://doi.org/10.1039/d0se00175a.

[67] R. Machado, "Physics-based model for Solid-Electrolyte Interphase (SEI) layer

growth in lithium-ion batteries," Unpublished Master thesis. University of Colorado - Colorado Springs, 2020.

[68] S. Santhanagopalan, K. Smith, J. Neubauer, G.-H. Kim, A. Pesaran, and M. Keyser, Design and Analysis of Large Lithium-Ion Battery Systems. Artech House Power Engineering, 2014.

[69] R. Zhang *et al.*, "State of the art of lithium-ion battery SOC estimation for electrical vehicles," Energies, vol. 11, no. 7, 2018, https://doi.org/10.3390/en11071820.

[70] D. N. T. How, M. A. Hannan, M. S. Hossain Lipu, and P. J. Ker, "State of Charge Estimation for Lithium-Ion Batteries Using Model-Based and Data-Driven Methods: A Review," IEEE Access, vol. 7, pp. 136116–136136, 2019, https://doi.org/10.1109/ACCESS.2019.2942213.

[71] L. Lu, X. Han, J. Li, J. Hua, and M. Ouyang, "A review on the key issues for lithium-ion battery management in electric vehicles," J. Power Sources, vol. 226, pp. 272–288, 2013, https://doi.org/10.1016/j.jpowsour.2012.10.060.

[72] Y. Zhang, W. Song, S. Lin, and Z. Feng, "A novel model of the initial state of charge estimation for LiFePO 4 batteries," J. Power Sources, vol. 248, pp. 1028–1033, 2014, https://doi.org/10.1016/j.jpowsour.2013.09.135.

[73] Y. Wang *et al.*, "A comprehensive review of battery modeling and state estimation approaches for advanced battery management systems," Renew. Sustain. Energy Rev., vol. 131, no. July, p. 110015, 2020, https://doi.org/10.1016/j.rser.2020.110015.

[74] M. Murnane and A. Ghazel, "A Closer Look at State of Charge (SOC) and State of Health (SOH) Estimation Techniques for Batteries," 2017, [Online]. Available: http://www.analog.com/media/en/technical-documentation/technical-articles/A-Closer-Look-at-State-Of-Charge-and-State-Health-Estimation-Techniques-....pdf.

[75] D. Capano, "Active Balancing of Lithium-ion Cells for Maximum Power Discharging By Master of Applied Science," 2018.

[76] G. Dong, J. Wei, C. Zhang, and Z. Chen, "Online state of charge estimation and open circuit voltage hysteresis modeling of LiFePO4 battery using invariant imbedding method," Appl. Energy, vol. 162, pp. 163–171, 2016, https://doi.org/10.1016/j.apenergy.2015.10.092.

[77] Y. Zheng, M. Ouyang, X. Han, L. Lu, and J. Li, "Investigating the error sources of the online state of charge estimation methods for lithium-ion batteries in electric vehicles," J. Power Sources, vol. 377, no. December 2017, pp. 161–188, Feb. 2018, https://doi.org/10.1016/j.jpowsour.2017.11.094.

[78] M. Coleman, C. K. Lee, C. Zhu, W. G. Hurley, and A. S. Soc, "State-of-Charge Determination From EMF Voltage Estimation : Using Impedance , Terminal Voltage , and Current for Lead-Acid and Lithium-Ion Batteries," vol. 54, no. 5, pp. 2550–2557, 2007.

[79] J. Kalawoun, K. Biletska, F. Suard, and M. Montaru, "From a novel classification of

the battery state of charge estimators toward a conception of an ideal one," J. Power Sources, vol. 279, pp. 694–706, 2015, https://doi.org/10.1016/j.jpowsour.2015.01.038.

[80] A. M. S. M. H. S. Attanayaka, J. P. Karunadasa, and K. T. M. U. Hemapala, "Estimation of state of charge for lithium-ion batteries - A Review," AIMS Energy, vol. 7, no. 2, pp. 186–210, 2019, https://doi.org/10.3934/ENERGY.2019.2.186.

[81] W. Choi, H. C. Shin, J. M. Kim, J. Y. Choi, and W. S. Yoon, "Modeling and applications of electrochemical impedance spectroscopy (Eis) for lithium-ion batteries," J. Electrochem. Sci. Technol., vol. 11, no. 1, pp. 1–13, 2020, https://doi.org/10.33961/jecst.2019.00528.

[82] F. Single, B. Horstmann, and A. Latz, "Theory of Impedance Spectroscopy for Lithium Batteries," J. Phys. Chem. C, 2019, https://doi.org/10.1021/acs.jpcc.9b07389.

[83] F. M. Wang *et al.*, "Aging effects to solid electrolyte interface (SEI) membrane formation and the performance analysis of lithium ion batteries," Int. J. Electrochem. Sci., vol. 6, no. 4, pp. 1014–1026, 2011.

[84] M. Steinhauer, S. Risse, N. Wagner, and K. A. Friedrich, "Investigation of the Solid Electrolyte Interphase Formation at Graphite Anodes in Lithium-Ion Batteries with Electrochemical Impedance Spectroscopy," Electrochim. Acta, vol. 228, pp. 652–658, 2017, https://doi.org/10.1016/j.electacta.2017.01.128.

[85] R. Scipioni, P. S. Jørgensen, C. Graves, J. Hjelm, and S. H. Jensen, " A Physically-Based Equivalent Circuit Model for the Impedance of a LiFePO 4 /Graphite 26650 Cylindrical Cell ," J. Electrochem. Soc., vol. 164, no. 9, pp. A2017–A2030, 2017, https://doi.org/10.1149/2.1071709jes.

[86] J. Kim and B. H. Cho, "State-of-charge estimation and state-of-health prediction of a Li-Ion degraded battery based on an EKF combined with a per-unit system," IEEE Trans. Veh. Technol., vol. 60, no. 9, pp. 4249–4260, 2011, https://doi.org/10.1109/TVT.2011.2168987.

[87] Z. Yu, R. Huai, and L. Xiao, "State-of-charge estimation for lithium-ion batteries using a Kalman filter based on local linearization," Energies, vol. 8, no. 8, pp. 7854–7873, 2015, https://doi.org/10.3390/en8087854.

[88] J. E. Bester, A. El Hajjaji, and A. M. Mabwe, "Modelling of Lithium-ion battery and SOC estimation using simple and extended discrete Kalman Filters for Aircraft energy management," IECON 2015 - 41st Annu. Conf. IEEE Ind. Electron. Soc., pp. 2433–2438, 2015, https://doi.org/10.1109/IECON.2015.7392467.

[89] N. Watrin, B. Blunier, and A. Miraoui, "Review of adaptive systems for lithium batteries state-of-charge and state-of-health estimation," 2012 IEEE Transp. Electrif. Conf. Expo, ITEC 2012, no. 3, 2012, https://doi.org/10.1109/ITEC.2012.6243437.

[90] C. H. Cai, D. Du Zhi, Z. Y. Liu, and H. Zhang, "Artificial neural network in estimation of battery state-of-charge (SOC) with nonconventional input variables selected by correlation analysis," Proc. 2002 Int. Conf. Mach. Learn. Cybern., vol. 3, no.

November, pp. 1619–1625, 2002, https://doi.org/10.1109/icmlc.2002.1167485.

[91] P. C. Draquino E Baroni Santos, A. C. Seabra, and E. Del-Moral-Hernandez, "Comparing methods for the estimation of a stationary battery's capacity," IEEE Int. Conf. Consum. Electron. - Berlin, ICCE-Berlin, vol. 2018-Septe, 2018, https://doi.org/10.1109/ICCE-Berlin.2018.8576203.

[92] R. S. Bhat, B. G. Kavya, R. P. Rao, and R. Ranjeeth, "Implementing Fuzzy Logic to Improve the Accuracy of SoC Estimation for Li-ion Battery," vol. 9, no. 09, pp. 937–941, 2020.

[93] A. J. Salkind, C. Fennie, P. Singh, T. Atwater, and D. E. Reisner, "Determination of state-of-charge and state-of-health of batteries by fuzzy logic methodology," J. Power Sources, vol. 80, no. 1, pp. 293–300, 1999, https://doi.org/10.1016/S0378-7753(99)00079-8.

[94] G. L. Plett, Battery Management Systems, Volume I: Battery Modeling. Norwood: Artech House Power Engineering, 2015.

[95] M. A. Xavier and M. S. Trimboli, "Lithium-ion battery cell-level control using constrained model predictive control and equivalent circuit models," J. Power Sources, vol. 285, pp. 374–384, 2015, https://doi.org/10.1016/j.jpowsour.2015.03.074.

[96] X. Hu, S. Li, and H. Peng, "A comparative study of equivalent circuit models for Li-ion batteries," J. Power Sources, vol. 198, pp. 359–367, 2012, https://doi.org/10.1016/j.jpowsour.2011.10.013.

[97] G. L. Plett, Battery Management Systems, Volume II: Equivalent-Circuit Methods. Norwood: Artech House. Power Engineering Series, 2015.

[98] C. Werckle, "Improved equivalent-circuit models of lithium-ion-iron-phosphate cells," University of Colorado Colorado Springs. Master thesis, 2019.

[99] J. L. Lee, A. Chemistruck, and G. L. Plett, "Discrete-time realization of transcendental impedance models , with application to modeling spherical solid diffusion," J. Power Sources, vol. 206, pp. 367–377, 2012, https://doi.org/10.1016/j.jpowsour.2012.01.134.

[100] J. L. Lee, A. Chemistruck, and G. L. Plett, "One-dimensional physics-based reduced-order model of lithium-ion dynamics," J. Power Sources, vol. 220, pp. 430–448, 2012, https://doi.org/10.1016/j.jpowsour.2012.07.075.

[101] C. Speltino, D. Di Domenico, G. Fiengo, and A. Stefanopoulou, "Comparison of reduced order lithium-ion battery models for control applications," Proc. IEEE Conf. Decis. Control, pp. 3276–3281, 2009, https://doi.org/10.1109/CDC.2009.5400816.

[102] G. Fan, X. Li, and M. Canova, "A reduced-order electrochemical model of li-ion batteries for control and estimation applications," IEEE Trans. Veh. Technol., vol. 67, no. 1, pp. 76–91, 2018, https://doi.org/10.1109/TVT.2017.2738780.

[103] L. Xia, E. Najafi, Z. Li, H. J. Bergveld, and M. C. F. Donkers, "A computationally efficient implementation of a full and reduced-order electrochemistry-based model for

Li-ion batteries," Appl. Energy, vol. 208, no. September, pp. 1285–1296, 2017, https://doi.org/10.1016/j.apenergy.2017.09.025.

[104] M. Doyle, T. F. Fuller, and J. Newman, "Modeling of Galvanostatic Charge and Discharge of the Lithium/Polymer/Insertion Cell," J. Electrochem. Soc., vol. 140, no. 6, pp. 1526–1533, 1993, https://doi.org/10.1149/1.2221597.

[105] A. Jokar, B. Rajabloo, M. Désilets, and M. Lacroix, "Review of simplified Pseudo-two-Dimensional models of lithium-ion batteries," J. Power Sources, vol. 327, pp. 44–55, 2016, https://doi.org/10.1016/j.jpowsour.2016.07.036.

[106] P. Kemper, S. E. Li, and D. Kum, "Simplification of pseudo two dimensional battery model using dynamic profile of lithium concentration," J. Power Sources, vol. 286, pp. 510–525, 2015, https://doi.org/10.1016/j.jpowsour.2015.03.134.

[107] C. R. Birkl, M. R. Roberts, E. McTurk, P. G. Bruce, and D. A. Howey, "Degradation diagnostics for lithium ion cells," J. Power Sources, vol. 341, pp. 373–386, 2017, https://doi.org/10.1016/j.jpowsour.2016.12.011.

[108] T. Waldmann, M. Wilka, M. Kasper, M. Fleischhammer, and M. Wohlfahrt-Mehrens, "Temperature dependent ageing mechanisms in Lithium-ion batteries - A Post-Mortem study," J. Power Sources, vol. 262, pp. 129–135, 2014, https://doi.org/10.1016/j.jpowsour.2014.03.112.

[109] P. Barai, K. Smith, C.-F. Chen, G.-H. Kim, and P. P. Mukherjee, "Reduced Order Modeling of Mechanical Degradation Induced Performance Decay in Lithium-Ion Battery Porous Electrodes," J. Electrochem. Soc., vol. 162, no. 9, pp. A1751–A1771, 2015, https://doi.org/10.1149/2.0241509jes.

[110] P. M. Attia, S. Das, S. J. Harris, M. Z. Bazant, and W. C. Chueh, "Electrochemical Kinetics of SEI Growth on Carbon Black: Part I. Experiments," J. Electrochem. Soc., vol. 166, no. 4, pp. E97–E106, Feb. 2019, https://doi.org/10.1149/2.0231904jes.

[111] M. B. Pinson and M. Z. Bazant, "Theory of SEI formation in rechargeable batteries: Capacity fade, accelerated aging and lifetime prediction," J. Electrochem. Soc., vol. 160, no. 2, 2013, https://doi.org/10.1149/2.044302jes.

[112] M. M. Kabir and D. E. Demirocak, "Degradation mechanisms in Li-ion batteries: a state-of-the-art review," Int. J. Energy Res., vol. 41, no. 14, pp. 1963–1986, Nov. 2017, https://doi.org/10.1002/er.3762.

[113] J. M. Reniers, G. Mulder, and D. A. Howey, "Review and Performance Comparison of Mechanical-Chemical Degradation Models for Lithium-Ion Batteries," J. Electrochem. Soc., vol. 166, no. 14, pp. A3189–A3200, 2019, https://doi.org/10.1149/2.0281914jes.

[114] Y. Preger *et al.*, "Degradation of Commercial Lithium-Ion Cells as a Function of Chemistry and Cycling Conditions," J. Electrochem. Soc., vol. 167, no. 12, p. 120532, 2020, https://doi.org/10.1149/1945-7111/abae37.

[115] R. Fu, S. Y. Choe, V. Agubra, and J. Fergus, "Development of a physics-based

degradation model for lithium ion polymer batteries considering side reactions," J. Power Sources, vol. 278, pp. 506–521, 2015, https://doi.org/10.1016/j.jpowsour.2014.12.059.

[116] M. R. Palacin and A. de Guibert, "Why do batteries fail?," Science (80-. )., vol. 351, no. 6273, pp. 1253292_1–7, Feb. 2016, https://doi.org/10.1126/science.1253292.

[117] J. Song, B. Xiao, Y. Lin, K. Xu, and X. Li, "Interphases in Sodium-Ion Batteries," Adv. Energy Mater., vol. 8, no. 17, p. 1703082, Jun. 2018, https://doi.org/10.1002/aenm.201703082.

[118] S. J. An, J. Li, C. Daniel, D. Mohanty, S. Nagpure, and D. L. Wood, "The state of understanding of the lithium-ion-battery graphite solid electrolyte interphase (SEI) and its relationship to formation cycling," Carbon N. Y., vol. 105, pp. 52–76, 2016, https://doi.org/10.1016/j.carbon.2016.04.008.

[119] J. Kasnatscheew *et al.*, "The truth about the 1st cycle Coulombic efficiency of LiNi1/3Co1/3Mn1/3O2 (NCM) cathodes," Phys. Chem. Chem. Phys., vol. 18, no. 5, pp. 3956–3965, 2016, https://doi.org/10.1039/c5cp07718d.

[120] F. Holtstiege, P. Bärmann, R. Nölle, M. Winter, and T. Placke, "Pre-Lithiation Strategies for Rechargeable Energy Storage Technologies : Concepts , Promises and Challenges," pp. 1–39, 2018, https://doi.org/10.3390/batteries4010004.

[121] T. Li, X.-Z. Yuan, L. Zhang, D. Song, K. Shi, and C. Bock, Degradation Mechanisms and Mitigation Strategies of Nickel-Rich NMC-Based Lithium-Ion Batteries, vol. 3, no. 1. Springer Singapore, 2020.

[122] A. Wang, S. Kadam, H. Li, S. Shi, and Y. Qi, "Review on modeling of the anode solid electrolyte interphase ( SEI ) for lithium-ion batteries," npj Comput. Mater., no. February, 2018, https://doi.org/10.1038/s41524-018-0064-0.

[123] J. Kasnatscheew *et al.*, "A Tutorial into Practical Capacity and Mass Balancing of Lithium Ion Batteries," J. Electrochem. Soc., vol. 164, no. 12, pp. A2479–A2486, 2017, https://doi.org/10.1149/2.0961712jes.

[124] S. Gantenbein, M. Schönleber, M. Weiss, and E. Ivers-Tiffée, "Capacity fade in lithium-ion batteries and cyclic aging over various state-of-charge ranges," Sustain., vol. 11, no. 23, pp. 1–15, 2019, https://doi.org/10.3390/su11236697.

[125] A. V. Randall, R. D. Perkins, X. Zhang, and G. L. Plett, "Controls oriented reduced order modeling of solid-electrolyte interphase layer growth," J. Power Sources, vol. 209, pp. 282–288, 2012, https://doi.org/10.1016/j.jpowsour.2012.02.114.

[126] P. Ramadass, B. Haran, P. M. Gomadam, R. White, and B. N. Popov, "Development of First Principles Capacity Fade Model for Li-Ion Cells," J. Electrochem. Soc., vol. 151, no. 2, pp. 196–203, 2004, https://doi.org/10.1149/1.1634273.

[127] M. Safari, M. Morcrette, A. Teyssot, and C. Delacourt, "Multimodal Physics-Based Aging Model for Life Prediction of Li-Ion Batteries," J. Electrochem. Soc., vol. 156, no. 3, p. A145, 2009, https://doi.org/10.1149/1.3043429.

[128] S. Wen, "Cell balancing buys extra run time and battery life," Analog Appl. J., pp. 14–18, 2009.

[129] A. J. Bard and L. R. Faulkner, Fundamentals and Applications. Vancouver, Canada: CRC Press, 2015.

[130] B. Li, D. Yang, J. Liu, M. Chen, and Z. Lu, "An Optimal Strategy of Balancing for LiFePO 4 Battery in Battery Energy Storage System," in 2nd International Conference On Systems Engineering and Modeling (ICSEM-13), 2013, pp. 363–370.

[131] M. Daowd, N. Omar, P. Van Den Bossche, and J. Van Mierlo, "A Review of Passive and Active Battery Balancing based on MATLAB/Simulink," Int. Rev. Electr. Eng., no. September, pp. 363–370, 2009.

[132] J. Jiang and C. Zhang, Fundamentals and Applications of Lithium-Ion Batteries in Electric Drive Vehicles, vol. 53, no. 9. 2013.

[133] R. D. Anderson, R. Zane, G. Plett, K. Smith, and M. S. Trimboli, "Life Balancing – A Better Way to Balance Large Batteries," no. April, pp. 4–6, 2017, https://doi.org/10.4271/2017-01-1210.Copyright.

[134] D. Hink and A. Heinzelmann, "A novel non-isolated active charge balancing architecture for lithium-ion batteries," in 2018 International Symposium on Industrial Electronics (ISIE), 2018, pp. 471–475, https://doi.org/10.1109/ISIE.2018.8433669.

[135] J. Qi and D. Dah-Chuan Lu, "Review of battery cell balancing techniques," 2014 Australas. Univ. Power Eng. Conf. AUPEC 2014 - Proc., no. October, pp. 1–6, 2014, https://doi.org/10.1109/AUPEC.2014.6966514.

[136] Y. Barsukov and J. Qian, Battery power management for portable devices. Boston : Artech House, 2013.

[137] L. Zheng, J. Zhu, G. Wang, F. Engineering, I. Technology, and T. Sydney, "A Comparative Study of Battery Balancing Strategies for Different Battery Operation Processes," 2016 IEEE Transp. Electrif. Conf. Expo, 2016, https://doi.org/10.1109/ITEC.2016.7520204.

[138] D. P. Finegan *et al.*, "In-operando high-speed tomography of lithium-ion batteries during thermal runaway," Nat. Commun., vol. 6, pp. 1–10, 2015, https://doi.org/10.1038/ncomms7924.

[139] D. A. J. Rand, D. P. Boden, C. S. Lakshmi, R. F. Nelson, and R. D. Prengaman, "Manufacturing and operational issues with lead-acid batteries," J. Power Sources, vol. 107, pp. 280–300, 2002.

[140] J. Garche, A. Jossen, and H. Dijring, "The influence of different operating conditions, especially over-discharge, on the lifetime and performance of lead/acid batteries for photovoltaic systems," J. Power Sources, vol. 67, no. 1–2, pp. 201–212, 1997, https://doi.org/https://doi.org/10.1016/S0378-7753(97)02601-3.

[141] D. Myall, D. Ivanov, W. Larason, M. Nixon, and H. Moller, "Accelerated reported battery capacity loss in 30 kWh variants of the Nissan Leaf," Preprints, no. March,

2018, https://doi.org/10.20944/preprints201803.0122.v1.

[142] "Tesla Battery Survey," 2021. https://docs.google.com/spreadsheets/d/1c3m9wqlxPBo8ziDYVm5cHRzNCHZbtI_2vVhlXksX9Jc/edit#gid=826479810 (accessed Jan. 16, 2021).

[143] D. Andrea, Battery management systems for large lithium battery packs. Artech House Publishers, 2010.

[144] Y. Barsukov and J. Qian, Battery Power Management for Portable Devices. Norwood: Artech House. Power Engineering Series, 2013.

[145] M. M. U. Rehman *et al.*, "Modular Approach for Continuous Cell-level Balancing to Improve Performance of Large Battery Packs," 2014 IEEE Energy Convers. Congr. Expo., pp. 4327–4334, 2014, https://doi.org/10.1109/ECCE.2014.6953991.

[146] Y. Barsukov, "Battery cell balancing: what to balance and how," Texas Instruments, pp. 1–8, 2005, [Online]. Available: http://focus.ti.com/download/trng/docs/seminar/Topic 2 - Battery Cell Balancing - What to Balance and How.pdf.

[147] Q. Ouyang and J. Chen, "Optimal Cell-to-Cell Balancing Topology Design for Serially Connected Lithium-Ion Battery Packs," IEEE Trans. Sustain. Energy, vol. 9, no. 1, pp. 350–360, 2018, https://doi.org/10.1109/TSTE.2017.2733342.

[148] M. Daowd, N. Omar, P. van den Bossche, and J. van Mierlo, "A review of passive and active battery balancing based on MATLAB/Simulink," Int. Rev. Electr. Eng., vol. 6, no. 7, pp. 2974–2989, 2011.

[149] T. H. Phung *et al.*, "Integrated converter network for active balancing structure of battery," in CIPS. International Conference on Integrated Power Electronics SystemsInternational Conference on Integrated Power Electronics Systems, 2016, p. 6.

[150] G. Min and J. Ha, "Active Cell Balancing Algorithm for Serially Connected Li-Ion Batteries based on Power to Energy Ratio," 2017 IEEE Energy Convers. Congr. Expo., pp. 2748–2753, 2017.

[151] B. Jiang, "Active Cell Balancing Algorithms in Lithium-ion Battery," 2020.

[152] B. Jiang, Y. Liu, X. Huang, and R. R. R. Prakash, "A New Battery Active Balancing Method with Supercapacitor Considering Regeneration Process," IECON Proc. (Industrial Electron. Conf., vol. 2020-Octob, pp. 2364–2369, 2020, https://doi.org/10.1109/IECON43393.2020.9254839.

[153] J. Cao, N. Schofield, and A. Emadi, "Battery balancing methods: A comprehensive review," 2008 IEEE Veh. Power Propuls. Conf. VPPC 2008, pp. 3–8, 2008, https://doi.org/10.1109/VPPC.2008.4677669.

[154] Z. B. Omariba, L. Zhang, and D. Sun, "Review of Battery Cell Balancing Methodologies for Optimizing Battery Pack Performance in Electric Vehicles," IEEE Access, vol. 7, pp. 129335–129352, 2019,

https://doi.org/10.1109/ACCESS.2019.2940090.

[155] T. Duraisamy and D. Kaliyaperumal, “Active cell balancing for electric vehicle battery management system,” Int. J. Power Electron. Drive Syst., vol. 11, no. 2, pp. 571–579, 2020, https://doi.org/10.11591/ijpeds.v11.i2.pp571-579.

[156] A. Ziegler, D. Oeser, B. Arndt, and A. Ackva, “Comparison of Active and Passive Balancing by a Long Term Test Including a Post-Mortem Analysis of all Single Battery Cells,” 2018 Int. IEEE Conf. Work. Óbuda Electr. Power Eng., pp. 15–20, 2018.

[157] L. Wei, L. Jie, S. Wenji, and F. Ziping, “Study on passive balancing characteristics of serially connected lithium-ion battery string,” in 2017 13th IEEE International Conference on Electronic Measurement & Instruments (ICEMI), Oct. 2017, vol. 2018-Janua, pp. 489–495, https://doi.org/10.1109/ICEMI.2017.8265862.

[158] Amin, K. Ismail, A. Nugroho, and S. Kaleg, “Passive balancing battery management system using MOSFET internal resistance as balancing resistor,” Proceeding - ICSEEA 2017 Int. Conf. Sustain. Energy Eng. Appl. "Continuous Improv. Sustain. Energy Eco-Mobility", vol. 2018-Janua, pp. 151–155, 2017, https://doi.org/10.1109/ICSEEA.2017.8267701.

[159] X. Wei and B. Zhu, “The research of vehicle power li-ion battery pack balancing method,” ICEMI 2009 - Proc. 9th Int. Conf. Electron. Meas. Instruments, pp. 2498–2502, 2009, https://doi.org/10.1109/ICEMI.2009.5274520.

[160] A. Baughman and M. Ferdowsi, “Double-tiered capacitive shuttling method for balancing series-connected batteries,” 2005 IEEE Veh. Power Propuls. Conf. VPPC, vol. 2005, pp. 109–113, 2005, https://doi.org/10.1109/VPPC.2005.1554531.

[161] H. S. Park, C. H. Kim, K. B. Park, G. W. Moon, and J. H. Lee, “Design of a charge equalizer based on battery modularization,” IEEE Trans. Veh. Technol., vol. 58, no. 7, pp. 3216–3223, 2009, https://doi.org/10.1109/TVT.2009.2015331.

[162] Y. Takeda and H. Koizumi, “Modularized double-Tiered switched capacitor voltage equalizer,” Proc. IECON 2017 - 43rd Annu. Conf. IEEE Ind. Electron. Soc., vol. 2017-Janua, pp. 2782–2787, 2017, https://doi.org/10.1109/IECON.2017.8216469.

[163] T. H. Phung, J. C. Crebier, A. Chureau, A. Collet, and V. Nguyen, “Optimized structure for next-to-next balancing of series-connected lithium-ion cells,” Conf. Proc. - IEEE Appl. Power Electron. Conf. Expo. - APEC, pp. 1374–1381, 2011, https://doi.org/10.1109/APEC.2011.5744771.

[164] C.-C. Hua, Y.-H. Fang, and J.-F. Huang, “Inductor based equalizer with a chain structure of switched capacitor to improve balancing speed,” in 2015 18th International Conference on Electrical Machines and Systems (ICEMS), Oct. 2015, pp. 2151–2154, https://doi.org/10.1109/ICEMS.2015.7385396.

[165] L. R. Yu, Y. C. Hsieh, W. C. Liu, and C. S. Moo, “Balanced discharging for serial battery power modules with boost converters,” ICSSE 2013 - IEEE Int. Conf. Syst. Sci. Eng. Proc., pp. 449–453, 2013, https://doi.org/10.1109/ICSSE.2013.6614708.

[166] T. H. Wu, C. S. Moo, and C. H. Hou, "A battery power bank with series-connected buck-boost-type battery power modules," Energies, vol. 10, no. 5, pp. 1–12, 2017, https://doi.org/10.3390/en10050650.

[167] R. Koch, A. Jossen, and R. Kuhn, "Novel bidirectional multiple-input multiple-output converter for simultaneous direct battery module balancing," World Electr. Veh. J., vol. 6, no. 3, pp. 495–501, 2013, https://doi.org/10.3390/wevj6030495.

[168] Y. S. Lee, C. Y. Duh, G. T. Chen, and S. C. Yang, "Battery equalization using bi-directional Cûk converters in DCVM operation," PESC Rec. - IEEE Annu. Power Electron. Spec. Conf., vol. 2005, pp. 765–771, 2005, https://doi.org/10.1109/PESC.2005.1581713.

[169] A. F. Moghaddam and A. Van den Bossche, "A Battery Equalization Technique Based on Ćuk Converter Balancing for Lithium Ion Batteries," in 2019 8th International Conference on Modern Circuits and Systems Technologies (MOCAST), May 2019, pp. 1–4, https://doi.org/10.1109/MOCAST.2019.8741779.

[170] Y. S. Lee, C. E. Tsai, Y. P. Ko, and M. W. Cheng, "Charge equalization using quasi-resonant converters in battery string for medical power operated vehicle application," 2010 Int. Power Electron. Conf. - ECCE Asia -, IPEC 2010, pp. 2722–2728, 2010, https://doi.org/10.1109/IPEC.2010.5542347.

[171] Y. S. Lee and G. T. Cheng, "Quasi-resonant zero-current-switching bidirectional converter for battery equalization applications," IEEE Trans. Power Electron., vol. 21, no. 5, pp. 1213–1224, 2006, https://doi.org/10.1109/TPEL.2006.880349.

[172] J. W. Shin, G. S. Seo, C. Y. Chun, and B. H. Cho, "Selective Flyback balancing circuit with improved balancing speed for series connected Lithium-ion batteries," 2010 Int. Power Electron. Conf. - ECCE Asia -, IPEC 2010, pp. 1180–1184, 2010, https://doi.org/10.1109/IPEC.2010.5543502.

[173] Feng Ran, Hao Xu, Yuan Ji, Jiaqi Qin, and Wenhui Li, "An active balancing circuit for lithium battery management system with optoelectronic switches," in TENCON 2015 - 2015 IEEE Region 10 Conference, Nov. 2015, pp. 1–5, https://doi.org/10.1109/TENCON.2015.7373096.

[174] C. Bonfiglio and W. Roessler, "A cost optimized battery management system with active cell balancing for lithium ion battery stacks," 5th IEEE Veh. Power Propuls. Conf. VPPC '09, pp. 304–309, 2009, https://doi.org/10.1109/VPPC.2009.5289837.

[175] A. Farzan Moghaddam and A. Van Den Bossche, "Flyback Converter Balancing Technique for Lithium Based Batteries," 2019 8th Int. Conf. Mod. Circuits Syst. Technol. MOCAST 2019, pp. 2019–2022, 2019, https://doi.org/10.1109/MOCAST.2019.8741893.

[176] M. Raeber, A. Heinzelmann, and D. O. Abdeslam, "Analysis of an Active Charge Balancing Method Based on a Single Nonisolated DC/DC Converter," IEEE Trans. Ind. Electron., vol. 68, no. 3, pp. 2257–2265, 2021, https://doi.org/10.1109/TIE.2020.2972449.

[177] X. Pichon, J. C. Crébier, D. Riu, and A. Collet, "Balancing control based on States of Charge and States of Health estimates at cell level," no. 1, pp. 204–211, 2015, https://doi.org/10.1109/ICCEP.2015.7177624.

[178] Z. Zhang and B. Sisk, "Model-based analysis of cell balancing of lithium-ion batteries for electric vehicles," SAE Int. J. Altern. Powertrains, vol. 2, no. 2, pp. 379–388, 2013, https://doi.org/10.4271/2013-01-1755.

[179] W. G. Hurley and W. H. Wölfle, Transformers and Inductors for Power Electronics Transformers and Electronics, vol. 8, no. September. Hoboken, NJ, USA, 2013.

[180] T. Eichhorn, "Boost Converter Efficiency Through Accurate Calculations," Power Electron. Technol. Mag. Online, vol. September, pp. 30–35, 2008, [Online]. Available: https://www.powerelectronics.com/power-management/boost-converter-efficiency-through-accurate-calculations.

[181] F. De Stasi, "Working with Boost Converters," no. June. Texas Instruments Incorporated, Dallas, TX, USA, pp. 1–11, 2015, [Online]. Available: http://www.ti.com/lit/an/snva731/snva731.pdf.

[182] Magnetics, "Inductor Design," 2018, 2018. https://www.mag-inc.com/Design/Design-Tools/Inductor-Design (accessed Jul. 15, 2018).

[183] A. Ayachit and M. K. Kazimierczuk, "Power losses and efficiency analysis of the quadratic buck converter in CCM," Midwest Symp. Circuits Syst., no. 5, pp. 463–466, 2014, https://doi.org/10.1109/MWSCAS.2014.6908452.

[184] D. Parth and E. Tonazzo, "Controller IC for Industrial Applications," 2011.

[185] J.-M. Liu, P.-Y. Wang, and T.-H. Kuo, "A Current-mode DC–DC buck converter with efficiency-optimized frequency control and reconfigurable compensation," IEEE Trans. Power Electron., vol. 27, no. 2, pp. 869–880, Feb. 2012, https://doi.org/10.1109/TPEL.2011.2162079.

[186] "Servei Meteorològic de Catalunya. Available online: http://www.meteo.cat/wpweb/climatologia/serveis-i-dades-climatiques/series-climatiques-historiques/ (accessed on 15 June 2018)." [Online]. Available: http://www.meteo.cat/.

[187] M. Daowd, M. Antoine, N. Omar, P. Lataire, P. Van Den Bossche, and J. Van Mierlo, "Battery Management System—Balancing Modularization Based on a Single Switched Capacitor and Bi-Directional DC/DC Converter with the Auxiliary Battery," Energies, vol. 7, no. 5, pp. 2897–2937, Apr. 2014, https://doi.org/10.3390/en7052897.

[188] X. Wei and B. Zhu, "The Research of Vehicle Power Li-ion Battery Pack Balancing Method," 2017 IEEE Energy Convers. Congr. Expo., pp. 498–502, 2009, https://doi.org/10.1109/ICEMI.2009.5274520.

[189] Traco Power, "Traco Power TEP 150WI," 2019. .

[190] J. Wang, B. Cao, Q. Chen, and F. Wang, "Combined state of charge estimator for electric vehicle battery pack," Control Eng. Pract., vol. 15, no. 12, pp. 1569–1576,

2007, https://doi.org/10.1016/j.conengprac.2007.03.004.

[191] E. M. Krieger, J. Cannarella, and C. B. Arnold, "A comparison of lead-acid and lithium-based battery behavior and capacity fade in off-grid renewable charging applications," Energy, vol. 60, pp. 492–500, 2013, https://doi.org/10.1016/j.energy.2013.08.029.

[192] M. Merlo, "Ngarenanyuki Secondary School (Tanzania)." http://www.e4g.polimi.it/?page_id=114 (accessed Jan. 25, 2021).

[193] UCCS, "Battery Management Systems, Volume I: Battery Modeling," 2015. .

[194] P. Van Overschee and B. De Moor, Subspace Identification for Linear Systems. Theory, Implementation and Applications. Boston, MA: Springer US, 1996.

[195] X. G. Yang, Y. Leng, G. Zhang, S. Ge, and C. Y. Wang, "Modeling of lithium plating induced aging of lithium-ion batteries: Transition from linear to nonlinear aging," J. Power Sources, vol. 360, pp. 28–40, 2017, https://doi.org/10.1016/j.jpowsour.2017.05.110.

[196] G. L. Plett, "Algebraic Solution for Modeling SEI Layer Growth," ECS Electrochem. Lett., vol. 2, no. 7, pp. A63–A65, Apr. 2013, https://doi.org/10.1149/1.004307eel.

[197] R. Machado, "Experimental parameter identification of a physics-based model for solid-electrolyte interphase (SEI) layer growth in lithium-ion batteries," Mater's thesis. University of Colorado Colorado Springs, 2020.

[198] J.-S. Yang, J.-Y. Choi, G.-H. An, Y.-J. Choi, M.-H. Kim, and D.-J. Won, "Optimal Scheduling and Real-Time State-of-Charge Management of Energy Storage System for Frequency Regulation," Energies, vol. 9, no. 12, p. 1010, 2016, https://doi.org/10.3390/en9121010.

[199] P. Ramadass, B. Haran, R. White, and B. N. Popov, "Mathematical modeling of the capacity fade of Li-ion cells," J. Power Sources, vol. 123, no. 2, pp. 230–240, 2003, https://doi.org/10.1016/S0378-7753(03)00531-7.

[200] A. M. Colclasure, K. A. Smith, and R. J. Kee, "Modeling detailed chemistry and transport for solid-electrolyte-interface (SEI) films in Li-ion batteries," Electrochim. Acta, vol. 58, no. 1, pp. 33–43, 2011, https://doi.org/10.1016/j.electacta.2011.08.067.

[201] R. R. Jobman, "Identification of Lithium-Ion-Cell Physics-Model Parameter Values," PhD Thesis. University of Colorado Colorado Springs, 2016.

[202] K. Kumaresan, G. Sikha, and R. E. White, "Thermal model for a Li-ion cell," J. Electrochem. Soc., vol. 155, no. 2, pp. 164–171, 2008, https://doi.org/10.1149/1.2817888.

[203] S. Yu, S. Kim, T. Y. Kim, J. H. Nam, and W. Il Cho, "Model prediction and experiments for the electrode design optimization of LiFePo4/graphite electrodes in high capacity lithium-ion batteries," Bull. Korean Chem. Soc., vol. 34, no. 1, pp. 79–88, 2013, https://doi.org/10.5012/bkcs.2013.34.1.79.

[204] J. Cannarella and C. B. Arnold, "The effects of defects on localized plating in lithium-ion batteries," J. Electrochem. Soc., vol. 162, no. 7, pp. A1365–A1373, 2015, https://doi.org/10.1149/2.1051507jes.

[205] M. Mastali, M. Farkhondeh, S. Farhad, R. A. Fraser, and M. Fowler, "Electrochemical modeling of commercial LiFePO4 and graphite electrodes: Kinetic and transport properties and their temperature dependence," J. Electrochem. Soc., vol. 163, no. 13, pp. A2803–A2816, 2016, https://doi.org/10.1149/2.1151613jes.

[206] D. R. Baker and M. W. Verbrugge, "Modeling overcharge at graphite electrodes: Plating and dissolution of lithium," J. Electrochem. Soc., vol. 167, no. 1, 2020, https://doi.org/10.1149/2.0042001JES.

[207] L. Kraft, J. B. Habedank, A. Frank, A. Rheinfeld, and A. Jossen, "Modeling and simulation of pore morphology modifications using laser-structured graphite anodes in lithium-ion batteries," J. Electrochem. Soc., vol. 167, no. 1, 2020, https://doi.org/10.1149/2.0062001JES.

[208] A. Rodríguez, G. L. Plett, and M. S. Trimboli, "Improved transfer functions modeling linearized lithium-ion battery-cell internal electrochemical variables," J. Energy Storage, vol. 20, no. April, pp. 560–575, 2018, https://doi.org/10.1016/j.est.2018.06.015.

[209] Z. Chu *et al.*, "A control-oriented electrochemical model for lithium-ion battery. Part II: Parameter identification based on reference electrode," J. Energy Storage, vol. 27, no. December 2019, p. 101101, 2020, https://doi.org/10.1016/j.est.2019.101101.

[210] S. G. Stewart, V. Srinivasan, and J. Newman, "Modeling the Performance of Lithium-Ion Batteries and Capacitors during Hybrid-Electric-Vehicle Operation," J. Electrochem. Soc., vol. 155, no. 9, p. A664, 2008, https://doi.org/10.1149/1.2953524.

[211] M. Tang, P. Albertus, and J. Newman, "Two-Dimensional Modeling of Lithium Deposition during Cell Charging," J. Electrochem. Soc., vol. 156, no. 5, p. A390, 2009, https://doi.org/10.1149/1.3095513.

[212] N. Kotak, P. Barai, A. Verma, A. Mistry, and P. P. Mukherjee, "Electrochemistry-mechanics coupling in intercalation electrodes," J. Electrochem. Soc., vol. 165, no. 5, pp. A1064–A1083, 2018, https://doi.org/10.1149/2.0621805jes.

[213] L. von Kolzenberg, A. Latz, and B. Horstmann, "Solid–Electrolyte Interphase During Battery Cycling: Theory of Growth Regimes," ChemSusChem, vol. 13, no. 15, pp. 3901–3910, 2020, https://doi.org/10.1002/cssc.202000867.

[214] S. Das, P. M. Attia, W. C. Chueh, and M. Z. Bazant, "Electrochemical kinetics of SEI growth on carbon black II: Modeling," arXiv, vol. 166, no. 4, 2019, https://doi.org/10.1149/2.0241904jes.

[215] R. Fu, S. Y. Choe, V. Agubra, and J. Fergus, "Development of a physics-based degradation model for lithium ion polymer batteries considering side reactions," J. Power Sources, vol. 278, pp. 506–521, 2015, https://doi.org/10.1016/j.jpowsour.2014.12.059.

[216] M. Safari, M. Morcrette, A. Teyssot, and C. Delacourt, "Multimodal physics-based aging model for life prediction of Li-Ion batteries," J. Electrochem. Soc., vol. 156, no. 3, pp. 145–153, 2009, https://doi.org/10.1149/1.3043429.

[217] G. L. Plett, "Reduced-Order multi-modal model of SEI layer growth for management and control of lithium-ion batteries," in 2017 IEEE Conference on Control Technology and Applications (CCTA), Kohala Coast, Hawai'i, Aug. 2017, vol. 2017-Augus, pp. 389–395, https://doi.org/10.1109/CCTA.2017.8062493.

[218] D. García Elvira, H. Valderrama Blavi, À. Cid Pastor, J. M. Bosque Moncusí, and L. Martínez Salamero, "Optimización del rendimiento de una microrred CC con tensión de bus variable," in Seminario Anual de Automática, Electrónica Industrial e Instrumentación (SAAEI), 2018.

[219] D. G. Elvira, H. V. Blaví, À. C. Pastor, and L. M. Salamero, "Efficiency Optimization of a Variable Bus Voltage DC Microgrid," Energies, vol. 11, no. 11, p. 3090, Nov. 2018, https://doi.org/10.3390/en11113090.

[220] D. G. Elvira, H. Valderrama Blavi, J. M. Bosque Moncusi, A. Cid Pastor, J. A. Garriga Castillo, and L. Martinez Salamero, "Active battery balancing via a switched DC/DC Converter: Description and performance analysis," 2019 16th Conf. Electr. Mach. Drives Power Syst. ELMA 2019 - Proc., no. June, pp. 6–8, 2019, https://doi.org/10.1109/ELMA.2019.8771697.

[221] J. A. Garriga, H. Valderrama-Blavi, D. Garcia-Elvira, J. A. Barrado, and A. Cid-Pastor, "Impedance matching for an inductive harvesting transducer," 2019 16th Conf. Electr. Mach. Drives Power Syst. ELMA 2019 - Proc., no. June, pp. 6–8, 2019, https://doi.org/10.1109/ELMA.2019.8771485.

[222] D. García Elvira, G. L. Plett, R. Machado, H. Valderrama Vlabi, À. Cid Pastor, and L. Martínez Salamero, "Modelo de degradación por crecimiento de la capa Interfase Sólido-Electrolito en una batería Li-NMC," in Seminario Anual de Automática, Electrónica Industrial e Instrumentación (SAAEI) 2020, 2020.

UNIVERSITAT ROVIRA I VIRGILI
CONTRIBUTIONS ON DC MICROGRID SUPERVISION AND CONTROL STRATEGIES FOR EFFICIENCY OPTIMIZATION THROUGH BATTERY MODELING, MANAGEMENT, AND BALANCING TECHNIQUES
David García Elvira

UNIVERSITAT
ROVIRA i VIRGILI